Fall 2011

Multiscale numerical analysis of airflow in CT-based subject specific breathing human lungs

Jiwoong Choi
University of Iowa

MULTISCALE NUMERICAL ANALYSIS OF AIRFLOW IN CT-BASED SUBJECT SPECIFIC BREATHING HUMAN LUNGS

by

Jiwoong Choi

An Abstract

Of a thesis submitted in partial fulfillment
of the requirements for the Doctor of
Philosophy degree in Mechanical Engineering
in the Graduate College of
The University of Iowa

December 2011

Thesis Supervisor: Professor Ching-Long Lin

ABSTRACT

An imaging-based computational framework for simulation of airflow in subject specific breathing human lungs is established. The three-dimensional (3D) airways of up to 9 generations and lobes are segmented and reconstructed from computed tomography (CT) images. Beyond the CT-resolved 3D airways, a volume filling method is applied to generate the one-dimensional (1D) conducting airway tree that bridges the central airway with the lung parenchyma. Through 3D-1D airway coupling, a novel image-registration-based boundary condition (BC) is proposed to derive physiologically-consistent regional ventilation for the whole lung and provide flow-rate fractions needed for the 3D airway model via the 1D-tree connectivity and the mass conservation. The in-house parallel finite-element large-eddy simulation (LES) code enables to capture genuinely complex airflow characteristics in a computationally-efficient manner. The 3D-1D coupling framework is multiscale because it can not only predict detailed flows in the 3D central airways at a local level, but also yields subject-specific physiologically-consistent regional ventilation at the whole lung level.

The framework has been applied to investigate pulmonary airflow and lung physiology. For example, the study of intra- and inter-subject variability provides insight into the effect of airway geometry on airflow structure. The relations between airflow structure, energy dissipation, and airway resistance under normal breathing condition have also been studied, showing similarity behaviors for inspiratory and expiratory flows. In the study of high-frequency oscillatory ventilation, we have compared counter-flow structures near flow reversal (namely phase change between inspiration and expiration) and quantified associated convective mixing in both idealized and CT-based airway models. Furthermore, the image-registration-derived displacement field is used to deform 3D-1D airway models for breathing lung simulation and estimate diameter changes of 1D airway segments during deformation. In conjunction with an arbitrary Lagrangian

Eulerian method, airflow in a breathing lung has been simulated and compared with that of a rigid airway model. The results show that the proposed computational framework is promising in better understanding the human lung physiology and improving the treatment of diseased lung.

Abstract Approved:_____
Thesis Supervisor

_____
Title and Department

_____
Date

MULTISCALE NUMERICAL ANALYSIS OF AIRFLOW IN CT-BASED SUBJECT SPECIFIC BREATHING HUMAN LUNGS

by

Jiwoong Choi

A thesis submitted in partial fulfillment
of the requirements for the Doctor of
Philosophy degree in Mechanical Engineering
in the Graduate College of
The University of Iowa

December 2011

Thesis Supervisor: Professor Ching-Long Lin

Graduate College
The University of Iowa
Iowa City, Iowa

CERTIFICATE OF APPROVAL

_____

PH.D. THESIS

_____

This is to certify that the Ph.D. thesis of

Jiwoong Choi

has been approved by the Examining Committee
for the thesis requirement for the Doctor of Philosophy
degree in Mechanical Engineering at the December 2011 graduation.

Thesis Committee: _____
Ching-Long Lin, Thesis Supervisor

_____
Jia Lu

_____
James H. Buchholz

_____
Eric A. Hoffman

_____
Merryn H. Tawhai

To the one who gave us breath

ACKNOWLEDGMENTS

The presented work in this thesis could not have been done without the great help of many people. I am very grateful for all the support from the staff and other students in the labs throughout the years. First of all, I would like to thank Dr. Ching-Long Lin, my thesis supervisor, for always giving great opportunities and supports with patience throughout this project. All his guidance and encouragement during the course of this research are sincerely appreciated. I would also like to thank Drs. Eric Hoffman, Merryn Tawhai, James Buchholz, and Jia Lu. Such an interdisciplinary project cannot go so smooth without the help from all those experts. I am also very grateful to Drs. Jung Yul Yoo and Haecheon Choi for having recommended me for this chance of study and for important advices, and to Dr. Noma Park for his studies and advices that helped me complete a challenging task at the early stage of the course of study.

I have also enjoyed working with the former lab colleagues Drs. Taehun Lee, Haegyun Lee, Guohua Xia, Haribalan Kumar, and Youbing Yin and also Andrew Lambert, as well as the current lab colleagues Shinjiro Miyawaki, Dan Wu, Nathan Ellingwood, Maged Awadalla, Sanghun Choi, and Nariman Jahani, tackling challenging issues of the digital human lung model. I want to thank them all for valuable discussions and academic supports. Sincerely, I would like to thank my parents, sister, and relatives for their love, sacrifices and trust to the end in this long journey. I also thank the members of the church family, who I cannot name all in the short acknowledgments, for their prayers and encouragements. I thank Mr. Sang Cheol Lee for providing me with valuable insights. Lastly, I offer my regards and blessings to all of those who supported me in any respect during the completion of the project.

This study was supported in part by NIH Grants R01-HL094315, R01-HL064368, R01-EB005823, and S10-RR022421. I also thank the Texas Advanced Computing Center

(TACC), San Diego Super Computing Center (SDSC), and TeraGrid/XSEDE sponsored by the National Science Foundation for the computer time.

ABSTRACT

An imaging-based computational framework for simulation of airflow in subject specific breathing human lungs is established. The three-dimensional (3D) airways of up to 9 generations and lobes are segmented and reconstructed from computed tomography (CT) images. Beyond the CT-resolved 3D airways, a volume filling method is applied to generate the one-dimensional (1D) conducting airway tree that bridges the central airway with the lung parenchyma. Through 3D-1D airway coupling, a novel image-registration-based boundary condition (BC) is proposed to derive physiologically-consistent regional ventilation for the whole lung and provide flow-rate fractions needed for the 3D airway model via the 1D-tree connectivity and the mass conservation. The in-house parallel finite-element large-eddy simulation (LES) code enables to capture genuinely complex airflow characteristics in a computationally-efficient manner. The 3D-1D coupling framework is multiscale because it can not only predict detailed flows in the 3D central airways at a local level, but also yields subject-specific physiologically-consistent regional ventilation at the whole lung level.

The framework has been applied to investigate pulmonary airflow and lung physiology. For example, the study of intra- and inter-subject variability provides insight into the effect of airway geometry on airflow structure. The relations between airflow structure, energy dissipation, and airway resistance under normal breathing condition have also been studied, showing similarity behaviors for inspiratory and expiratory flows. In the study of high-frequency oscillatory ventilation, we have compared counter-flow structures near flow reversal (namely phase change between inspiration and expiration) and quantified associated convective mixing in both idealized and CT-based airway models. Furthermore, the image-registration-derived displacement field is used to deform 3D-1D airway models for breathing lung simulation and estimate diameter changes of 1D airway segments during deformation. In conjunction with an arbitrary Lagrangian

Eulerian method, airflow in a breathing lung has been simulated and compared with that of a rigid airway model. The results show that the proposed computational framework is promising in better understanding the human lung physiology and improving the treatment of diseased lung.

TABLE OF CONTENTS

LIST OF TABLES

Table

LIST OF FIGURES

Figure

CHAPTER 1

INTRODUCTION

1.1 Motivation

In the past decades, computational fluid dynamics (CFD) has been developed as a promising tool for the understanding of the structure-function relationships of pulmonary air flow in human lungs. It is capable of a non-invasive analysis of the flow field with the limitation of the understanding regarding in vivo conditions. Since flow characteristics are mainly dependent on the geometrical configuration of airways and regional parenchymal mechanics, it is desirable to conduct a subject specific CFD with anatomically realistic airway geometry and a physiologically consistent boundary condition (BC). Due to the complexity of the human tracheobronchial tree, most early CFD studies of pulmonary air flow used either the symmetric Weibel model (Weibel 1963) or the asymmetric Horsfield model (Horsfield *et al.* 1971). A representative, though not exhaustive, list of such studies can be found in Comer *et al.* (2001a,b), Nowak *et al.* (2003), Zhang and Kleinstreuer (2002, 2004), and van Ertbruggen *et al.* (2005). Although those studies provide insights into the characteristics of flow in systems of bifurcating tubes, their idealized airway models lack subject specific geometrical features for assessing an individual's flow patterns and the rate of lung structure in determining gas and particle distribution patterns.

Recent advancements in imaging capabilities and parallel computation make it possible to compute airflow in anatomically accurate and subject specific physical domains (Hoffman *et al.* 2004, Allen *et al.* 2004, Ma and Lutchen 2006, Brouns *et al.* 2007). This approach enables correct incorporation of the influence of anatomical features such as curved airways, cartilage ridges, and diameter variation along an airway (Nowak *et al.* 2003, Tawhai *et al.* 2004). However, despite the evidence that geometrical details are important (Brouns *et al.* 2007, Menon *et al.* 1985, Martonen *et al.* 1994, Zhang

and Finlay 2005, Lin *et al.* 2007) most numerical studies using medical image-based airway geometries are still limited to a few generations of intra-thoracic airways without the upper airways (de Rochefort *et al.* 2007) or are simplified down to smooth and straight shapes (Heenan *et al.* 2003). Furthermore, the morphological features of these airways, and therefore their effects on the flow, are tied to a single subject upon whom the realistic model was based. More recently, three-dimensional (3D) realistic airway geometries with major branches derived from high resolution computed tomography (CT) images have been used in CFD analyses (Freitas and Schröder 2008, Lin *et al.* 2007, 2009). In addition, the use of one-dimensional (1D) centerline airway models from subject specific lobe configurations was introduced by Tawhai *et al.* (2004), and this airway tree generation has been used to investigate gas mixing (Tawhai and Hunter, 2001).

In most of the CFD studies for human lungs, simple uniform BCs (either uniform velocity, uniform pressure, or uniform flow distribution) were imposed on the distal ends of the peripheral airway segments, which may limit the accuracy of the results due to the inability to take into consideration the realistic nonuniform ventilation. De Backer *et al.* (2008) attempted to describe a subject specific BC by using two different pressure values at the 3D CT-resolved ending segments in left and right lungs for a steady inspiratory flow. While De Backer *et al.* (2008) predicted a different flow rate between left and right lungs, their approach is not sufficient to capture the heterogeneity of ventilation. Recently, Tawhai *et al.* (2006, 2009) developed a soft-tissue-mechanics-based model for elastic deformation of compressible lung tissue, in which the local volume change of peripheral tissue can be used for setting a flow BC for the 1D centerline airway model. And Lin *et al.* (2009) proposed a multi-scale CFD framework that couples a 3D CT-resolved central airway tree with a 1D centerline airway tree in a physiologically and morphometrically consistent manner: the 1D peripheral airway tree serves as a link between 3D central airway tree and lung parenchyma. With the 1D and 3D coupling frameworks, a subject

specific BC can be imposed on the 3D central airways via the 1D tree using the information of regional ventilation, and the flow properties can be represented in an entire conducting airway.

Regional ventilation has been measured using imaging techniques, such as magnetic resonance (MR) (Salerno *et al.* 2002, van Beek *et al.* 2004) and xenon CT (Chon *et al.* 2007, 2005). Currently MR is only partially quantitative because of its limited capability for a depiction of anatomic details and its high cost. Xenon CT can predict a high resolution ventilation map but it requires the use of expensive xenon gas and associated hardwares for a controlled gas delivery. Alternatively, regional ventilation can be generated by registering two volumetric CT datasets (Christensen *et al.* 2007, Guerrero *et al.* 2006, Reinhardt *et al.* 2008, Yin *et al.* 2009a). In contrast to MR or xenon CT, such a registration-based analysis of regional ventilation requires only two volumetric datasets of lungs at different levels of inflation and the resulting ventilation map has a high resolution.

Another common limitation found in most of the CFD studies is the numerical approach itself. Most CFD studies on pulmonary airflow have been conducted by Reynolds averaged Navier-Stokes simulation (RANS). However, RANS has been developed by tuning up for single types of flow conditions and usually for wall-induced turbulent transition, which is different from the airflow in subject specific human lungs, in which complex features of various flow types coexist.

1.2 Aims

The main objective of this study is to establish a CT-data-driven, multiscale, high-fidelity parallel computing framework to study the structure-function relationship in subject specific human lungs. Potential applications of this study are to improve the following fields of study:

- Lung physiology (for a better understanding of structure-function relationship),

- Drug delivery (for a targeted drug delivery),
- Biomedical imaging (for the advancement of Xenon/Helium enhanced CT/MRI imaging), and
- Life/health sciences (for individualized medicine).

To achieve this goal, the present study has two main frames of specific aims. The first is to integrate a comprehensive set of methodologies to solve the multiscale airflow field in the entire conducting airway. The mothods include

- The reconstruction of subject specific human airway models in CT-resolved and unresolved regions,
- Physiologically consistent boundary conditions,
- The large eddy simulation (LES) as a CFD method to capture complex flow characteristics,
- Multiscale simulation algorithm including the 1D fluid solver and 3D-1D coupling algorithm, and
- Additional methods for breathing lung simulation in consideration of lung deformation.

The second is to analyze the pulmonary airflow from viewpoints of fluid mechanics and respiratory physiology. This includes

- The investigation of variability of airflow in subject specific human lungs,
- A better understanding of the relationship between airway structure, airflow, and airway resistance of normal breathing,
- An application for the investigation of a clinically advantageous flow phenomenon, e.g. the counter-flow phenomenon of high frequency oscillatory ventilation (HFOV) and its role in convective mixing, and
- The examination of the structure-function relationship of lung deformation with the multiscale airflow characteristics in a breathing lung.

1.3 Thesis overview

To achieve the specific aims in Section 1.2, Chapters 2 through 4 integrate comprehensive methods for a multiscale numerical analysis of airflow in subject specific human airways. First, we review the CT-based reconstruction methods of multiscale human lungs in 3D and 1D frameworks, and present the development of physiologically consistent subject specific BCs using 3D-1D coupling in Chapter 2. Flow results of the proposed BCs and traditional BCs will be compared. Chapter 3 is devoted to the high fidelity CFD methods to accurately predict the flow behaviors in the CT-resolved complex human airway configurations. It includes appropriate setups of the in-house LES model and its pertinence to the target flow phenomenon. In Chapter 4, the methods and results of multiscale numerical simulation are presented. First, the 1D energy-based flow model is introduced and then 3D-1D coupling algorithm in association with the physiological BCs presented in Chapter 2.

Chapters 5 through 8 show extensive studies based on the presented methods on numerical, physiological, and physical issues for the airflow in subject specific human lungs. Chapter 5 provides a study on the intra- and intersubject variabilities of airflow, consisting of the effects of Reynolds number (Re), geometry dependency, and the effects of upper airway truncation. Airflow structure and viscous dissipation in the airway are studied during inspiration and expiration in Chapters 6 and the study is extended in Chapter 7 to improve an understanding of airway resistance, revealing similarity behavior and providing new coefficients of the energy-based airway resistance model (Pedley *et al.* 1970a) at both inspiration and expiration. This is an example of the capability of the current numerical model to reveal physiologically important issues in conjunction with the underlying flow physics. In addition, the flow structure and convective mixing process of high frequency ventilation is clarified in Chapter 8, in comparison with normal breathing. This is an example of applying the current numerical method to elucidate the mechanism of the clinically advantageous flow physics.

In Chapter 9, airway and lobe deformation is considered in the previously presented multiscale framework. Image registration-derived mapping is used to provide a regional displacement field and the volume deformation of 3D and 1D airway models. Also using the registration-derived regional deformation, an approach is proposed to estimate the diameter variation according to a change in the lung volume. The 3D and 1D simulation results are presented in central airways and in the entire conducting airway, and are discussed with respect to the effects of deformation and physiological consistency. Chapter 10 closes the thesis with concluding remarks and presents a list of topics for future work.

It is noted that parts of the thesis are based on the previously published journal articles: Section 4.2.4 is based on Yin *et al.* (2010), Chapter 5 is based on Choi *et al.* (2009), and Chapter 8 is based on Choi *et al.* (2010). Parts of these papers are also reorganized in this thesis.

CHAPTER 2
CT-BASED MULTISCALE HUMAN LUNG RECONSTRUCTION AND BOUNDARY CONDITIONS

A correct representation of geometry and boundary conditions are critical steps to the accurate analysis of the fluid motion. Multi-detector row computed tomography (MDCT)-derived airway reconstruction enables the representation of subject specific characteristics of the conducting airway and hence accurate analyses of gas flow behavior in individual human lungs. In this chapter, we review the reconstruction of the 3D and 1D subject specific airways from MDCT scans and a series of boundary conditions for the CFD analysis used in the current study.

2.1 CT-resolved 3D airway reconstruction

The imaging data were acquired using a Siemens Sensation 64 multi-detector row computed tomography (MDCT) scanner at the Iowa Comprehensive Lung Imaging Center (I-Clic), The University of Iowa. The CT data sets were then analyzed and the airway trees were segmented using the software suite Pulmonary Workstation (PW) series (VIDA® Diagnostics, Coralville Iowa) developed at the University of Iowa (Hoffman *et al.* 1992, 2003, Tschirren *et al.* 2002, Palágyi *et al.* 2003, Aykac *et al.* 2003). Details of the airway segmentation algorithms used are provided in Hoffman *et al.* (2004) and Tschirren *et al.* (2005a, 2005b). A detailed description regarding airway geometry reconstruction from MDCT images for CFD can be found in Lin *et al.* (2007). The imaging studies of human subjects were approved by the University of Iowa Institutional Review Board. Three human respiratory tracts reconstructed from MDCT scans are used in the current study.

Subject 1 was a non-smoking, white, non-Hispanic 20 year old female, with weight of 65.1 kg, height of 172.8 cm, and body mass index (BMI) of 21.8. Pulmonary

function test (PFT) provides with the forced expiratory volume in one second (FEV1) of 3.03 l/min (79.95%), the forced mid-expiratory flow rate (FEF25-75) of 2.55 liters (57.82%), the forced vital capacity (FVC) of 4.11 liters (92.99%), and the total lung capacity (TLC) of 6.19 liters (110.34%). Percentages in the parentheses denote statistically predicted values based on database for the patients of similar characteristics. It is noted that this patient, who was a self-reported normal, may have had small airway pathology (acute or chronic) indicated by an FEF25-75 which was only of 57.82% of that predicted, while other test results such as FVC% of 92.99 are normal. The thickness and in-plane resolution of the CT scans are 0.75 mm and 0.5254×0.5254 mm^2, respectively. Subject 2 is used for our inter-subject comparisons only where we have sought to evaluate structure-function (geometry-flow) relationships using the complete airway geometry. Subject 2 was also a non-smoking, white, non-Hispanic, 20 year old female, with similar body features of weight 62.1 kg, height of 170.6 cm, and BMI of 21.34. PFT of subject 2 reports FEV1 of 3.47 l/min (93.03%), FEF25-75 of 4.01 liters (91.55%), FVC of 3.45 liters (80%), and TLC of 6.22 liters (113%). This subject had fully normal PFT results. The thickness and in-plane resolution of the CT scans are 0.60 mm and 0.5430×0.5430 mm^2, respectively. Subject 3 is a 32-year old white non-Hispanic male. This subject has normal pulmonary function test (PFT) results. Two 3D CT volumetric datasets were acquired from subject 3 during breath-holds in a single scanning section. Scan parameters were: 120 kV, 100 mAs, slice thickness 1.3 mm, reconstruction kernel B, field of view 350 mm, rotation speed 0.5 sec, pitch 1.25. The subject lay supine and breathed through a mouthpiece during the scanning session. Each dataset consists of 553 slices with a spacing of 0.6 mm and a reconstruction matrix of 512×512 pixels. In-plane pixel spatial resolution is 0.68×0.68 mm^2. At the time of CT scanning for this subject, the CT images of this subject did not include the upper airways in order to reduce the radiation dose. To imply the effect of a laryngeal jet, the geometry of the upper airways from subject 2 was appended to the geometry of the central airways of subject 3.

2.2 CT-resolved airway tree analysis

A representative analysis of the airway tree of subject 3 is made in this section. Figure 2.1 shows the airway geometry that is composed of 5-7 generations of airway branching. The upper airway geometry, which comprises the mouth cavity, the oropharynx, and the larynx, is located above the letter "A" in the figure. There are a total of 70 ending airway segments in the CT-resolved 3D airway geometry.

The CT resolved airway tree was skeletonized using VIDA® to identify centerlines of individual branches and branch-point locations as shown in Figure 2.1. Table 2.1 lists the abbreviations and dimensions of the major airway segments of the subject and their corresponding generation number and lobar number. The units for average area, average diameter, and length of the branches are mm^2, mm, and mm, respectively. A detailed topological schematic of the segmented airway tree is illustrated in Figure 2.2. The five lobes are numbered from 1 to 5 corresponding to the left upper lobe (LUL), the left lower lobe (LLL), the right upper lobe (RUL), the right middle lobe (RML), and the right lower lobe (RLL). The trachea, the left main bronchus (LMB), the right main bronchus (RMB) and the intermediate bronchus (BronInt) are not anatomically classified into any of those lobes and are assigned a lobar number of 0. In the left lung, the commonly known bronchi LB1, LB2, LB3, LB4, and LB5 belong to the LUL, and the bronchi TriLB6, LB8 (LB7 non-existent), LB9, and LB10 belong to the LLL. In the right lung, the bronchi RB1, RB2, and RB3 are found in the RUL, RB4 and RB5 exist in the RML, and RB6, RB7, RB8, RB9 and RB10 reside in the RLL. The bronchus with an abbreviation and name containing an "X" is an aberrant bronchus which may not typically be found in other subjects (Boyden 1954).

The average diameters of those segments by generation are compared with the Weibel airway model (1963) scaled to a lung volume of 3 liters (L) and the Finlay model (see Table 5.1 in Finlay 2001). The current CT-based airway data agree well with both

Weibel and Finlay airway models. In particular, the data are in a better agreement with the Finlay model for generations 0-2 and with the Weibel model for generations 3-5.

2.3 1D centerline airway model

In addition to the CT-resolved 3D airway model for CFD, the 1D centerline model for the entire 25-generation conducting airway tree is generated for subject 3 by the volume filling method (Tawhai *et al.* 2000, 2004). This method uses the peripheral airways (ending branches) in the 3D CT-resolved airway model as the initial condition and the lobar surfaces as the boundary condition to fill lobes with bifurcating trees starting from the 3D peripheral airways. To date, this is the only published method that has been demonstrated to produce human airway models consistent with morphometric measurements. The volume filling method generates the 1D centerline airway model based on the image close to TLC with the assumption that the pulmonary acini are uniformly distributed. A set of seed points is uniformly distributed in the lung with the number approximately equal to the expected number of terminal bronchioles (30,000). Each terminal branch supplies a unique point that represents the center of an acinus, i.e. a parenchymal unit. The 3D and 1D models overlap at the 3D peripheral airway segments (Lin *et al.* 2009). The resulting 1D centerline model is specific to the geometry of the subject's lung, and its geometric properties, such as mean length and diameter of each airway segment, and branching angles, are physiologically consistent.

Figure 2.3 shows these Strahler-order-based log plots of the number of branches and mean length for our generated 1D model with regression line shown for each. The Strahler ordering scheme is commonly used for a tree and it starts at the terminal branches (order 1) and proceeds up towards the trachea. The parent branch is one order higher than the child branch only if all child branches are of equal order; otherwise the parent has the same order as the child branch of the highest order. The figure clearly reflects the trend of morphometric analysis for the human bronchial tree that shows a

linear relationship if the number of branch and mean length of branches at each order are plotted on a log scale against the Strahler order.

2.4 Development of subject specific boundary conditions

2.4.1 Motivation

In a viewpoint of fluid mechanics, human conducting airway is a pipe system comprising a fractal tree structure. Since air is considered incompressible except for coughing, boundary conditions can be determined by two properties, flow rate (or velocity) and pressure, with regard to mass conservation and momentum equations. For the internal flow in a bifurcating tree structure, once flow rates at all terminal exits are determined at an instant, the sum yields the total flow rate at the zeroth generation, e.g. the mouth and the trachea, due to mass conservation. On the other hand, pressure distribution in the branching system is more complicated to determine as it is a variable in the nonlinear momentum equation. A key advantage of the in-vivo medical imaging based flow boundary condition is that it allows the flow rate distribution to be predetermined with physiologically consistency, which is not guaranteed by other boundary conditions such as uniform pressure boundary condition or uniform velocity boundary conditions. It should be worth emphasizing this in regard to subject specific studies in order to achieve physiologically consistent phenomena in both local and global ventilation. In the following subsections introduced are in-vivo image based subject specific boundary conditions that have been applied to the cases in this study: first, velocity boundary condition based on the left-to-right airway volume ratio; second, 3D-1D coupled flow boundary condition based on the lobar air intensity change; and lastly, 3D-1D coupled regional flow boundary condition for individual terminal bronchioles using image registration.

2.4.2 Left-right asymmetry

At the first stage of considering subject specific boundary conditions, asymmetry between left and right lungs was considered. The air volumes at left and right lungs are calculated from the Pulmonary Analysis Software Suite (PASS, Hoffman *et al.* 2004) at the total lung capacity (TLC) was applied, and the uniform velocity is given at the 3D ending airway segments of each lung to maintain the left to right flow rate ratio being the same as the left to right air volume ratio. This boundary condition is applied to the early studied cases in Chapter 5.

2.4.3 3D-1D coupled approach with lobar ventilation

To employ physiologically-consistent boundary conditions at the 3D CT-resolved peripheral airway segments, the air volumes in five lobes at two different lung volumes of the same subject are analyzed from CT images using the PASS. The differences between the air volumes at two lung volumes in each of the five lobes, ΔV_i where i is the lobar number, are then used to determine the partition of air flowing into each of the five lobes. With the ΔV_i information and assuming that ventilation within each of the five lobes is approximately proportional to the cross-sectional area of each terminal bronchiole, the flow rate fraction at the terminal bronchioles of the 1D centerline airway model can be estimated as

$$q_i^j = \left(\Delta V_i / \sum_{i=1}^{5} \Delta V_i \right) \left(A_i^j / \sum_{j=1}^{M_i} A_i^j \right) \tag{2.1}$$

where A_i^j is the cross-sectional area of the j-th terminal bronchiole and M_i is the total number of terminal bronchioles in the i-th lobe. Once the flow rate at the mouth piece is prescribed, the flow rates at the 1D terminal bronchioles can be determined. By mass conservation and branching connectivity, the flow rates at the 3D CT-resolved peripheral

airway segments are calculated by summation of the flow rates at the 1D terminal bronchioles. These flow rates are then used to prescribe parabolic velocity profiles at the 3D peripheral airway opening faces.

The advantages of this approach are twofold. First, they produce physiologically-consistent lobar ventilation, which is important in studying airway resistance. Second, the flow boundary condition is subject specific. Since this approach is applied to the most of the simulations with subject 3 in the later chapters, specific analysis is presented here. The resulting ventilation distribution by lobe is (LUL, LLL, RUL, RML, RLL) = (0.145, 0.349, 0.130, 0.052, 0.324) and the distribution by lung is (left lung, right lung) = (0.494, 0.506). Thus, the ratio of the air volume delivered to the left lung over the right lung is 0.976, which is exactly the value obtained by PASS from the CT images.

2.4.4 3D-1D coupled subject specific regional ventilation

We present a novel image-based technique to estimate a subject specific BC for CFD simulation of pulmonary air flow. The information of regional ventilation for an individual is derived by registering two CT lung datasets and then passed to the CT-resolved airways as the flow BC. The CFD simulations show that the proposed method predicts lobar volume changes consistent with direct image-measured metrics, whereas the other two traditional BCs (uniform velocity or uniform pressure) yield lobar volume changes and regional pressure differences inconsistent with observed physiology.

Figure 2.4 shows a flow chart of the entire process of determining BCs from CT image data. Two CT datasets are acquired at different levels of inflation in the same scanning session and is matched using a mass-preserving image registration (Yin *et al*. 2009b) to estimate regional ventilation. Meanwhile, a subject specific 1D centerline airway tree is generated based on the image with larger lung volume using a volume filling method (Tawhai *et al*. 2004) that fills lobes with bifurcating tree spanning the entire conducting airways from the ending segments of CT-resolved central airways to

terminal bronchioles. The registration-derived regional ventilation map is then associated with the 1D tree to estimate air flows at the approximately 30,000 terminal branches. Terminal airway flows are used to produce the subject specific flow BC for the CT-resolved 3D central airways by utilizing the connectivity information between the 3D airways and the associated downstream 1D airway branches. The proposed subject specific BC is then applied to CFD and is compared against two traditional outlet BCs (either uniform velocity or uniform pressure). In this study, the two 3D CT volumetric datasets from subject 3 were used. One volumetric dataset was acquired at 85% of VC, referred to hereafter as image I_1 or the reference image, and the other was at 55% of VC, referred to hereafter as image I_2 or the floating image. The segmented airways were further skeletonized to obtain the centerlines of individual branches. A mass preserving image registration method was used to match the two volumetric CT datasets. This registration method estimates local tissue (parenchyma plus blood) and air fraction within the lung and minimizes the local tissue volume difference. Let $I(\mathbf{x})$ denote the Hounsfield unit (HU) for a voxel at $\mathbf{x}$. The tissue and air fraction can be estimated as (Hoffman 1985, Hoffman *et al*. 2003)

$$\beta_{air}(\mathbf{x}) = \frac{HU_{tissue} - I(\mathbf{x})}{HU_{tissue} - HU_{air}} \quad \text{and} \quad \beta_{tissue}(\mathbf{x}) = \frac{I(\mathbf{x}) - HU_{air}}{HU_{tissue} - HU_{air}} \tag{2.2}$$

where *HUair* and *HUtissue* refer to the HUs of air and tissue, respectively. In this work, we used -1000 for *HUair* and 55 for *HUtissue*. Based on Eq. (2.2), we can then define the similarity measure as the sum of squared local tissue volume difference (SSTVD):

$$E = \sum_{\mathbf{x}\in\Omega} \left[V_1(\mathbf{x})\beta_{tissue\,1}(\mathbf{x}) - V_2(T(\mathbf{x}))\beta_{tissue\,2}(T(\mathbf{x})) \right]^2 , \tag{2.3}$$

where $T(\mathbf{x})$ is the transform function to be optimized and a cubic B-spline model is adopted in this work. V_1 and V_2 are total volumes of corresponding regions in the two

images, respectively, and V_2 can be calculated from the Jacobian value J_T of the deformation as $V_2 = J_T V_1$. For complete details, please refer to Yin *et al*. (2009b). This method has previously been validated based on six pairs of volumetric CT datasets and it has been shown to be effective at registering intra-subject lung CT datasets (Ding *et al*. 2009, Yin *et al*. 2009b).

Once the image registration is performed, we can further calculate regional ventilation, which is also referred to as the local air volume difference in this work. The local air volume difference is jointly estimated from changes in local air fraction along with the registration derived local Jacobian value (Yin *et al*. 2009a). The regional ventilation map describes local air volume changes between the two volumetric datasets. Thus, it can be used to provide a subject specific BC for the 3D central airways in a 3D and 1D coupling framework (Lin *et al*. 2009). Using 1D centerline airway tree (see Section 2.3), the air flow at each terminal bronchiole can then be calculated as the sum of registration-derived regional ventilation of all voxels in that unit. By mass conservation the air flow at an ending segment of the CT-resolved 3D central airways can be determined by summing the air flows of terminal bronchioles with the connectivity information between the 3D airway and the associated downstream 1D airway branches.

2.5 Effect of the boundary condition

Case description

Simulations of inspiratory flows using the proposed BC and two conventional uniform BCs were performed in this study. Large eddy simulation (LES) was adopted to capture transitional and turbulent flow. Details of computational setup in this study are presented in Chapter 3. An unstructured mesh with 899,465 nodes and 4,644,447 tetrahedral elements was generated for the CT-resolved upper and central airways. The whole computational domain was divided into 256 partitions and the simulation was conducted on the Lonestar cluster at the Texas Advanced Computing Center. The time

step was set to 2.0×10^{-5} *s*, resulting in an average Courant-Friedrichs-Lewy (CFL) number of about 0.044. A constant flow rate of 0.342 *L/s* was imposed at the mouthpiece inlet, resulting in a Reynolds number of 1,380 in the trachea. This represents the peak inspiration of normal breathing. The outlet BCs at the ending airway segments were set with the proposed subject specific regional ventilation BC (case 1), uniform velocity BC (case 2) and uniform pressure BC (case 3), respectively. The reference pressure was selected at the tracheal inlet.

Results

Registration-derived regional ventilation was validated by comparison with measured global values: (1) the average Jacobian value and (2) the total air volume difference. The measured average Jacobian value is defined as the ratio of the total lung volume of image I_2 to that of image I_1, where the total lung volumes for images I_1 and I_2 are 7.60 liter (*L*) and 6.09 *L*, respectively. The measured total air volumes can be calculated from the total lung volume and the average air fraction, where the average air fraction is estimated from average HU inside the lung with Eq. (2.2). For the images I_1 and I_2 used in this study, the measured total air volumes are 6.72 *L* and 5.20 *L*, respectively. Thus, the measured total air volume difference is 1.52 *L* between the two images. In contrast to the measured values, the registration-derived average Jacobian value is calculated from local Jacobian values in the lungs and the registration-derived total air volume difference is the sum of local air volume difference of all voxels in the lungs. Table 2.2 shows the comparison between the measured values and the registration-derived values. It is clear that the registration-derived average Jacobian value matches well with the measured one and the registration-derived total air volume difference is also close to the measured value with a small error of 2.6%.

Figure 2.5(a) shows the surface geometries of the lobes, CT-resolved upper and central airways for image I_1. These surface geometries are obtained by converting the

segmentation into surface meshes with a Marching Cubes algorithm (Lorensen and Cline, 1987) and further smoothing the meshes using a without-shrinkage smooth technique (Taubin, 1995). Figure 2.5(b) shows the generated 1D centerline airway tree. The 3D CT-resolved upper and central airways with the central airway skeleton are also shown in Figure 2.5(b). The lobes and lobar airway trees are shown in different colors: green for the left upper lobe (LUL), red for the left lower lobe (LLL), cyan for the right upper lobe (RUL), blue for the right middle lobe (RML) and purple for the right lower lobe (RLL).

Figure 2.6 compares the distributions of outlet velocity and static pressure for the three cases. The distributions in Figure 2.6(a) for the proposed BC are more heterogeneous than those of the uniform velocity BC in Figure 2.6(b) and the uniform pressure BC in Figure 2.6(c). In particular, the proposed BC predicts much greater pressure drop at the airways in the LLL and the RLL shown in Figure 2.6(a). In contrast, the uniform velocity BC yields greater pressure drop in the RML than others, whereas the uniform pressure BC enforces the same pressure drop in all five lobes. Quantitative comparisons of lobar distribution of air flow are presented in Figure 2.7. The proposed method results in larger deviation between lobes, reflecting the nature of heterogeneity of ventilation in the human lung. The measured values (the lobar difference of air content) are also shown. The lobar distributions predicted by the proposed method match well with these measured values with an overall relative error of 4.79%, seen from Table 2.3. The large relative error for RML is due to the small measured value for that lobe (0.052). However, the uniform outlet velocity and uniform outlet pressure methods yield errors of 43.42% and 27.08%, respectively. The uniform velocity BC results in over-prediction (more than twice) of the ventilation to the RML, yielding a greater pressure drop in the RML shown in Figure 2.6(b). Both uniform pressure and uniform velocity BCs under-predict the ventilation to the two lower lobes LLL and RLL.

Discussion

In contrast to the idealized symmetric airway models, the real human airways are asymmetric and BCs at periphery most certainly play an important role in determining the regional distributions of basic flow properties. Advantages of the current BC have been investigated by comparing the CFD results using the proposed subject specific BC against two traditional BCs (uniform outlet velocity and uniform outlet pressure). The results showed that the lobar and regional distributions of pressure and flow rates in the bronchioles were noticeably affected by the outlet BCs. As compared with the measurement data, the proposed method yielded physiologically reasonable regional distribution of flow, which was not accomplished by the other two BC methods.

The method proposed here uses two volumetric images of the lung acquired at different lung volumes and produces BCs that are specific to the subject and to their change in regional lung volume. This method can be extended to match multiple lung volumes acquired between TLC and the functional residual capacity (FRC) in the same scanning session, thus providing a way to develop a computational lung model with realistic time-varying BCs in a breathing period. In addition, the proposed method would benefit from further validation of the registration-derived regional ventilation, such as comparing with the measurements from xenon CT, or hyperpolarize ^{3}He MR (Chon *et al*. 2007, Fuld *et al*. 2008). The validated technique would then be applicable to studying pulmonary airflow in subjects with lung diseases that affects ventilation distribution, such as asthma or chronic obstructive pulmonary disease. In these cases, a next step will be to adjust the airway model based upon additional image-based information related to regional tissue destruction (Hogg *et al*. 2009).

2.6 Flow rate at the inlet

In a series of cases presented in this thesis, either steady or pulsatile flow rate is imposed at the proximal inlet of the airway. For a pulsatile flow condition for normal

breathing, either asymmetric or sinusoidal flow-rate waveform is used to produce a typical tidal volume of 500 *ml* (0.0005 m^3) during quiet breathing. The time period of the waveform is 4.8 *s*, which is equivalent to 12.5 breaths per minute. Figure 2.8 shows the asymmetric waveform and the corresponding air volume that is breathed in and out of the lung. The parabola-shaped velocity boundary condition is imposed at the opening of the mouth piece, whose function during CT experiments is to direct gases into the mouth cavity of the subject. For the case without the upper airways, the either parabola-shaped or uniform velocity profile is imposed at the proximal inlet cross-section, depending on the specific purpose. For simplification and consistent reproduction, sinusoidal waveforms are used in the later conducted cases.

Table 2.1 Nomenclature and properties of the CT-based human airway tree of subject 3.

Abbreviation	Name	Lobe	Gen.	Area (mm^2)	Diameter (mm)	Length (mm)
Trachea	Trachea	0	0	276.78	18.77	92.38
LMB	Left Main Bronchus	0	1	111.99	11.94	59.60
RMB	Right Main Bronchus	0	1	204.48	16.14	22.68
BronInt	Intermediate Bronchus	0	2	116.14	12.16	33.08
TriLUL	Trifurcation Left Upper Lobe Segment	1	2	82.33	10.24	15.80
LB1+2	Left Apical-posterior Bronchus	1	3	17.50	4.72	16.49
LB1	Left Apical Bronchus	1	4	9.08	3.40	13.76
LB2	Left Posterior Bronchus	1	4	10.17	3.60	12.99
LB3	Left Lateral Bronchus	1	3	17.79	4.76	9.97
LBX3	Left X Lateral Bronchus	1	3	16.83	4.63	15.59
LB4+5	Left Superior-inferior Bronchus	1	3	27.56	5.92	18.19
LB4	Left Superior Bronchus	1	4	16.42	4.57	8.68
LB5	Left Inferior Bronchus	1	4	12.36	3.97	11.17
LLB6	Left Lower Bronchus	2	2	90.29	10.72	11.04
TriLB6	Trifurcation Left Bronchus	2	3	33.01	6.48	15.00
TriLLB	Trifurcation Left Lower Bronchus	2	3	52.10	8.14	22.65
LB8	Left Anterior-basal Bronchus	2	4	17.72	4.75	17.80
LBX8	Left Subsuperior -Basal Bronchus	2	4	10.20	3.60	16.00
LB9	Left Medial-basal Bronchus	2	4	20.60	5.12	24.35
LB10	Left Posterior-basal Bronchus	2	4	25.07	5.65	19.38
TriRUL	Trifurcation Right Upper Lobe Segment	3	2	50.91	8.05	17.89
RB1	Right Apical Bronchus	3	3	17.64	4.74	13.44
RB2	Right Anterior Bronchus	3	3	21.34	5.21	15.31
RB3	Right Posterior Bronchus	3	3	19.06	4.93	12.76
RB4+5	Right Lateral-medial Bronchus	4	3	37.44	6.90	25.69
RB4	Right Lateral Bronchus	4	4	12.68	4.02	12.25
RB5	Right Medial Bronchus	4	4	18.27	4.82	17.81
RBX5	Right X Anterior Bronchus	4	4	10.24	3.61	16.45
RB6	Right Posterior-basal Bronchus	5	3	30.23	6.20	9.16
RLL7	Right Lower Lobe Segment	5	3	81.07	10.16	7.82
RB7	Right Medial-basal Bronchus	5	4	12.47	3.98	21.05
TriRLL	Trifurcation Right Lower Lobe Segment	5	4	59.27	8.69	15.33
RB8	Right Anterior-basal Bronchus	5	5	21.65	5.25	16.80
RB9	Right Lateral-basal Bronchus	5	5	19.29	4.96	13.98
RB10	Right Posterior-basal Bronchus	5	5	31.67	6.35	22.48

Table 2.2 Comparison between measured and registration-derived values for average Jacobian value and total air volume difference

	Average Jacobian value	Total air volume difference (liters)
Measured	0.80	1.52
Registration-derived	0.80	1.56
Error percentage (%)	0.0	2.6

Table 2.3 Relative errors of the lobar flow rate fractions for the three outlet BCs against measured values

	Proposed (%)	Uniform velocity (%)	Uniform pressure (%)
LUL	3.13	38.61	39.19
LLL	0.09	28.81	16.56
RUL	3.86	18.99	1.00
RML	14.73	117.93	67.69
RLL	2.12	12.76	10.94
Overall	4.79	43.42	27.08

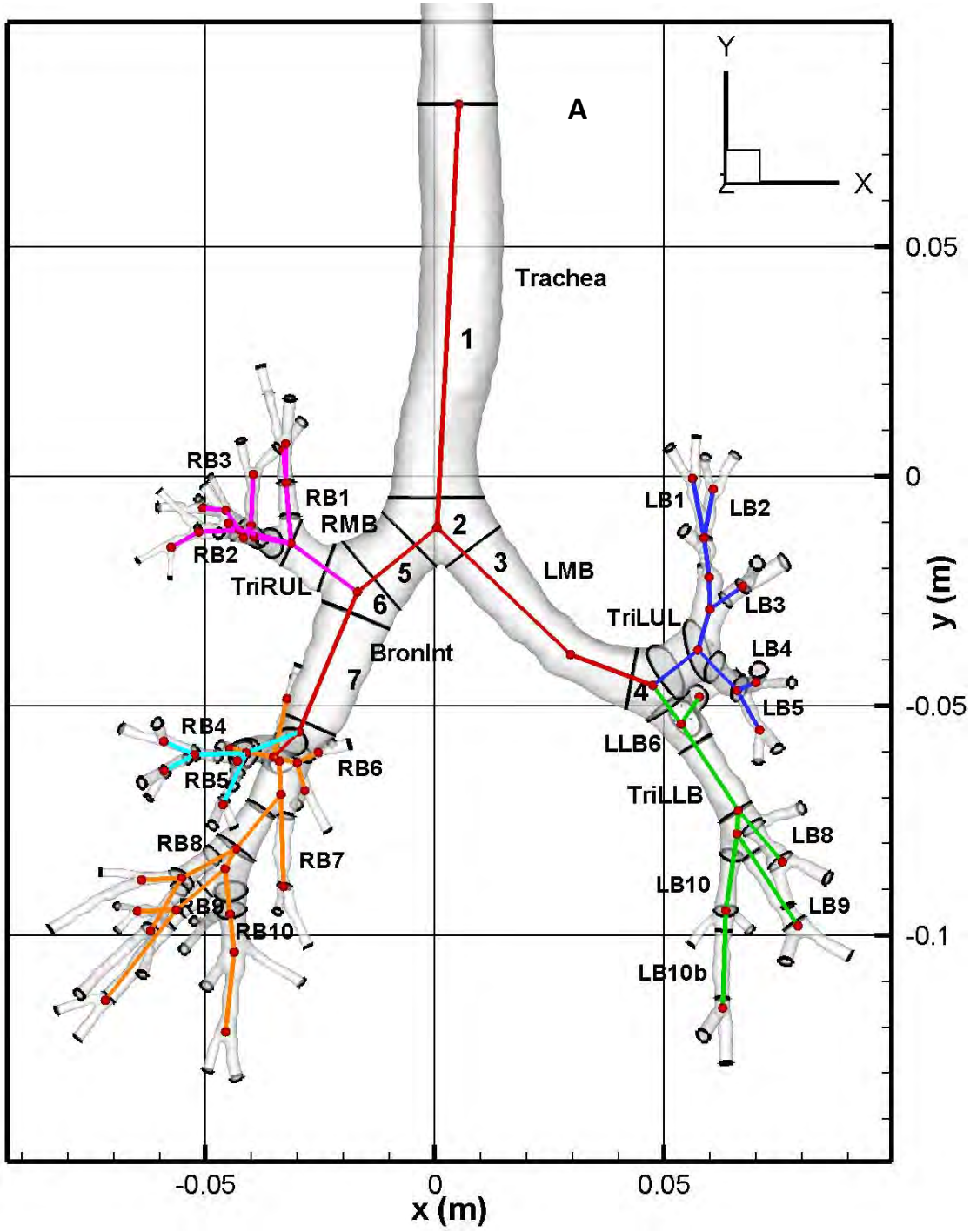

Figure 2.1 Geometry, centerlines, and labels of the CT-based human airway tree (subject 3). The 3D domain is partitioned into 65 sub-volumes for energy budget analysis. Sub-volume: 1, trachea; 2, first bifurcation; 3, LMB (left main bronchus); 4, prior TriLUL (trifurcation before left upper lobe); 5, RMB (right main bronchus); 6, prior BronInt (before intermediate bronchus); 7, BronInt (intermediate bronchus).

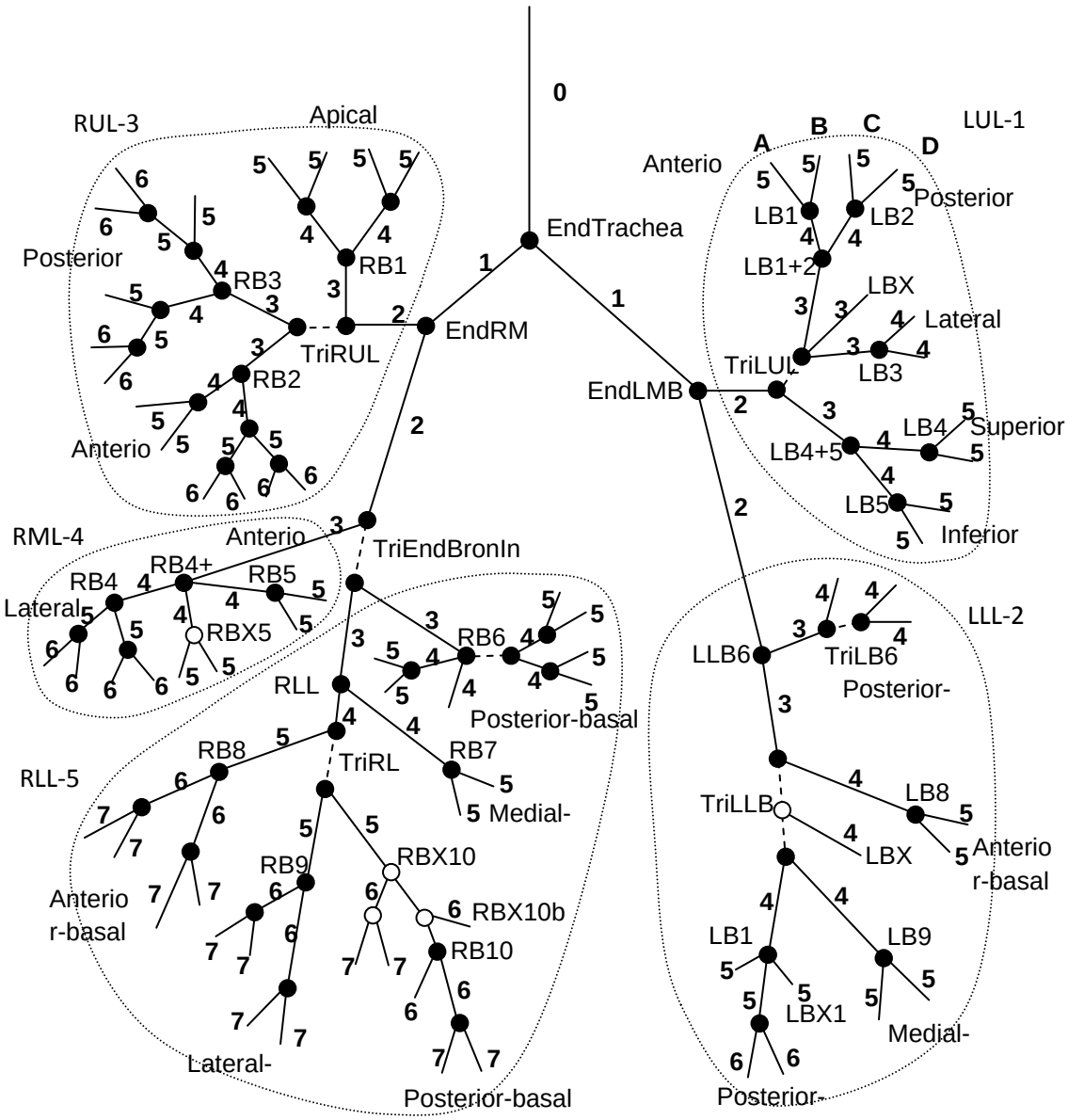

Figure 2.2 Generation number, branch points, and lobar partitions of the CT-based human airway tree.

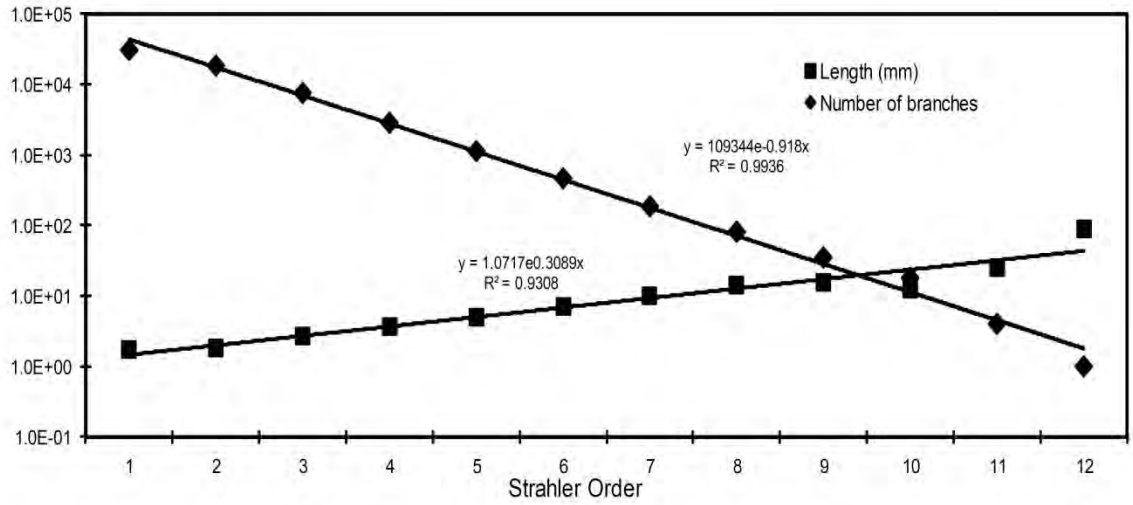

Figure 2.3 Plots of the number of branches and the mean length on log scales against Strahler order. Regression line for each plot is also shown.

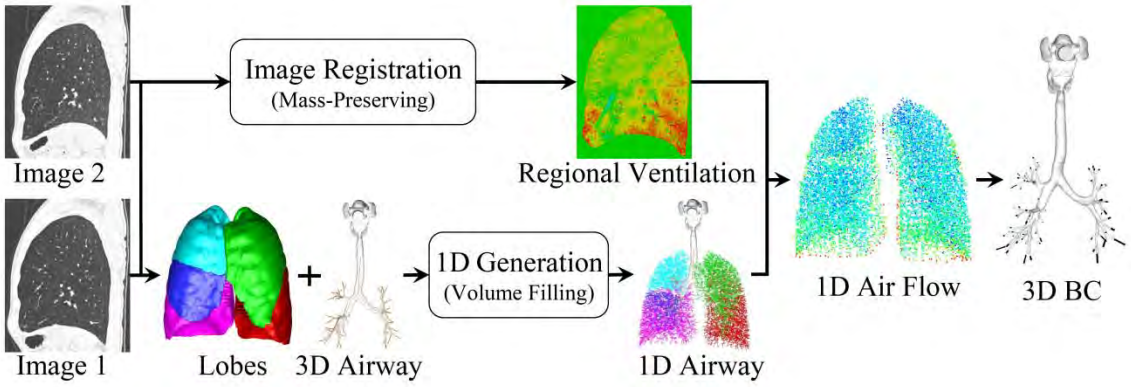

Figure 2.4 A flow chart of the entire process of determining BCs from CT image data.

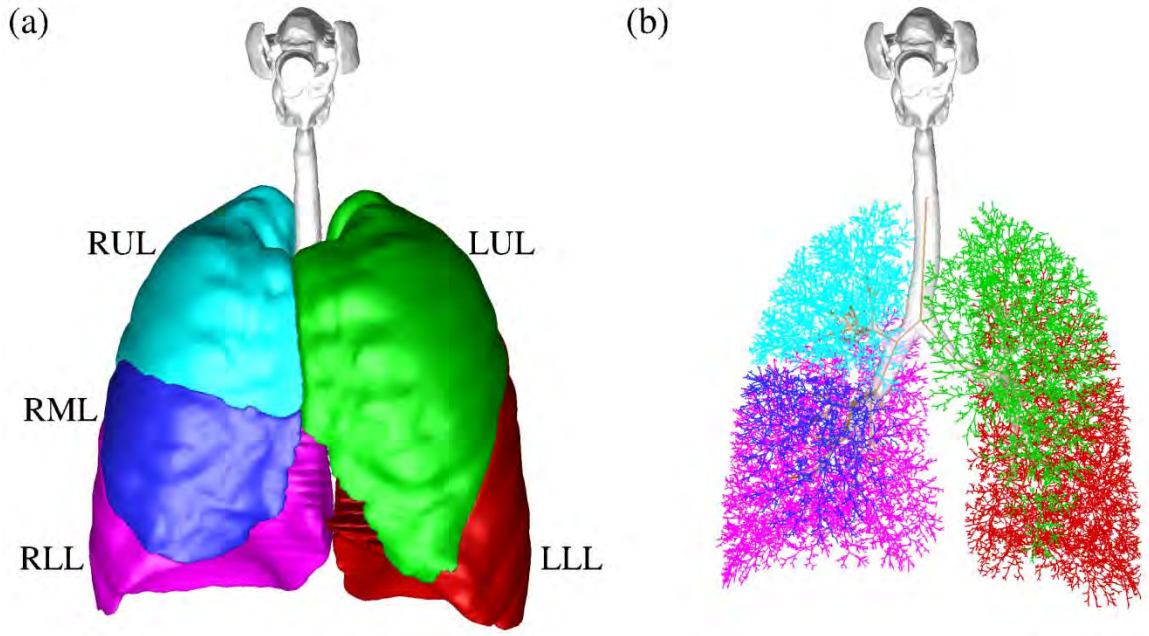

Figure 2.5 Reconstructed geometry of lungs. (a) Surface geometries of the lobes (LUL: left upper lobe; LLL: left lower lobe; RUL: right upper lobe; RML: right middle lobe; RLL right lower lobe), CT-resolved upper and central airways for image I_1; (b) Combination of generated 1D centerline airway tree with the 3D CT-resolved upper airway, central airway tree and central airway skeleton.

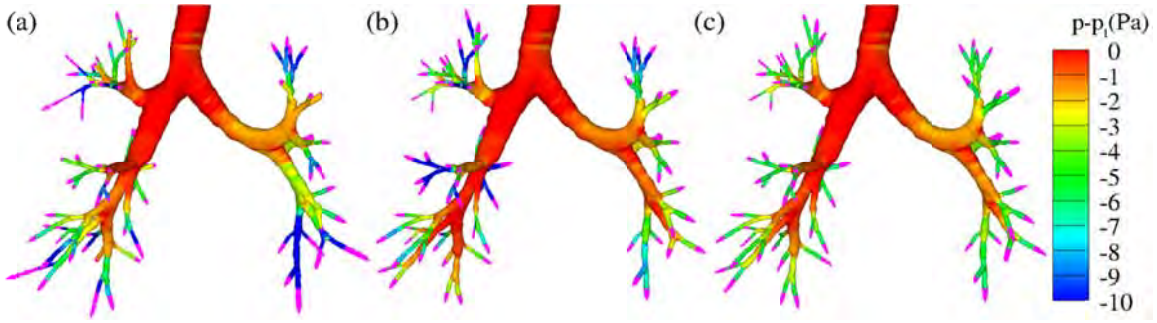

Figure 2.6 Outlet velocity vectors (pink) and pressure contours for the three different outlet BCs: (a) proposed; (b) uniform velocity; (c) uniform pressure.

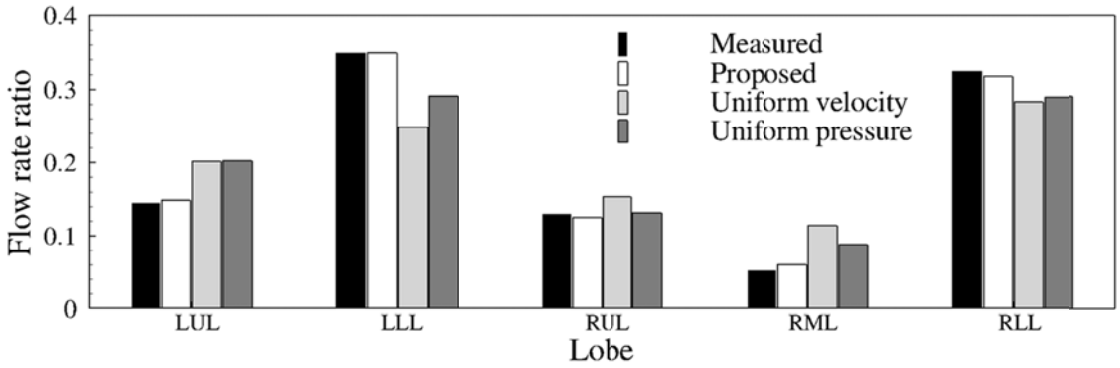

Figure 2.7 Lobar distribution of flow rate ratio for the three cases with different outlet BCs.

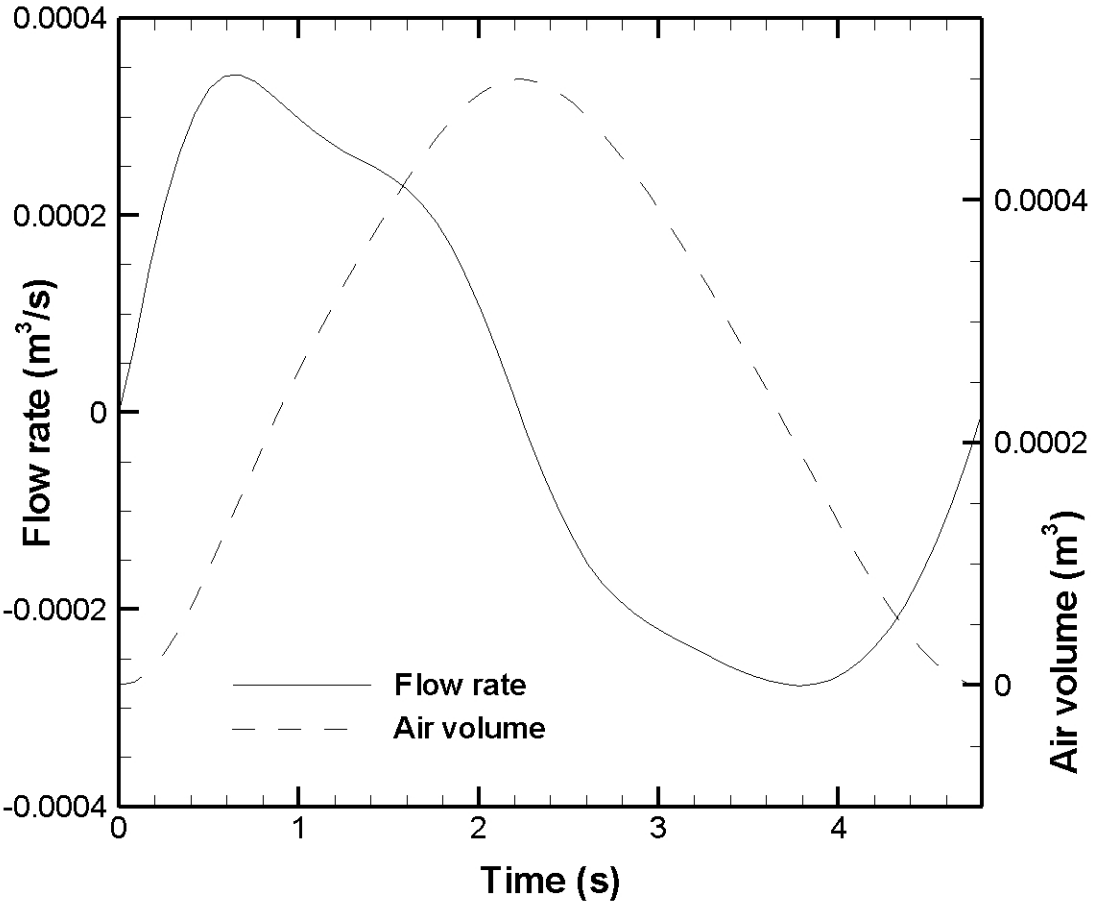

Figure 2.8 Time histories of flow rate and air volume through the mouth to the lung.

CHAPTER 3
HIGH FIDELITY CFD METHODOLOGY FOR GAS FLOW IN HUMAN LUNG

3.1 Challenges in pulmonary airflow simulation

Traditionally, human airway has been modeled as straight circular cylinders for study of fundamental flow physics. And model airways have represented averaged features. A subject specific human airway, in reality, exhibits more complex geometry, that an accurate prediction of pulmonary gas flow involves many challenging issues such as capturing turbulence transition. For example, sudden expansion of airway conduit, such as between the glottal constriction and the subglottal region, causes the turbulent laryngeal jet flow. The onset of turbulent transition for the realistic pulmonary airflow implies some notable characteristics:

- In normal breathing condition, the Reynolds number is usually lower than the critical Reynolds number of the straight pipe flow (~2,300), however large enough for transition of jet flow.
- It is hard to reach fully developed turbulence but mostly transitional.
- The major origins of turbulence are free-shear layers around jet from the oral and glottal constriction, rather than boundary layer of airway tubes.

A numerical simulation of the airflow at normal breathing becomes more challenging due to the co-presence of laminar to turbulent characteristics of various flow types, such as pipe flow in straight or curved geometry, confined jet flow that may impinge on the airway wall, bifurcating flow (inhalation), co-flow (exhalation), and so on. It is important to recognize that the co-existing features of these flow types are different from isotropic turbulence or fully developed turbulent channel flow at high *Re*, where fundamentals of numerical modeling of turbulent flows have been mainly examined for past several

decades. That is, care should be taken in applying numerical models developed in single-flow type conditions.

3. 2 Large eddy simulation

3. 2.1 Governing equations

The large eddy simulation (LES) is a promising CFD tool, directly resolving the large energy containing turbulent eddy motions and models the dissipating energy in the unresolved scales. The adapted LES model solves the filtered continuity and Navier-Stokes equations for incompressible flow.

$$\frac{\partial u_j}{\partial x_j} = 0 \tag{3.1}$$

$$\frac{\partial u_i}{\partial t} + \left(u_j - u_j^{ALE}\right)\frac{\partial u_i}{\partial x_j} = -\frac{1}{\rho}\frac{\partial p}{\partial x_i} + \frac{\partial}{\partial x_j}\left[\left(\nu + \nu_T\right)\frac{\partial u_i}{\partial x_j}\right] \tag{3.2}$$

where u_i is the grid filtered velocity component in the i direction, p is the grid filtered pressure, ρ is the fluid density, ν (= μ/ρ, μ the dynamics viscosity) is the kinematic viscosity, and ν_T is the subgrid-scale (SGS) turbulent eddy viscosity. u_j^{ALE} is the velocity of fluid mesh and $u_j - u_j^{ALE}$ represents the arbitrary Lagrangian Eulerian (ALE) convective velocity induced by the difference between the fluid velocity and the mesh velocity when the fluid mesh deforms during breathing cycles. Application of ALE for the airflow in deforming airway is presented in Chapter 9. The air properties of ρ = 1.2 kg/m^3 and ν = 1.7 × 10^{-5} m^2/s are adopted. Hereafter (x_1, x_2, x_3) and (x, y, z) are interchangeable, so are (u_1, u_2, u_3) and (u, v, w).

The fractional four-step method is applied to solve the continuity and momentum equations [Eqs. (3.1) and (3.2)]. The continuity equation is enforced by solving a pressure-Poisson equation. The implicit characteristic-Galerkin approximation together

with the fractional four-step algorithm is employed to discretize the governing equations, being of second-order accuracy in time and space (Lin *et al.* 2005).

In order to predict the transport of passive scalar such as a concentration of fresh air inhaled through the mouth, a convection diffusion equation is also implemented. The differential form of the passive scalar transport equation of a variable ϕ can be written as

$$\frac{\partial \phi}{\partial t} + u_i \frac{\partial \phi}{\partial x_i} = \frac{\partial}{\partial x_i}\left[\left(D_\phi + \frac{\nu_T}{Sc_T}\right)\frac{\partial \phi}{\partial x_i}\right] \tag{3.3}$$

where D_ϕ is the diffusion coefficient of ϕ in the fluid with the velocity u_i. Turbulent Schmidt number Sc_T of air is set to 0.9.

3.2.2 Subgrid modeling

The eddy viscosity model proposed by Vreman (2004) has been demonstrated to yield zero SGS dissipation for various laminar shear flows. Although the implementation of this model is not more complicated than the well known Smagorinsky model, it has been proved in various types of flows that its anisotropic nature results in the performance comparable to the dynamic Smagorinsky model without requiring any wall-damping functions (Vreman 2004, Park *et al.* 2006, You and Moin 2007). Thus, this model is adopted here to deal with both transitional and turbulent flows in a complex geometry. The SGS model reads

$$\nu_T = C_v \sqrt{B_\beta / (\alpha_{ij}\alpha_{ij})} \tag{3.4}$$

where

$$\alpha_{ij} = \frac{\partial u_j}{\partial x_i} \tag{3.5}$$

$$\beta_{ij} = \Delta^2 \alpha_{mi} \alpha_{mj} \tag{3.6}$$

$$B_\beta = \beta_{11}\beta_{22} - \beta_{12}^2 + \beta_{11}\beta_{33} - \beta_{13}^2 + \beta_{22}\beta_{33} - \beta_{23}^2 . \tag{3.7}$$

The model coefficient is $C_v \approx 2.5C_S^2$ where the Smagorinsky coefficient C_s is set to 0.065 (Moin and Kim 1982). A local grid filter size Δ is defined as 0.5×[(volume of tetrahedral element)/0.11785]$^{1/3}$. This model has been verified and validated on turbulent channel flow and pulmonary airflow (Lin *et al.* 2007).

The current LES has been validated with turbulent channel flow (Lin *et al.* 2007). In Section 3.5, the LES is further validated against wall shear stress in straight pipes analytically, flow through a constricted pipe experimentally, and existing experimental data for flow though a larynx.

3.3 Verification and validation

3.3.1 LES vs. DNS vs. RANS

As for all other types of flows, a question arises for numerical analysis of human airway flow: what is the most appropriate approach to study all necessary features without wasting resources? Three common categories of numerical approaches to predict turbulent flows are direct numerical simulation (DNS), large eddy simulation (LES) and Reynolds averaged Navier-Stokes (RANS) simulation. DNS is known to be the most accurate since it resolves the finest turbulent scales without necessity to model unresolved scales, while it costs the most. LES directly resolves the large scale turbulent eddies and model the SGS energy cascade. RANS simulation is associated with various types of modeling for the full range of turbulent dissipation. The laryngeal jet and the

stenotic pipe flow have common features with diversity of flow characteristics. RANS have had successful predictions for single type of flow with careful tuning.

For the constriction induced transitional flow such as stenotic pipe flow and human laryngeal jet flow, *k-ω* model with low Reynolds number (LRN) assumption is most popular in RANS modeling and showed performances better than or not inferior to other RANS models (Varghese and Frankel 2003, Zhang and Kleinstreuer 2003, Longest and Vinchurkar 2007, Varghese *et al.* 2008). In 2008, Varghese *et al.* (2008) studied the performances between popular two-equation RANS models, preliminary LES, and DNS for eccentric stenotic pipe flow. They confirmed the known drawbacks of RANS in simulating post-stenotic transition, that upwinding schemes used for the RANS calculations are overly dissipative. They also reported that the jet breakdown in the preliminary LES result is much closer to the DNS results than RANS result. With regard to the potential difference of LES and DNS for post-stenotic jet breakdown, it is considered that the absence of upstream disturbance may increase the sensitivity of jet breakdown to the mesh size. In more complex conduit of realistic human airways, the difference between DNS and LES is rather expected to be less due to the existence of upstream disturbance in the supraglottal space.

To date, there has been no comparison between all three of RANS, LES and DNS of the gas flow in the human airways using anatomically realistic geometry including upper airways. Some studies comparing two-equation turbulence models for RANS (Zhang and Kleinstreuer 2003, Longest and Vinchurkar 2007) do not provide acceptable agreements of the velocity and pressure fields with those from experiments or DNS. Jayaraju *et al.* (2008) provided comparison of RANS using k-ω model without near wall correction, detached eddy simulation (DES) and LES with experimental measurement, observing DES and LES results are closer to the experimental results. However, their LES results also deviate from the experimental results and the source of the error is unclear, which can be the limited performance of their LES model, experimental

uncertainty or both. The main objective of the current study is to provide comparison of the three popular numerical approaches to predict the human inspiratory air flow at moderate Reynolds numbers of normal breathing, regarding accuracy and efficiency in capturing important features, in association with recently published analyses using DNS (Lin et al. 2007) and LES (Choi et al. 2009, or see Chapter 5).

Two in-vivo airway models are reconstructed from multi detector row computed tomography (MDCT) scans of self-reported normal human subjects. Detailed process from CT scans to the CFD mesh can be found in Lin *et al.* (2007). Selected information of airway models and flow parameters for two subjects is presented in Table 3.1. Values used in DNS and fine mesh LES are enclosed by parentheses. Fluid properties and discussion on the intersubject variability can be found in Choi *et al.* (2009). The Reynolds number is calculated based on the spatially averaged air speed in the trachea, U, defined by the flow rate over the average cross-sectional area. The length scale for the RANS simulation can be greater than that for LES since RANS in nature does not directly resolve motions of turbulent eddies at all. In the current study, however, the same mesh is used for RANS and LES to avoid the effect of the mesh density in comparison. For subject 2, LES with a finer mesh instead of DNS is compared. For all cases, velocities are prescribed at inlet and exit boundaries, at given flow rates and the cross-sectional areas. The flow rate fraction distribution in the airway of subject 3 is prescribed by in-vivo image-driven lobar air volume changes between CT images at two lung inflation levels (see Section 2.4.3).

Varghese and Frankel (2003) tested various two-equations RANS models for post-stenotic flow and concluded that the LRN k-ω model resulted in the better agreement with experimental results (Ahmed and Giddens 1983) than others available in FLUENT (ANSYS, Inc., Canonsburg, PA). In addition, Varghese *et al.* (2008) reported no significant differences of shear stress transport (SST) k-ω model for post-stenotic flow simulations. Thus, in the current study, LRN k-ω model is adopted for comparison with

LES and DNS. Governing equations and SGS model are presented in Section 3.2. The inherent capability of correctly reproducing the anisotropic and transitional flows needs to be remarked as these are the challenging characteristics for the examined flow type. For normal breathing in the human airways, the main site where the onset of turbulent transition occurs is the laryngeal jet from the glottis into the trachea. Thus, explicit comparisons have been performed by refining mesh size from the original mesh used for RANS and LES cases with (without) the SGS model turned off for subject 3 (subject 2). In average, about 4 (2) times greater volumes of tetrahedral finite elements than the original mesh are used for the presented DNS (fLES) for subject 3 (subject 2).

Figure 3.1 presents the mean speed and the turbulent kinetic energy (TKE) contours on the vertical planes along the centers of the tracheas of the two subjects. In Figures 3.1(a) and 3.1(c), The mean speed contours in the LES results are essentially the same as in the DNS or fLES results, while the laryngeal jet streams stretch further downstream in the RANS results. The less dispersed jet stream by RANS model is associated with the failure in capturing turbulent behaviors. As presented in Figures 3.1(b) and 3.1(d), LES reproduces the same features of turbulent kinetic energy (TKE) as DNS or fLES in both subjects. The high TKE regions are observed along the mixing layer between the jet core and the ambient air as well as the jet transition region near the end of jet core region. The differences between two subjects are mainly attributed to the cross-sectional area constriction ratio of the glottis to the trachea and the curved shape of the airway tube (see also Choi *et al.* 2009, or Chapter 5). Constriction of subject 3 is only about 50% and limits the formation of mixing layer before the open cavity-like region on the rear side of the curved trachea, where the maximum TKE is observed. In contrast, RANS simulations result in only small amounts of unsteadiness near the center of the jet through the glottis for subject 3, and about 5 times smaller TKE in the jet mixing layer for subject 2. It is assessed that RANS simulations fail to model the jet induced turbulent behavior, which involves the anisotropic nature of the high shear region in the jet mixing

layer and the transition region at the end of the jet core. This is attributable to the over-dissipation of the upwinding schemes popularly used for RANS as well as the limitation of the isotropic turbulence based model formulation without any direct resolution of turbulent motions. This drawback is not likely to be overcome by employing the low Reynolds number assumption. Turning off the wall damping function is known to reduce the error near wall at “low” Reynolds numbers, at which the wall induced turbulence is not fully developed. However, it cannot directly improve the performance in representing anisotropic characteristics of the post-stenotic disturbance that resides mostly away from the wall.

Figures 3.2 and 3.3 provide more quantitative comparison of the mean and fluctuation of the velocity along the jet centerline in the axial direction of the trachea. Both mean velocity and root-mean-square (rms) velocity fluctuations are normalized by the average velocity in the trachea. The axial distance is normalized by the average diameter of the trachea. To avoid the effect of the uncertainty in detecting the jet centerline, spatial average has been taken within 20% in the radial direction. Thus, the mean denoted in the figures is slightly less than the value exactly on the centerline. On the contrary, the rms velocity fluctuation includes high values in the radial direction around the jet core. It is apparent in Figures 3.2 and 3.3 that agreements of LES with DNS or fLES in the normalized mean and fluctuation velocities are excellent. On the other hand, the mean speed predicted by RANS decays slower in the axial direction compared to LES or DNS results in both subjects, as also shown in Figure 3.1. The error by the RANS modeling with respect to the DNS (fLES) at a distance of 6D (6.5D) is about 13% (33%), while LES leads to the error less than 1% in both subjects. About 75% greater normalized centerline velocity at the glottis in subject 2 than in subject 3 is attributable to the greater area constriction ratio in subject 2. Figure 3.3 shows that the normalized rms velocity fluctuations reach the maximum of about 0.25 (0.7) in the axial distance between 3D to 4.5D (2.5D to 4D) in subject 3 (subject 2). The peaks of the rms

velocities are associated with high TKE region shown in Figure 3.1. RANS simulation significantly underestimates the rms velocities for both subjects. The error at 3D (3.5D) is about 61% (64%), while LES has the error less than 10% in both subjects. Failure in capturing correct local turbulent characteristics of the laryngeal jet by the RANS simulations eventually affects the axial pressure distribution as well. Since there is no noticeable variation of the static pressure in radial direction, spatial average has been taken on cross sections at each discrete distance level. Figure 3.4 presents the pressure coefficient, $C_P=(P-P_0)/(\rho U^2/2)$, from the supra-glottal region to the nearly end of the trachea. While the magnitude is about five times greater in subject 2 than in subject 3, resulting from differences in the tracheal diameters and the glottal constriction, the same pattern of the pressure distribution in the axial direction is observed in two subjects. The pressure distribution by LES falls into the result of DNS or fLES. However, the RANS simulations underestimate the pressure increase in the downstream of the trachea, as the result of slowly decaying mean speed around the centerline in the axial direction.

To summarize, this study demonstrates that the tested LES resolves subject specific behaviors of the laryngeal jets in excellent agreements with DNS or fine mesh LES in two CT-based human airway models, saving relatively a large amount of computational cost. In contrast, RANS simulation with k-ω turbulent model improved with the low Reynolds number assumption fails to capture the turbulent characteristics as the same was reported for constricted pipe flow Varghese *et al.* (2008). It is suggested that a well performed LES can be the most appropriate numerical method to simulate complex airflow phenomena in the human lungs, fulfilling both accuracy and efficiency in resolving important features of the multiscale transitional flow. In addition, it may be necessary to note that application of a SGS model for LES requires careful consideration in order not to distort the resolved field, as pointed out by many of turbulence modeling studies.

3.3.2 Stenotic pipe flow and laryngeal jet

The laryngeal jet exhibited in Figure 3.1 is dynamically similar to the jet formed in stenotic flows (Ahmed and Giddens 1983, Sherwin and Blackburn 2005, Varghese *et al*. 2007, Vétel *et al*. 2008) because the jets in both cases are generated by flow passing a constriction in a pipe. Two key parameters in this type of flow in the convective regime are the stenotic area reduction and *Re*. Ahmed and Giddens (1983) investigated the flow through an axisymmetric constriction with 25, 50, and 75% area reduction in a rigid tube with the *Re* range of 500-2,000 using laser Doppler anemometry. Vétel *et al*. (2008) studied the flow through a smooth axisymmetric 75% constriction in a tube using stereoscopic and time-resolved particle image velocimetry in the *Re* range of 100-1,100. Sherwin and Blackburn (2005) and Varghese *et al.* (2007) studied the flow through a smooth axisymmetric 75% constriction with *Re* = 750 and 1,000, using DNS. In our CT-based airway model of subject 3, the ratio of the glottal area to the average tracheal cross-sectional area is 45%, thus a 55% constriction, and the glottis aperture exhibits an asymmetric oval shape.

We simulate the steady flow through a smooth axisymmetric 50% constriction at *Re* = 2,000 for two reasons. First, the geometrical feature and flow condition are similar to those of the trachea in the airway model. Second, the experimental data of Ahmed and Giddens (1983), e.g. mean wall shear stress and root-mean-square (RMS) velocity fluctuations of the jet, are available for comparison. Simulation of the stenotic flow is non-trivial because the onset of flow instabilities and transition to turbulence depends on upstream noise in experiment, which is unknown (Vétel *et al*. 2008). In the absence of upstream flow perturbation, the DNS of Varghese *et al.* (2007) produced a laminar flow downstream of an axisymmetric constriction. We adopt the computational domain size, the sinusoidal stenosis, and the boundary conditions recommended by Varghese *et al.* (2007). The length of the tube is *19D* and the distance between the stenosis and the outlet face is *16D*, where the diameter *D* is set to the average diameter of the trachea. A

Poiseuille parabolic velocity profile is imposed at the inlet and the outflow boundary condition is imposed at the exit. The grid spacing is set to that of the airway mesh, resulting in 355,520 points and 1,981,649 elements. The average ratio of ν_T /ν in the range of $0 \leq x/D \leq 10$ is 0.6%. This case allows validation of the current LES model as well as assessment of the airway mesh quality. Random velocity perturbations are superimposed on the inlet velocity profile to emulate upstream noise (Vétel *et al*. 2008).

Figure 3.5(a) displays an instantaneous flow field of the stenotic flow. The jet stemming from the constriction is deflected towards the wall resulting in a one-sided recirculation region. This phenomenon is known as Coanda-type wall attachment and has been observed by Sherwin and Blackburn (2005) and Vétel *et al*. (2008). The flow appears to undergo transition from laminar to turbulent flow beginning at $x/D \approx 3$. A comparison of mean wall shear stresses in Figure 3.5(b) shows that the normalized stresses in the upstream and far-downstream of the constriction agree well with the theoretical values for laminar and turbulent pipe flows (Prandtl's friction law for smooth pipes, Pope 2003), respectively. In the post-stenosis region, the negative stress is due to the recirculation zone and the increasing stress at $x/D \approx 3$ suggests transition to turbulence. They agree with the experimental data of Ahmed and Giddens (1983). Figure 3.5(c) compares the distributions of normalized RMS axial and non-axial velocity fluctuations along the axial x-direction in the centerline region with those of Ahmed and Giddens (1983). To assess the distribution of these fluctuations in the core region of the jet, we calculate the RMS values within the half-radius radial distance of the tube and show the standard deviation bars. Two important experimental observations of the jet flow in pipes by Ahmed and Giddens (1983) are reproduced: the development of the axial velocity fluctuation is faster than that of the non-axial component and the peak normalized RMS velocity fluctuation (disturbance intensity) exceeds 30%. Given the uncertainties in the intensity and nature of the upstream noise in the experiment (Vétel *et*

al. 2008), the overall agreements between our LES prediction and the experimental data near the wall and in the core region of the jet are good.

Since the disturbance intensities of the three cases are similar, Figure 3.5(c) displays the distributions of the normalized RMS axial and non-axial velocity fluctuations along the centerline region of the trachea for the pulsatile-flow case of subject 3. It is noted that the axial axis of the pipe is the x axis, whereas for the trachea the distance from the glottis is used because the trachea is curved and the axial direction is approximately along the y axis. The two aforementioned observations in the constricted pipe flow are also found here: the axial velocity fluctuation develops faster than the non-axial fluctuation and the disturbance intensity exceeds 30%. Simone *et al*. (1982) measured the RMS axial velocity fluctuation about 5 cm downstream of the glottis (about 40% constriction) in a cast of a cadaveric human larynx, which was mounted to a long tube of 1.6 cm diameter, at the Re = 1,110, 2,310, and 4,210. They found that the glottis generated turbulence with the normalized RMS axial velocity fluctuation of about 0.21 at x/D (= 5/1.6) ≈ 3. This level of turbulence agrees with our data in the trachea at the same location shown in Figure 3.5(c). Our data also exhibits strong non-axial velocity fluctuations near the glottis because of Taylor-Görtler-like or Dean-like vortices (Lin *et al.* 2007, Choi *et al.* 2009). These upstream vortical flow disturbances together with flow recirculation and separation intensified by the curved trachea may augment the RMS fluctuations in the current model at the moderate Re = 1,380 as seen in Figure 3.5(c). Furthermore, Cassanova and Giddens (1978) and Menon *et al*. (1985) found in experiments that sharp-edged constrictions, or glottis apertures, yielded greater disturbance and shorter recirculation at a lower Re. Thus, the non-axisymmetric glottis aperture in the CT-based model may also enhance RMS fluctuations.

We shall also comment on the change of the glottis opening area during breathing although the airway model in this study is assumed rigid. The glottis opening depends on breathing maneuvers and it is larger on inspiration than on expiration. Stănescu *et al.*

(1972) reported a correlation between glottis opening, lung volume and flow rate during panting and slow expirations. Using their correlation to estimate the area change associated with the change of the airflow rate in the range of 150-342 ml/s (the range under study for airway resistance) and the corresponding air volume change of about 142 ml on inspiration, the glottis area is estimated to vary by about 9%, resulting in a constriction varying between 55% and 59%. Given the convective nature of the flow and with the above range of variation in constriction, the level of turbulent fluctuation is not expected to change dramatically within the range of the flow rate studied. For expiratory flow, the change of the glottis area is even smaller and will have little effect on the flow in the central airways. This is because the glottis is located on the downstream side of the flow in the trachea during expiration. Since this work aims to study the airway resistance and flow structures in the conducting airways, the expected outcome of including the upper airways is to produce physiologically-consistent intensity of flow disturbance in the central airways during inspiration. The above analysis indicates that the level of turbulent fluctuation produced by the jet agrees with the literature and is physiological.

Table 3.1 Selected information of airway models and flow parameters.

	Subject 3	Subject 2
Glottal area constriction (%)	50	75
Flow rate (l/min)	20	15
Reynolds number (Re) at the trachea	1,380	1,337
Number of elements	4,644,447 (15,333,431)	5,156,875 (8,406,696)

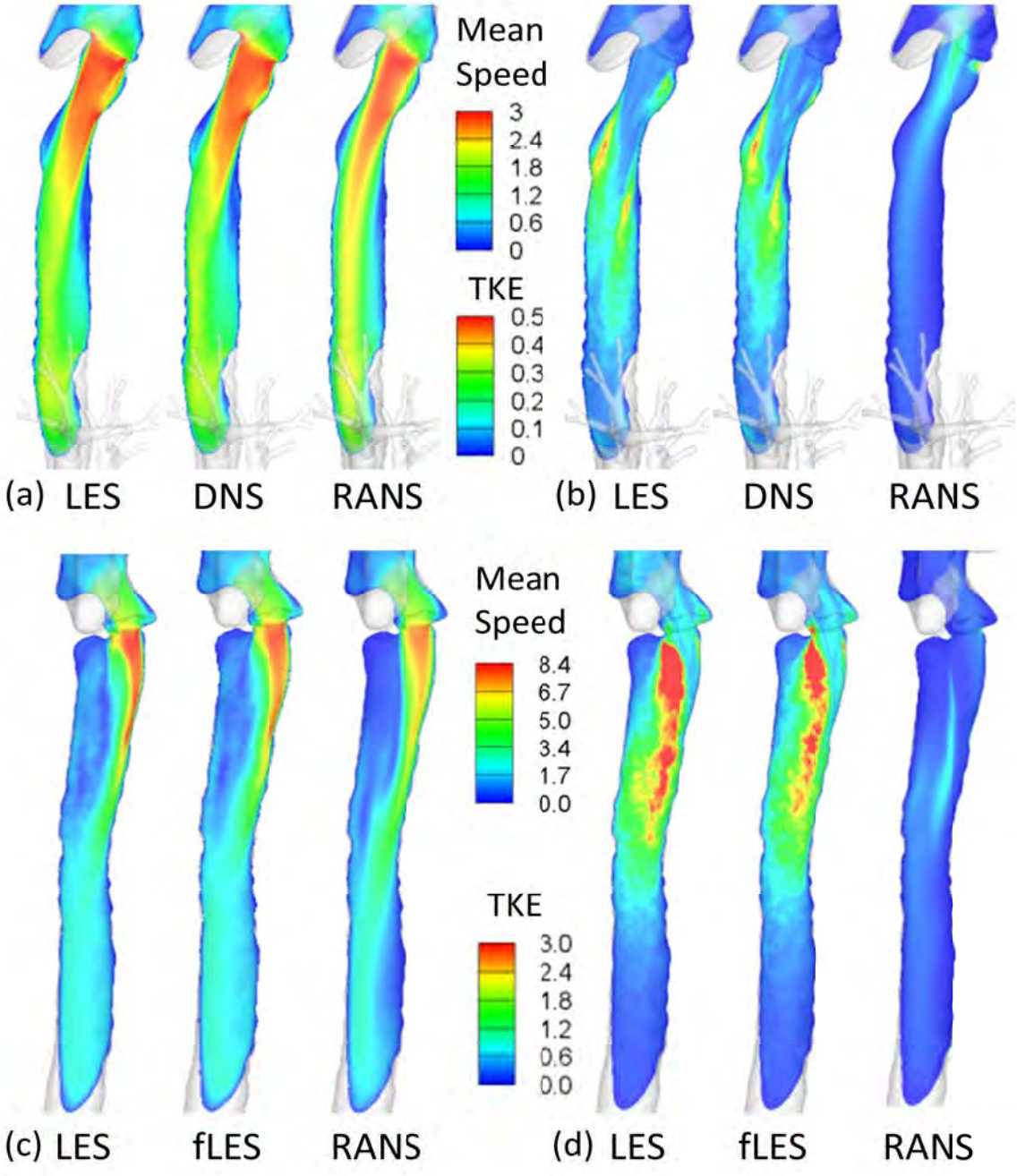

Figure 3.1 Mean speed (m/s) and TKE (m^2/s^2) on a vertical plane through the center of glottis. (a) Mean speed of subject 3; (b) TKE of subject 3; (c) Mean speed of subject 2; (d) TKE of subject 2.

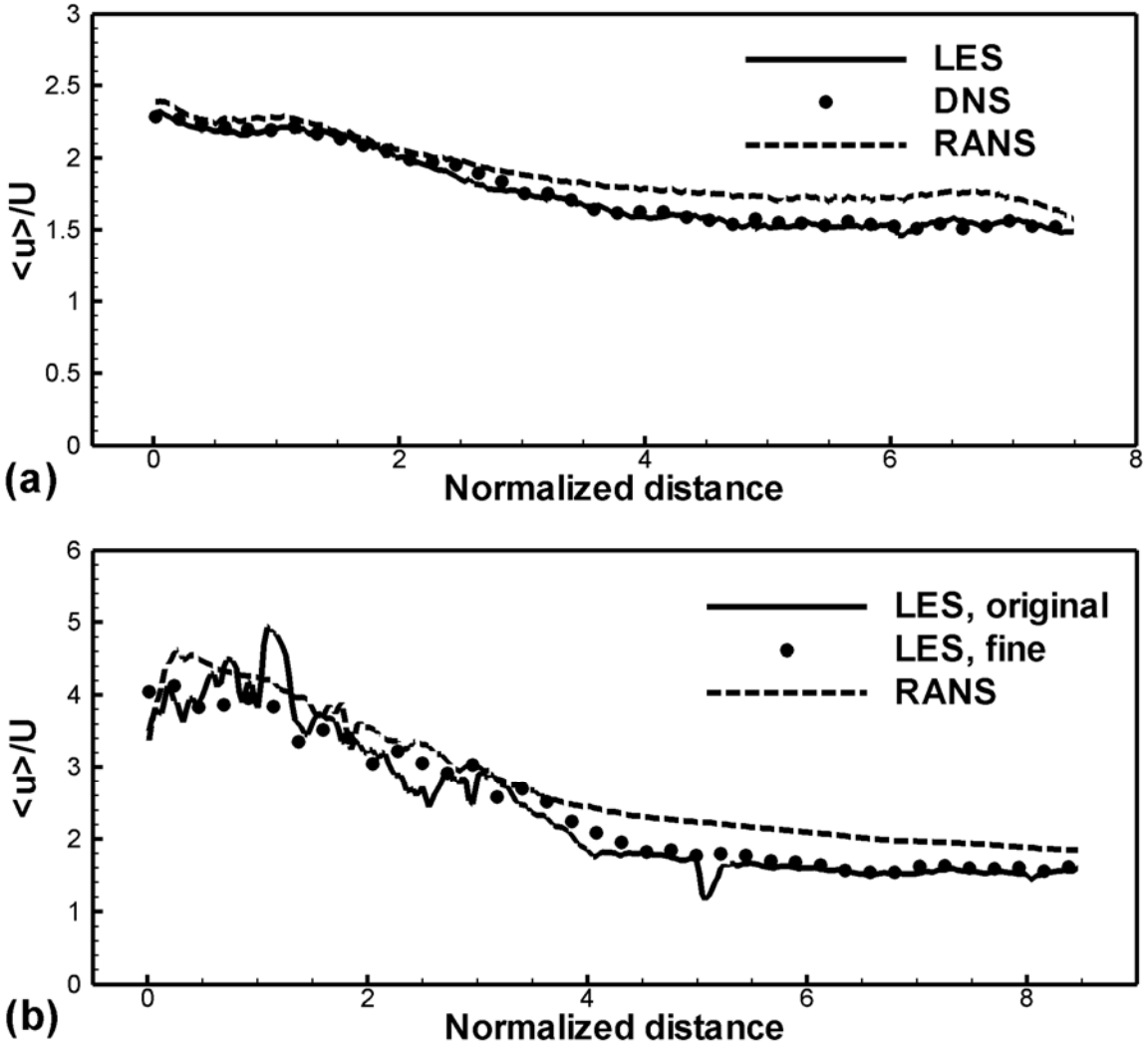

Figure 3.2 Normalized mean speed along the jet centerline in the trachea for (a) subject 3 and (b) subject 2.

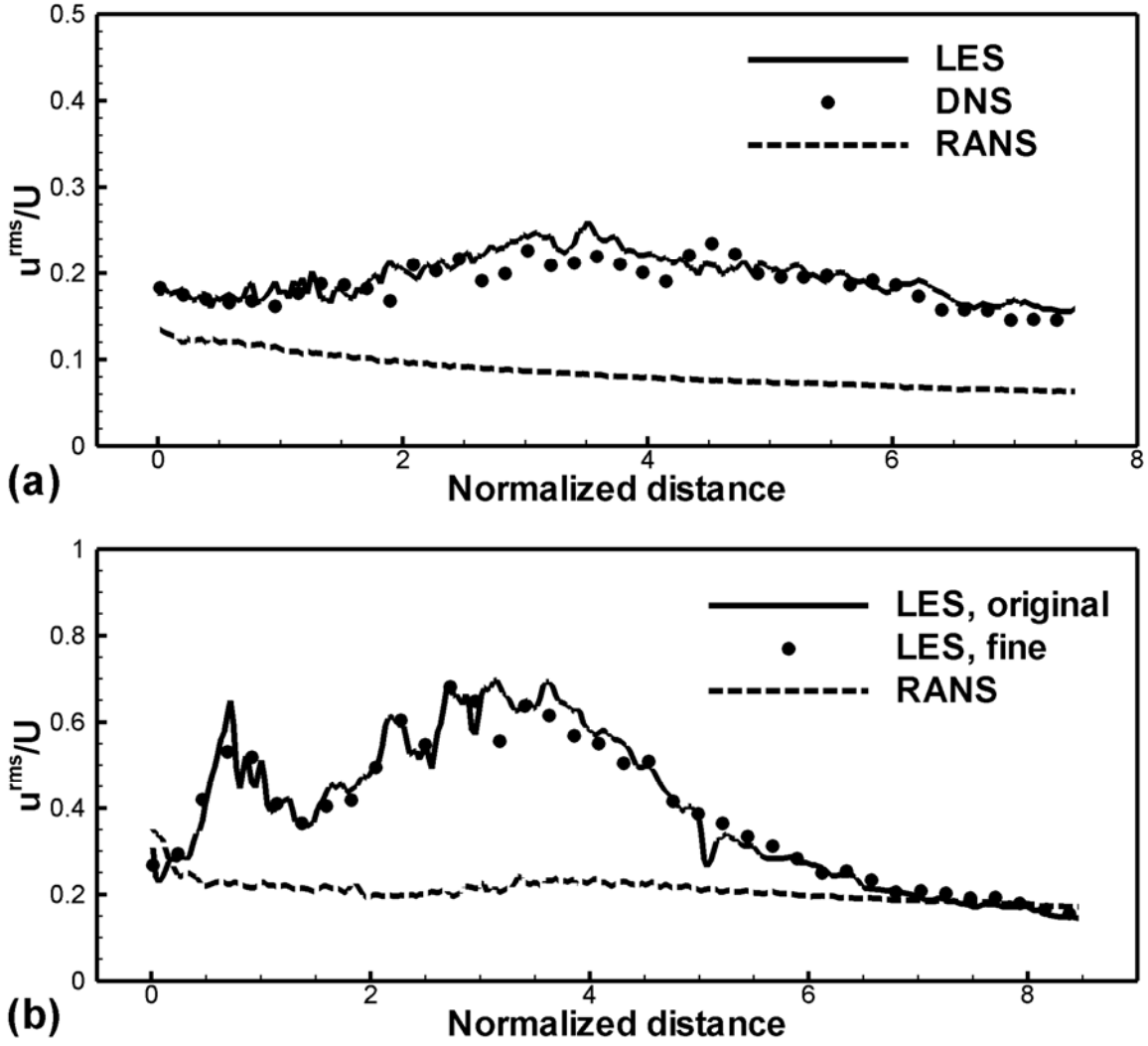

Figure 3.3 Normalized RMS velocity fluctuations along the jet centerline in the trachea for (a) subject 3 and (b) subject 2.

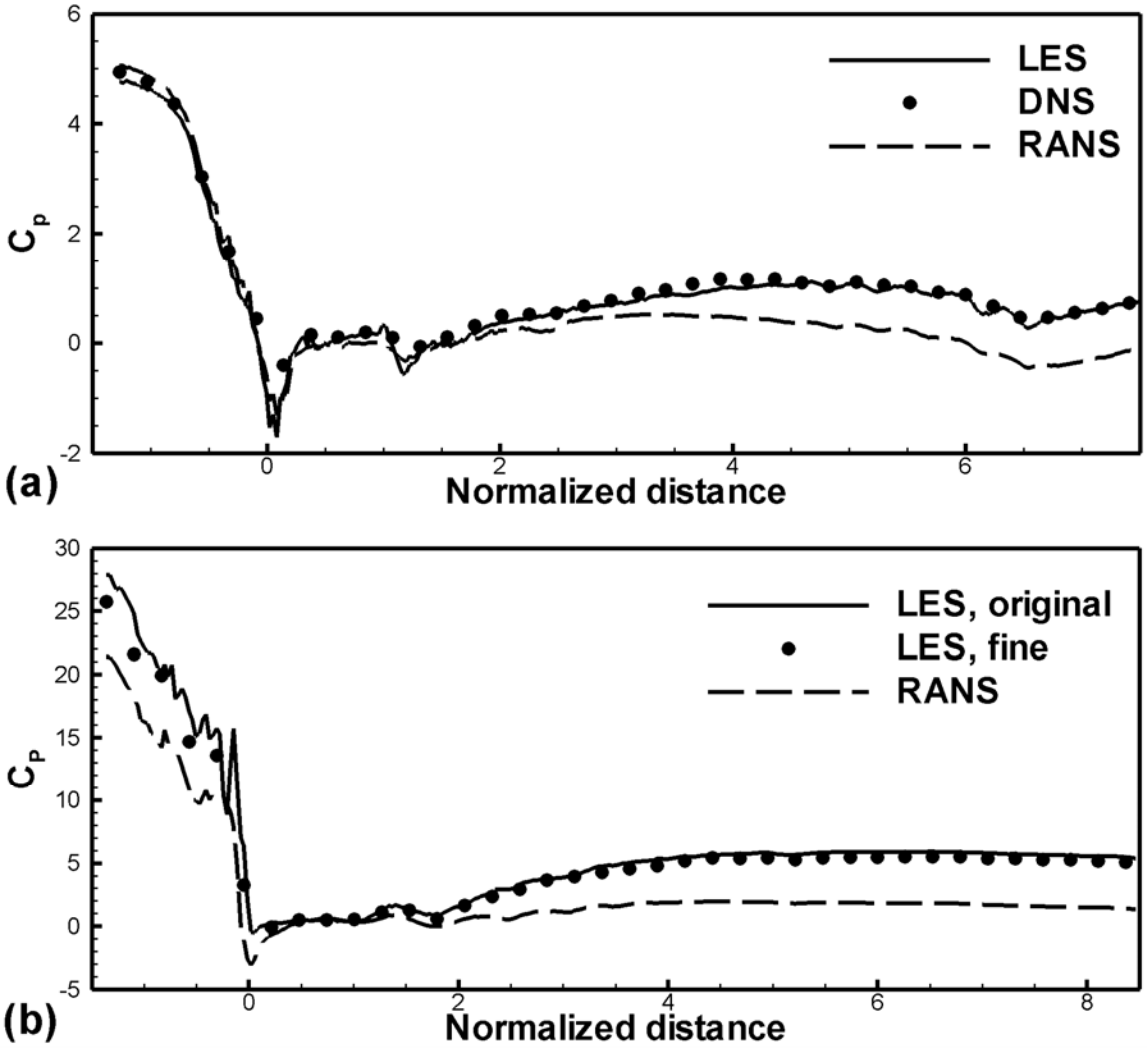

Figure 3.4 Pressure coefficient distribution from the mid pharynx to the end of the trachea for (a) subject 3 and (b) subject 2.

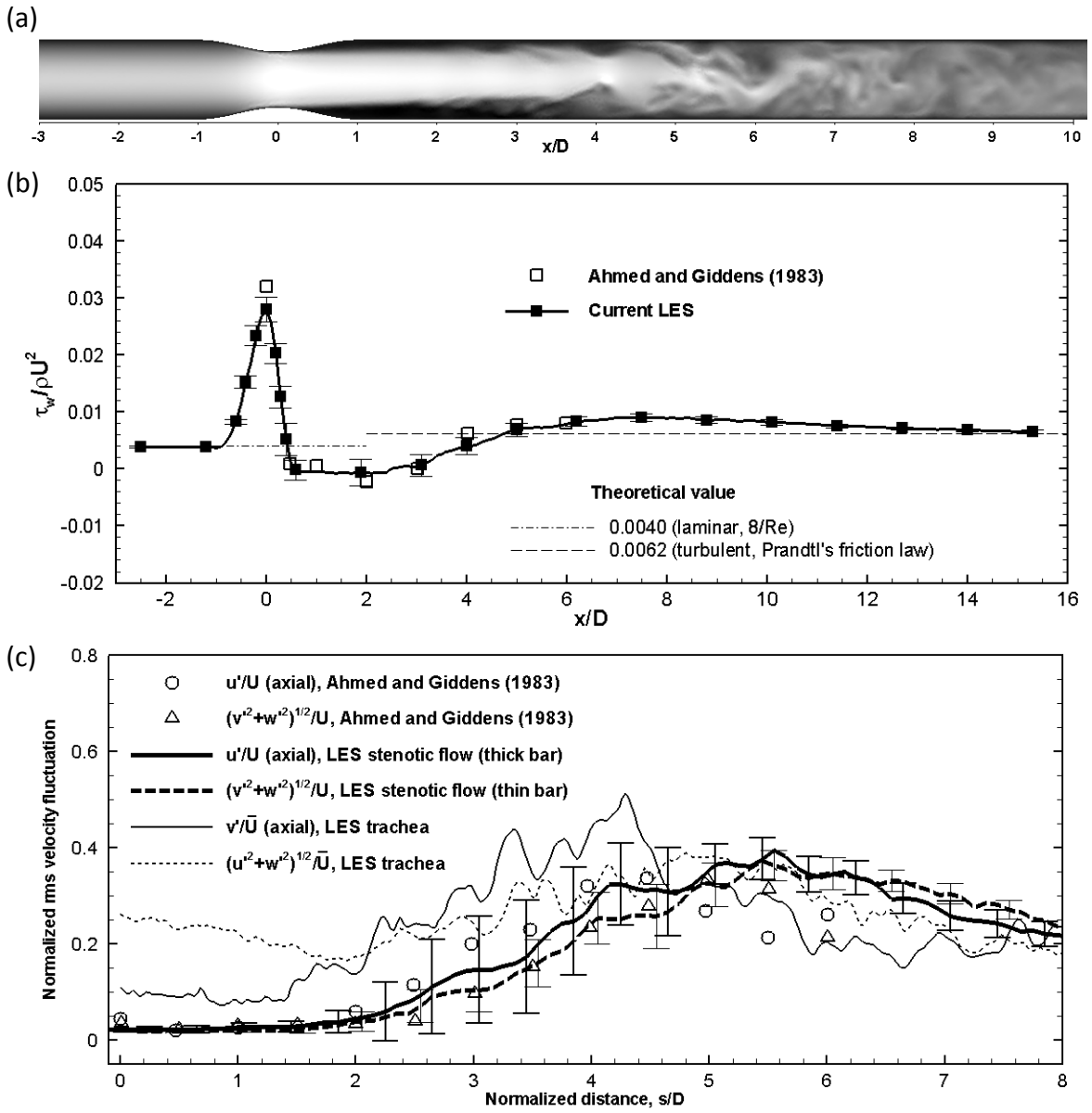

Figure 3.5 Validation of LES model. (a) Contours of the instantaneous axial velocity component u in a x-y plane passing the centerline of the flow through a 50% constriction at Re = 2,000, (b) comparison of wall shear stress with the analytical values and experimental data of Ahmed and Giddens (1983), (c) comparison of RMS velocity fluctuations along the centerline region with the experimental data. U and $\bar{U}$ are the mean speeds based on the tubal diameter and average tracheal diameter of subject 3, respectively. s denotes x in the pipe flow and the distance from the glottis in the trachea.

CHAPTER 4

MULTISCALE AIRFLOW SIMULATION

4.1 Concept of multiscale flow simulation in human lung

The entire path of conducting airway comprises 10-25 generations. The gas flow characteristics vary from the upper and large airways to small airways and multiple flow regimes exist at the same time (in space) and in the same region (in time). In general, it is more complex in large airways than in small airways as the Reynolds number is relatively high and the flow is convection-dominated. The flow characteristics in small airways are relatively simple and are assumed to be parameterized by the Reynolds number, the length, and the diameter. Thus, the complex gas flow in large airways, which may be turbulent or transitional, is solved by high fidelity 3D CFD simulation, and the basic flow field (mean speed and pressure) in 1D centerline tree is solved by energy balance based entry flow model. This 3D-1D coupling approach provides the local flow map over the entire conducting airway in the lung. The terms “3D” and “1D” are referred to as the dimensions of each model. Even though 1D airway tree includes xyz-coordinates for 3D space such that the 1D tree can be displayed in 3D Cartesian coordinates, each individual segment is composed of a line segment. It does not form surface area (2D) or volume (3D) as it is. Moreover, they represent the dimensions of the governing equations. In “3D” airway volume mesh, 3D continuity and momentum equations are solved for the fluid flow fields, and 1D energy based equation, 1D PDE, or 1D ODE are solved in 1D airway tree.

As introduced in Chapter 2, recent advances in medical imaging enable providing regional ventilation map in the lung, and multiscale mesh generation delivers physiological boundary conditions for multiscale CFD simulation in the entire conducting airways. 1D airway tree generated by volume filling method (Tawhai *et al.* 2000, 2004) links anatomically consistent 3D airway to the lung periphery. In this chapter, we propose

an algorithm for 3D-1D coupled airflow simulation of an entire conducting airway consisting of CT-resolved 3D airway and CT-unresolved 1D airway sub-trees, and also demonstrate the full 3D simulation in the entire path airway model. First, a brief description of 1D flow model (Hedges *et al.* 2004) is presented, followed by the 1D flow results in the entire conducting airway and discussion on them. Then the 3D-1D coupling algorithm is introduced. The results are discussed on physiological consistency is discussed in association with the boundary conditions proposed in Chapter 2.

4.2 Energy balance based 1D flow solver

4.2.1 Viscous pressure drop

Pedley *et al.* (1970a, 1970b, 1971, 1977) analyzed the pressure drop in the airways based on the branched-tube measurements of Schroter and Sudlow (1969) using the integral form of the energy equation for an open system having one inlet and one outlet.

$$\Delta p_u + \Delta p_k \approx \Delta p_v \tag{4.1}$$

$$p_u = \left(\int_A p u_i n_i dA \right) / \left(\int_A u_i n_i dA \right) \tag{4.2}$$

$$p_k = \left(\int_A \frac{\rho u_j u_j}{2} u_i n_i dA \right) / \left(\int_A u_i n_i dA \right) \tag{4.3}$$

$$\Delta p_v = \Phi / Q \tag{4.4}$$

$$\Phi = \int_V \mu \left(\frac{\partial u_i}{\partial x_j} + \frac{\partial u_j}{\partial x_i} \right) \frac{\partial u_i}{\partial x_j} dV \tag{4.5}$$

where $\Delta p_\alpha = p_{\alpha 1} - p_{\alpha 2}$ with subscript $\alpha = u$ or k and subscripts *1* and *2* correspond to the respective inlet and outlet faces of an open pipe system. The inlet face of an open system is defined as a face having a negative surface integral term of the denomination in Eqs. (4.2) and (4.3), where A is the cross-sectional area of the face and n_i is the unit vector outward normal to the face. Thus, an inlet face of an open system at inspiration becomes an outlet face at expiration. Q is the volumetric flow rate and defined by the absolute value of the denomination of Eqs. (4.2) and (4.3). V is the volume of an open system. Pedley *et al.* (1970a, 1971, 1977) defined the ratio of actual viscous energy dissipation over Poiseuille dissipation as

$$Z = \frac{\Phi}{\Phi_p} = \frac{\Delta p_v}{\Delta p_{vp}} \tag{4.6}$$

where $\Phi_p = 8\pi\mu\overline{U}^2 L$ is Poiseuille dissipation, L is the airway length, and $\Delta p_{vp} = \Phi_p / Q$. For Poiseuille flow, Eq. (4.6) gives Z = 1, corresponding to the smallest possible pressure drop in a laminar pipe flow. When the flow is disturbed from the Poiseuille parabolic profile, Z is greater than unity. Thus, the Z factor measures the effect of flow structure that deviates from Poiseuille flow behavior, and Z ≥ 1. Pedley *et al.* (1970a, 1971, 1977) adopted a symmetric cylinder-based airway bifurcation model and applied a boundary-layer entry flow model to derive the following formula for inspiratory flow.

$$Z = \gamma\left(\mathrm{Re}\frac{D}{L}\right)^{1/2} \tag{4.7}$$

where $\gamma = C / 4\sqrt{2}$. Pedley *et al.* (1970a, 1971, 1977) found the average value of C based on their model is 1.85, yielding γ = 0.327. Using Eqs. (4.4), (4.6), and (4.7), the viscous pressure drop is expressed as

$$\Delta p_v = \left[256 \sqrt{\frac{\rho \mu L}{\pi^3 D^8}} \right] \gamma Q^{1.5} \tag{4.8}$$

Details of the velocity weighted average static pressure drop, Eq. (4.2), and the pressure drop induced by the kinematic work, Eq. (4.3), are discussed in Chapter 6 in comparison with 3D LES results.

4.2.2 1D flow solver in an asymmetric airway tree

A human conducting airway consists of a tree structure. To examine the fluid dynamical behaviors on inspiration and expiration in airway segments and bifurcations, we consider the energy balance Eq. (4.1) for individual airway segments and mass conservation, Eq. (4.9), at the junctions of segments.

$$Q_{parent} = \sum Q_{child} \tag{4.9}$$

In a symmetrically branching airway model, the pressure drop is the same in the airway segments at the same generation, and the flow rate at *i*-th generation is independently determined by $Q_t/2^i$, where Q_t is the volumetric flow rate at the trachea. Thus, the viscous pressure drop can be analytically solved only by Eq. (4.8). In an asymmetric airway tree, however, the pressure drop in each segment is, in general, determined by solving a set of Eqs. (4.8) and (4.9) simultaneously for all airway segments the bifurcations. The Newton-Raphson iterative method is adapted in the current solver in the current solver to solve the system of equations in asymmetric airway trees for various combinations of BC. On the other hand, given the flow rates at all terminal bronchioles from in-vivo image derived boundary conditions (see Section 2.4.4), the flow rates at all segments are determined *a priori* by Eq. (4.9). Now pressure drops at individual segments can be solved by Eqs. (4.1)

through (4.8) by using a reference pressure at the inlet of the trachea. This is an advantage of using image driven velocity boundary conditions at the terminal bronchioles.

4.2.3 1D simulation results

Generational distribution

The current 1D flow solver is first verified by reproducing the viscous resistance at an inspiratory flow rate of 167 ml/s in a symmetric airway model (Weibel model A) presented by Pedley *et al.* (1970b). Figure 4.1 shows that our model correctly reproduced their results. Then the model is applied to an asymmetric subject specific 1D tree model of an entire conducting airway of subject 3 (see Sections 2.1 and 2.3 for details). A sinusoidal waveform of the total flow rate is imposed with the tidal volume of 500 ml and the period of 4.8 s, and allocated into each terminal bronchiole according to the local flow rate fraction from the 1D model (See section 2.5 for details). Reference pressure is assigned at the tracheal inlet. Figure 4.2 shows the generational distributions of the viscous resistance at selected time points during a breathing cycle and diameter. Similarly to the results in a symmetric airway model, the peak resistance is found at the 4^{th} generation. On the other hand, two major differences are observed. First, the resistance at the trachea (the 0^{th} generation) and the main bronchi (the 1^{st} generation) are greater than the resistance at the 2^{nd} generation. This is attributable to the difference in the airway geometry of the trachea and the main bronchi from the symmetric airway model. This is further discussed in Chapter 7. Another distinct result is that the slight increase of airway resistance at high generations. Starting from 14^{th} generation, the generation-averaged airway resistance increase again rather than decrease to the highest (21^{st}) generation. This is attributable to the accurate representation of regional ventilation in an asymmetric airway, and is discussed in Section 4.2.4. It is noted that in the presented case the parameters of the viscous resistance model at the same flow rate are identical for inspiration and expiration and the airway is assumed rigid. Further studies for airway

resistance with different parameters between inspiration and expiration and for the effect of the airway deformation are presented in Chapters 7 and 9, respectively.

Distribution along the lung height

Figure 4.3 shows the regional distribution of pressure and ventilation at the terminal bronchioles with respect to two normalized lung heights. Quantities are averaged at 100 sections between the base to the apex and between the dorsal to the ventral regions. Smooth distributions observed in all figures. Figures 4.3(a) and 4.3(c) show base (0%) to apex (100%) distributions of flow rate fractions and pressures, respectively. The closer to the base, the more ventilation is observed. Pressure distributions are presented at the peak expiration (t/T = 0.25) and inspiration (t/T = 0.75) of the sinusoidal breathing cycle with the tidal volume of 500 ml and the period of 4.8 s. In Figure 4.3(c), the least pressure drop is observed around the normalized height of 60%. Although the flow rate fraction is not the least in this region, the distance of the path from the 0^{th} generation to the terminal bronchiole is the shorted in this region. The highest pressure drop near the base is attributable to the most ventilation and the longest paths near the base. Dorsal to ventral distributions in Figures 4.3(b) (flow rate fraction) and 4.3(d) (pressure) are relatively flat. However, more ventilation in dorsal region (near 0%) represents the effect of shape of the diaphragm. It is noted that the average pressure drop from the mouth to the terminal bronchioles at the peak flow rate during a normal breathing is known to be about 1 cmH_2O = 98 Pa. Less pressure drop is observed in the presented case because the simulation was conducted at greater lung volume of 85%VC, while the lung volume for normal breathing remains near FRC, at which the diameters are smaller and pressure drop shall increase, as the pressure drop is proportional to the 4^{th} power of the diameter. This has been examined in consideration of the lung deformation, using the method introduced in Chapter 9, and a reasonable range of pressure drop was observed.

4.2.4 Discussion

In a subject specific airway model, large airways are explicitly reconstructed from airway segmentation of CT scans. The CT-unresolved airways are generated from the periphery of CT-resolved airway to the terminal bronchioles, by volume-filling method (Tawhai *et al.* 2000, 2004; Section 2.3). In this section, we discuss some issues relating 1D tree (structure) to airway resistance and ventilation distribution (function).

Effect of diameter

According to the current 1D flow model, the airway resistance is proportional to negative 4th power of the diameter, at a given flow rate and length, regardless of Z factor, defined at Eq. (4.7). Z factor is the correction factor multiplied by the resistance of Poiseuille flow, to manipulate the effect of the flow structure. Assuming circular cross section of airway segment, it can be written as

$$Z = \gamma\left(\mathrm{Re}\frac{D}{L}\right)^{1/2} = \gamma\left(\frac{\overline{U}D}{\nu}\frac{D}{L}\right)^{1/2} = \gamma\left(\frac{4Q}{\pi\nu D}\frac{D}{L}\right)^{1/2} = \gamma\left(\frac{4Q}{\pi\nu L}\right)^{1/2} \sim Q^{1/2}L^{-1/2}, \quad (4.10)$$

where Re is the Reynolds number, $\overline{U}$ is a average velocity magnitude, Q is the flow rate, ν is kinematic viscosity, L is the length of the airway segment, and γ is a constant. $\overline{U}$ is calculated by Q/A, where A is the cross-sectional area. Airway resistance in Poiseuille flow (R_{vp}) can be written by Q, D and L as

$$R_{vp} = \frac{\Delta p_{vp}}{Q} = \frac{\Phi_p}{Q^2} = \frac{8\pi\mu\overline{U}^2 L}{Q^2} = \frac{8\pi\mu Q^2 L}{A^2 Q^2} = \frac{8\pi\mu L}{\left(\pi D^2/4\right)^2} = \frac{128\mu L}{\pi D^4} \sim LD^{-4} \quad (4.11)$$

where Φ_p is the viscous dissipation in Poiseuille flow, μ is the dynamic viscosity. It implies that the diameter dependency of airway resistance is in principle independent of the flow structure.

Effect of seed points and voxels

In volume-filling method (Tawhai 2000, 2004), distribution of seed points plays an important role in generating 1D airway structure in each of five lobes. Through the surfaces of the lobes, voxels are only partially included within the lobe geometry. Allowing or not seed points to be in those voxels affects both the tree structure and the regional ventilation map, because ending points of terminal bronchioles are chosen among seed points which have not been used for growth of other airway branches. If seed points are not placed in the voxels that are partially included in lobe geometry, air ventilation (air volume change) in those voxels is added to the terminal bronchioles at the seed points adjacent to those voxels. Accordingly, the relative ventilation estimation can be greater or smaller near lobe boundary surfaces. An alternative way, to generate a tree to have more correct ventilation near the boundary surfaces of lobes, is to place seed points only in the voxels of which more than half of the volume belongs to the lobe geometry.

Regional vs. lobar ventilation

As observed in Figure 4.2, the generational airway resistance does not keep decreasing as the generation number increases. Instead, it becomes greater at higher generations than the 14th generation when regional ventilation BC (Section 2.4.4) is adapted. However, the resistance does not increase when the lobar ventilation BC (Section 2.4.3) is employed as compared in Figure 4.4(a). For the lobar ventilation, uniform air speed is assumed at the terminal bronchioles of the same lobe, as it is calculated by dividing the total airflow change by the total cross-sectional area of

terminal bronchioles in the lobe. Instead, the regional ventilation is locally prescribed by image registration, which reflects the local difference within a lobe. Thus, the regional ventilation map allows reproducing physiologically consistent distribution, reflecting that lower region of the lung near the diaphragm has more ventilation.

Figure 4.4(b) compares the flow rate distributions of lobar ventilation BC and of regional ventilation BC in the same tree. The flow rates at the terminal bronchioles only of high generations are plotted over the same range. Regional ventilation BC provides more eminent regional differences and allows accuracy in a local level. Ventilation in the lower region of both left and right lungs is much higher with the regional ventilation [Figure 4.4(b)] than the lobar ventilation [Figure 4.4(a)] where the distribution is more uniform. This explains why generational average of airway resistance increases back after the 14^{th} generations. Besides, the least ventilation (blue dots) are observed around the dorsal region, which may be near the thorax cage, and near the central region, in which not much space would exists.

To sum up, an accurate prediction of airway resistance in the entire conducting airway requires reasonable reconstruction of airway tree, correct estimation of diameters of airway branches, and the physiologically accurate regional ventilation map in a local sense.

4.3 3D-1D coupled simulation

4.3.1 Coupling algorithm

In Section 2.4.4, the 3D-1D coupling approach for geometry and boundary conditions is introduced. In the approach, the flow rates at the boundary faces of the 3D mesh can be determined by mass conservation and branching connectivity between the 3D boundary faces and the associated downstream 1D branches (Lin *et al.*, 2009). Once the computational domain of 3D-1D coupled airway and the boundary conditions are set up as illustrated in Section 2.4.4, 3D CFD simulation is first conducted in the 3D airway.

Given the total flow rate at the mouth of the trachea at an instant, the flow rates are determined at the distal ends of 3D airway according to the flow rate fraction distribution prescribed by the 3D-1D coupled airway tree structure (see Section 2.4.4), and then an LES is carried out to produce the velocity and the pressure field in the 3D volume mesh. As described in Figure 4.5(a), the pressures at the last bifurcations of 3D airway tree (red sphere) are passed to the proximal inlet of the 1D airway sub-trees. With the flow rates prescribed at the terminal bronchioles (distal ends of 1D sub-trees) [see Figure 4.2(b) and Section 2.4.4], a system of equations of 1D flow model (see Section 4.2) are solved for flow rates at all airway segments and the pressures at all bifurcations in 1D sub-trees.

Figures 4.5(c) and 4.6 show demonstrations of the 3D-1D coupled simulation of pulmonary airflow in an entire subject specific human lung. A resulting pressure distribution in the entire conducting airway (the upper airway is not shown) provides smooth transition between 3D and 1D airways as shown in the enlarged box of Figure 4.5(c). Computation in the 3D mesh provides locally accurate predictions of complex pressure and velocity fields in the large airways, whereas the 1D mesh provides a more extensive domain and a link across scales with lung parenchyma for all five lobes. Figure 4.6(a) shows the front view of the local pressure fluctuation in the air speed isosurface of 1.5 m/s resolved by 3D simulation, and the 1D airways in color-coded five lobes. Figure 4.3(b) exhibits the instantaneous turbulent laryngeal jet identified by air speed in a vertical plane, and the velocity vectors employed at the 3D ending segments. We emphasize in these figures that this 3D-1D approach enables fine-scale meshing in focus areas, and leaves other regions of the airway tree as 1D mesh for computational efficiency (Lin *et al.*, 2009).

4.3.2 Application and discussion

This simple coupling algorithm between 3D and 1D airways enables to assess the regional distributions of airflow and pressure in the entire conducting airway. We studied

the effect of the boundary conditions for 3D CFD simulations in large airways on the regional ventilation and pressure drop at terminal bronchioles, by comparing vertical (base to dorsal) distribution of the pressure and the flow rate at the terminal bronchioles are presented in Figure 4.7. The total flow rate of 20 L/min is imposed at the mouth. The height of the lung is divided into 100 sections, and the average and the standard deviation are calculated at each normalized vertical level, where 0% and 10% denote the base and the apex of the lung. Three cases are solved imposing different boundary conditions, the lobe-based flow rate distribution (denoted by “lobar flow”, Section 2.4.3), the uniform flow rate (“unif flow”), and the uniform pressure (“unif pres”), at the ending segments of 3D CT-resolved airway. The pressures computed from the 3D simulations are applied to respective 70 inlets of 1D sub-trees. To minimize the effect of 1D boundary condition, the terminal bronchioles generated from the same 3D ending segment are given the same flow rate distribution for all three cases. Details of the 3D CFD simulations can be found in Chapter 3. Apparent effects of the boundary condition at the 3D peripheries on the vertical distribution of pressure and the flow rates are found. The “lobar flow” case shows that the average pressure drop is relatively small between 55% and 77% heights, where are the locations near the root of the five lobes and distance from the trachea is relatively short. And the pressure drop gradually increases toward the apex and the base, forming “>” shape distribution similarly to the 1D simulation case (Section 4.2.3). Due to the longer distance from the trachea, pressure drop near the base is greater than near the apex. It is noted that the gravity effect is neglected as the density of air is small enough. On the other hand, the other two cases (“unif flow” and “unif pres”) result in distributions which are rather opposed to the physiological interpretation. The standard deviation (SD) distribution in Figure 4.7(b) is the most uniform by the “lobar flow” boundary condition. The flow rate distribution in Figures 4.7(c) (average) and 4.7(d) (SD) also shows the smooth and physiologically reasonable distribution for the “lobar flow” case. It is attributable to the distance from the diaphragm that more ventilation occurs near the base

than the apex. This is not obtained by the other two boundary conditions, and the flow rates near the 50% height deviate even 400% greater than “lobar flow” case by employing uniform pressure (“unif pres”).

In summary, the 3D-1D coupling algorithm is proposed for CT-based airflow simulation in the entire human conducting airways, taking into account the multiscale effects that are associated with a turbulent laryngeal jet and lobar ventilation. The former is achieved by incorporating the upper airway geometry and solving the 3D flow field with high fidelity LES model, and the latter uses the 1D centerline airway model to bridge 3D CT-resolved airways and lung parenchyma, in which the pressure and flow are solved by simplified energy-based model. The proposed method is found to produce physiologically reasonable regional distribution of pressure and flow ventilation.

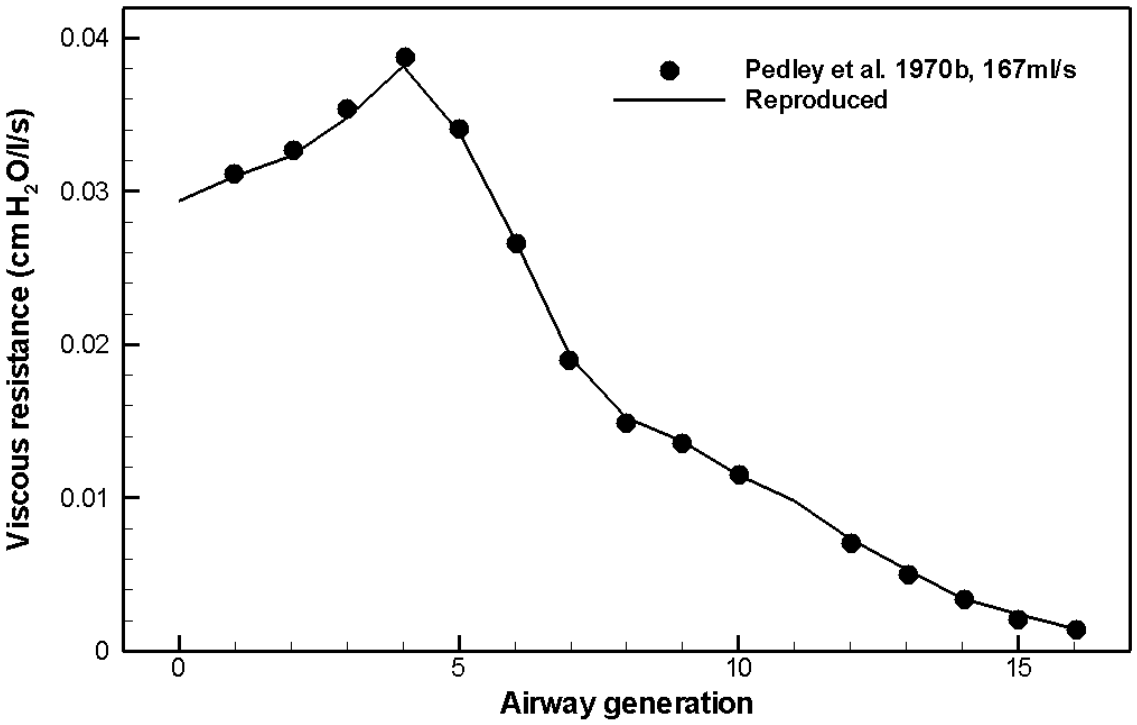

Figure 4.1 Viscous resistance by generation in a symmetric airway model (Weibel model A). The symbols denote the digitized data from Pedley et al. (1970b), and the line denotes the reproced result by the current model.

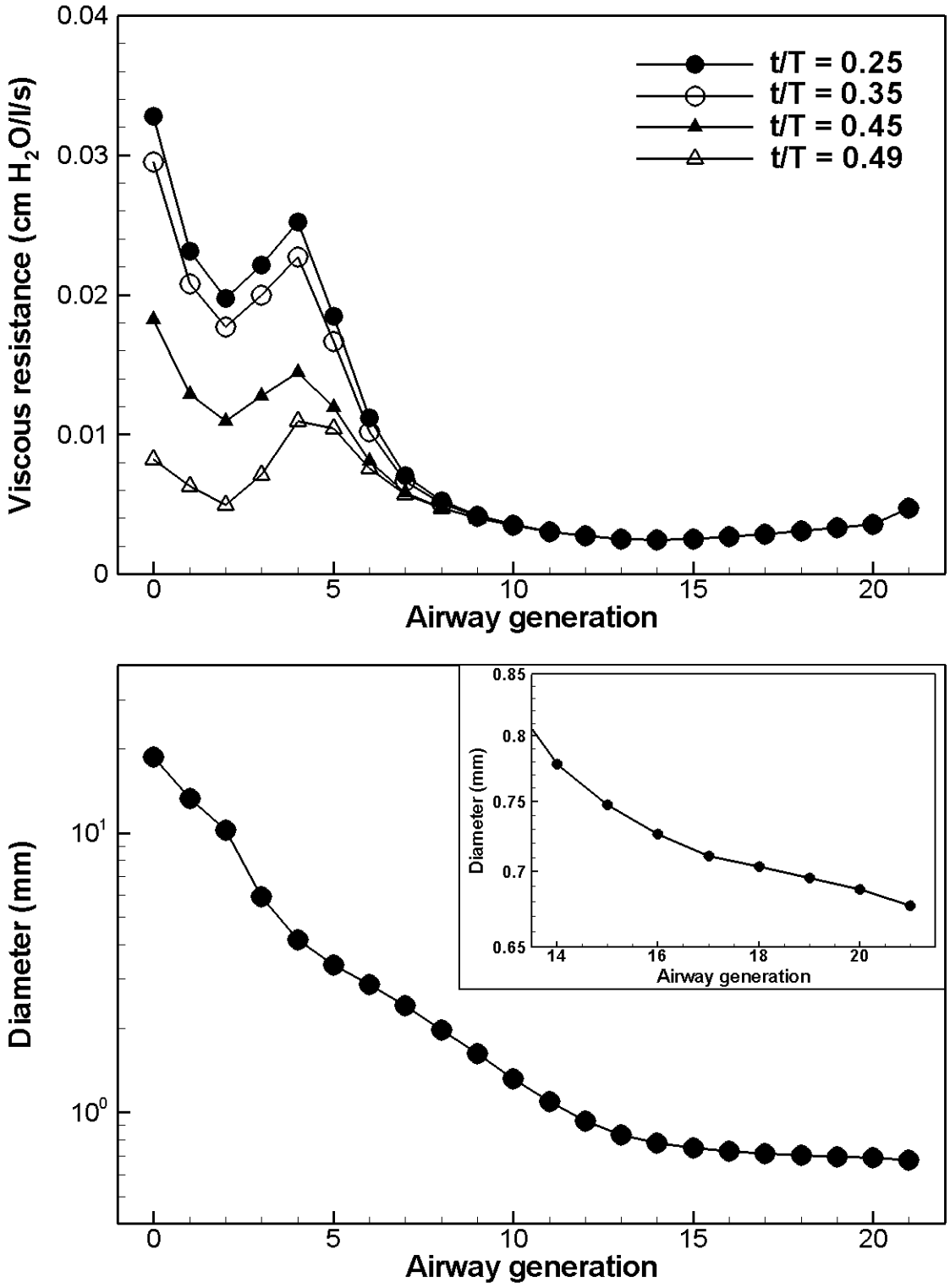

Figure 4.2 Generational distributions of (a) viscous resistance and (b) diameter in an asymmetric subject specific airway tree. Resistance varies in time with sinusoidal flow rate wave form employed at the tracheal inlet.

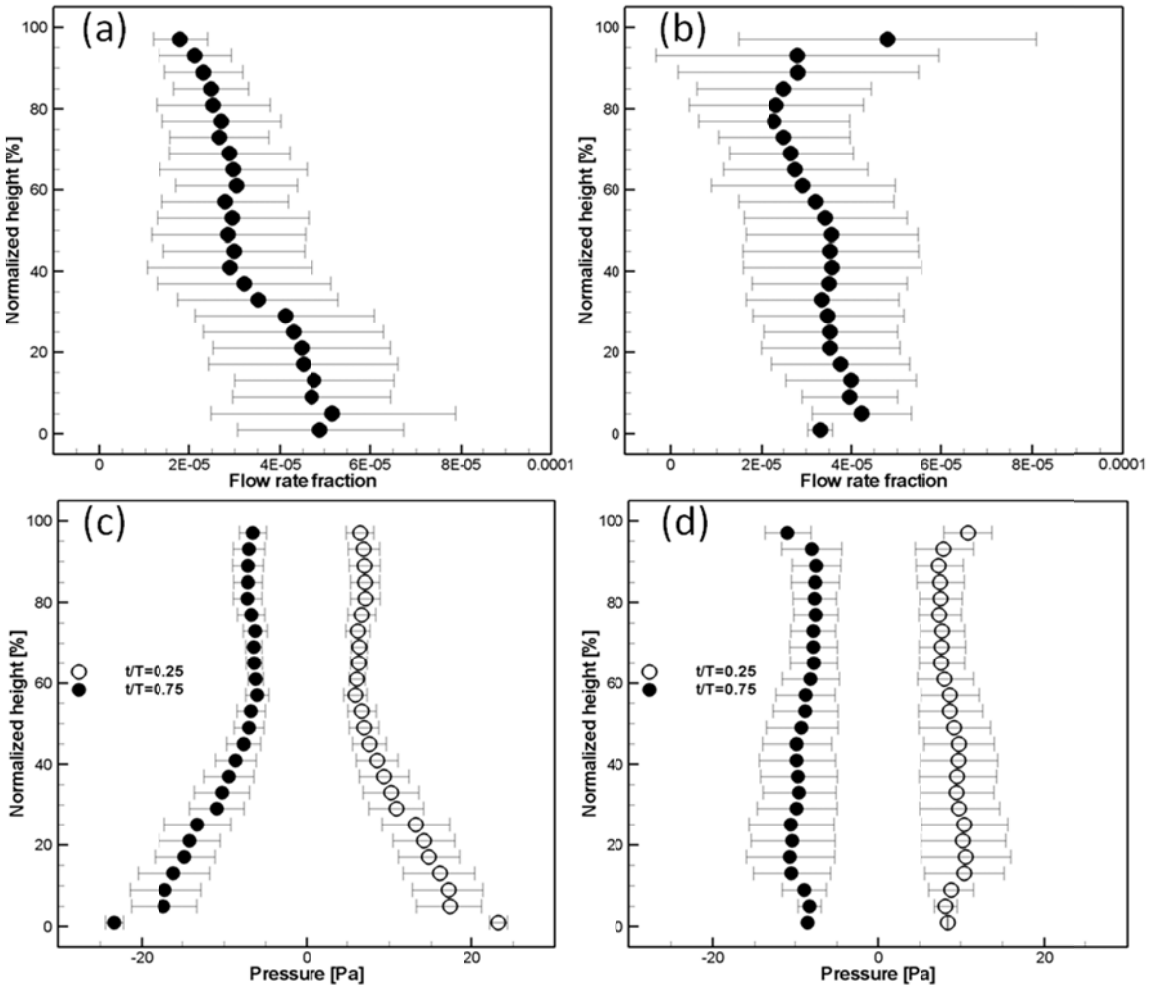

Figure 4.3 Regional distributions of flow and pressure. (a,c) Basal (0 %) to apical (100 %) and (b,d) dorsal (0 %) to ventral (100 %) distributions of (a,b) air flow ventilation fractions and (c,d) terminal airway pressures, averaged over the distal ends of terminal bronchioles at the same level of normalized height. Solid and open symbols in (c) and (d) correspond to the peak inspiration and the peak expiration.

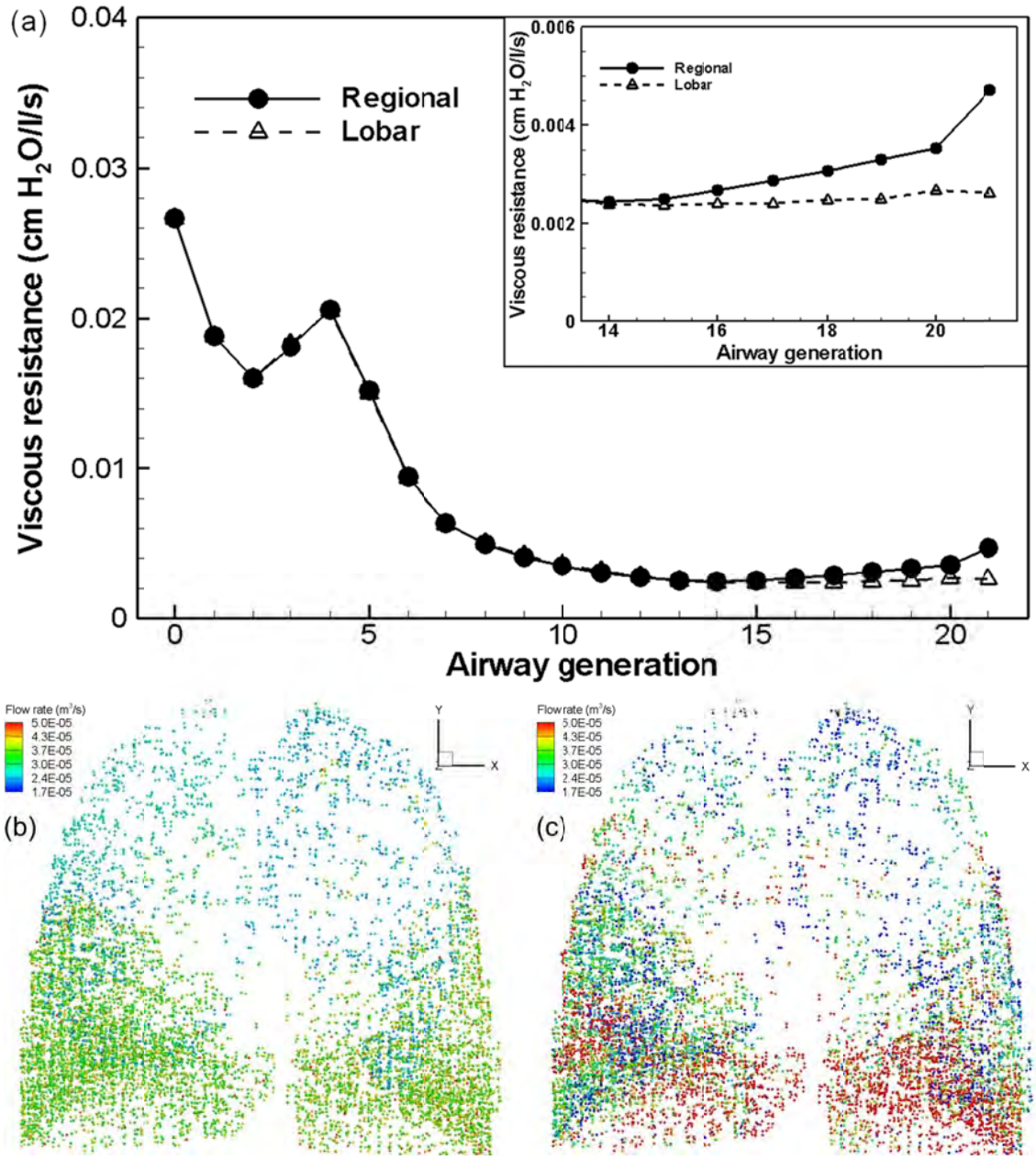

Figure 4.4 Comparison of lobar and regional ventilation. (a) Generational distribution of viscous airway resistance. Regional ventilation map at the terminal bronchioles from the 15th to the 21st generations, with (a) lobar ventilation BC and (b) regional ventilation BC.

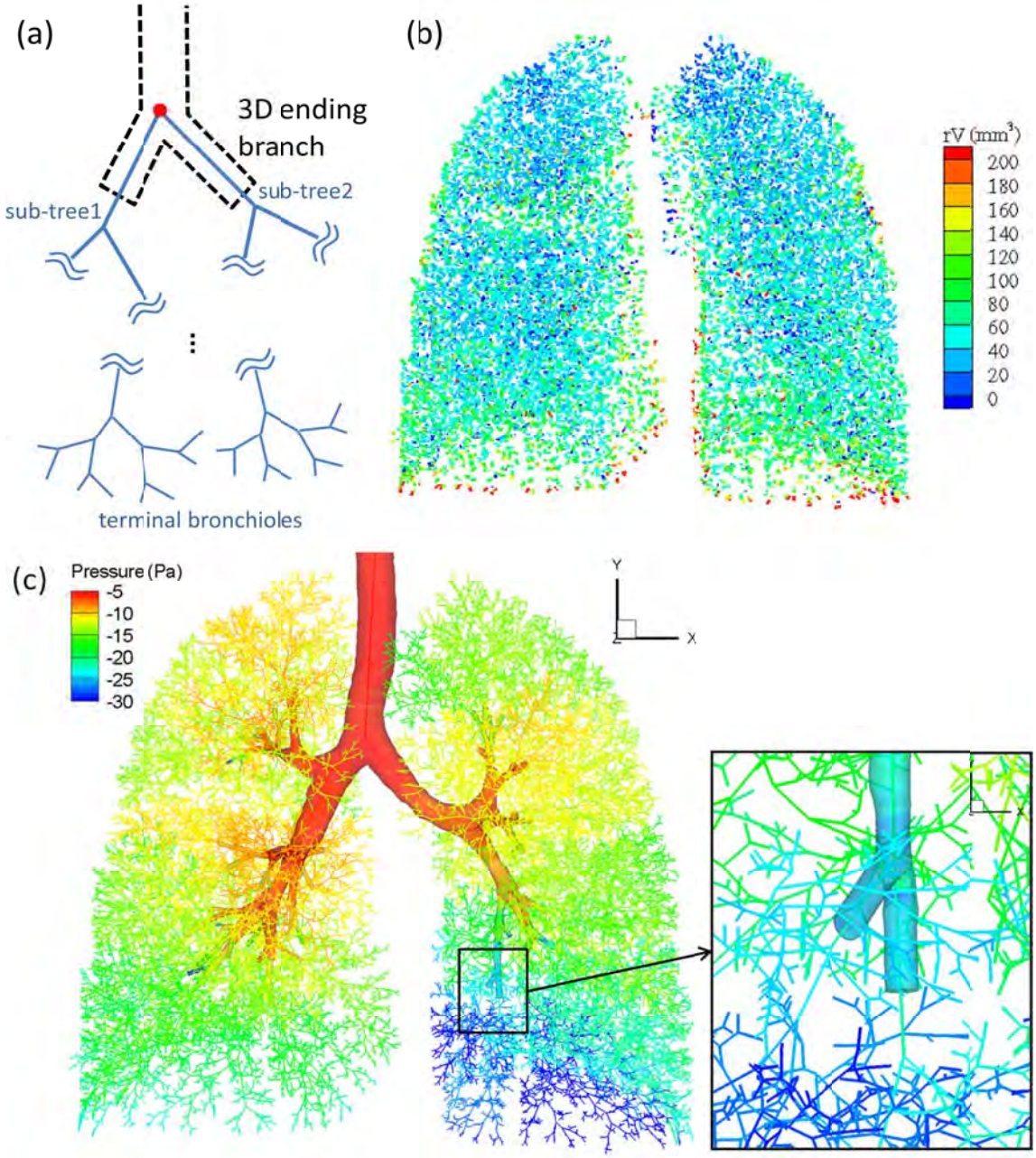

Figure 4.5 Coupling of 3D and 1D models. (a) A schematic; (b) regional ventilation map at terminal bronchioles; (c) the regional pressure distribution in the entire conducting airway from a 3D-1D coupled simulation.

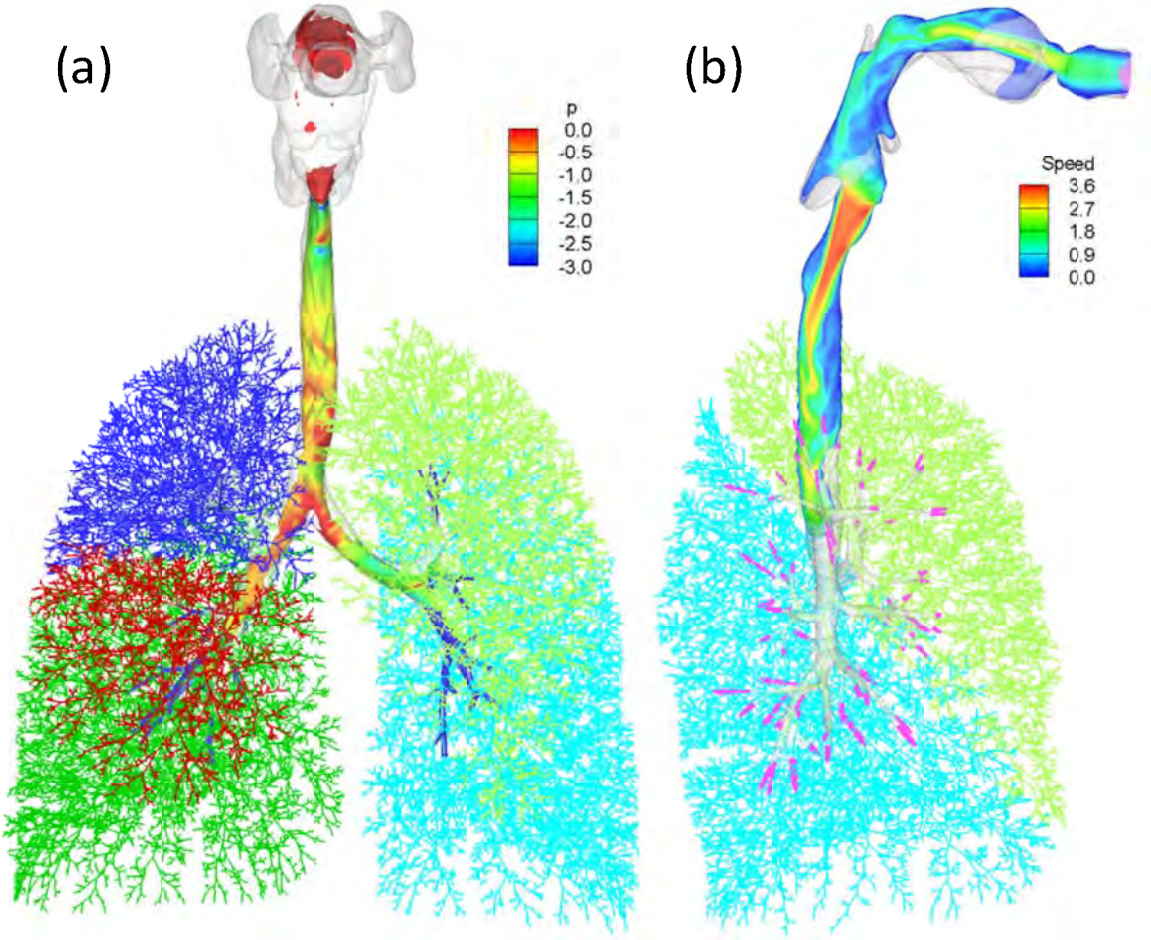

Figure 4.6 A 3D-1D coupled simulation. (a) 3D CT-resolved airways coupled with 1D airways in the color-coded five lobes (front view). The laryngeal jet at peak inspiration is revealed by the isosurface of the air speed at 1.5 m/s. The jet is color-coded by the pressure contours. (b) Side view with the contours of the air speed in a vertical plane.

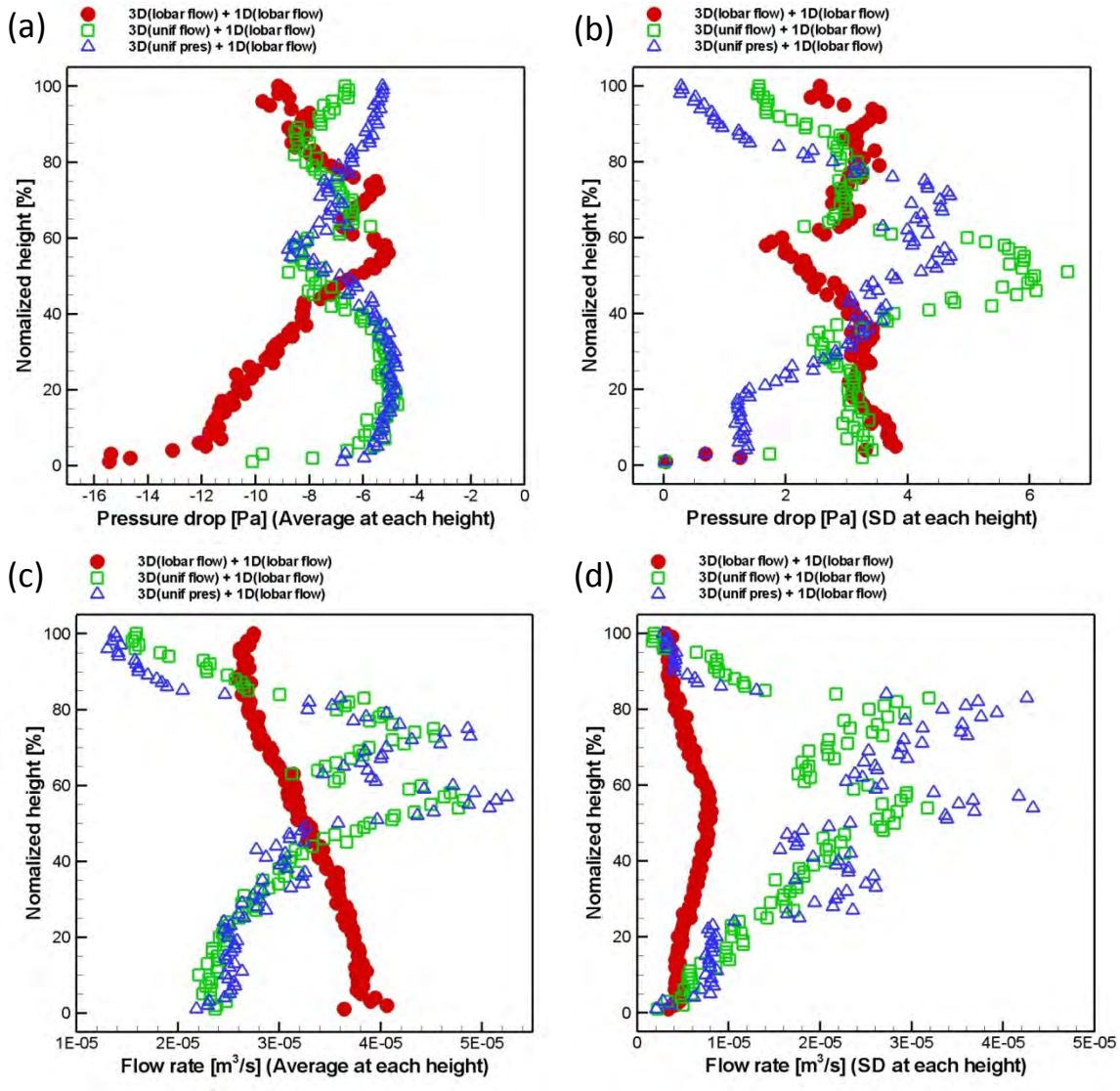

Figure 4.7 The effect of boundary condition imposed at the 3D ending branches. Vertical distributions of pressure (a,b) and flow rate (c,d) at the exits of terminal bronchioles. The average (a,c) and the standard deviation (b,d) by normalized height from the apex (100%) to the base (0%).

CHAPTER 5

INTRA- AND INTERSUBJECT VARIABILITIES OF AIRFLOW

5.1 Introduction

The laryngeal jet is the most prominent inhalation flow phenomenon that determines mean and fluctuating behaviors of the flow downstream in the tracheobronchial airways (Lin *et al.* 2007). According to the complex geometry, the flow in the laryngotracheal region in reality has a wide range of Reynolds number (Re) and involves a mixture of various flow types, such as non-circular confined turbulent jet, open cavity flow, shear layer, and curved and bifurcating turbulent and transitional pipe flow. However, most numerical and experimental studies on human respiratory flow exclude the upper airway tract from the mouth to the larynx (van Ertbuggen *et al.* 2005, West 1959, Sera *et al.* 2003, Green 2004, Adler and Brücker 2007) and use circular straight tubes to construct airway trees, (Zhang and Kleinstreuer 2004, van Ertbruggen *et al.* 2005, Heenan *et al.* 2003, Martonen *et al.* 2002) as not many image-based data contain both extra- and intra-thoracic airways, in part. It is because the information regarding the importance of subject specific geometry in CFD calculations are lacking and such image data sets are not routinely acquired in clinical practice or if they are, they are not readily available to the CFD community. Recently, Lin *et al.* (2007) reported that the inclusion of the upper airways is essential in generating the turbulent laryngeal jet that significantly affects mean and turbulent flow structures and wall shear stress. From the physiological viewpoint, the upper airways play an important role in conditioning (temperature modification, humidification, and filtration) ambient air before it enters the lungs. Diseases of the laryngotracheal airway, which are likely due to the interplay between genotype, phenotype and environmental factors, are commonly life threatening since this anatomic location is the bottleneck of air passage in the respiratory system (Proctor 1977).

To fully explore the potential for subject specificity effects in CFD output as well as the role of the upper airway geometries in understanding respiratory track airflow dynamics, we present here data from two subject specific airway models that variably include the intra-thoracic airways, the complete upper airway geometry or the upper airway geometry with various distal sections eliminated. The specific objectives of this work are two-fold. The first objective is to investigate the effect of reduced airway geometries of the same subject on CFD-simulated flow structures in the trachea, where the flow is most complex under various flow conditions. The intrasubject variabilities are introduced by the change of flow rates and the truncation of upper airways. Assessment of reduced airway geometries allows us to quantify the errors associated with these geometries, leading to strategies that minimize the errors and reduce the imaging and computational costs. The second objective is to assess the effect of intersubject variabilities in airway morphology on flow structures. The intersubject study aims to better understand the structure-function relationship. Here structure is referred to as airway morphological structure unique in individuals and function is flow that can change ventilation, wall shear stress and transport of particles, affecting different aspects of lung function. The chapter is organized as follows. Section 5.2 presents the CT datasets and the methodologies used in LES and data analysis. Section 5.3 discusses the effects of Reynolds number. In section 5.4, the results of intersubject study based upon two subjects are presented. Section 5.5 examines the effect of reduced airway geometries and proposes a boundary condition for improved solutions in use of reduced airway models. The discussions and concluding remarks are made in section 5.6.

5.2 Methods

5.2.1 MDCT-based airway reconstruction

Two human respiratory tracts reconstructed from MDCT scans (subjects 1 and 2) are described in Section 2.1. The respiratory tracts of the two subjects include the extra-

thoracic airways of the mouth, the oropharynx, the laryngopharynx, the larynx and the trachea, as well as the intra-thoracic airways. The trachea is counted as generation 0, and the image-based airway tree consists of up to seven generations of airway branches. Figure 5.1 displays the entire geometry including the upper respiratory tract structure of subject 1. The geometrical characteristics of the airway tree for subject 1 are listed in Table 5.1 in terms of the length, the minimum and the maximum diameters, and the average cross-sectional area. *Name*, *Length*, *minD*, *maxD*, *avgArea*, and *Gen* denote the name of the airway branch, the length of the airway branch in mm, the minimum diameter in mm, the maximum diameter in mm, the average cross-sectional area in mm^2, and the generation number of the airway branch, respectively. Because the cross sections of the airway segments are not circular (even though they are sampled perpendicular to the local long axis of each airway segment), both minimum and maximum diameters are given. A brief summary of the geometrical features of the airway tree for subject 2 is given later.

5.2.2 Numerical simulation

LES is adopted to capture transitional and turbulent flow. Details of the method are presented in Chapter 3. For the cases in this chapter, time steps ranging from 2×10^{-5} to 2×10^{-4} s are used to satisfy the Courant-Friedrichs-Lewy (CFL) condition for various cases. The meshes adopted for the simulation cases vary from 0.4 to 1 million nodal points and 2 to 5 million tetrahedral elements (Table 5.2). *NGen* and *avgL* denote the number of branches at each generation and the average length of the airway branch in mm, respectively. The mesh sensitivity test is presented in section 5.2.5. These meshes are adequate to resolve near Taylor microscale, which is estimated based on the Reynolds number in accord with the description of Dimotakis (2005). The average distance of the first grid from the tracheal wall near the jet impingement or at the vocal cords in wall units, viz. normalized by ν/u_τ where u_τ is the friction velocity, is about 3. The meshes are

partitioned into 64 or 128 sub-domains for parallel computation. The simulations were performed on the TeraGrid clusters Lonestar and Ranger at the Texas Advanced Computing Center (TACC).

Fifty instantaneous volume data sets are sampled with a time interval of 0.012 s for statistical analysis. The interval is based upon the spectral analysis of velocity fluctuations in the trachea (Lin *et al.* 2007). The ensemble mean of a physical quantity *f* is calculated by

$$\langle f(x_i) \rangle = \sum_{k=1}^{N_v} f(x_i, t_k) / N_v, \tag{5.1}$$

where t_k denotes the time of the k-th volume data and N_v is the number of volume data. The cross-sectional average is defined as

$$F = \int_A \langle f(x_i) \rangle dA / A, \tag{5.2}$$

where A denotes the cross-sectional surface. The reference average speed U is the cross-section-averaged speed at the trachea, by which most of the data are normalized in the following analysis. For intrasubject and intersubject comparisons, we will not only examine the above-defined mean and turbulence statistics, but also compare turbulent coherent structures from a deterministic viewpoint using the methodology described in the following section.

5.2.3 Flow structure extraction

Coherent vortical structures are known to play an important role in turbulent jet flow phenomena, such as mixing and entrainment (Dimotakis 2005), and in transition to turbulence (Liu 1989). The proper orthogonal decomposition (POD) technique proposed

by Holmes *et al.* (1996) is a powerful tool in analyzing coherent structures. For example, the POD has been applied to study spectral signature and self-sustained oscillations in the flow over open cavities (Pastur *et al.* 2005, Rowley and Williams 2006). It has also been applied to study pulmonary airflow for subject 2 (Lin *et al.* 2007). Here it is applied to the above 50 volumes of three-dimensional velocity fields for subject 1 to extract and examine the fluctuating velocity fields of coherent structures. In the context of the POD, coherent structures are also known as eigenmodes. Low-order (large-scale), high-ranking (significant) fluctuating eigenmodes are most energetic. Thus, in the following only the first two high-ranking eigenmodes are considered. A subzone of most interest includes the laryngopharynx, the supraglottal space, and the glottis. The λ_2 method (Jeong and Hussain 1995) is then applied to the velocity fields of the POD-extracted spatial eigenmodes for visualization of coherent vortical structures. For a detailed description about the POD procedure, please refer to Lin *et al.* (2007).

5.2.4 Study cases

A total of 12 cases based upon subject 1 are conducted. Table 5.2 shows the airway models, the computational mesh, and the flow conditions of these cases. They consist of four airway models with different levels of truncation, two flow rates, and various inlet boundary conditions for the intrasubject study. The case header "H" denotes the "higher" inspiratory flow rate of Q = 15.2 l/min = 2.53×10^{-4} m^3/s, which is a moderate value (van Ertbruggen *et al.* 2005, Heenan *et al.* 2003, Johnstone *et al*. 2004) of inspiratory flow during normal breathing cycles with a tidal volume of 500 ml. The case header "L" denotes the "lower" flow rate of Q = 5.0 l/min = 0.833×10^{-4} m^3/s. The flow rate is controlled by the velocity boundary condition that is imposed at the exits of the terminal branches in the left and right lungs of the airway model. The exit velocity magnitude in each lung is assumed uniform and is calculated by dividing the flow rate partitioned to each of the lungs with the total cross-sectional area of the exit faces of the

terminal branches in the respective lung. Other boundary conditions based upon multiscale strategies are found in Lin *et al.* (2009). The flow partition to the left and right lungs of subject 1 is 0.912, which is the ratio of the air volumes in both lungs determined from MDCT images. The velocity boundary condition imposed at the exits of the terminal branches produces the desired flow rate and the subject specific flow partition. It is noted that all the cases in this study are performed with a quasi-steady flow rate condition in order to investigate the turbulent statistics at certain flow rates. The stroke length (L) divided by the radius (a) of the trachea, L/a, was proposed by Jan *et al.* (1989) to classify the oscillatory flow regime in a model bifurcation. Considering normal breathing with a tidal volume of 500 ml, the L/a values for subject 1 and 2 are about 446 and 400, respectively. They are far above the criterion for the unsteady flow regime, $L/a \approx 3$. Thus, the overall flow characteristics at peak inspiration during normal breathing can be fairly treated as quasi-steadiness. Furthermore, Pedley and Kamm (1997) stated that flow in the human lung is quasi-steady or nearly so in all airways, at least near peak inspiration during normal breathing. Nevertheless, it is noted that the unsteady behavior of the flow may alter mixing rate with ambient fluid (Zhang and Johari 1996) for gas transport and increase the deposition of micro-size aerosol particles in the mouth-throat region (Grgic *et al.* 2006, Jin *et al.* 2007).

Case 1 (referring to both cases 1H and 1L) uses the original complete geometry [see Figure 5.1(a)]. For cases 2, 3, and 4, the geometries are generated by truncating the original geometry along the dashed lines marked by 2, 3, and 4 in Fig. 1(b). Case 2 contains only the trachea and the intra-thoracic airways, as in many conventional studies (van Ertbruggen 2005, Sera 2003, Green 2004, Adler and Brucker 2007). Case 3 includes the vocal cords (glottis) that may allow the formation of a laryngeal jet. Case 4 further includes the laryngopharynx space and the bifurcation between the larynx and the esophagus, which may create vortical structures (Lin *et al.* 2007). Cases 4Ha and 4Hb (or cases 4La and 4Lb at the lower flow rate) are used to examine the effects of inlet

boundary conditions using the same airway models as case 4H (or 4L). Case 0 is based upon subject 2 for the intersubject comparison. The mean velocities, cross-sectional areas, effective diameters, and Reynolds numbers at three different locations of the complete airway cases for subjects 1 and 2 are summarized in Table 5.3. Due to the curved, non-circular, and asymmetric shape of the airway cross-section, the Reynolds number is calculated by

$$\mathrm{Re} = \frac{UD}{\nu} = \frac{2Q}{\nu\sqrt{\pi A}}, \tag{5.3}$$

where $D = \sqrt{4A/\pi}$ is the effective diameter, Q is the flow rate, and $U = Q/A$ is the average velocity at the cross-section of the airways. The jet Reynolds numbers at the glottis are 2,676 and 852 for high and low flow rates, respectively. A no-slip condition is applied on the airway wall. And the pressure boundary condition is imposed at the inlet of the airway models 1, 2 and 4. The use of an inlet pressure boundary condition allows development of non-uniform velocity at the inlet. A parabolic velocity inlet condition is employed to the narrow inlet of model 3 because a pressure boundary condition may lead to a concentrated high-speed stream at the small inlet area at the supraglottis that strictly constrains the time step and adversely affects numerical stability.

5.2.5 Spatio-temporal convergence

In this section, the mesh sensitivity test for case 1H is presented. The original mesh contains about 0.97 million nodal points and 5.2 million tetrahedral elements, and the fine mesh contains 1.6 million nodal points and 8.4 million elements. The meshes at the glottis and at the distance of 2D from the glottis in the trachea are displayed in Figure 5.2. The time steps for the original mesh and the fine mesh are 2×10^{-5} s and 1×10^{-5} s, respectively. Figure 5.3 shows the distributions of the mean and the axial and non-axial

root-mean-square (RMS) velocity fluctuations along the jet centerline. The jet centerline is defined as the loci where the maximum mean velocity at each axial station along the trachea is located. The axial distance from the glottis is normalized by the tracheal effective diameter $D \approx 14.2$ mm. The location of the normalized axial distance relative to the trachea is illustrated in the insert of Figure 5.3(a). Furthermore, the mean and the RMS fluctuations of the velocity are normalized by the tracheal average velocity of U = 1.6 m/s at Q = 15.2 l/min, whereas U = 0.528 m/s for cases at a lower flow rate of Q = 5.0 l/min in later sections. The results show that the mean [Figure 5.3(a)] and RMS fluctuations [Figure 5.3(b)] of the jet computed from the two meshes are in excellent agreement, indicating that the original mesh is adequate to capture the characteristics of the turbulent jet.

5.3 Intrasubject study on effect of Reynolds number

In this section, the flow characteristics in the pharynx, the larynx and the trachea of subject 1 are examined at two flow rates to assess the effect of Reynolds number.

5.3.1 Mean flow

The flow rate for case 1H is about three times higher than case 1L, resulting in the ratio of Re (case 1H)/Re (case 1L) ≈ 3 in the pharynx, the glottis and the trachea as listed in Table 5.3(a). Figure 5.4 displays the three-dimensional iso-surface of the normalized mean speed of the airflow at the two Reynolds numbers. The iso-surface outlines the laryngeal jet. The basic structures of the jet, such as orientation, impingement, and shape, remain qualitatively similar regardless of Reynolds number. The jet impinges on the tracheal front wall at a distance of about 1D downstream from the glottis as marked by the arrow in Figure 5.4(a). Due to impingement, the jet produces swirling motions along the tracheal wall. Because of the forward inclination of the upper portion of the trachea, the jet stream eventually detaches from the tracheal front wall, moves toward the rear

side of the trachea and then presses against it, creating swirling motions in the lower portion of the trachea. Afterwards, the jet is dispersed and the secondary motion is weakened.

Figures 5.5(a) and 5.5(b) show the contours of normalized mean speed and the velocity vectors in several vertical and horizontal cross-sections. The cross-sections S1 and S2 (S4 and S5) for case 1H (1L) correspond to the two local maxima of turbulent fluctuations as will be discussed in section 5.3.2. S1 and S2 (S4 and S5) correspond to the respective distances of 0.75D and 2.5D (1.75D and 3.75D). The mean flow structures at the two flow rates exhibit similar features. The air flowing into the mouth experiences deceleration when passing through the wide and curved passage of the oral cavity, the oropharynx, and the laryngopharynx. The dashed line in the vertical plane (side view) of Figure 5.5(a) denotes the location where the mean speed is low and the velocity is uniformly distributed as compared with other regions of the upper airways. The air then flows through the constricted glottis into the lower respiratory tract and forms the laryngeal jet. Figure 5.5 also displays the velocity profiles in black at these sections. These profiles are qualitatively similar regardless of Reynolds number. The impingement of the jet on the tracheal front wall generates asymmetric counter-rotating motions, which are particularly clear at stations S2 and S5. Further downstream, as the jet detaches from the tracheal wall, the angles between the jet and the tracheal wall (see Figure 5.4) for cases 1H and 1L are about 12.5^{o} and 7.5^{o}, respectively. The larger angle in case 1H is attributable to higher inertia.

The jet potential core region, whose mean speed along the centerline of the jet is equal to the mean speed at the jet inlet (Kwon and Seo 2005), persists up to a downstream distance of 1.5D (2D) for case 1H (1L). The observation that the jet develops in a shorter axial distance at higher Re (case 1H) than at lower Re (case 1L) agrees with earlier experimental studies of a round jet (Kwon and Seo 2005, Malmstrom *et al.* 1997). The distributions of mean speed $\langle u \rangle / U$ along the jet centerline for both cases are shown in

Figure 5.6. The normalized mean speed is about 4 in the jet core, and then drops below 2 further downstream. Because the centerline (maximum) speed in a fully developed laminar pipe (Poiseuille) flow is twice higher than the average speed, the lower-than-two normalized centerline mean speed indicates that the flow is turbulent.

5.3.2 Turbulent fluctuation

In this section, turbulence characteristics for cases 1H and 1L at two Reynolds numbers are discussed. Figures 5.5(c) and 5.5(d) show the contours of $(u^{rms}/U)^2$, the normalized turbulent kinetic energy (TKE), in the same vertical plane and cross-sections as above. Two local maxima of $(u^{rms}/U)^2$ are found in the trachea at S1 and S2 for case 1H (S4 and S5 for case 1L). The local maxima at S1 and S4 are associated with the mixing layer formed between the jet core region and the ambient resident air. This becomes clear by comparing the contours of $<u>/U$ and $(u^{rms}/U)^2$ in Figure 5.5. At higher *Re*, strong turbulence is produced along the mixing layer as soon as the flow exits the glottis, and upstream flow disturbances (e.g., see Section 5.3.3) can also enhance mixing and turbulent activities. The second local maxima in the trachea at S2 and S5 are located near the end of the jet core [see Figures 5.5(a) and 5.5(b)] and are attributable to the transition of the jet to turbulence. For case 1L both local maxima occur further downstream than case 1H. The region associated with high RMS velocity fluctuations increases with increasing Re, which agrees with previous studies on a turbulent jet. (Kwon and Seo 2005, Malmstrom *et al.* 1997, Bogey and Bailly 2006) The normalized TKE is overall twice stronger in case 1H than case 1L.

The laryngeal jet flow formed at the vocal cord bears a resemblance to the flow through a constricted pipe. Ahmed and Giddens (1983) studied the stenotic flow in smooth pipes with 25%, 50% and 75% constriction at comparable Reynolds numbers, and measured mean $<u>/U$ and RMS fluctuations u^{rms}/U. The ranges of the current $<u>/U$ and u^{rms}/U shown in Figure 6.6 agree with their measurements. The high axial

fluctuation of $u^{rms}_{axial}/U \approx 0.8$ for case 1H (0.6 for case 1L) is found around the first local TKE maximum in the jet core close to the glottis. After the jet core u^{rms}/U increases along the jet centerline with its axial fluctuation reaching a local maximum around 3.5D (4D) for case 1H (1L), agreeing well with Ahmed and Giddens (1983). One notable feature of the stenotic flow in a constricted pipe is that the axial u^{rms}/U is greater than its non-axial component before reaching their maxima (Ahmed and Giddens 1983, Varghese *et al.* 2007). This feature is also observed in the current jet flow in Figure 6.6. After reaching the maxima, the jet is dispersed and turbulence becomes more uniformly distributed at S3 (4.25D) and S6 (5D) as shown in Figure 5.5. And Figure 5.6 shows that the axial and non-axial components along the jet centerline have about the same magnitude after about 5D. Overall, our results agree well with previous studies on turbulent jets (Kwon and Seo 2005, Malmstrom *et al.* 1997, Dimotakis *et al.* 1983, Liepmann 1991, Naib and Sanders 1997, Dimotakis 2000, Babu and Mahesh 2004) and constricted pipe/channel flows (Mittal *et al.* 2003, Ahmed and Giddens 1983, Varghese *et al.* 2007) in spite of the complexity of the airway geometry.

5.3.3 Coherent structure

The POD analysis for subject 1 is presented to examine turbulent coherent structures (eigenmodes). These structures are identified by the iso-surface of λ_2. Figure 5.7 displays the side and front views of the first, most energetic eigenmode in the larynx for cases 1H and 1L. Similar longitudinal vortical structures are observed at the above two flow rates. These vortices originate in the lower laryngopharynx (viz. the closed esophageal space at the bifurcation between the esophagus and the larynx) and stretch downstream to the supraglottis and subglottis space, being consistent with Lin *et al.* (2007) who studied subject 2. In Figures 5.7(b) and 5.7(d) the velocity vectors of this eigenmode in a vertical plane [corresponding to the solid line in Figures 5.7(a) and 5.7(c)] confirm the rotational nature of the structure. The vortices in the second eigenmode rotate

in the opposite direction to those of the first eigenmode (not shown). These vortical structures contribute to the local maximum u^{rms}/U formed between 0.5D and 1D in Figure 5.6 [or Figure 5.3(b)], viz. the first local maximum TKE at S1 and S4 in Figures 5.5(c) and 5.5(d). The relative energy contents in the zeroth (mean), the first (fluctuating) and the second (fluctuating) eigenmodes are 91%, 0.6% and 0.5% in case 1H (97%, 0.6% and 0.4% in case 1L) of the total energy content, respectively. These counter-rotating longitudinal vortices are attributed to the centrifugal instability associated with the curved geometry. These vortices were referred to as Taylor-Gőrtler-like vortices by Lin *et al*. (2007) because they bear a resemblance with the vortices found in the flow past an open cavity. (Podvin *et al.* 2006) Since the curved tubular passage of the larynx also resembles a curved channel, one may regard them as Dean vortices. As pointed out by Saric, (1994) Taylor, Dean, and Gőrtler instabilities share the same physical mechanics (centrifugal instability) and the distinction between them depends on whether they are closed or open systems and whether they are parallel or boundary-layer flows. But their distinction here has not been clear given the complexity of the current airway geometry. For readers who are interested in Taylor, Dean, Gőrtler problems in various geometries and systems, please refer to Drazin (2004), Finlay and Nandakumar (1990), Patel and Sotiropoulos (1997), and Khoury *et al.* (2009).

5.4 Intersubject study on airway morphology

CT-based airway models retain subject specific airway morphology, and accordingly flow characteristics in airway models of different subjects may vary. Thus, a question arises: Would the flow structures identified in one subject be found in other subjects? In this section, case 1H for subject 1 is compared with case 0 for subject 2 to shed light on this issue. The geometrical features of the two CT-based airway models and the flow parameters are listed in Table III. The flow rates for cases 1H and 0 are about the same. There are three major differences in airway morphology between the two

airway models. First, the ratios of the glottal area over the average tracheal cross-sectional area are 25% and 75% for subjects 1 and 2 (namely, area constrictions of 75% and 25% at the glottis), respectively. Second, the tracheas for the two subjects are curved in the opposite directions (cf. Figures 5.5 and 5.8).

Figure 5.8(a) displays the contours of mean air speed for case 0 in a vertical plane. The inhaled air is first accelerated in the oral cavity and is then dispersed in the wide area of the mid pharynx, thus having the slowest velocity there. When the air flows through the glottis into the trachea, it is accelerated to form the laryngeal jet. This process is essentially the same for both subjects. Elongated vertical structures are also found at the bifurcation between the larynx and the esophagus (Lin *et al.* 2007), resembling Figure 5.7 for subject 1. However, unlike subject 1 the laryngeal jet for subject 2 is directed toward the rear wall of the trachea. Due to the curved trachea around “A” marked in Figure 5.8(a), the jet impinges on the tracheal rear wall, leading to the formation of longitudinal vortices over the shallow open cavity-like geometry (Lin *et al.* 2007). Furthermore, the high normalized TKE region is primarily located in the solid box marked in Figure 5.8(b), which is different from the elongated shape found in subject 1 with two local maxima in Figure 5.5. This is because the mild glottal constriction in subject 2 (25% reduction in area at the glottis) results in a jet that is too weak to induce significant mixing with its ambient fluid. As a consequence, the normalized mean speed is smaller and longer, and the strong turbulence region in the trachea is not as elongated as in subject 1. In addition, at the same flow rate turbulence intensity is overall weak in subject 2 compared to subject 1 because the normalized TKE ranges from 0 to 0.1 in case 0 [Figure 5.8(b)] while it ranges from 0 to 0.8 in case 1H [Figure 5(c)]. Thus, it can be concluded that flow structures in different subjects at the same flow rate are only qualitatively similar and turbulent intensity in the trachea is dependent upon the area constriction at the glottis and the curvature and shape of the trachea.

5.5 Intrasubject study on truncated upper airways

For the above two human subject studies, about 30-50% of the computational mesh and computing time are allocated to the oral cavity, yielding rather expensive computational cost if the regions of interest are merely in the central airways. Thus, for practical applications it would be desirable to use reduced upper airway geometries that only include part of the upper airways for CFD analysis. Furthermore, a reduced geometry means a reduction in exposure of human subjects to radiation. For this purpose, three reduced airway geometries are generated by truncating the original complete geometry at various levels. In this section, airflow simulations are conducted using the geometries based upon subject 1 at two flow rates. Results are compared with those of the complete geometry cases 1H and 1L to determine the effect of truncation.

5.5.1 Effect of truncation levels

Three levels of truncation are marked by the dashed lines in Figure 5.1(b). For cases 2, 3, and 4, the airways are truncated at below the glottis, slightly above the glottis, and the mid laryngopharynx, respectively. For case 4, inclusion of the bifurcation between the larynx and the esophagus intends to provide the geometric condition that may be needed for formation and sustenance of the vortical structures shown in Figure 5.7.

The contours of normalized mean speed in a vertical plane for these cases at 15.2 l/min are displayed in Figure 5.9. For case 2 (referring to both cases 2H and 2L), the mean flow characteristics are fundamentally different from case 1 because of the absence of the turbulent laryngeal jet. The velocity distribution exhibits a quasi-parabolic shape, which is a characteristic of laminar pipe flow. This observation is consistent with Lin *et al.* (2007). As the glottis is included in cases 3 and 4, the laryngeal jet is formed. However, the narrow stream core begins at the inlet above the glottis in the laryngopharynx rather than at the glottis. The distributions of the normalized mean speed

$\langle u \rangle / U$ along the jet centerline for these cases are compared in Figure 5.10. The absence of the upper airways in case 2 yields a fairly uniform distribution due to the quasi-parabolic velocity feature. In contrast, cases 1, 3, and 4, which include the constricted glottal space, allow formation of the laryngeal jet, thus exhibiting a sequence of airflow acceleration, turbulent mixing and deceleration. Because the jets in cases 3 and 4 begin at the inlet in the supraglottis [Figures 5.9(b) and 5.9(c)], the $\langle u \rangle / U$ values near the glottis are over-predicted in these cases. Overall, case 4 agrees better with the complete geometry case 1 because it includes more upper airways that can reduce the effect of boundary condition.

The effect of truncation is more evident in terms of turbulence statistics. The axial and non-axial components of RMS velocity fluctuations for these cases are compared in Figures 5.11 and 5.12 for high and low flow rate cases, respectively. Again case 4 agrees better with case 1 than cases 2 and 3. The absence of vortices at the junction of the larynx and the esophagus in cases 3H and 4H is reflected in the under-prediction of the non-axial velocity fluctuations in Figure 5.11(b). At a low flow rate in Figure 5.12, the lack of upstream disturbances above the glottis due to the absence of vortices in the larynx significantly affects post-stenotic velocity fluctuations and may delay the transition of the laryngeal jet to turbulence. In fact, Vétel *et al.* (2008) reported that the dynamic behaviors of the jet flow formed in a smooth constricted pipe depend on upstream flow disturbances, and without upstream disturbances the transition from laminar to turbulence may be delayed or suppressed.

5.5.2 Improved inlet boundary condition

As previously discussed, the truncated pharyngeal airway with a pressure inlet boundary condition leads to the formation of an un-physiological jet stream above the vocal cord. If that portion of the jet stream could be eliminated, would the jet flow in the trachea be better predicted? To answer this question, one can impose a velocity inlet

boundary condition based upon mean and RMS velocities of the flow found in case 1. The mean and fluctuating velocity distributions of case 1H at level 4 in Figure 5.1(b), viz. the inlet of case 4, are displayed in Figure 5.13. The distributions of mean speed and RMS fluctuations in Figures 5.13(a) and 5.13(b) are fairly uniform. The data along lines A-A' (front to rear) and B-B' (right to left) are extracted and plotted in Figures 5.13(c) and 5.13(d). The variation of the data along B-B′ appears to be more significant than along A-A′ perhaps due to its longer distance and narrower path. The normalized mean speed along A-A' ranges from 0.17 to 0.24, whereas it ranges from 0.09 to 0.22 along B-B'. Thus, the flow at the mid laryngopharynx is 4-10 times slower than those at the glottis and the jet core. The spatial averages of u^{rms}/U at this cross-section are 0.29 and 0.13 for cases 1H and 1L, respectively.

Based upon the above analysis, we apply the uniform velocity condition without (case 4a) and with (case 4b) velocity perturbation at the inlet of case 4 (see Table 5.2). Figure 5.14 shows that the new boundary conditions significantly improve the mean velocity distributions for both flow rates. The axial and non-axial components of u^{rms}/U exhibited in Figures 5.15 and 5.16 show improvement after the local maximum at about 3.5D (4.5D) for Q = 15.2 (5.0) l/min. Perturbation imposed at the inlet only slightly increases velocity fluctuations near the glottis. All three 4H cases under-predict the velocity fluctuations in the post-glottal region because of their inability to produce vortices at the bifurcation between the larynx and the esophagus. The under-prediction of post-stenotic velocity fluctuations becomes more significant at a lower flow rate.

5.5.3 Spectral analysis

In any case with truncated upper airways, the vortex tubes formed at the bifurcation between the larynx and the esophagus (Figure 5.7) are not identifiable by the POD analysis, although the mean flows for cases 4a and 4b are in a good agreement with

that of case 1. In this section, the spectral features of the turbulent laryngeal jet are examined to better understand the unsteady behaviors of the jet.

Energy spectra in the frequency domain at three locations for cases 1H and 4Hb are presented in Figure 5.17. The kinetic energy (E) is normalized by $U^2/2$ ($E/U^2/2$) and the frequency is normalized by U/D (S). Figure 5.17(a) shows that for case 1H the broadband energy spectrum with high energy content is already present at the entrance of the glottis. The slope of -5/3, which is characteristic of the well-known inertial subrange, appears to be limited to a narrow range between $S = 1\times10^2$ and 3×10^2. The slope then gradually changes to -10/3 around $S = 10^3$ and finally becomes -7, indicating the dominance of viscous forces. Figures 5.17(c) and 5.17(e) show the energy spectra at two downstream stations from the glottis along the centerline of the laryngeal jet. At 0.5D, the energy spectrum is elevated in the high frequency range, as compared with Figure 5.17(a), with a wider -5/3 range and a noticeable -10/3 slope in the vicinity of $S = 10^3$. The -10/3 spectrum is a characteristic of post-stenotic flow as reported by Kim and Corcoran (1974), Lu *et al.* (1980), Mittal *et al.* (2003) and Varghese *et al.* (2007). At 2.5D, the -5/3 spectrum is further widespread to higher frequency with a narrower -10/3 range. For case 4Hb with a truncated airway model but an improved inlet boundary condition, the spectrum near the entrance of the glottis is hardly reproduced. A comparison of Figures 5.17(a) and 5.17(b) shows that the energy content near the glottis for case 4Hb is much lower than case 1H because of the absence of turbulence. At 0.5D, Figure 5.17(d) shows that the energy content rises although it is still much under-predicted compared to case 1H. Further downstream at 2.5D, the energy spectrum in Figure 5.17(f) almost recovers that of case 1H in Figure 5.17(e), especially in the high frequency range. These results are consistent with the analysis of RMS velocity fluctuations in Figure 5.15, which shows similar levels of RMS velocity fluctuations at 2.5D for both cases. For the low flow rate cases , the spectra are qualitatively similar to those of the high flow rate cases except that the energy contents are much under-predicted in cases 4L and the spectrum is recovered

much further downstream at about 5D (see Figure 5.16). Thus, we conclude that: (1) inclusion of more laryngopharynx space is essential in capturing turbulent structures in the supra- to sub-glottal region, and (2) with a reduced airway model and an improved velocity boundary condition, like case 4Hb (4Lb), turbulent structures can be fairly recovered at a distance of about 2.5D (5.0D) downstream from the glottis.

5.5.4 Pressure distribution

Accurate prediction of pressure distribution along the airways is important for analysis of the respiratory flow. This is because the current diagnostics of human respiratory systems is mainly based on pressure drop from the mouth inlet to the central or peripheral airways. The largest error in prediction of pressure drop occurs between the inlet and the first few generations of the airways where the flow is either transitional or turbulent. This section aims to assess the effect of truncated upper airway geometries on pressure variation.

The pressure coefficient is defined as $C_P = (P\text{-}P_o)/(\rho U^2/2)$, viz. the difference between the cross-sectional average pressure P and the reference pressure P_o normalized by $\rho U^2/2$, where ρ is the air density and U is the average air velocity in the trachea. In all cases the pressure at the tracheal inlet, viz. the inlet of case 2, is used as the reference pressure. Figures 5.18 and 5.19 show the C_P distributions from the mid pharynx to the end of the trachea. The lowest C_P value is observed at the glottis. The pressure coefficient increases primarily between 2D and 4D, where the transition of the laryngeal jet to turbulence takes place and the RMS velocity fluctuations are strong. An increase in pressure along the trachea acts to decelerate the flow. A comparison of Figures 5.18(a) and 5.18(b) reveals that this trend is similar at both flow rates. For case 1H (1L), the C_P decreases from the mid pharynx to the glottis by about 29 (31) and then increases to 5.8 (3.6). These results are noticeably different from the simplified analytical solutions assuming that the trachea is a straight circular pipe without considering the effect of the

laryngeal jet. For example, the C_P estimated by the Hagen-Poiseuille viscous pressure formula decreases by 0.4 (1.2) over a distance of 8D (an approximate distance between the glottis and before the first bifurcation) for Q = 15.2 (5.0) l/min. And the one-dimensional model of Pedley *et al.* (1970) for viscous pressure predicts a decrease of the C_P by 2.5 (4.3) for Q = 15.2 (5.0) l/min over the same distance.

In our results, case 2 is similar to the pipe flow because of exclusion of the upper airways. Because the flow has no jet motion and is laminar, the flow needs a higher pressure at the inlet of the trachea to push the flow through the trachea. Different from other cases, the pressure along the trachea decreases slightly and appears almost constant. For case 2H (2L) in Figure 5.18, the C_P decreases only by 0.3 (0.4) between the entrance and the exit of the trachea. For cases 4H and 4L, the pressure drops from the inlet to the glottis are under-estimated by 17% and 29%, respectively. For cases 3H and 3L, they are under-estimated by about 31%. With the proposed velocity inlet boundary condition (cases 4a and 4b), the discrepancies in pressure drop are significantly reduced as shown in Figure 5.19. The C_P distributions from the mid pharynx inlet to the glottis for cases 4a and 4b almost collapse with those of cases 1H and 1L regardless of Reynolds number. This again suggests that a reduced airway model with the proposed velocity boundary condition can adequately capture the pressure distribution in the trachea.

5.5.5 Effect on the flow in distal airways

In the previous sections, we focus on the intra- and inter- subject variabilities in the upper airways as well as the trachea since the laryngeal jet is of most interest. This section is concerned with the variabilities in the main bronchi and bronchioles. Figure 20 shows the contours of normalized mean speed and TKE in a vertical plane for cases 1H, 2H, and 4Hb. In the presence of the laryngeal jet, the mean fluid streams in the main bronchi and bronchioles of case 1H are more dispersed than those of case 2H due to turbulent mixing. The difference between them is more significant for velocity

fluctuations. While the trace of velocity fluctuation is still observable in the 2^{nd}-4^{th} generations in case 1H [Figure 5.20(d)], it almost vanishes in case 2H [Figure 5.20(e)]. On the other hand, using a reduced airway model and an improved boundary condition (case 4Hb), the differences in mean and fluctuation are remarkably reduced. Figure 5.20(c) shows the mean speed distribution is almost identical to case 1H in the whole plane. The difference in the TKE levels is also small although their distributions, e.g. in the dashed boxes in Figures 5.20(d) and 5.20(f), are slightly different. Zhang and Finlay (2005) observed an effect of Reynolds number on particle deposition efficiency in the trachea, but the effect does not seem to propagate to the bifurcation downstream. If particle transport is mainly dependent upon the mean flow, cases 1H and 4Hb are expected to produce almost the same particle deposition efficiencies. However, if both mean and fluctuating velocities play a role in particle transport, how the difference in the TKE distribution affects particle deposition in the upper and central airways is yet to be investigated.

5.6 Discussion and summary

Intra- and intersubject variabilities of the inspiratory flow in the human lungs are studied by using large eddy simulation on the MDCT-based airway models. The mean and turbulent characteristics of the flows at two different flow rates in the airway model, which includes the upper respiratory tract, are found to have a strong resemblance. The turbulent laryngeal jet, which is the most dominant feature during inhalation, shows qualitatively similar dynamic behaviors regardless of Reynolds number. At a higher flow rate, the jet core is found shorter (about 0.5D), and detaches from the tracheal wall with a larger inclination angle. We attribute these differences to the effect of inertia. Two local TKE maxima are observed in the trachea at both flow rates. The first maximum is observed at the mixing layer close to the glottis and the jet core, and the second is found further downstream following the jet core. The POD analysis reveals Taylor-Gőrtler-like

or Dean vortices as identified by Lin *et al.* (2007). These vortices appear to originate in the cavity-like region at the esophagus and extend to the subglottal space in the trachea.

The variability of the flow characteristics in two human subjects is investigated. In general, the flows in the upper respiratory tracts of the two subjects behave similarly. Vortical structures at the bifurcation between the larynx and the esophagus are observed in both subjects. However, the detailed mean flow and turbulent characteristics of the laryngeal jet are different. The major differences are caused by the constriction at the glottis, and the curvature and shape of the airways. A less area reduction results in a longer jet core and weaker turbulent activities. Depending upon subject specific airway morphology, the laryngeal jet can impinge on the tracheal wall at different locations and in different directions.

The intrasubject dependences of airflow in the airway models are examined through the change of flow rates and the truncation of upper airways. Assessment of reduced airway geometries allows us to quantify the errors associated with these geometries, leading to new strategies that minimize errors and reduce imaging and computational costs. The more the upper airways are truncated, the more inaccurate the CFD-predicted flow fields become. Without including any upper respiratory tract, the flow behaves as a laminar pipe flow. The maximum speed is under-estimated by about 50% (30%) at 15.2 (5.0) l/min as compared with the complete upper airway cases. Even when part of the upper airways is included, the characteristics of the laryngeal jet are not entirely reproduced. A velocity boundary condition is then proposed to improve the accuracy of the solutions for the truncated airway model. The boundary condition is based upon the observation that the velocity in the mid pharynx of the complete geometry cases is 4-10 times slower than those at the glottis and in the trachea. Besides, the distributions of mean and fluctuation velocities are fairly uniform. Thus, two boundary conditions are examined. Both conditions employ uniform velocity. One of them further includes random velocity perturbation to account for turbulent fluctuations. Both velocity

boundary conditions yield a laryngeal jet that behaves similarly to that of the complete geometry cases. The predicted maximum mean velocity and RMS fluctuation downstream in the trachea are improved substantially, although turbulent intensity close to the glottis is still under-estimated. Spectral analysis reveals the well-known spectral behaviors of turbulence in the larynx and the trachea. The pressure distributions in the complete and truncated airway models are also compared. For the complete geometry case, the pressure along the airway decreases rapidly to the subglottal region and then increases in the trachea as approaching the bifurcation. With the truncated geometries, however, the pressure distribution along the centerline is under-estimated near the inlet when the uniform pressure condition is given. By applying the proposed velocity boundary condition, the pressure drop between the inlet and the subglottis is well predicted.

In the distal airways, without including upper airways both mean flow and TKE are affected and the flow becomes almost laminar. By applying the proposed boundary condition with partial inclusion of the pharynx, only small differences in the TKE distribution are observed in the distal airways.

In summary, the turbulent laryngeal jet is a dominant feature in the human inspiratory flow. The characteristics of the jet are highly affected by the upper airway geometry, such as the constriction at the glottis, the airway shape and size, and the flow conditions in the pharynx and the larynx. The major flow features are not entirely reproduced by use of a truncated upper airway model. However, if the complete upper airway geometry is not available, an airway geometrical model truncated at the mid pharynx could be used together with the proposed boundary condition to improve the accuracy of solution.

Table 5.1 Analysis of the airway geometry of subject 1.

(a) Analysis of the major airway branches

Name	*Length*	*minD*	*maxD*	*avgArea*	*Gen*
Trachea	98.7	13.2	15.2	157.8	0
LMB	56.1	9.31	11.6	85.1	1
RMB	26.6	10.2	14.2	114.4	1

(b) Analysis of the airway geometry by generations

Gen	*NGen*	*avgL*	*minD*	*maxD*	*avgArea*
0	1	98.7	13.2	15.2	157.8
1	2	41.3	9.8	12.9	99.7
2	4	18.9	6.4	9.7	49.9
3	8	12.8	4.5	6.4	23.2
4	16	14.1	3.2	4.4	12.0
5	4	17.7	3.6	4.9	14.6
6	2	22.6	3.7	4.9	14.5
7	2	13.8	2.8	4.0	9.2

Table 5.2 Case summary for subject 1.

Case (Inlet)	1 (Mouth)	2 (Trachea)	3 (Supra-glottis)	4 (Mid pharynx)		
Nodes	975,807	407,275	533,893	613,707		
Elements	5,156,875	2,110,327	2,808,214	3,239,948		
Output size (Mbytes)	391	161	213	246		
15.2 l/min	Case 1H	Case 2H	Case 3H	Case 4H	Case 4Ha	Case 4Hb
5.0 l/min	Case 1L	Case 2L	Case 3L	Case 4L	Case 4La	Case 4Lb
Inlet boundary condition	Uniform velocity	Pressure	Parabolic velocity	Pressure	Uniform velocity	Perturbed velocity

Table 5.3 Geometrical and flow properties on the cross-sections of interest.

(a) Subject 1

	Case 1H/Case1L		
Q [l/min]	15.2/5.0		
Cross-section	Mid pharynx	Glottis	Trachea
U [m/s]	0.630/0.201	6.43/2.05	1.60/0.528
A [mm^2] (D [mm])	401 (22.6)	39.3 (7.074)	157.8 (14.2)
Re	838/267	2676/852	1337/440

(b) Subject 2

	Case 0		
Q [l/min]	15.3		
Cross-section	Mid pharynx	Glottis	Trachea
U [m/s]	0.512	2.13	1.58
A [mm^2] (D [mm])	906 (34.0)	120 (12.4)	161 (14.3)
Re	558	1550	1332

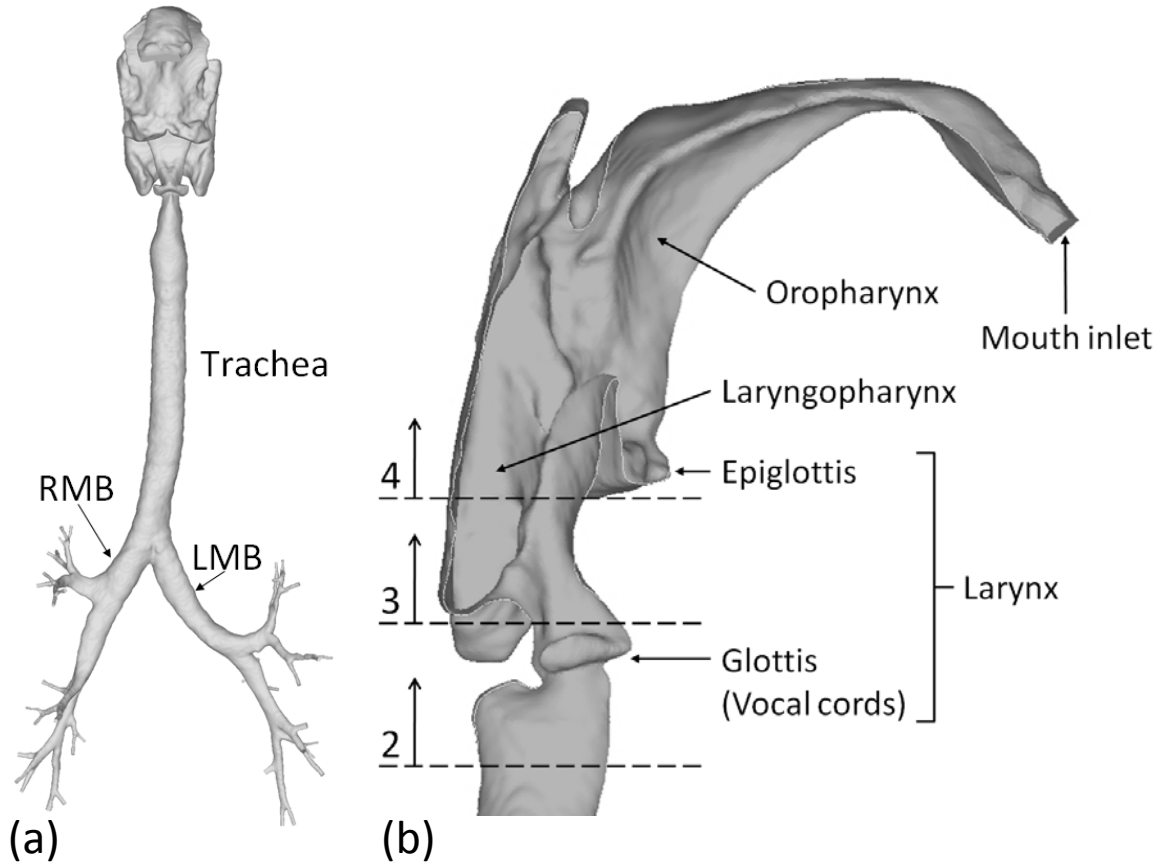

Figure 5.1 The respiratory tract for human subject 1: (a) front view of the CT-based human airway model, (b) inside oblique view of the upper airways. LMB, left main bronchus; RMB, right main bronchus.

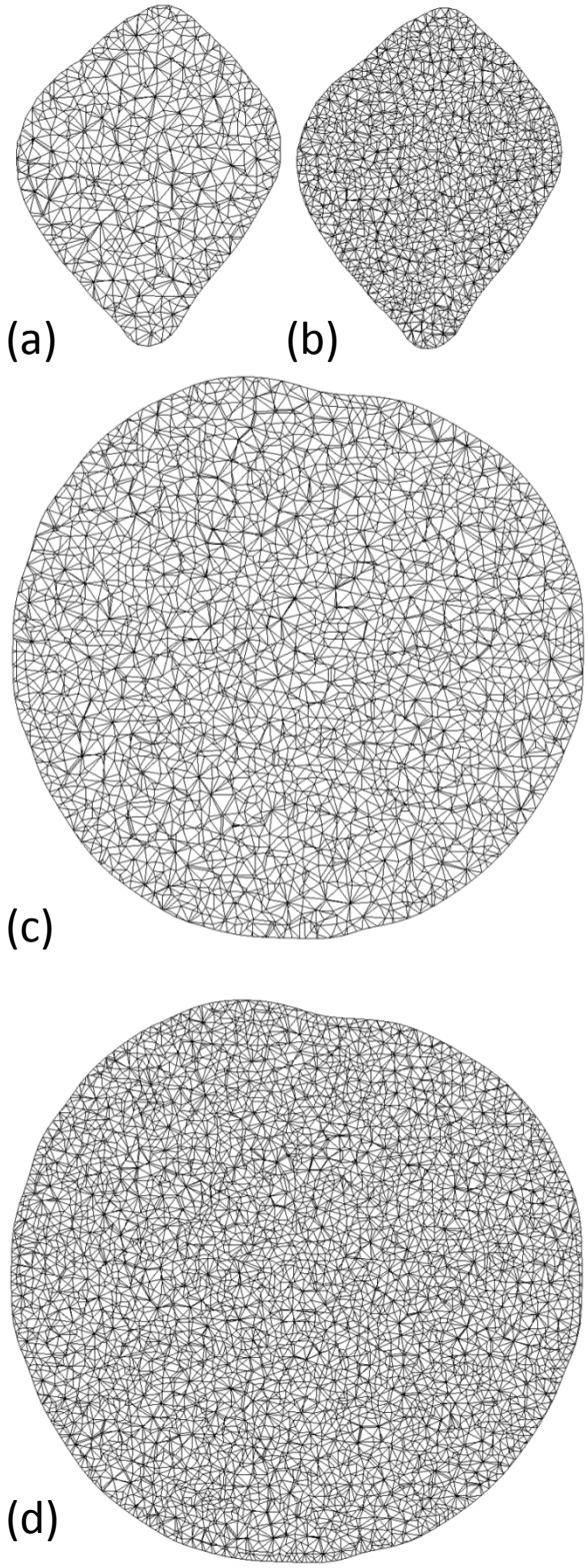

Figure 5.2 Cross-sectional views of the meshes at the glottis of: (a) the original mesh and (b) the fine mesh, and at the trachea of: (c) the original mesh and (d) the fine mesh.

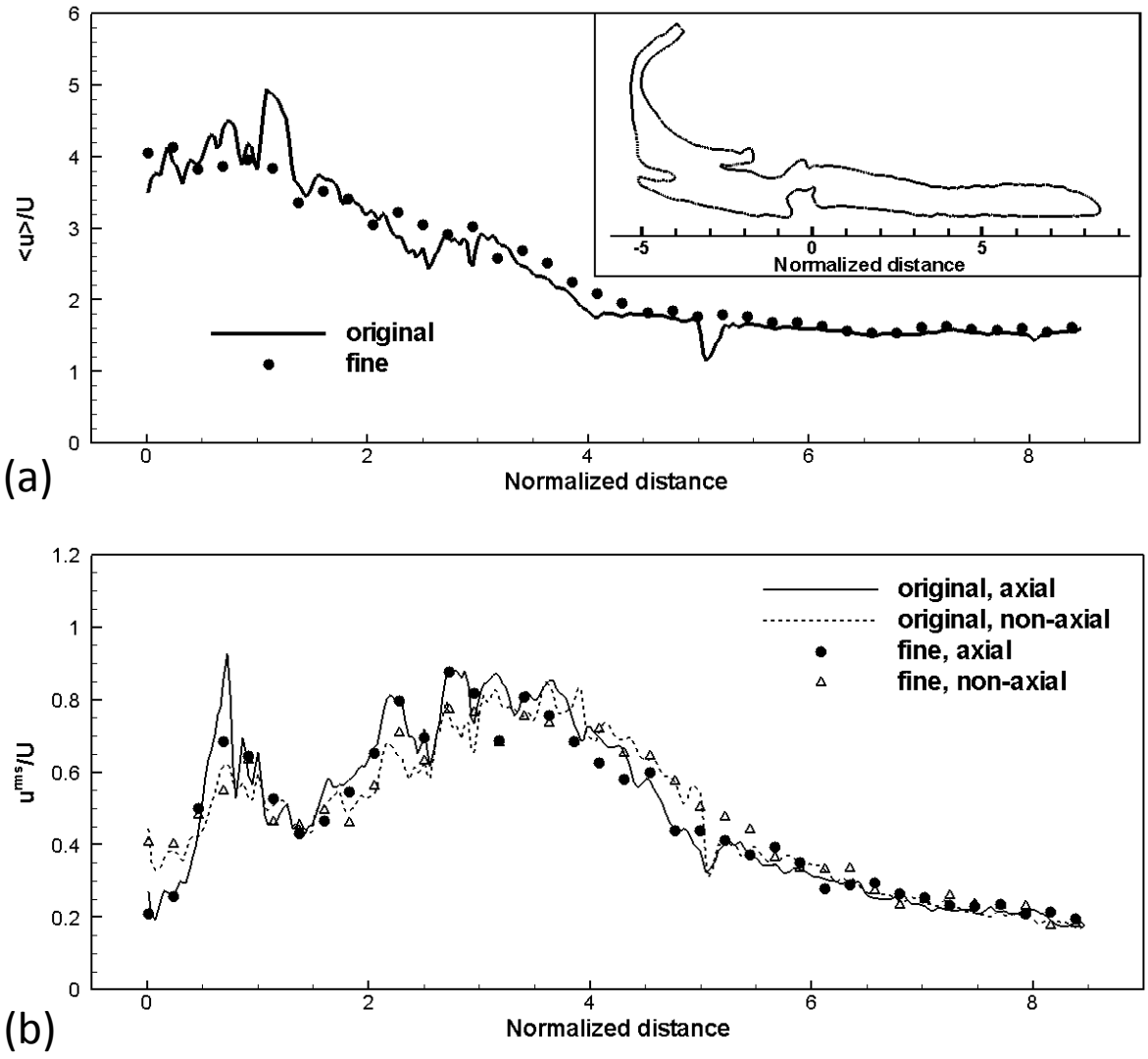

Figure 5.3 Velocity along the jet centerline in the trachea. (a) Normalized mean speed and (b) normalized rms velocity fluctuations along the jet centerline in the trachea. Lines, the original mesh; symbols, the fine mesh.

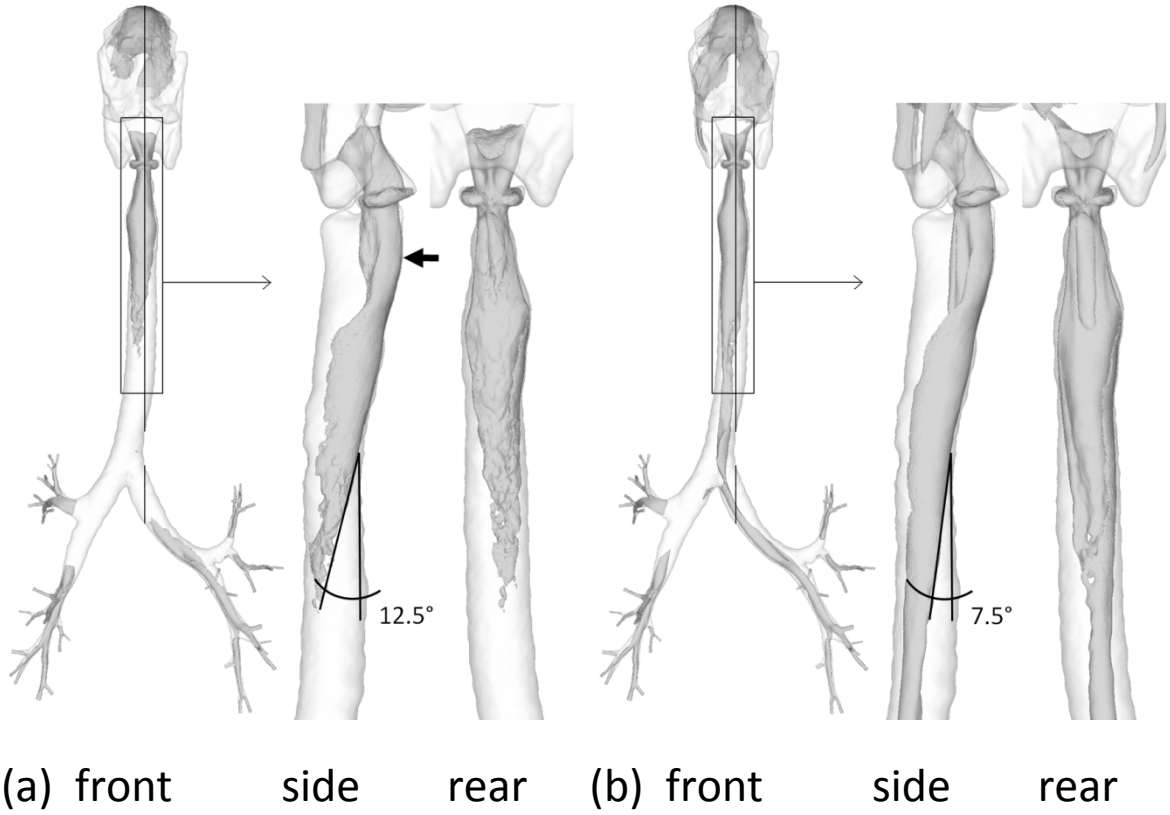

Figure 5.4 Iso-surface of normalized mean speed with $\langle u \rangle / U = 1.65$ for: (a) case 1H and (b) case 1L.

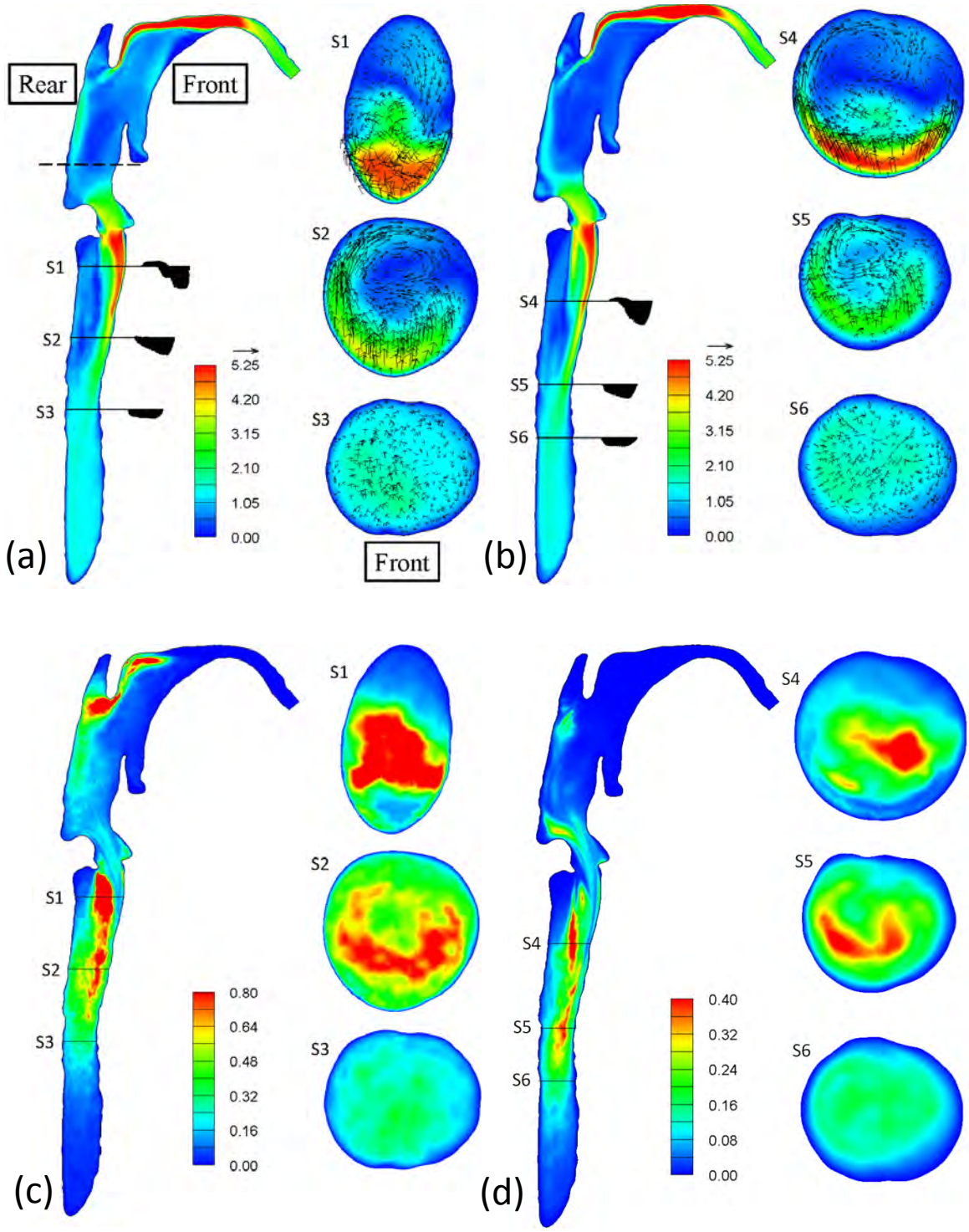

Figure 5.5 Normalized mean speed $\langle u \rangle / U$ for: (a) case 1H and (b) case 1L. Normalized turbulent kinetic energy $(u^{rms}/U)^2$ for: (c) case 1H and (d) case 1L.

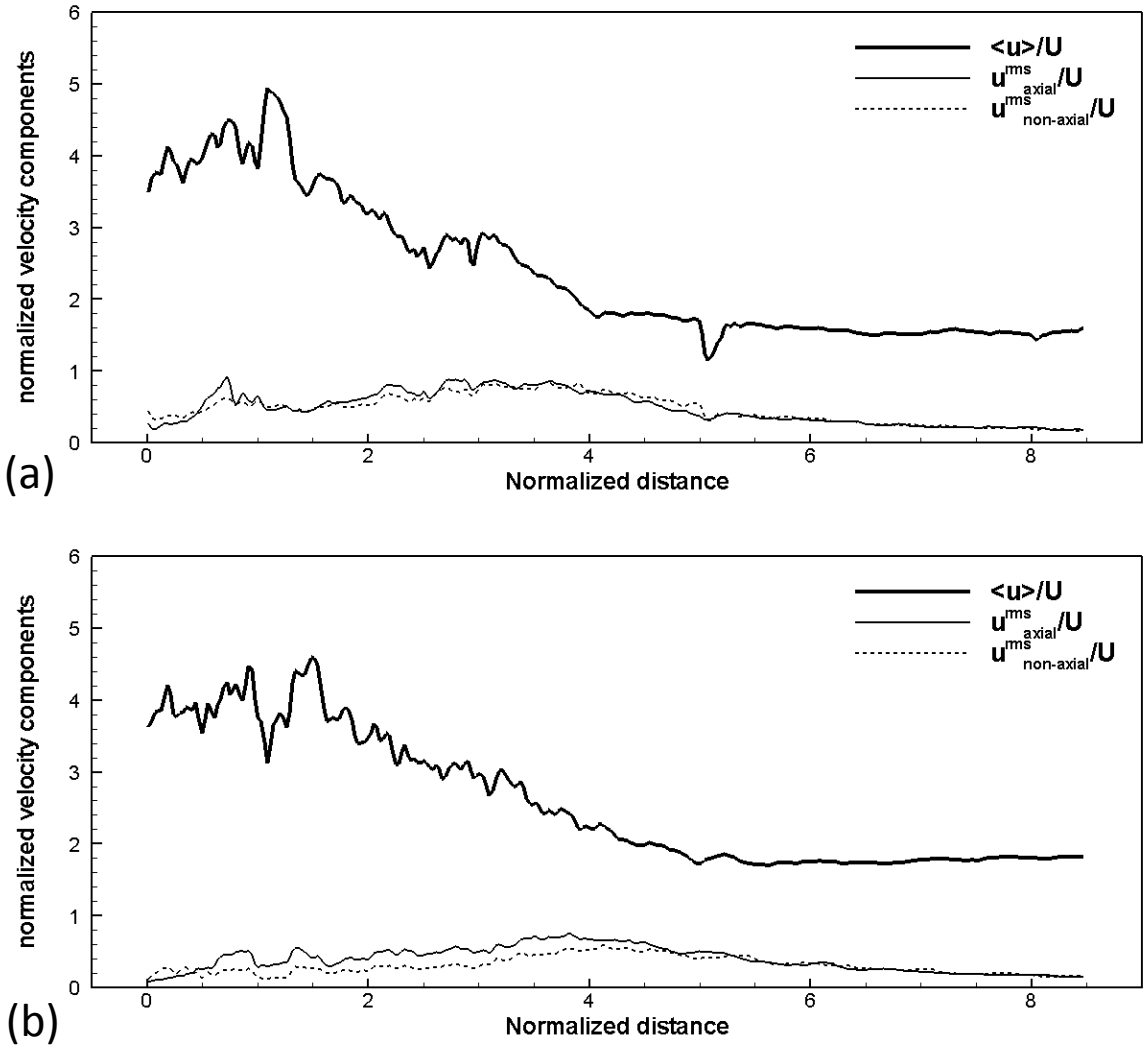

Figure 5.6 Normalized mean and rms fluctuations of the velocity along the jet centerline for: (a) case 1H and (b) case 1L.

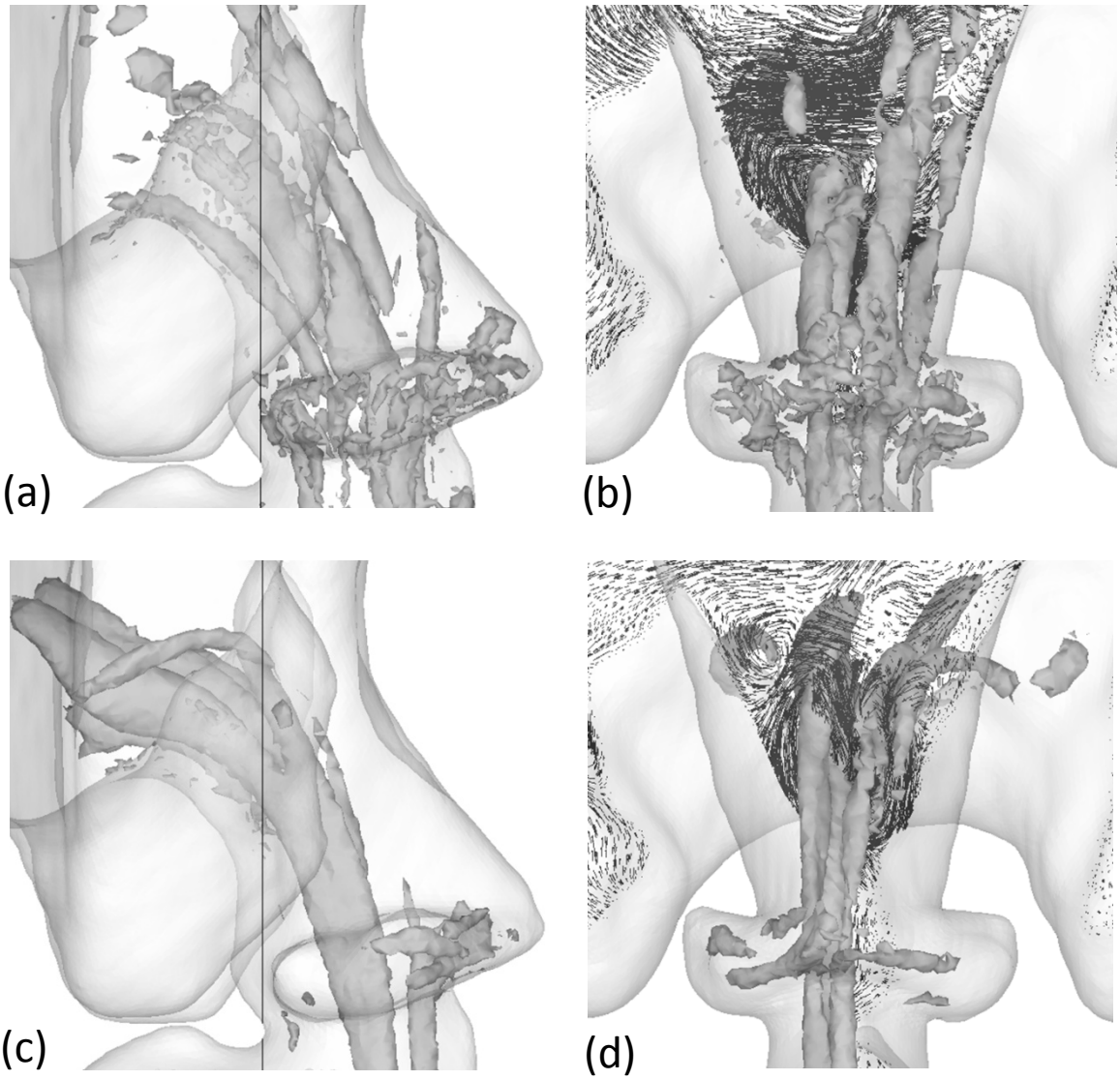

Figure 5.7 The first fluctuating eigenmode (POD-derived coherent vortical structure) identified by $\lambda_2 = -20$. (a) Side and (b) front views of case 1H; (c) side and (d) front views of case 1L.

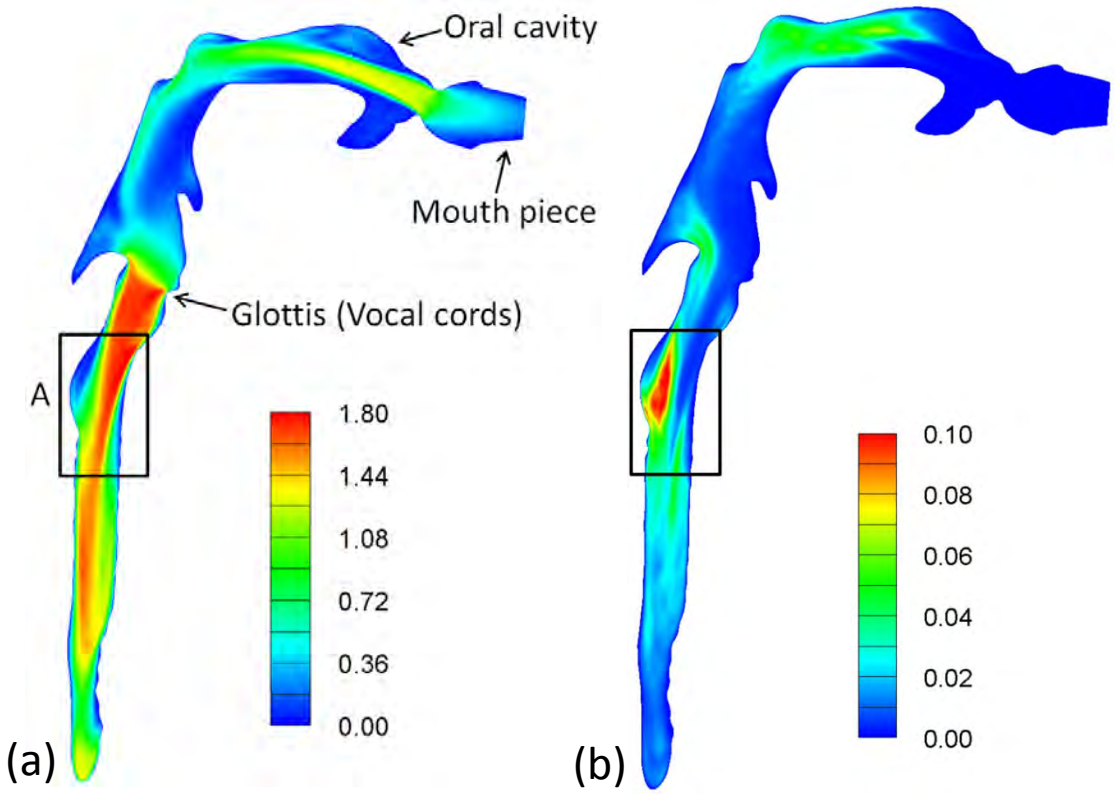

Figure 5.8 Contours of: (a) normalized mean speed $\langle u \rangle / U$, (b) normalized turbulent kinetic energy $(u^{rms}/U)^2$ for case 0 (subject 2).

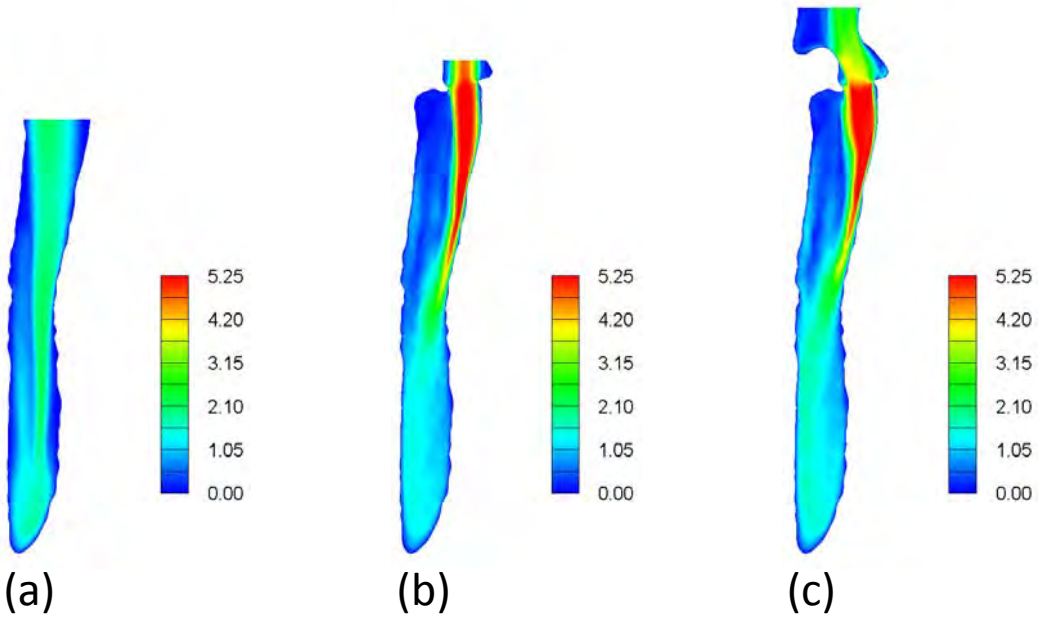

Figure 5.9 Contours of normalized mean speed $\langle u \rangle / U$ in a vertical plane. (a) Case 2H, (b) case 3H and (c) case 4H.

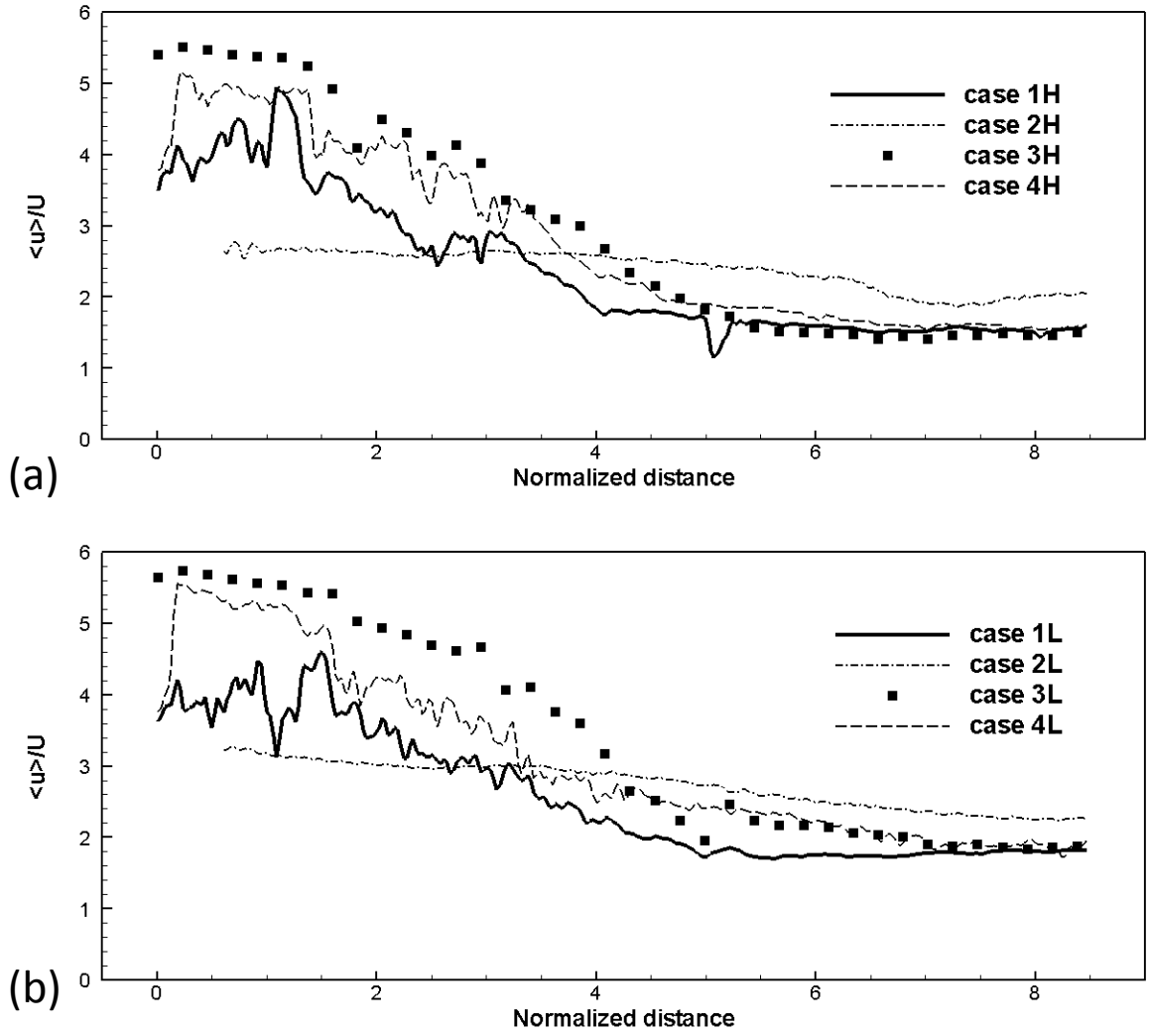

Figure 5.10 Normalized mean speed along the jet centerline at the flow rate of : (a) 15.2 l/min and (b) 5.0 l/min.

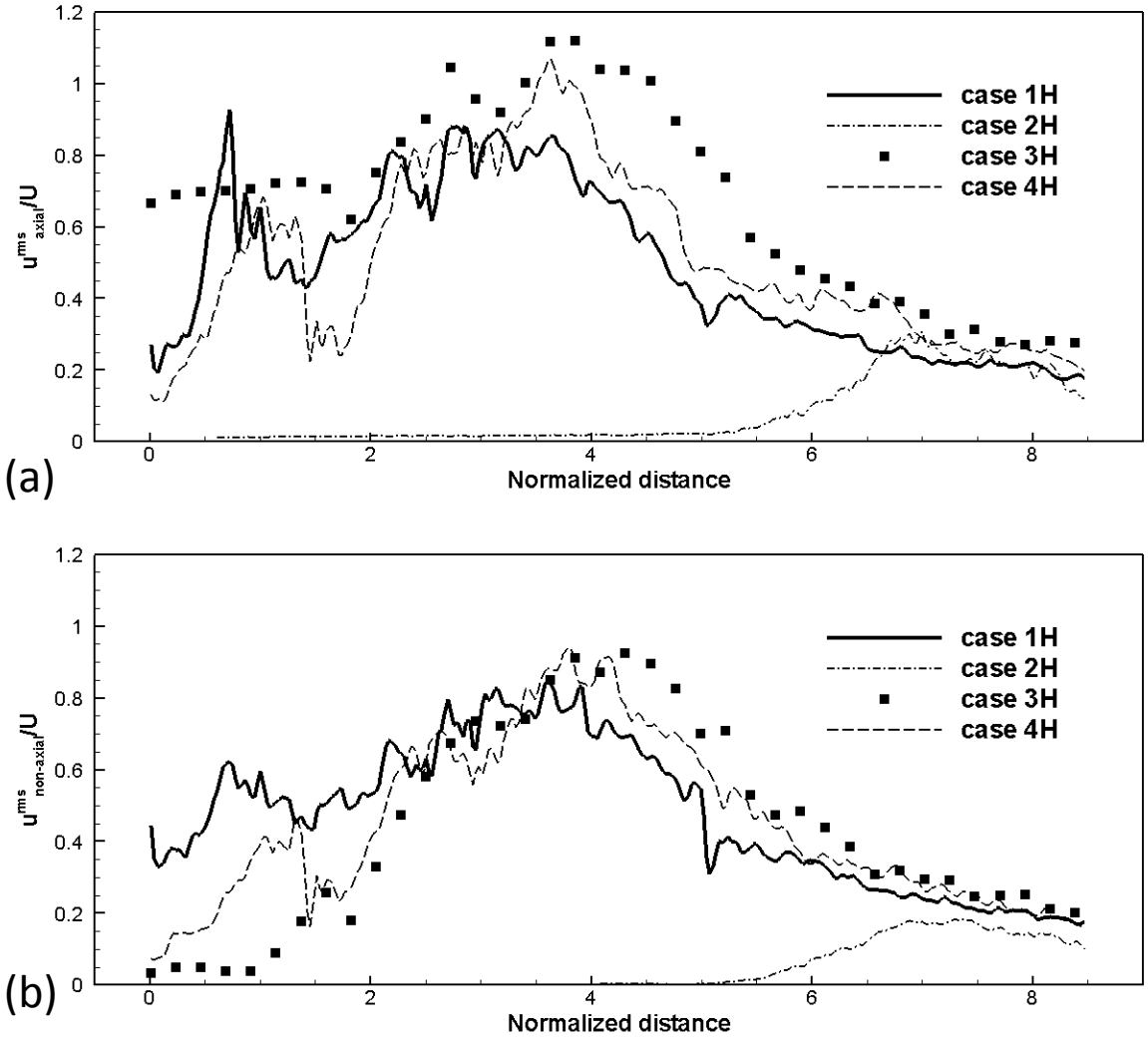

Figure 5.11 Normalized rms velocity fluctuations along the jet centerline at 15.2 l/min. (a) Axial component and (b) non-axial component.

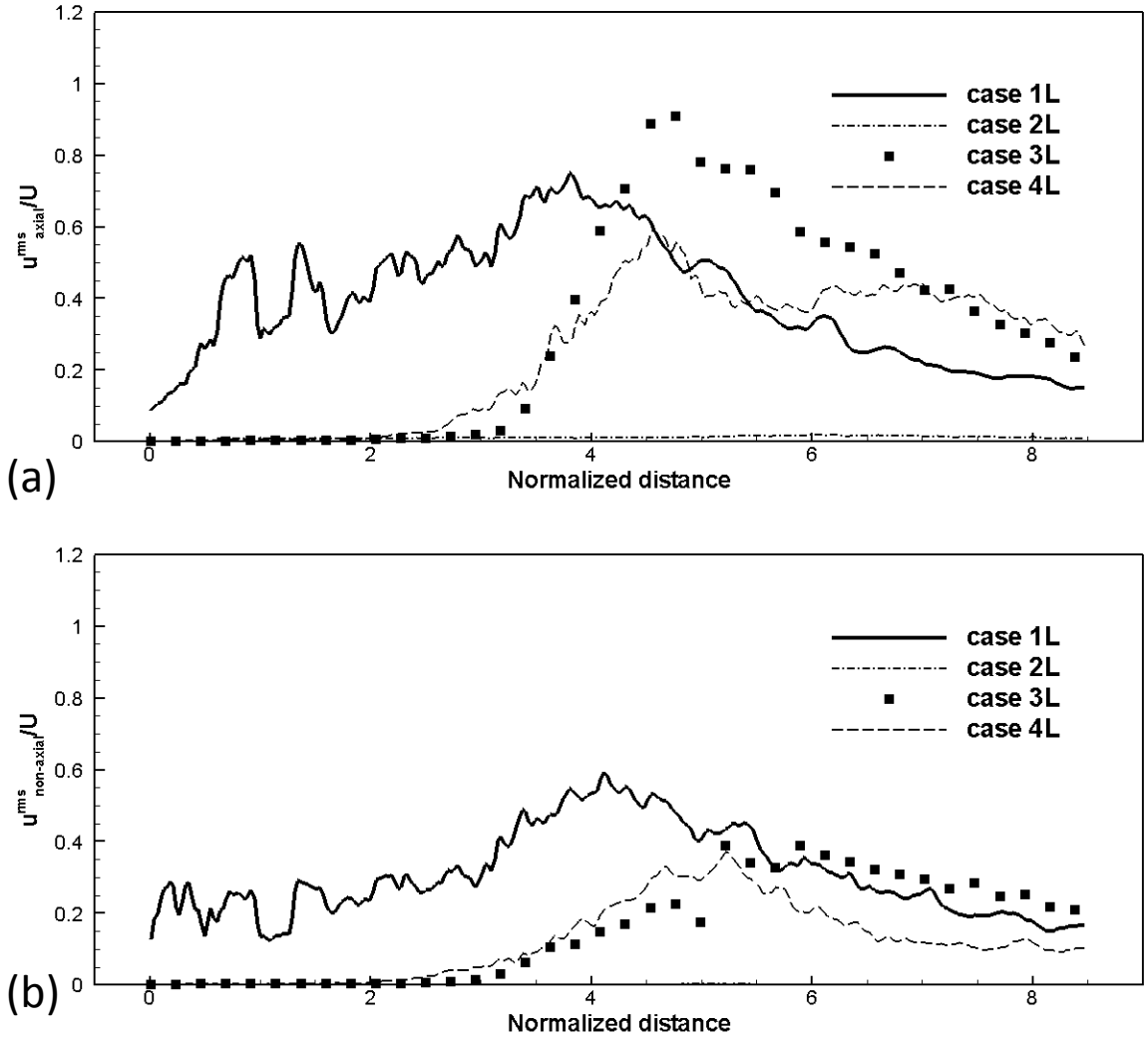

Figure 5.12 Normalized rms velocity fluctuations along the jet centerline at 5.0 l/min. (a) Axial component and (b) non-axial component.

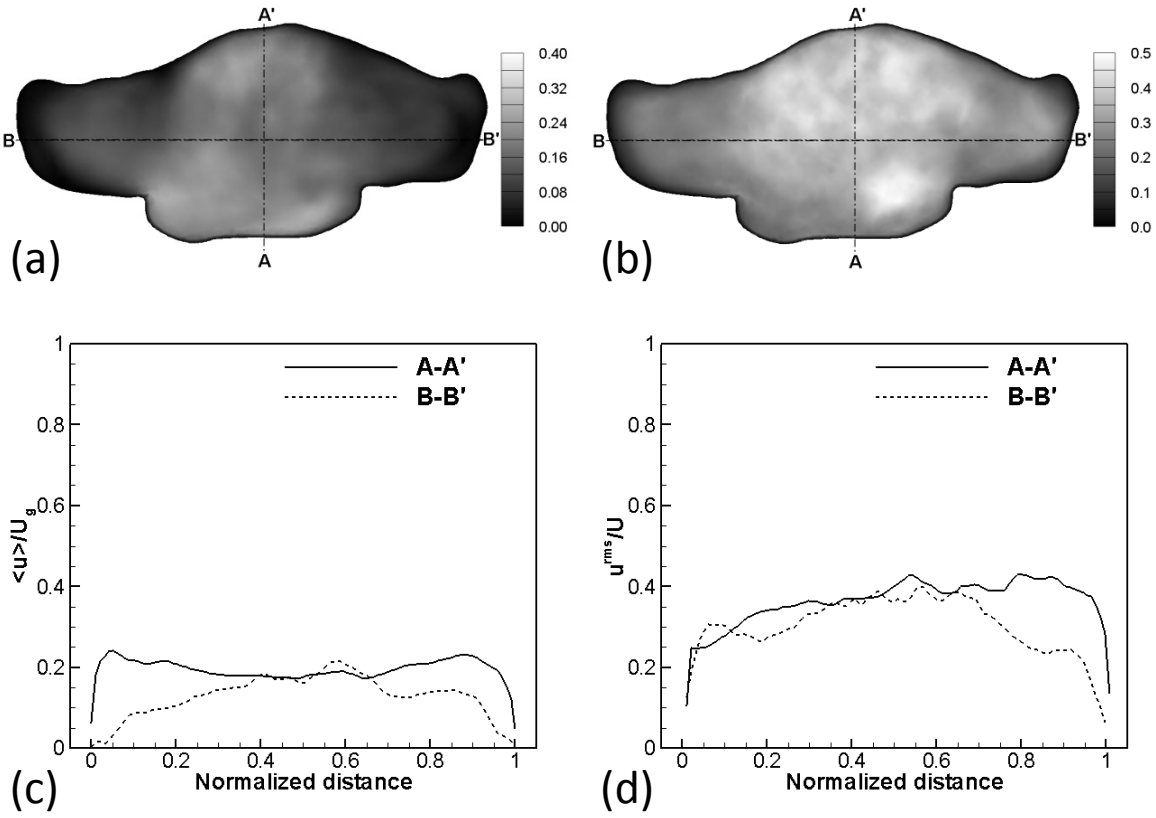

Figure 5.13 Flow statistics at the epiglottal level 4 marked in Fig. 1(b). The cross-sectional views of: (a) mean speed normalized by the average velocity at the glottis $\langle u \rangle / U_g$ and (b) rms velocity fluctuations normalized by the average tracheal velocity u^{rms}/U. The distributions of: (c) $\langle u \rangle / U_g$ and (d) u^{rms}/U along A-A' and B-B'.

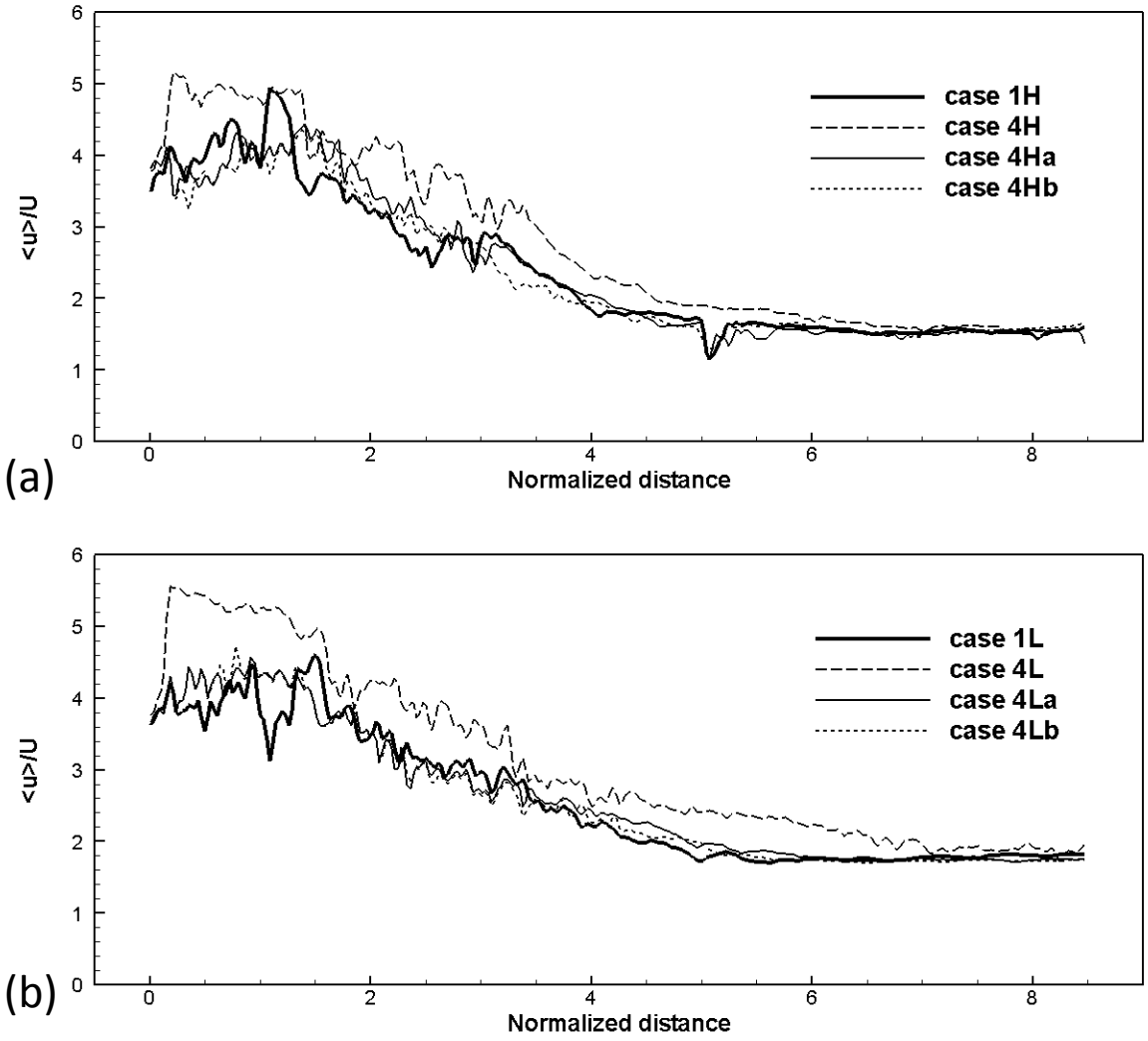

Figure 5.14 Normalized mean speed $\langle u \rangle / U$ along the jet centerline in the trachea at the flow rate of: (a) 15.2 l/min and (b) 5.0 l/min.

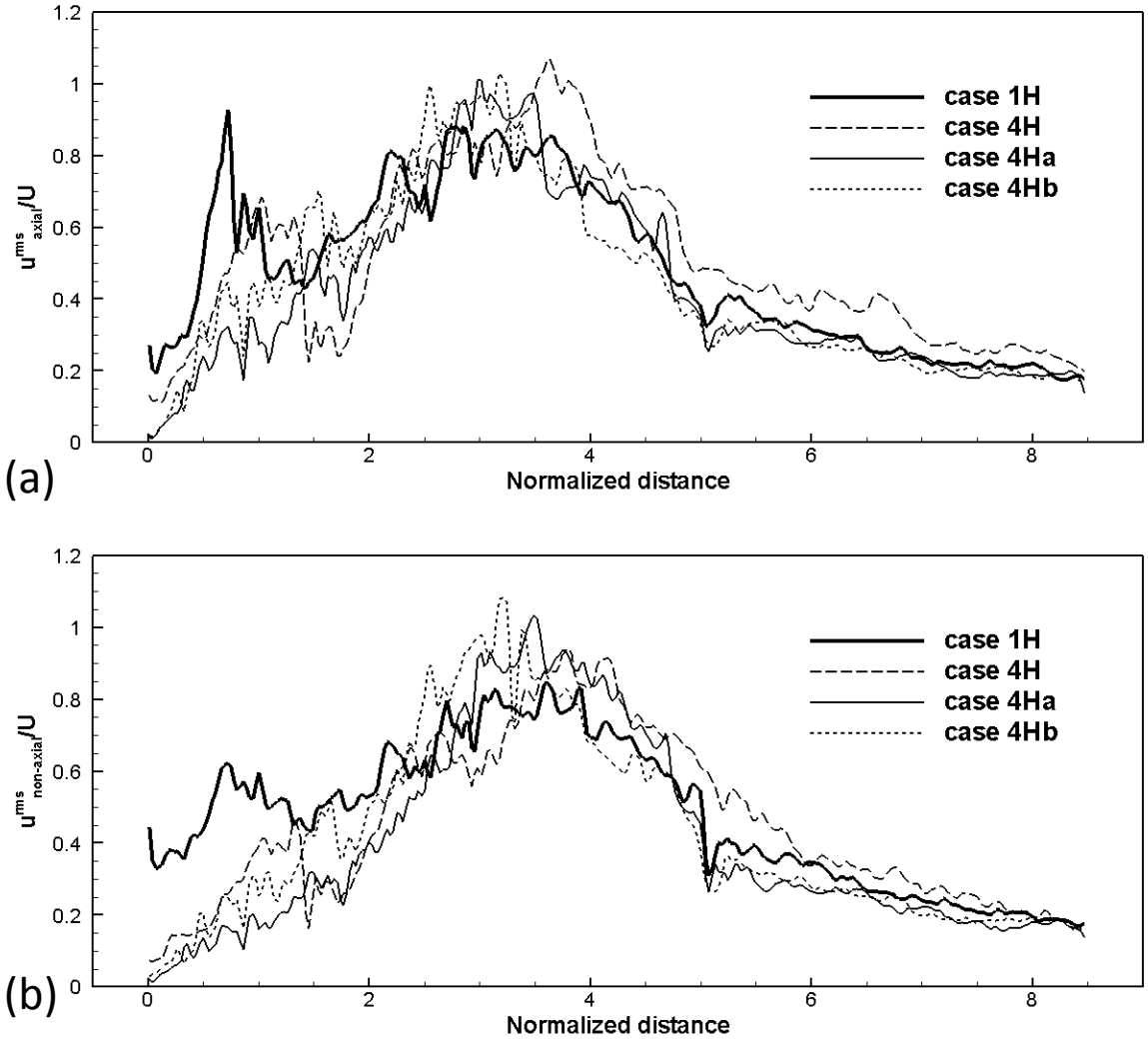

Figure 5.15 Normalized rms velocity fluctuations along the jet centerline in the trachea at the flow rate of 15.2 l/min. (a) Axial component and (b) non-axial component.

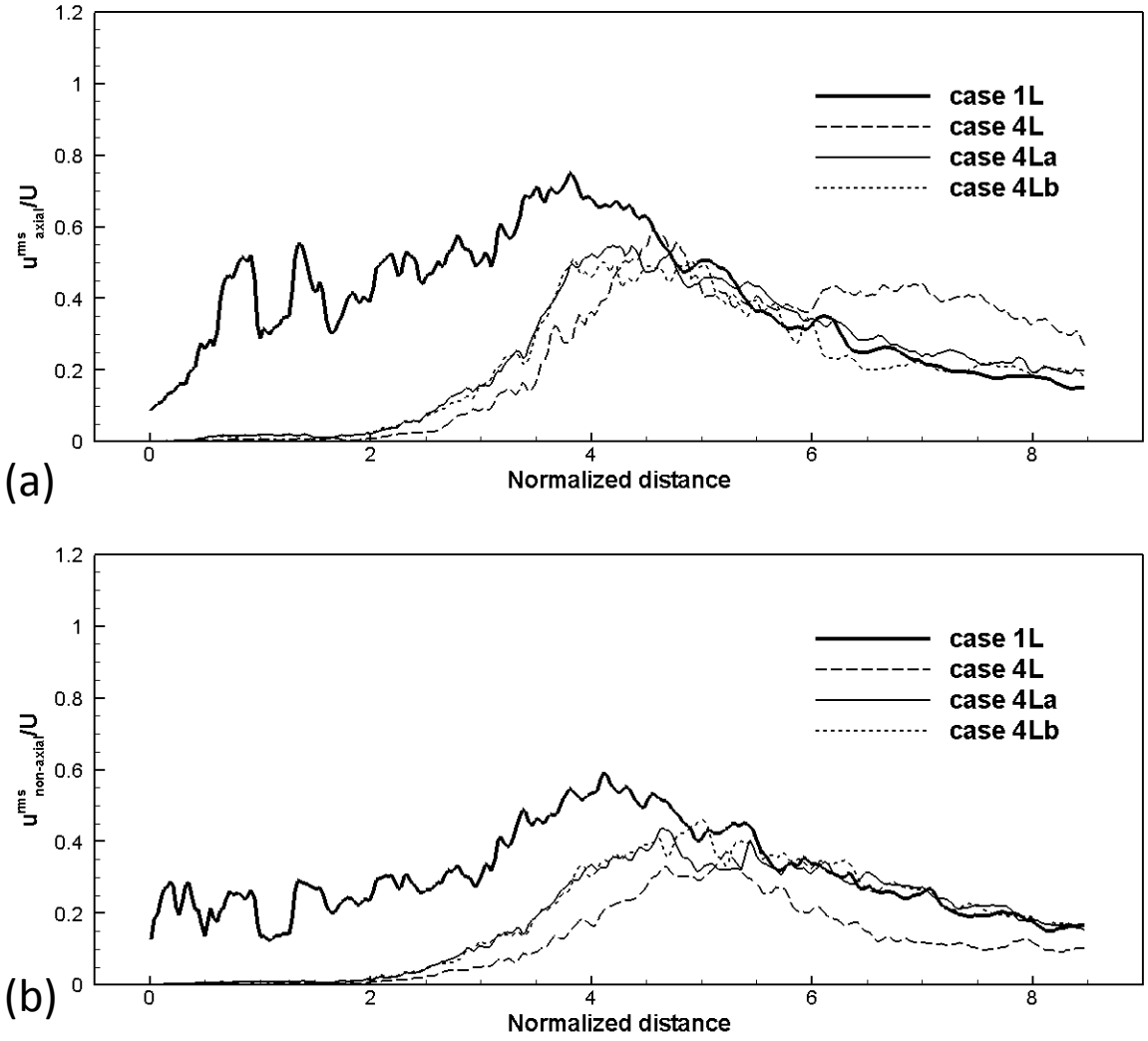

Figure 5.16 Normalized rms velocity fluctuations along the jet centerline in the trachea at the flow rate of 5.0 l/min. (a) Axial component and (b) non-axial component.

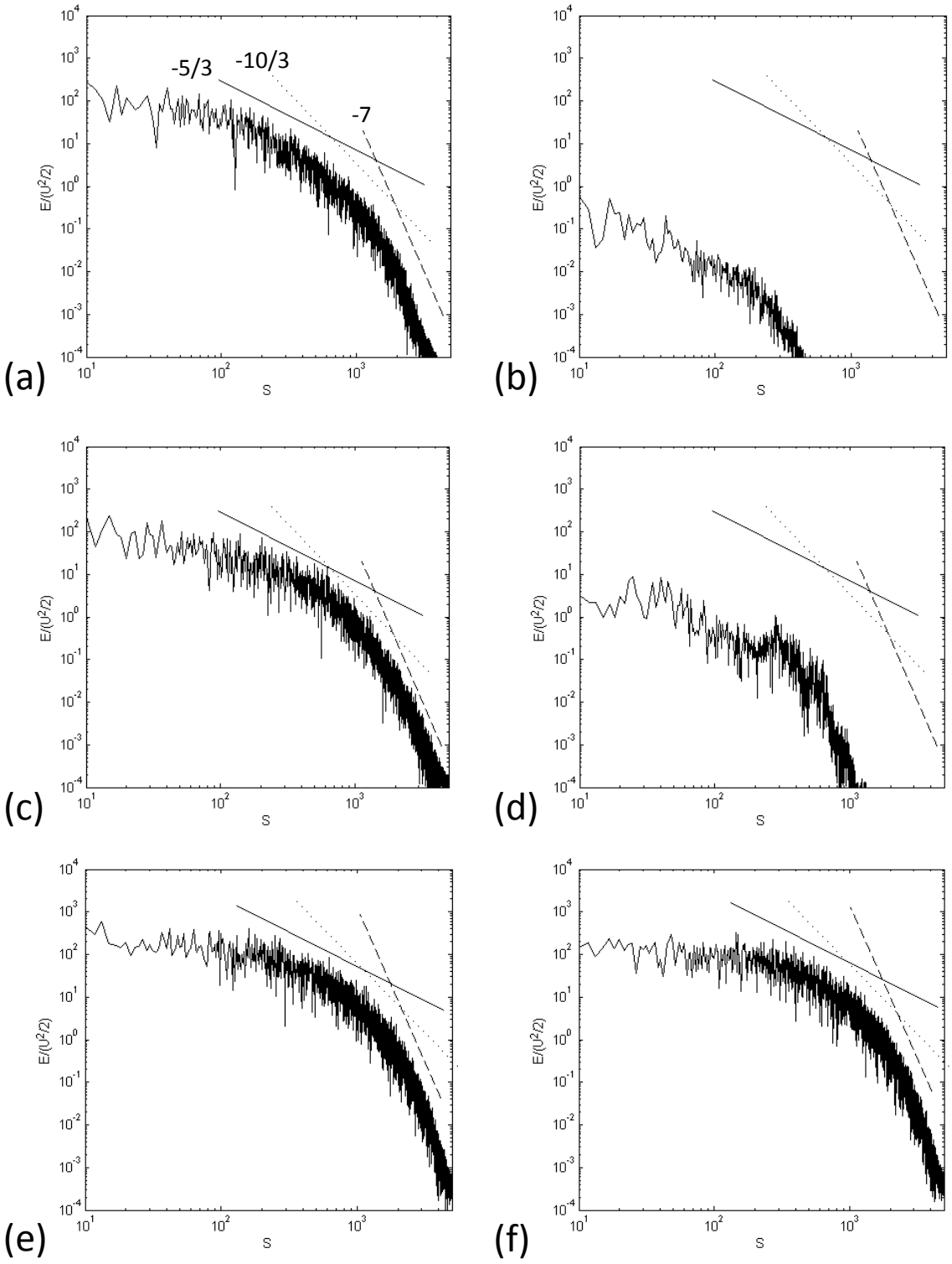

Figure 5.17 Energy spectra of : (a,c,e) case 1H and (b,d,f) case 4Hb at : (a,b) the entrance of the glottis -0.5D, (c,d) 0.5D and (e,f) 2.5D. S is the normalized frequency. Solid, dotted and dash lines denote the slopes of -5/3, -10/3 and -7, respectively.

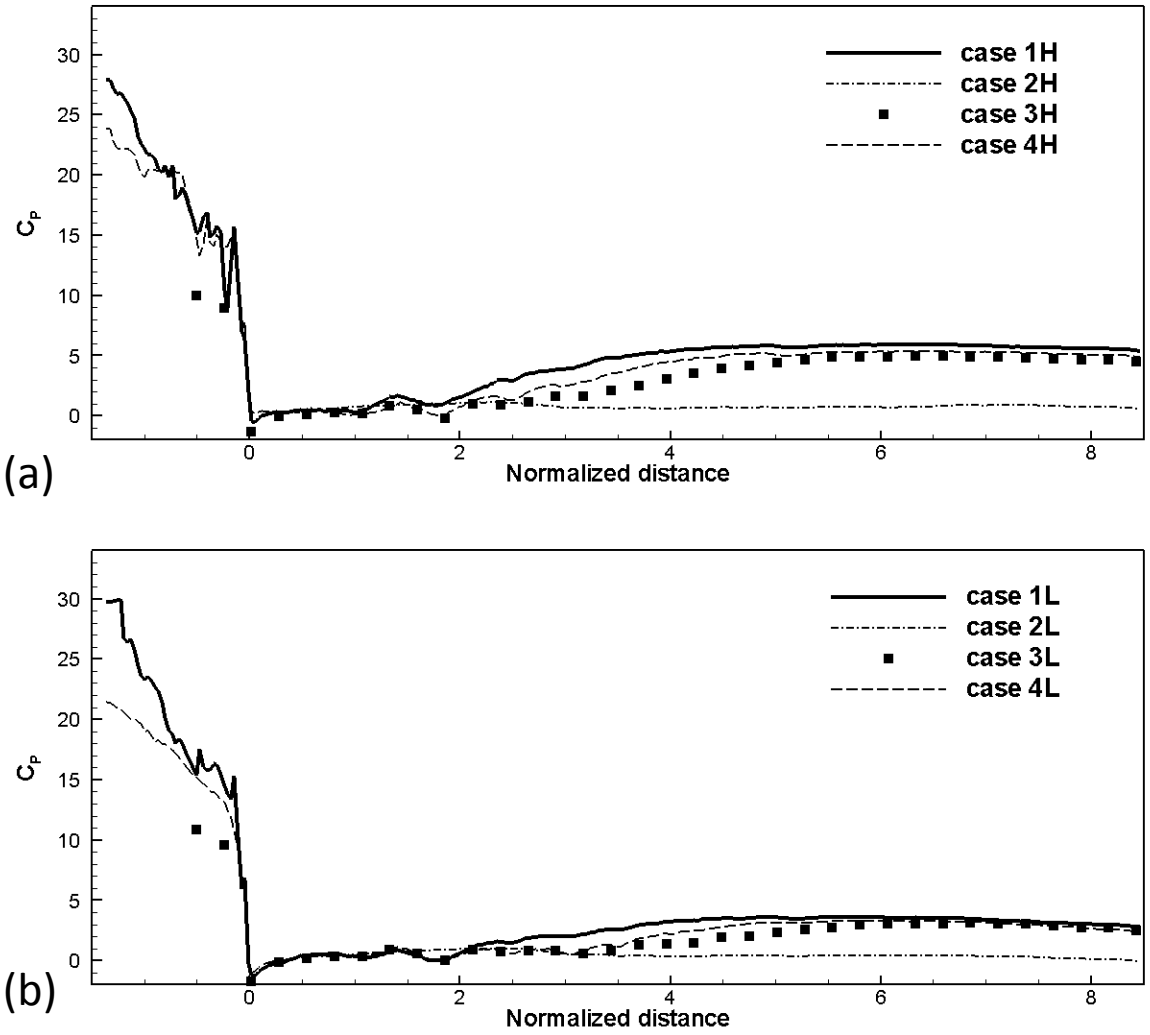

Figure 5.18 Distributions of pressure coefficient C_P from the mid pharynx to the lower trachea. (a) Cases 1H, 2H, 3H and 4H, (b) cases 1L, 2L, 3L and 4L.

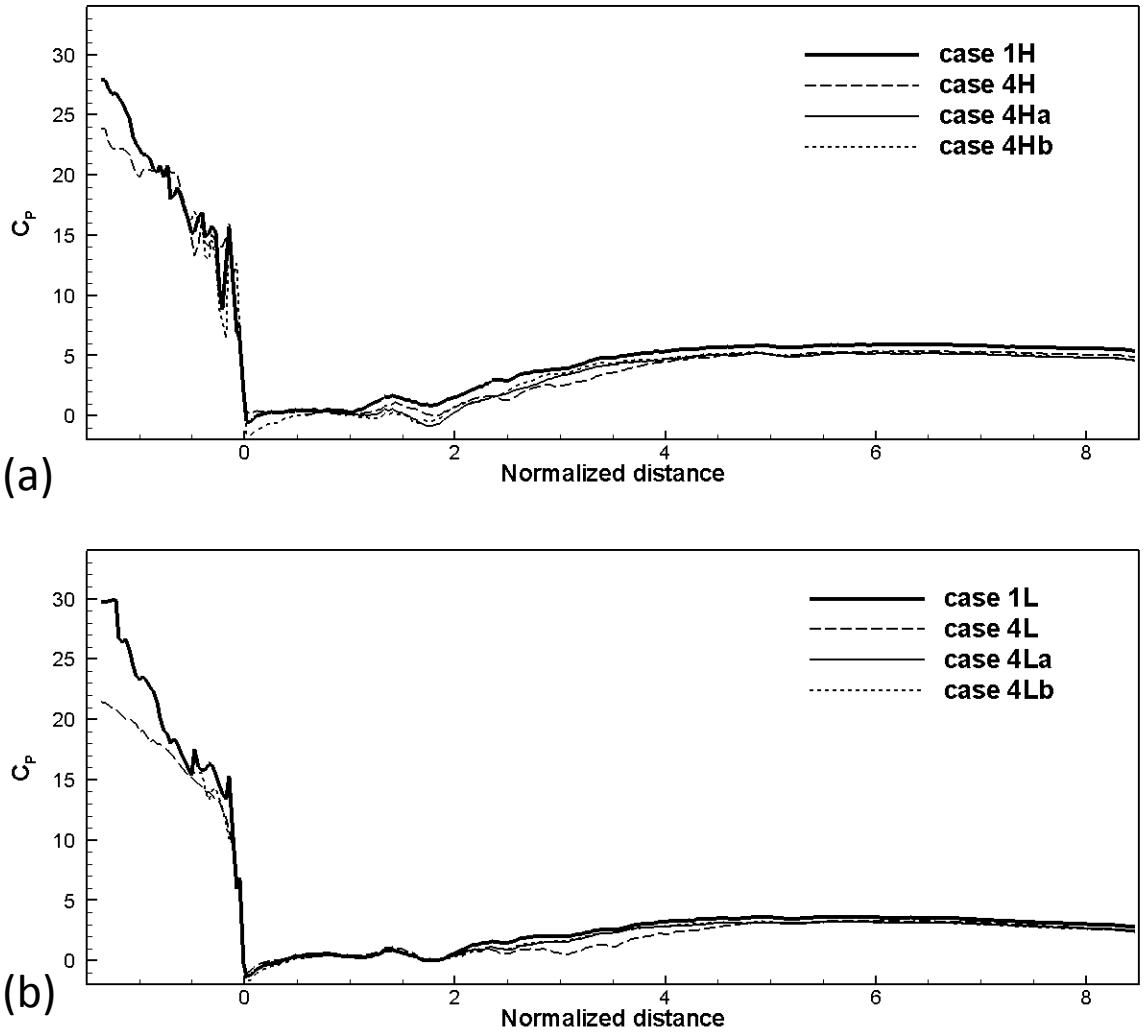

Figure 5.19 Distributions of pressure coefficient C_P from the mid pharynx to the lower trachea. (a) Cases 1H, 4H 4Ha and 4Hb, (b) cases 1L, 4L, 4La and 4Lb.

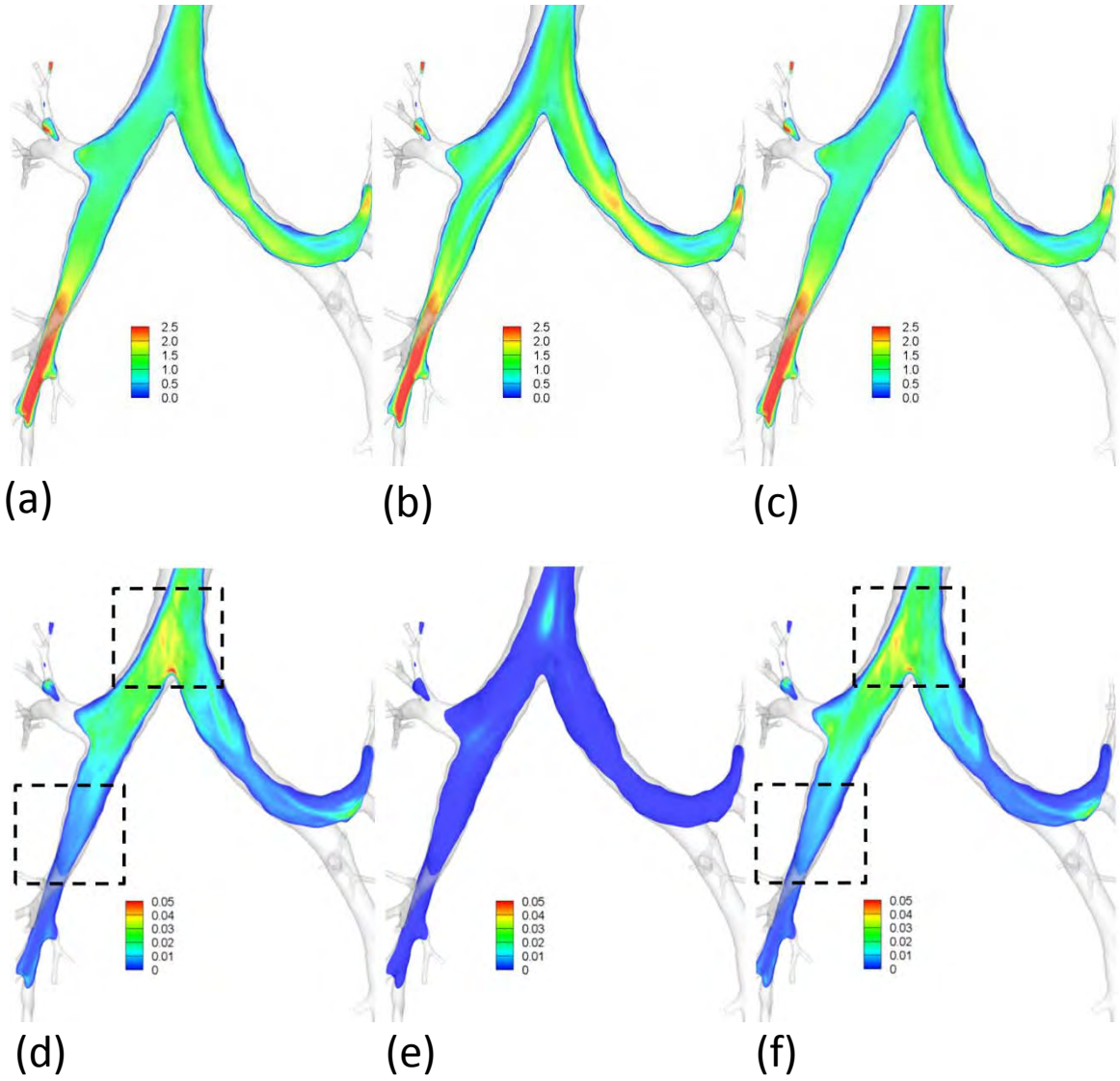

Figure 5.20 Contours of : (a-c) normalized mean speed $\langle u \rangle / U$ and (d-f) normalized TKE $(u^{rms}/U)^2$ in a vertical plane (front view) for cases: (a,d) 1H, (b,e) 2H and (c,f) 4Hb.

CHAPTER 6

AIRWAY FLOW STRUCTURE AND DISSIPATION

6.1 Introduction

In this chapter, we focus on the flow structures in the central airways and their physical correlation with the dissipation rate $\varepsilon = 2\nu s_{ij}s_{ij} = \nu(\partial u_i/\partial x_j + \partial u_j/\partial x_i)\partial u_i/\partial x_j$, where $s_{ij} = (\partial u_i/\partial x_j + \partial u_j/\partial x_i)/2$. We first present the results based on an idealized cylindrical symmetric model in Section 6.2. This is because the symmetric models have been studied extensively and the flow structures in these models are well recognized. Establishment of the structure-dissipation relationship in this simplified model can greatly facilitate explanation of this relationship in the realistic CT-based airway model in Sections 6.2 and 6.3.

6.2 Idealized symmetric model

A cylindrical symmetric 4-generation model is shown in the insert of Figure 6.1. The diameters and lengths (*D*, *L*) of the 0^{th} (trachea), 1^{st}, 2^{nd}, 3^{rd} generations (G0, G1, G2, G3) are (17.6, 119.9), (11.7, 47.6), (7.83, 19.0) and (5.12, 17.6) mm, respectively. The branching angle between child branches is 60 degrees. Like Schroter and Sudlow (1969) and Pedley *et al*. (1971), the flow is assumed laminar without disturbance to produce the well-known vortical structures in the symmetric model. Steady parabolic velocity profiles are imposed at the inlets of G0 and G3 at inspiration and expiration, respectively. *Re* at G0 is 1,365, close to that of the trachea in the CT-based model. The grid distance similar to that of the CT-based mesh is employed. The isosurfaces of the air speed at inspiration and expiration are shown in Figures 6.1(a) and 6.1(b), respectively. The cylinder-shaped isosurfaces of the air speed at G0 during inspiration and at G3 during expiration are due to the imposed parabolic velocity profiles.

On inspiration, the impact of the flow on the first bifurcation forms a high-speed boundary layer along the inner wall of G1 due to the effect of inertia. Here “high-speed” is to emphasize that the boundary layer is influenced by the “fast-moving” core flow biased toward the wall. The velocity contours and vectors in three cross-sections (S1, S2, S3) are shown in Figures 6.2(a), 6.2(b), and 6.2(c). The high-speed boundary layer induces the well-known counter-rotating vortices (Schroter and Sudlow 1969, Pedley *et al*. 1971). Figure 6.1(a) also shows that the layered structure at G1 is split into two streams when entering G2. Although the layered structure is still visible at G2, it becomes more complicated in that its opening side (referring to the top side facing the boundary layer in Figure 6.2(c)) is now facing toward the inner wall of G2 and the bottom face (referring to the bottom side of the contour line in Figure 6.2(c)) of the high-speed layered structure moves toward the core region of the G2 branch.

On expiration, the streams coming off G3 meet at G2. Due to the symmetry of the G3 branches, the two jet-like streams press against each other in the core region of the G2 branch, resembling the flow structure at S1 in Figure 6.2(d). The merged stream is then directed toward the wall by inertia and when reaching the wall, it is diverted laterally to form the high-speed boundary layer. Thus, the high-speed boundary layer can be formed at both inspiration and expiration due to impingement of air streams on the airway wall. Since at expiration air streams coming off the daughter branches first collide symmetrically in the core region of the mother branch, the I-shaped high-speed structure is formed at G2 in Figure 6.2(b). The I-shaped structure induces two pairs of counter-rotating vortices, a well-recognized flow structure at expiration (Schroter and Sudlow 1969, Pedley *et al*. 1971). The flow structures at G1 are more complicated because the two air streams coming off G2 exhibit an I shape, rather than a cylindrical shape as seen at G3. The sequence of the events at S3, S2, and S1 when the two I-shaped streams collide at G1 is displayed in Figures 6.2(f), 6.2(e) and 6.2(d). The two near-wall high-speed streams in Figure 6.2(f) move toward the central I-shaped stream with increasing

downstream distance. The central I-shaped stream results from merging of the two near-core ends of the I-shaped streams from G2, and the two triangle-like streams correspond to the other two near-wall ends of the I-shaped streams from G2. Due to inertia, they eventually merge to form a single I-shaped stream, resulting in two pairs of counter-rotating vortices in Figure 6.2(d). Likewise, at G0 the two I-shaped streams from G1 join together, resembling Figure 6.2(f). Figure 6.2(g) further displays the development of the boundary layer thickness δ along the axis X' (see the insert) aligning with the G1 branch. Overall δ^2 is linearly proportional to X' as marked by solid and dashed lines in Figure 6.2(g) except near S3. At inspiration, S3 is close to the 2^{nd} bifurcation where the G1 diameter is reduced to merge with G2. At expiration, the two I-shaped streams from G2 merge in the core region between S3 and S2. The boundary layer growth becomes evident only after merging of the two streams into a single I-shaped stream around S2. This suggests that the entry flow theory and model of Pedley *et al*. (1971) may work for both inspiratory and expiratory flows.

To understand the structure-dissipation relationship, Figures 6.2(a-f) overlay the region of the high dissipation rate with the high-speed stream. At inspiration, the high dissipation region is located in the boundary layer along the cylindrical wall, supporting the entry flow model of Pedley *et al*. (1971). It is noteworthy that the high-speed jet-like stream also yields local maximum dissipation along its free shear side, e.g., the concave side of the speed contour lines in Figures 6.2(a-c) facing the center of the tube. At expiration, in addition to the boundary layer, the high dissipation region is also found in the core region due to free shear accompanying the I-shaped jet-like flow structures. In comparison of Figures 6.2(a-c) and 6.2(d-f), the high dissipation associated with free shear flows is more prevalent at expiration than at inspiration.

6.3 Inspiratory phase in CT-based model

For the CT-based airway model, Figure 6.3(a) shows the contours of the instantaneous air speed in a vertical cross-section at z = 0.002 m at peak inspiration. The high-speed stream located at the upper trachea is associated with the laryngeal jet illustrated in Figure 3.1. The air speed near the outer wall of the right main bronchus RMB is particularly low as compared with other regions. The high-speed air in the lower lobes LLL and RLL may be attributable to the higher ratios of ventilation (LLL, RLL) = (0.349, 0.324) than other lobes. Thus, more air is drawn into these two lobes at inspiration. The contours of the mean speed at peak inspiration are exhibited in Figure 6.3(b), whereas its side view is shown in Figure 3.1(c). The laryngeal jet formed at the glottis impinges on the rear side of the tracheal wall. The jet generates turbulence in the recirculation region, and downstream in the core region of the jet due to flow instabilities and transition to turbulence (Ahmed and Giddens 1983, Sherwin and Blackburn 2005, Vétel *et al*. 2008). As a result, velocity fluctuations with high TKE are produced in the trachea as shown in Figure 6.3(c). Because turbulence intensity is calculated based upon local mean speed, high local TKE and low local MKE can result in high intensity. Figure 6.3(d) shows that high turbulence intensities are found in the trachea, RMB and bifurcations, where low local mean flow speed is formed due to flow stagnation and recirculation. The turbulence intensities in these regions can reach more than 40%. In contrast, for the case without the upper airways the flow in the trachea is laminar, being consistent with Olson *et al.* (1972), Menon *et al*. (1985) and Lin *et al.* (2007).

The flow structures at inspiration in three cross-sections S1, S2 and S3 along the left main bronchus LMB in Figure 6.3(a) with and without the presence of turbulence are examined in Figure 6.4. Without the upper airways in the absence of turbulence, the high-speed stream forms the boundary layer on the inner (bottom) wall of the branch, resembling those of a symmetric model. The boundary layer is associated with the high dissipation rate. The counter-rotating vortices are more asymmetric in S3 than S1 perhaps

due to the non-cylindrical, non-planar, curved, subject specific shape of the branch, being consistent with the observations by Caro et al. (1996) in arterial flow. In the presence of turbulence, the flow disturbances produced by the laryngeal jet and the curved trachea shed into the LMB, modulate and displace the high-speed stream away from the boundary layer toward the core region. Subsequently, free shear associated with high-speed streams yields high dissipation in the core region of the segment.

6.4 Expiratory phase in CT-based model

At expiration the flow is essentially laminar except in the upper airways. Figure 6.5 shows the front and side views of the contours of the mean speed in two vertical planes at peak expiration. Like inspiration, the maximum mean speed of the airflow is found in the two lower lobes. An interesting observation is that as the air streams enter the mother branch from the daughter branches, they can either twist together or remain as separate streams. This resembles the expiratory flow in the symmetric model (Figure 6.1(b)), the flow through sudden expansion in a pipe, and the flow through a constricted pipe. For example, the laminar air jets emanating from LB1, LB2, LB4 and LB5 enter the mother branch TriLUL, staying in the core region of the TriLUL rather than its boundary layer (see the insert in Figure 6.5(a)) and later joining the stream from the LLB6. Because the stream from the LLB6 is stronger and the airway branching is asymmetric, the merged air stream impinges on the upper wall of the LMB, which creates a strong swirling stream along the upper wall. Further downstream, this stream is deflected toward the lower portion of the LMB, due in part to the curvature of the LMB, before entering the trachea. The cross-sectional views of this stream are displayed in Figures 6.4(g), 6.4(h), and 6.4(i). Unlike the I-shaped structures and four counter-rotating vortices formed at expiration in a symmetric model, the flow structures in the CT-based airway model depend on geometric features of the airways, such as diameters, branching

angles, and rotation angles of the airways, and regional ventilation in the lung parenchyma that determines flow partition and intensity of air streams in branches.

Nevertheless, one common feature between idealized and realistic airway models during the expiratory phase is that the streams emanating from the daughter branches behave like laminar jets that enter an enlarged mother branch. Consequently, viscous dissipation associated with free shear is more likely to occur outside boundary layers as shown in Figures 6.4(g), 6.4(h) and 6.4(i). These jet-like structures are also prominent in the BronInt on the right lung and in the trachea (see Figure 6.5). Even without the upper airways, the flow structures at peak expiration are essentially the same as those with the upper airways because the characteristics of expiratory flow in the central airways depend on airway geometry and regional ventilation rather than the downstream glottis opening area. Another interesting observation is that during expiration the impingement of jet-like flow structures on the airway wall forms high-speed boundary layers of high dissipation rate. This mechanism resembles the one during inspiration that a high-speed stream is split at bifurcation and impinges on the airway wall to form high-speed boundary layers of high dissipation rate. This suggests that the entry flow model of Pedley *et al*. (1971) for inspiratory flow may be applicable to expiratory flow. Nonetheless, little attention has been paid to the free shear side of these high-speed jet streams (as opposed to the boundary layer side), which also contributes to viscous dissipation and airway resistance. The role played by free shear flows in airway resistance and viscous dissipation will be quantified and discussed later in comparison with that of boundary layers.

6.5 Summary

The spatial correlation between flow structure and viscous dissipation is first established on the symmetric airway model, showing that high-speed boundary layers with strong viscous dissipation are formed at both inspiration and expiration. This explains why Pedley's resistance formula (19710a) based on an entry flow model for

inspiratory flow is also applicable to expiratory flow. At expiration, jet-like free-shear structures become prevalent, contributing significantly to viscous dissipation. This structure-dissipation spatial correlation is also identified in the MDCT-based airway model.

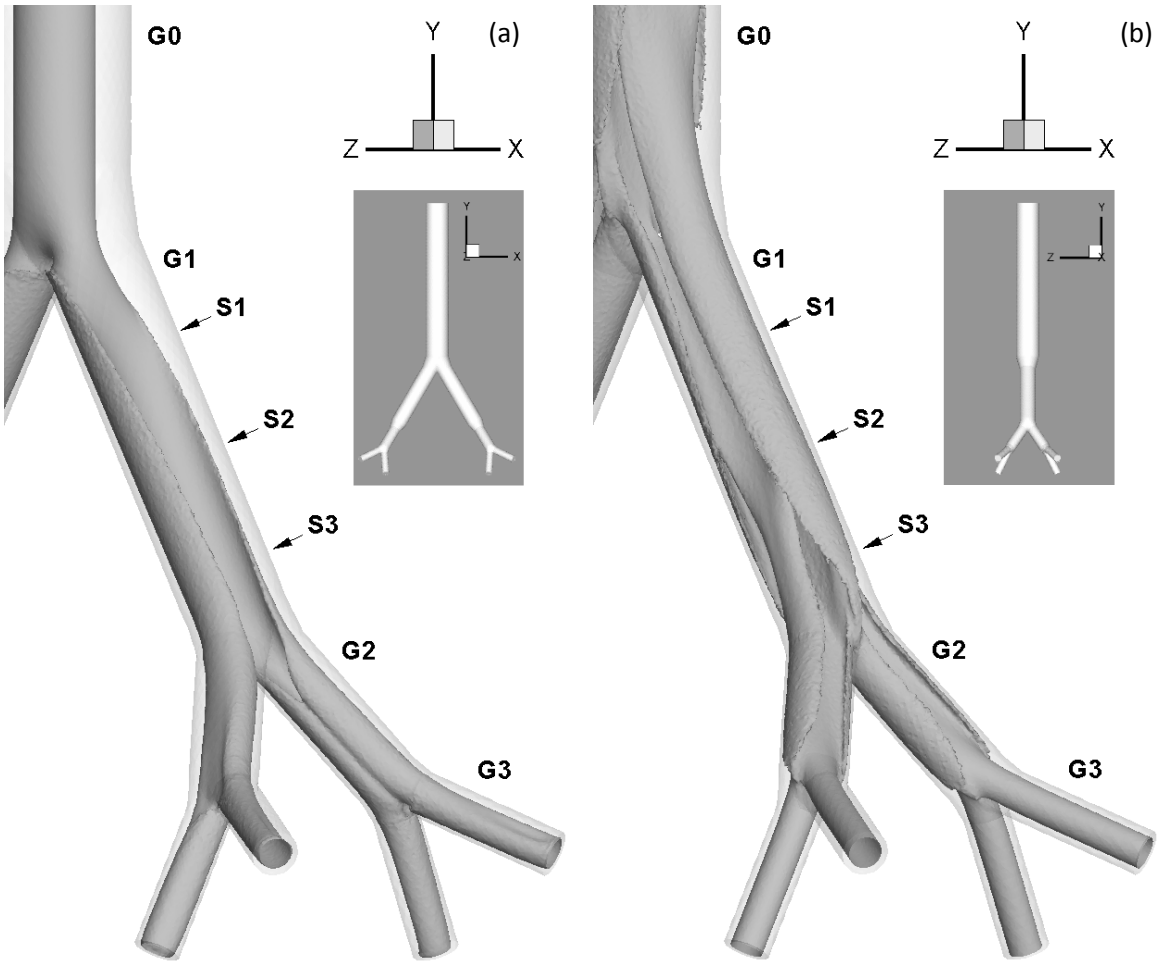

Figure 6.1 Steady flow cases using an idealized, cylindrical symmetric 4-generation airway model at *Re*=1,365. Isosurface of air speed (1.7 m/s) at: (a) inspiration, (b) expiration. Inserts in (a) and (b) are the respective front and side views of the model. G0, G1, G2, and G3 denote the zeroth (trachea), first, second and third generations of the airway model, respectively.

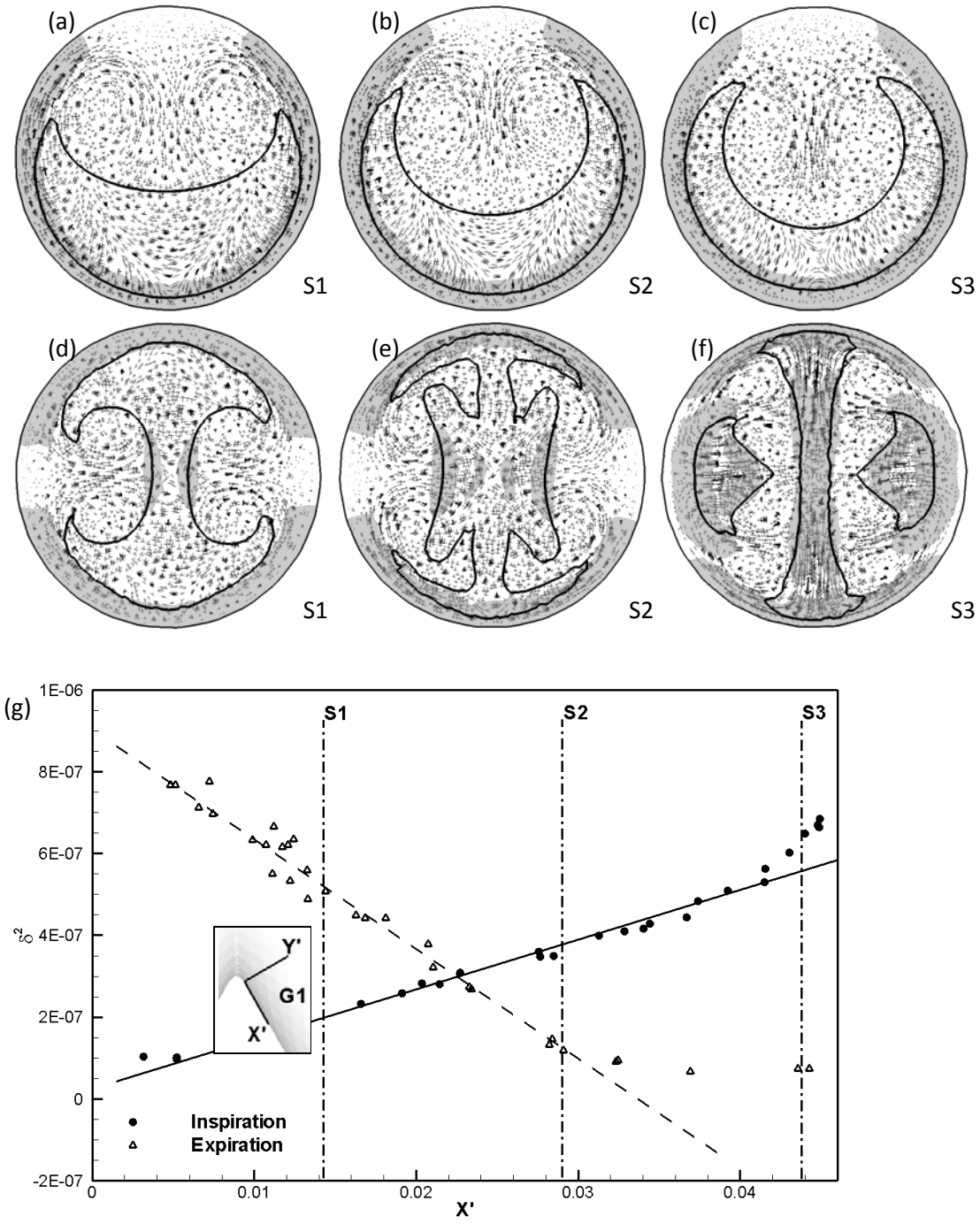

Figure 6.2 Flow structures in a cylindrical model in three cross-sections at (a,b,c) inspiration and (d,e,f) expiration. Contour line of air speed at 1.7 m/s with increasing speed inside the enclosed area; gray shaded region, dissipation rate in excess of 16.7 m^2/s^3. (g) δ^2 versus X′, where δ is the boundary layer thickness defined with ~1.7 m/s (see the insert for the local coordinates X′- Y′ near the first bifurcation).

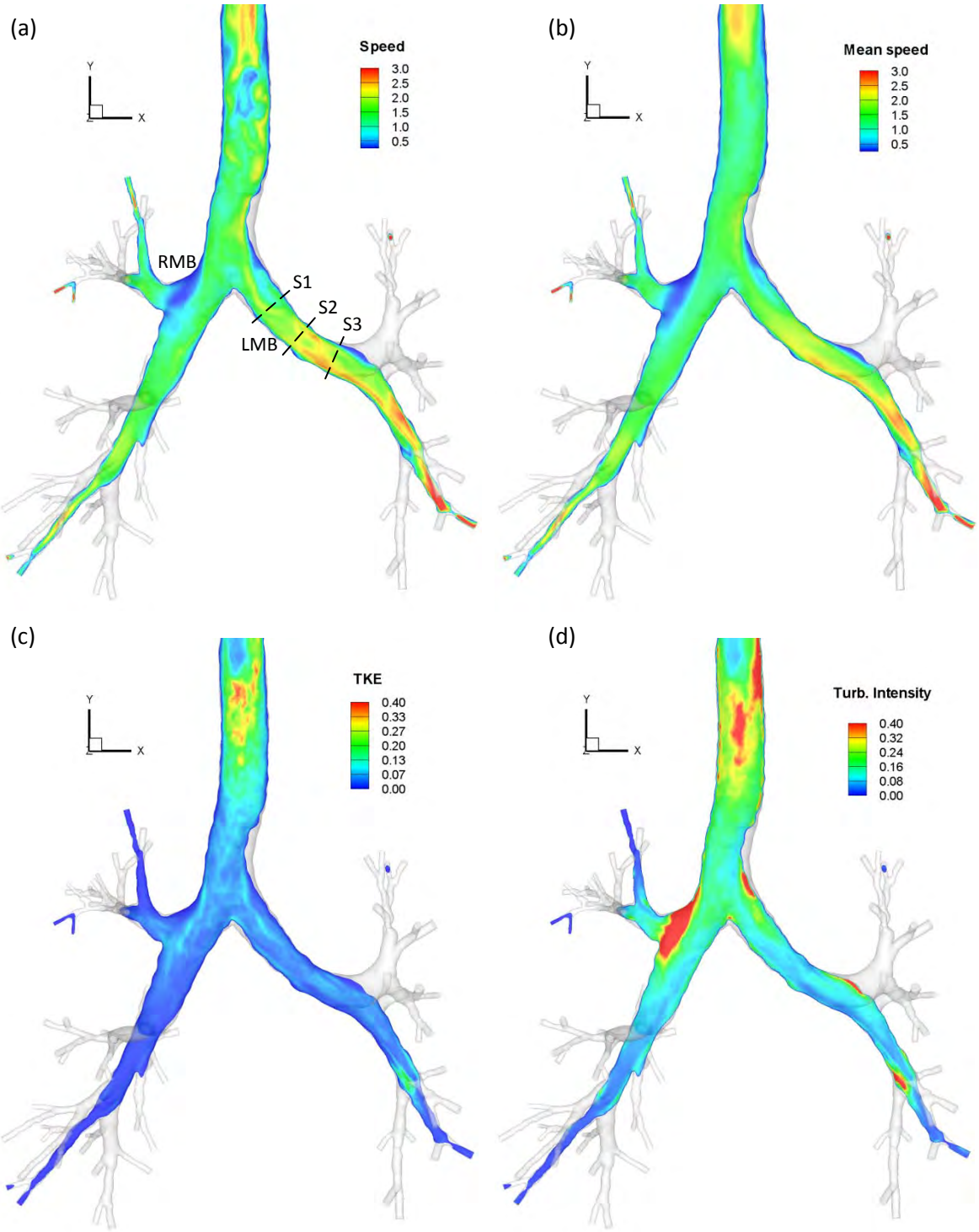

Figure 6.3 Flow structures at peak inspiration. Contours of (a) instantaneous air speed (m/s), (b) ensemble-averaged mean air speed (m/s), (c) TKE (m^2/s^2), (d) turbulence intensity in a vertical plane at z=0.002m.

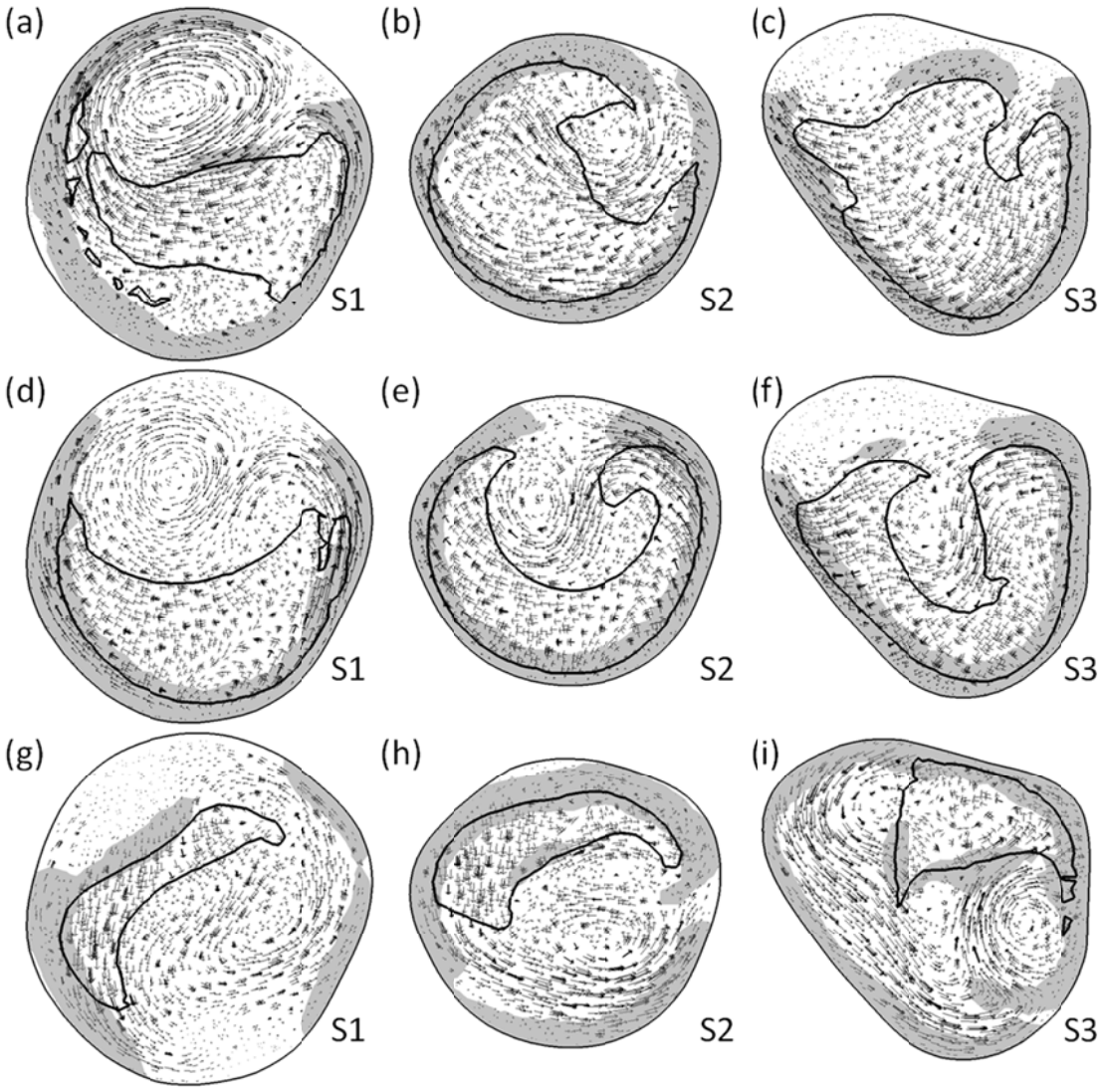

Figure 6.4 Instantaneous flow structures in the CT-based airway model in three cross-sections at (a,b,c,d,e,f) inspiration and (g,h,i) expiration. (a,b,c,g,h,i) with upper airways; (d,e,f) without upper airways. Contour line of air speed at 1.7 m/s with increasing speed inside the enclosed area; gray shaded region, dissipation rate in excess of 16.7 m^2/s^3.

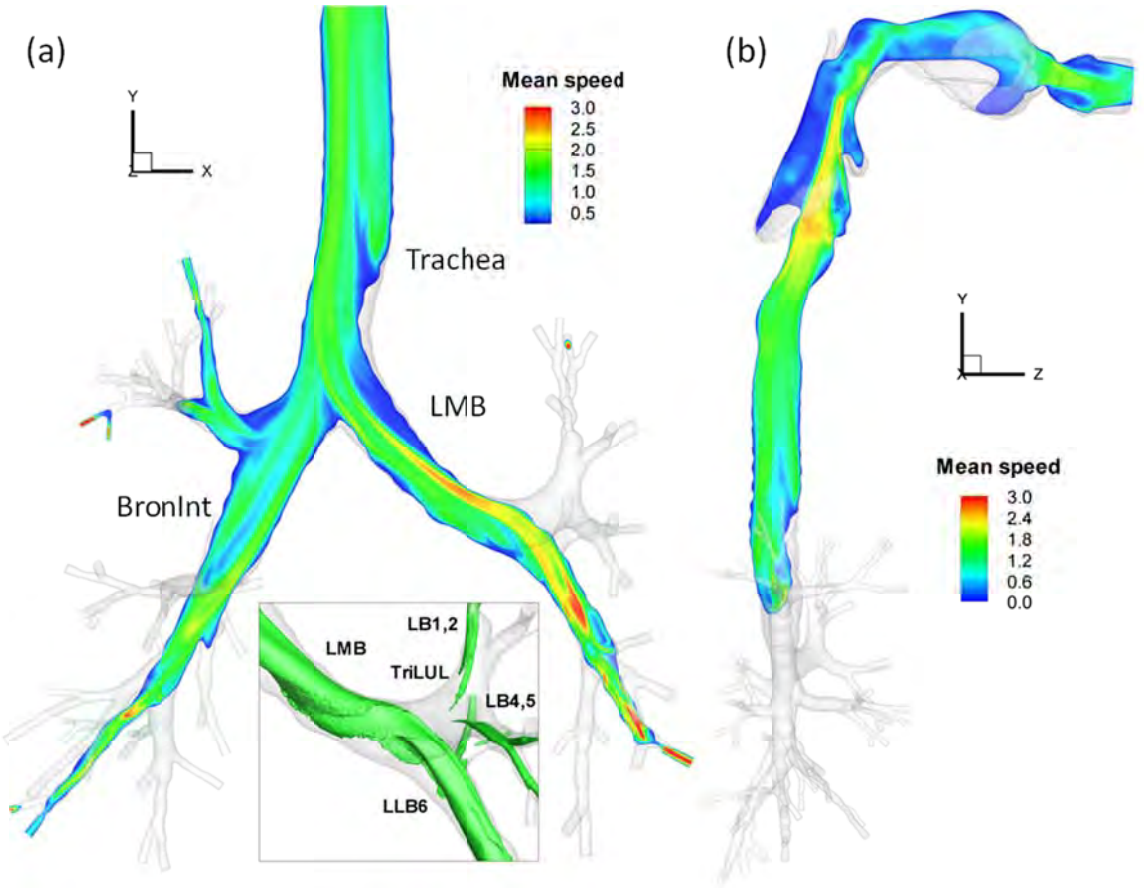

Figure 6.5 Flow structures at peak expiration. Contours of ensemble-averaged mean air speed in a vertical plane: (a) z=0.002 m, (b) x=0.005 m. The insert in (a) shows the isosurface of air speed at 1.5 m/s near the bifurcation prior TriLUL (sub-volume 4 in figure 1).

CHAPTER 7

AIRWAY RESISTANCE

7.1 Introduction

The regional distribution of ventilation in the human lungs depends upon airway resistance and tissue compliance. Airway resistance is determined by airway geometry and flow characteristics. It varies between healthy individuals, and can increase due to lung disease. Therefore, a better understanding of the relationship between airway structure, airflow, airway resistance, and regional ventilation in the human lungs is the first important step in improving diagnosis and treatment of lung disease, advancing pulmonary pharmaceutical drug delivery methods, and preventing adverse effects on lung development in children due to early exposure to environmental pollutants (Gauderman *et al.* 2004).

Comprehensive reviews of pulmonary flow and transport phenomena can be found in Pedley (1977), Pedley and Kamm (1997) and Grotberg (1994, 2001). Early insights into pulmonary airflow and airway resistance were mostly gained from experimental and analytical studies. For example, Schroter and Sudlow (1969) and Pedley *et al.* (1970a, 1970b, 1971, 1977) performed pioneering studies on airflow and airway resistance in a physical symmetrical bifurcation model. They compared the energy dissipation in the model with that of Poiseuille flow and proposed an airway resistance model. Wagner *et al.* (1990) and Yanai *et al.* (1992) showed that the resistance of the small airways of less than 2 mm in diameter contributes 15 to 24% of the airway resistance in a normal subject and much more in a subject with airways disease. Further studies have shown that the major airway resistance comes from the medium-sized lobar and segmental bronchi (West 2005).

The main objective of this chapter is to examine Pedley's theory and model from a fundamental fluid dynamical viewpoint at a local level, and extend the model to predict

airway resistance under normal breathing in a realistic human lung at a global level. In particular, we seek to understand the dynamical behaviors of viscous resistance in response to flow rate and airway dimension at inspiration and expiration, and identify their relationships with 3D flow structures observed in an airway branching network. To achieve this we employ a multiscale CFD method that can produce laryngeal-jet-induced flow disturbances in the central airways and physiologically-consistent lobar ventilations in the lung parenchyma in a MDCT-based human lung model. 3D CFD solutions from the multiscale method are compared with Pedley's theory and model to understand the underlying physics that cause different model parameters for inspiratory and expiratory flows. The comparison is done segment by segment at a local level over 31 airway segments. To further assess the collective behavior of segmental resistance at an organ level due to branching pattern, the viscous resistance in the whole asymmetric airway tree model is compared with that of the Weibel symmetric model.

7.2 Pressure drop and airway resistance by generation

Airway resistance is defined as

$$R = \Delta p / Q \tag{7.1}$$

where Δp is the static pressure drop across an airway segment. At low *Re*, the resistance in a fully-developed laminar pipe flow is given by Poiseuille's law. If *Re* exceeds ~2,300, the pipe flow becomes unstable and transition to turbulence begins. At *Re* ≈ 3,000, the turbulent flow is fully developed with $\Delta p \propto Q^{1.75} R$ (Pedley 1977). The static pressure drop between two bifurcation points associated with an airway segment is plotted as a function of airway generation for both inspiration and expiration. The volume-averaged p_V is used in calculation of static pressure drop because the area used in the area-averaged p_A or the velocity-weighted p_u is not uniquely defined at a bifurcation. Figures 7.1(a) and

7.1(b) show the distributions of pressure drop and airway resistance during inspiration and expiration, respectively. At inspiration, the pressure drop in the trachea is negative, indicating that the static pressure increases when the air flows downstream along the trachea. The mean resistance $\overline{R}$ is computed from equation (7.1) as $\overline{R} = \overline{\Delta p} / Q_t$, where Q_t is the volumetric flow rate at the trachea. Thus, the static-pressure resistance at the trachea is negative and is attributable to the presence of the laryngeal jet (see Section 7.3). Except for the trachea, the static pressure drop is positive at inspiration and reaches local maxima at the 4th and 6th generations. The local maximum $\overline{\Delta p}$ at the 4th generation reads 2.48 Pascal (*Pa*). The mean resistance at the 4th generation reads ~0.075 cm H_2O/l/s at peak inspiration. However, the local maximum pressure drop and resistance found at the 6th generation are caused by lack of samples. This is because there are only 5 airway segments at the 6th generation and they are all located in the RLL, which has higher lobar ventilation than middle and upper lobes RML, RUL, and LUL. To examine the sensitivity of $\overline{R}$ to Q_t, equation (7.1) is applied to the data that meet the criterion of $Q_t \geq 0.00015$ m^3/s to exclude large resistance caused by nearly zero Q_t. About 76% of the data in a breathing cycle satisfy the criterion. Those $\overline{R}$ data are averaged again by generation. Figure 7.1 shows that the average $\overline{R}$ at the 4th generation decreases slightly to 0.064 cm H_2O/l/s.

At expiration, the pressure drop and resistance by airway generation are shown in Figure 7.1(b). The maximum pressure drop and mean resistance are now found at the 5th generation with a value of ~0.05 cm H_2O/l/s. It is also noted that the $\overline{R}$ value at the 2nd generation is smaller than other generations. The $\overline{R}$ value at the trachea becomes positive, and those of the LMB and RMB decrease slightly in comparison with those at inspiration.

7.3 Energy budget analyses for airway segments and bifurcations

In this section, the energy budgets of the sub-volumes shown in Figure 2.1 are used to study the distribution of viscous pressure drop Δp_v by generation. Because of the

complexity of the airway geometry, we first adopt the energy-based equal-partition approach to analyze the distributions of Δp_v, Δp_u and Δp_k of nine airway segments (of generations 0-3). In this approach, the "energy" budget of a bifurcation is "equally" divided and distributed to its corresponding mother and daughter branches to examine the effect of bifurcations on the energy budget of an airway segment. However, this approach becomes impractical for small airways because partition of a branching sub-volume among the connected segments in these airways is difficult due to the complexity in the shape, dimension, and branching pattern of the sub-volume. We then introduce the length-scaled approach, which approximates viscous dissipation at bifurcations as described later, to study the Δp_v distribution of 31 airway segments which have one inlet and one outlet.

The Δp_v values of nine segments of generations 0-3 are calculated by the energy-based equal-partition approach. They are then averaged over all the Δp_v data having a tracheal flow rate of $Q_t \geq 0.00015$ m^3/s to compare with the data shown in Figure 7.1. The average Δp_v data are also tabulated in Table 7.1. Table 7.1 shows that inclusion of the viscous dissipation at bifurcations increases the Δp_v of an airway segment. These Δp_v data are then classified and averaged again by generation. Figure 7.2 shows the distributions of the average Δp_v, Δp_u and Δp_k of these nine airway segments by generation. See the data labeled by "E: 9 seg. with bifurcation", where "E:…with bifurcation" means use of the energy-based approach to include viscous dissipation at bifurcations, and "9 seg." means nine segments. The distributions of the velocity-weighted Δp_u based upon these segments with bifurcation for both inspiration and expiration agree very well with those of the volume-averaged static pressure drop shown in Figure 7.1. Furthermore, at inspiration Δp_k is positive (deceleration) at the trachea and is slightly negative (acceleration) at generations 1-3. Δp_k is much smaller than Δp_v for generations 1-3 (the average $|\Delta p_k/\Delta p_v| \approx 0.17$) due to flow stagnation at bifurcation. At expiration Δp_k is

reversed, being negative at the trachea and positive at generation 1-3, and the average $|\Delta p_k/\Delta p_v|$ for generations 1-3 is 0.37.

To estimate how inclusion of branching volumes affects the viscous pressure drop in small airways, we apply the length-scaled approach. This approach assumes that the viscous dissipation per unit volume in each of the aforementioned 31 airway segments of generations 0-6 is approximately constant. For instance, an airway segment is represented by the cylinder with the solid line (plane view) illustrated in the insert of Figure 7.2(a). The length of the airway segment is denoted by *Lo*, which is shorter than the length of the centerline between two branching points *Lw*. To estimate the effect of the bifurcating regions A and B, the boundary faces of the airway segment (denoted by *a* and *b* in the insert) are extruded from their original locations to the branching points (denoted by the dashed line). With the assumption of constant viscous dissipation per unit volume, the Δp_v of the extended volume that includes bifurcations is estimated as Δp_{vo} *Lw/Lo*, where Δp_{vo} is the viscous pressure drop of the original segment. In Figure 7.2, the Δp_v values of the above nine segments based upon the length-scaled approach (denoted by "L:" in the figures) are compared with those of the energy-based equal-partition approach (denoted by "E: …with bifurcation") for assessment. The agreement between them is good for both inspiration and expiration (see also table 7.1). Then the length-scaled approach is applied to all of the 31 segments because the data on Δp_{vo}, *Lw*, and *Lo* are available for these segments. The Δp_v distribution for the 31 airway segments without including bifurcation (labeled by "E: 31 seg. without bifurcation") is also displayed in Figure 7.2 for comparison. The result shows that inclusion of bifurcation overall increases Δp_v for airways of generations 0-6. These viscous pressure drops will be used later to evaluate Pedley's theory and model, and examine their relationship with the boundary-layer and free-shear flow structures discussed in Chapter 6 at inspiration and expiration.

7.4 Similarity behavior for viscous pressure drop

Pedley *et al.* (1970a, 1971, 1977) proposed formula (4.8) to predict the viscous pressure drop of the airflow in the Weibel symmetric 1D airway tree model. This formula has not previously been tested in a realistic human airway model. In this section, the dimensionless form of the formula (7.2) will be examined.

$$\Delta\hat{p}_v = \gamma\left(\mathrm{Re}\frac{D}{L}\right)^{1.5}, \textit{ where } \Delta\hat{p}_v = \frac{\Delta p_v}{\left(32\frac{\mu^2 L^2}{\rho D^4}\right)} \tag{7.2}$$

The normalized viscous pressure drop is denoted by $\Delta\hat{p}_v$. Because the coefficient γ is defined for an airway segment with one inlet and one outlet, the data based upon the 31 sub-volumes without including bifurcation are plotted in Figure 7.3(a) for the inspiratory phase. The three dot-dashed lines in the figure have a slope of 1.5. The result shows that all of the data almost collapse to a narrow region with a slope of ~1.5 for the flow rate of $Q_t \geq 0.00015$ m^3/s. They all exhibit a similarity behavior regardless of generation, dimension, and flow rate. The slope, however, appears to decrease in the lower range of *ReD/L*, which will be discussed later. The time histories of the corresponding γ values calculated by equation (4.6) are shown in Figure 7.4. The condition $Q_t \geq 0.00015$ m^3/s is imposed to avoid a large increase of the γ value associated with a small flow rate. In spite of the complexity of airway geometry and flow condition in the realistic airway model, Pedley's formula works remarkably well for small airways as well as large airways. The γ value of each segment seems insensitive to the flow rate as long as the flow rate is not diminishing. All but three branches have a γ value less than 0.4. Although Pedley's formula (4.8) was originally developed for inspiratory flow, it works as well for expiratory flow because the data in Figure 7.3(b) also exhibit a similarity behavior with a slope of ~1.5. Like inspiration, the slope is also noted to decrease with decreasing *ReD/L*.

The γ values of all the airway segments shown in Figure 7.4 are further averaged over time separately for both inspiration and expiration. They are then classified and averaged again by generation. Figure 7.5(a) shows that the γ value varies by generation and has a higher value at the 2nd generation (see the data labeled by "E: 31 seg. without bifurcation"). An inspection of the γ value for each segment in Figure 7.4 shows that the 2nd-generation segment TriLUL has a high value of 0.766 at inspiration and 0.499 at expiration. The TriLUL is a short segment with a large diameter that branches out to the segments LB1+2, LB3, and LB4+5, thus a "tri"-furcating segment (Figure 2.2). The airway dimension and the branching pattern vary from segment to segment. They affect the composition of boundary-layer and free-shear flow structures and the intensity of viscous dissipation (see Figures 6.2 and 6.4), leading to different levels of viscous pressure drops in different segments. That is why the γ value at the 2nd generation is higher than the others and the γ value varies by segment (Figure 7.4) and by generation (Figure 7.5). Another notable observation in Figure 7.5 is that except for the trachea, the γ values at inspiration are less than those at expiration. The mean γ values averaged over all segments are 0.280 and 0.341 for inspiration and expiration, respectively. They are close to the value of 0.327 proposed by Pedley *et al.* (1970a, 1971, 1977). While the current γ value at inspiration is slightly less than Pedley's value, which is consistent with Comer *et al.* (2001) and van Ertbruggen *et al.* (2005), the above analysis does not take into account viscous dissipation at bifurcations.

To estimate the γ value including bifurcation, we use the length-scaled approach to estimate the viscous pressure drop. The γ values of the nine segments listed in Table 7.1 calculated from the energy-based equal-partition approach are compared with those obtained from the length-scaled approach (denoted by "E:" and "L:" respectively in the figure). The agreement between them is good. The greater γ value at the 2nd generation is predicted by the two approaches and is attributable to the TriLUL branch. The length-scaled approach is then applied to calculate the γ values of the 31 segments, which are

shown in Figure 7.5 and Table 7.2. As compared with those without bifurcation "E: 31 seg. without bifurcation", the γ values increase for all generations at both inspiration and expiration. The standard deviations of the γ values using the length-scaled approach vary from 35% (at the 6th generation) to 68% (the 2nd generation) during inspiration and 23% (the 6th generation) to 55% (the 3rd generation) during expiration (see table 3). The average γ values marked by the dashed lines in Figure 7.5 are 0.357 at inspiration and 0.460 at expiration with standard deviations of 55% and 50% of their respective γ values. The average γ value at inspiration is in good agreement with the γ value of 0.327 with a standard deviation of 15% proposed by Pedley *et al.* (1970a) for inspiratory flow. Thus, Pedley's formula does not over-predict the Z, γ and Δp_v values, but is rather accurate for a realistic airway model.

7.5 Effect of free shear dissipation

One major finding in Section 7.4 is that the average γ value is greater at expiration than at inspiration. This finding is based upon the relationship of $\Delta\hat{p}_v = \gamma(\mathrm{Re}\, D/L)^n$ where n=1.5, thus a larger γ value at a given *ReD/L* implies more viscous dissipation. It is noted in Figure 7.3 that the slope n regardless of respiratory phases appears to be smaller than 1.5 in the lower range of *ReD/L*. The flow visualization in Chapter 6 reveals that a high-speed jet stream yields not only high dissipation in the wall boundary layer, but also local maximum dissipation on its free shear side. In addition, jet-like free shear flow structures are prevailing in the core region at expiration. In this section we investigate the respective roles of boundary-layer (BL) and free-shear (FS) structures in viscous pressure drop. We adopt the boundary layer thickness formula $\bar{\delta} = (2\nu L/\bar{U})^{1/2}$ used in the entry flow model of Pedley *et al.* (1971) with L as the length scale and $\bar{U}$ the velocity scale to estimate the boundary layer thickness for each segment. The volume obtained by sweeping inwards from the airway wall along the wall normal direction by a distance of $\bar{\delta}$ is defined as the BL zone. The volume outside the BL zone is designated as the FS

zone. The volume integral of dissipation Φ in equation (4.5) is then split into Φ_{BL} and Φ_{FS} for the BL and FS zones, respectively, so is the viscous pressure drop Δp_v into $\Delta p_{v,BL}$ and $\Delta p_{v,FS}$. The flow characteristics in the two zones are subsequently examined by $\Delta \hat{p}_{v,BL} \propto (\mathrm{Re}\, D/L)^n$ and $\Delta \hat{p}_{v,FS} \propto (\mathrm{Re}\, D/L)^n$, separately. The data shown in Figure 7.3 for each segment on a logarithmic scale are fitted to a straight line using the chi-square fitting algorithm to determine the optimal *n* value. The optimal *n* value for each segment is constant within the *ReD/L* range of the corresponding data. We then calculate the average optimal *n* value as a function of *ReD/L* based on the *n* values of all the segments.

At inspiration (Figure 7.6(a)), the average optimal *n* value based upon all the data in both BL and FS zones is about 1.4. At expiration (Figure 7.6(b)), the average optimal *n* value is about 1.6. They are smaller in the lower range of *ReD/L* regardless of phases. By considering the BL zone alone, Figures 7.6(c) and 7.6(d) show that the average *n* value is about 1.3 at inspiration and about 1.4 at expiration. For the FS zone, Figures 7.7(e) and 7.7(f) show that the *n* value is about 2.5 at inspiration and about 2.4 at expiration, being greater than those of the BL zone. A distinct feature in the FS zone is that the optimal *n* value increases dramatically with decreasing *ReD/L* in the range of *ReD/L* < 85. The increasing *n* value in this range is due to the exponential decrease of $\Delta \hat{p}_{v,FS}$ with decreasing *ReD/L*. This implies that the dissipation in the FS zone diminishes and becomes insignificant. The ratio of *L/D* in the range of *ReD/L* is about 3.5. Thus, irrespective of inspiration and expiration, the critical *Re* ≈ 300 signifies the change of the dynamic behavior of the FS structure. Back and Roschke (1972) and Hammad et al. (1999) noted that the critical *Re* for the onset of flow instabilities in the laminar flow through an axisymmetric sudden expansion is about 300. Gach and Lowe (2000) found that the transition regime of the flow through a 75% axisymmetric abrupt stenosis begins at a stenotic *Re* of 250. Vétel *et al*. (2008) reported that the laminar flow through a smooth axisymmetric 75% sinusoidal constriction becomes unstable at a critical *Re* of

400. The current critical *Re* noted in Figures 7.6(e) and 7.6(f) agrees with those found in the flows of similar type. By excluding the data in the range of *ReD/L* < 85 in calculation of the average *n* value for the FS zone, we obtain the average *n* values of 2.3 and 2.2 for inspiration and expiration, respectively. These *n* values agree with the Borda-Carnot relation (Batchelor 2000, Massey and Ward-Smith 2006) that the energy loss due to viscous dissipation in the pipe flow through a sudden expansion (in which dissipation occurs in free shear flows) is approximately proportional to the square of the mean flow speed before or after expansion. Reynolds and Lee (1981) noted in experiments using canine airway casts that the pressure-flow relationship based on a single power law may not be sufficient because the power *n* varies between 1 and 2, and adopted Rohrer's equation $\Delta p_v = K_1 Q + K_2 Q^2$ for data fitting, where K_1 and K_2 are constants. The notion of having two powers is phenomenologically consistent with the above finding, but the fundamental fluid mechanical basis is not understood, leading to Pedley's entry flow theory and model (1970a).

To quantify the respective contributions of the BL and FS zones to viscous dissipation, Figure 7.7 shows the ratio of Φ_{FS}/Φ as a function of *ReD/L* for inspiration and expiration. Overall, the contribution of the FS dissipation is more significant at expiration. This may explain why the average *n* value of 1.6 at expiration for all the data in both BL and FS zones (Figure 7.6(b)) is greater than 1.4 at inspiration (Figure 7.6(a)). Therefore, by fixing *n*=1.5 for both inspiration and expiration, the γ value for expiration becomes greater. The contribution of the FS dissipation during expiration can exceed 50% at high *ReD/L*, but during inspiration it is less than 50% in the current range of *ReD/L*. The Φ_{FS}/Φ ratio decreases rapidly with decreasing *ReD/L* to 18% and 8% at *ReD/L* = 100 for inspiration and expiration, respectively. This may explain the smaller *n* values in the lower range of *ReD/L* in Figures 7.6(a) and 7.6(b). Because viscous dissipations at both inspiration and expiration are caused by the BL and FS structures with various composition, this explains why Pedley's formula with *n* = 1.5 works for both phases with

a larger γ value on expiration. In fact, Pedley and Kamm (1997) reported that viscous pressure drop or resistance is found to be greater at expiration in experiments using canine casts (Reynolds and Lee 1981) and human subjects *in vivo* (Hyatt and Wilcox 1963). Although the secondary motions formed in the curved tube can elevate dissipation (Collins *et al*. 1993), this study suggests that both BL and FS structures contribute to dissipation at inspiration and expiration, and the FS structure plays a key role in increasing dissipation at expiration. The reason why the FS structure is prevalent at expiration is that laminar jets tend to be formed in the core region when airflow undergoes expansion between generations of airway segments as illustrated in Figures 6.1 and 6.5. The ratios of the airway cross-sectional areas between generations are A_i/A_{i+1} = (1.79, 1.86, 3.56, 2.00, 1.47) or constrictions of $(1-A_{i+1}/A_i)$ = (44, 46, 72, 50, 32)% for i = 0, 1, 2, 3, 4, respectively, where A_i is the average area of the i-th generation airways.

7.6 Viscous resistance in 1D airway tree models

In this section, the newly calibrated model parameters (γ = 0.357 for inspiration and γ = 0.460 for expiration) together with Pedley's formula (4.8) are applied to the current asymmetric 1D airway tree model (see the insert in Figure 7.8) to assess the dependence of viscous resistance on the airway branching pattern at a global (organ) level. To verify our 1D flow model, we first calculate the average viscous resistance in the Weibel symmetric airway model (see the insert in Figure 7.8) at an inspiratory flow rate of 167 ml/s (10 l/min), which was analyzed by Pedley *et al.* (1970b). Figure 7.8 shows that the agreement between their data and our model prediction is excellent, verifying our 1D flow model. The flow rate is then set to 342 ml/s corresponding to the peak inspiration of the breathing waveform shown in Figure 2.8. As expected from equation (4.8), the viscous resistance increases with increasing flow rate. The 1D flow solution at peak inspiration based upon the asymmetric airway model is also displayed in Figure 7.8. High viscous resistance is found at the trachea and the 1st and 4th generations.

The high resistance in the trachea is attributable to the presence of the turbulent laryngeal jet. The 1st generation airway segments consist of the left and right main bronchi LMB and RMB. The high resistance at the 1st generation is caused by the LMB because of its longer length and smaller diameter than the RMB (see Tables 2.1 and 7.1). At the 4th generation there exists a local maximum resistance, which is consistent with Pedley's solutions for the Weibel model. After the 4th generation, the average resistance decreases with generation. Overall the resistance in the current airway tree model is lower than that of the Weibel model due to the smaller airway diameters in the Weibel model. The resistance in the asymmetric airway model at peak expiration is also shown in Figure 7.8. Its distribution resembles that of inspiration and is about 15% higher than inspiration for the first 6 generations. This is in good agreement with Hyatt and Wilcox (1963) that in normal human subjects *in vivo*, inspiratory frictional resistance is approximately 85% of expiratory resistance.

To re-examine the increasing Δp_v after the 4th generation which is based upon the 31 airway segments (see Figure 7.2), the average Δp_v based upon the 1D flow solutions of these 31 segments is analyzed. The 31-sample-based Δp_v exhibits the same trend as Figure 7.2 that the Δp_v keeps increasing after the 4th generation. CT imaging can resolve more small airways in the lower lobes because of higher lobar ventilation and volume inflation (flow rate) in these lobes. The biased sampling toward the lower lobes with high lobar ventilation yields higher average viscous pressure drop shown in Figure 7.2. By including all the airways in analysis, the average Δp_v value peaks locally at the 4th generation. We further partition the Δp_v by lobe, whereupon it becomes evident that the two lower lobes LLL and RLL have higher resistance than the others and the RML has the lowest resistance, which are consistent with physiological data.

7.7 Summary

In this chapter we studied airway resistance in a MDCT-based airway tree model, extended from Chapter 6. Our results show that the airflow in all the airway segments follows Pedley's formula at both inspiration and expiration in spite of the complexity of the airway geometrical and morphological structures in the realistic asymmetric airway model. That is, the dimensionless viscous pressure drop exhibits a similarity behavior, being proportional to $Re^{1.5}$. The model parameter γ proposed by Pedley is 0.327. The average γ values derived from our data for airway segments including bifurcations are 0.357 and 0.460 for inspiration and expiration, respectively. Thus, the three important observations are the following. First, Pedley's airway resistance model is applicable to a subject specific realistic airway tree. Second, Pedley's model works for both inspiratory and expiratory flows but with different model parameters. Third, airway resistance is greater at expiration than at inspiration. Our analysis also shows that the γ value varies between segments, suggesting its dependence on airway geometry, such as airway dimensions and branching patterns, thus its variability between subjects requires further investigation. These findings are important for future application of the 1D airway resistance model to studying lung functions and structure-function relationships in healthy and diseased lungs in a subject specific manner over a large population.

To understand the roles played by boundary-layer and free-shear structures in viscous dissipation, each segment is partitioned into boundary-layer and free-shear zones. The data in both zones are fitted with $\Delta p_v \propto (ReD/L)^n$. The results that the average n value for the free-shear zone ($n \approx 2$) is greater than that of the boundary-layer zone, and the contribution from the free-shear zone to viscous dissipation is more significant at expiration. This explains why the model parameter γ fitting with $n = 1.5$ yields a larger value at expiration than at inspiration.

The 1D resistance model together with the newly calibrated model parameters is then applied to the current subject specific asymmetric airway tree model and the Weibel

symmetric model. The results show that the large airway resistance occurs at the trachea, the main bronchi (due to the left main bronchus LMB), and the 4^{th} generation in the current tree model. In the Weibel model, the maximum resistance occurs only at the 4^{th} generation.

Table 7.1 Average model parameter γ and viscous pressure drop Δp_v for 9 airway segments with (W) or without (WO) bifurcation ("E", energy-based approach; "L", length-scaled approach).

Name (Generation)		Inspiration γ	Inspiration Δp_v	Expiration γ	Expiration Δp_v
Trachea	W (E)	0.298	0.696	0.233	0.443
(G0)	W (L)	0.308	0.720	0.238	0.452
	WO	0.297	0.670	0.229	0.420
LMB	W (E)	0.307	0.727	0.453	0.876
(G1)	W (L)	0.343	0.812	0.509	0.983
	WO	0.302	0.631	0.449	0.763
RMB	W (E)	0.266	0.178	0.251	0.138
(G1)	W (L)	0.303	0.202	0.255	0.140
	WO	0.216	0.103	0.182	0.071
BronInt	W (E)	0.179	0.229	0.253	0.262
(G2)	W (L)	0.178	0.227	0.253	0.261
	WO	0.158	0.178	0.224	0.205
TriLUL	W (E)	0.842	0.504	0.865	0.414
(G2)	W (L)	0.987	0.592	0.645	0.310
	WO	0.764	0.355	0.499	0.186
TriRUL	W (E)	0.306	0.284	0.560	0.427
(G2)	W (L)	0.400	0.370	0.838	0.639
	WO	0.292	0.197	0.612	0.341
TriLLB	W (E)	0.171	0.603	0.258	0.734
(G3)	W (L)	0.189	0.668	0.283	0.806
	WO	0.165	0.508	0.246	0.613
RB4p5	W (E)	0.438	0.443	0.760	0.637
(G3)	W (L)	0.330	0.334	0.592	0.498
	WO	0.282	0.244	0.506	0.363
RB2	W (E)	0.338	0.494	0.427	0.515
(G3)	W (L)	0.372	0.543	0.401	0.480
	WO	0.297	0.347	0.320	0.307

Table 7.2 The values of γ and the standard deviation (STD) by generation based upon the 31 airways using the length-scaled approach.

Generation	Inspiration γ	STD	Expiration γ	STD
0	0.308	0.000	0.238	0.000
1	0.323	0.116	0.382	0.167
2	0.522	0.353	0.579	0.265
3	0.341	0.170	0.452	0.250
4	0.396	0.187	0.522	0.241
5	0.288	0.117	0.383	0.142
6	0.275	0.097	0.449	0.102

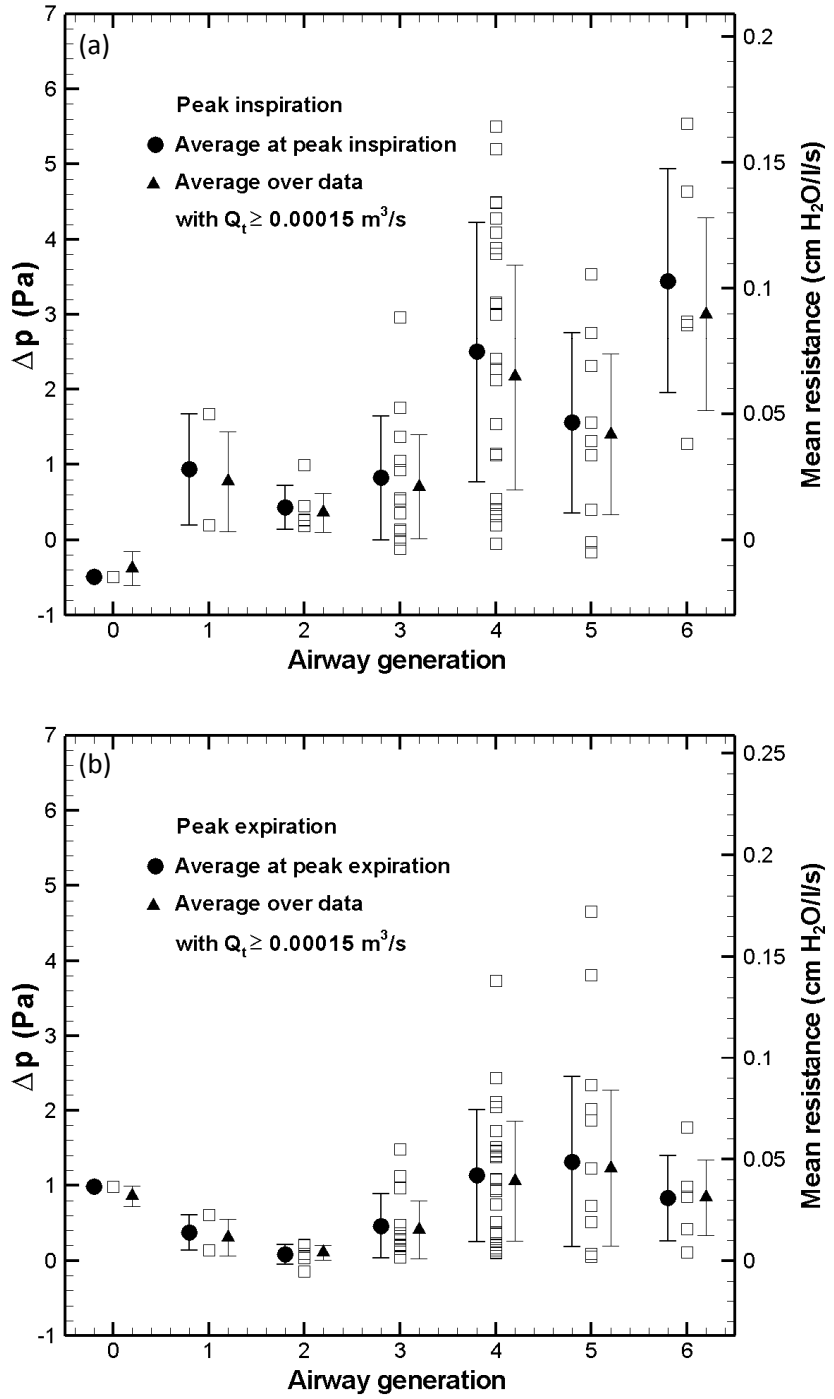

Figure 7.1 Distributions of airway pressure drop (left vertical axis) and average resistance (right vertical axis) by generation at (a) inspiration, (b) expiration. Open square, individual airway segments; solid circle, average over segments of the same generation at peak inspiration; solid triangle, average over segments of the same generation with $Q_t \geq 0.00015$ m^3/s (Q_t is the flow rate at the trachea).

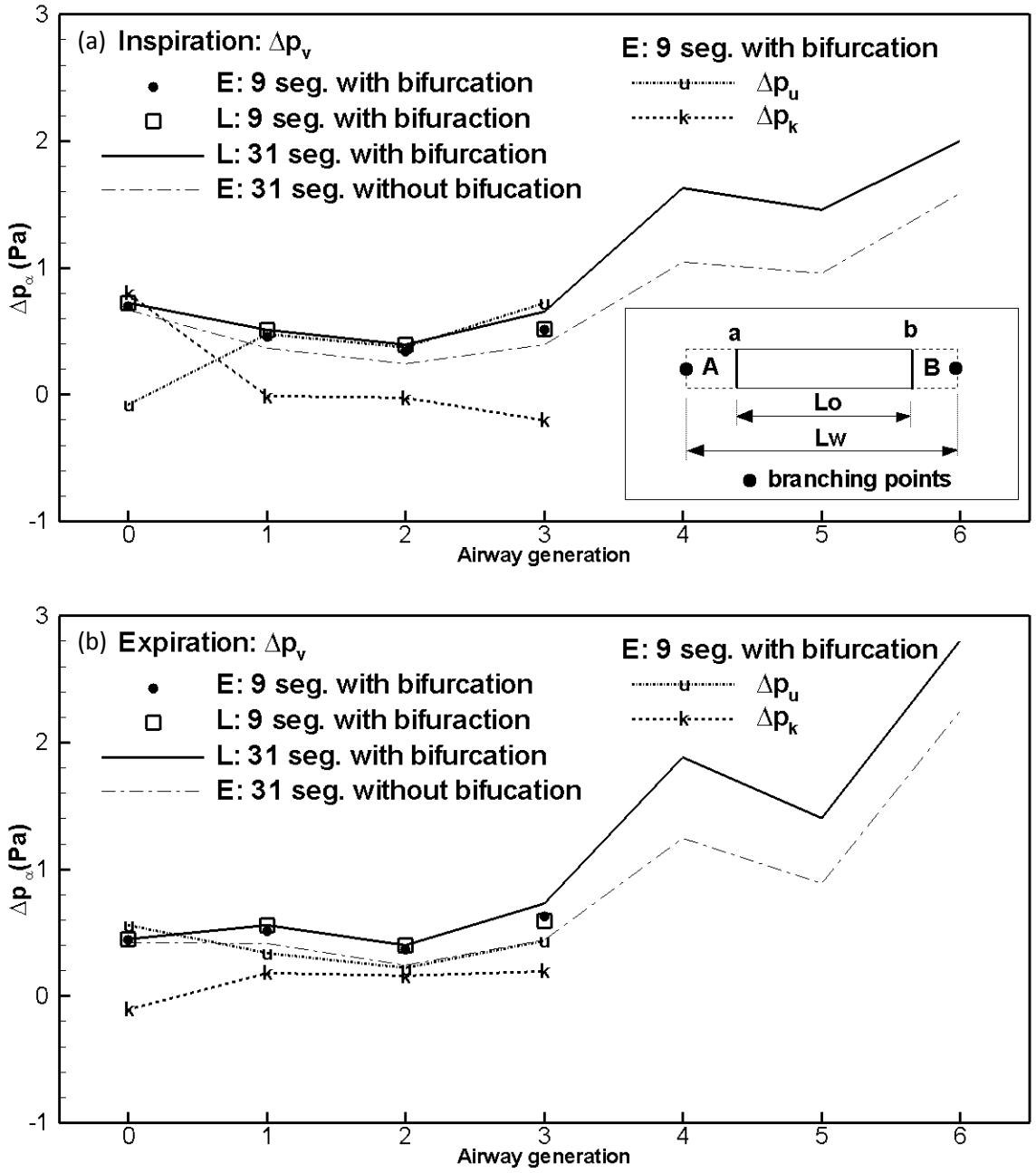

Figure 7.2 Distributions of average Δp_v, Δp_k, and Δp_u by generation with or without bifurcation computed by the energy-based ("E") and length-scaled ("L") approaches. (a) Inspiration, (b) expiration. The ensemble-averaged Δp_α of each segment is first averaged over time for data with $Q_t \geq 0.00015$ m^3/s, and then averaged by generation.

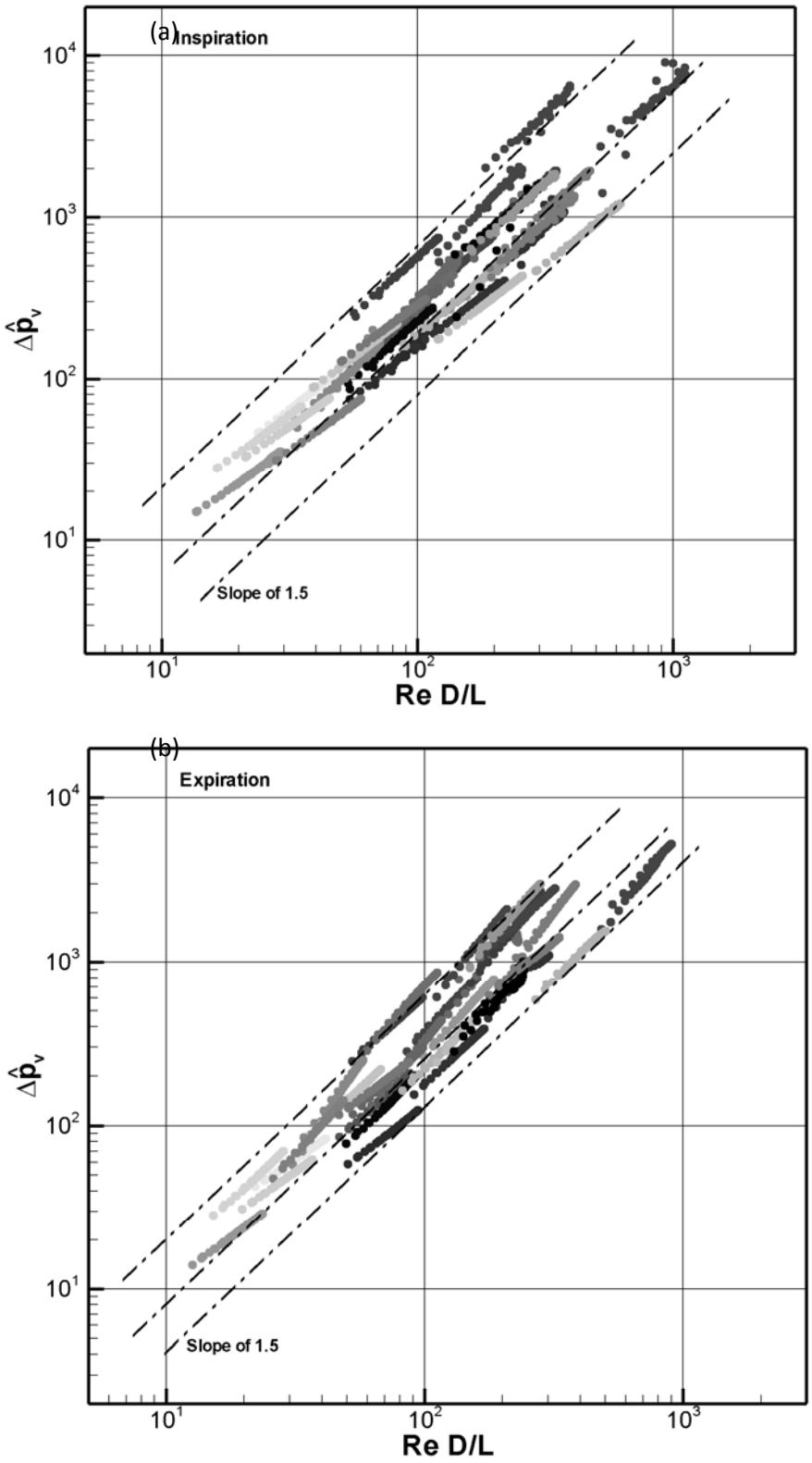

Figure 7.3 Dimensionless ensemble-averaged viscous pressure drop Δp_v versus (ReD/L) for the 31 airway segments. (a) Inspiration, (b) expiration.

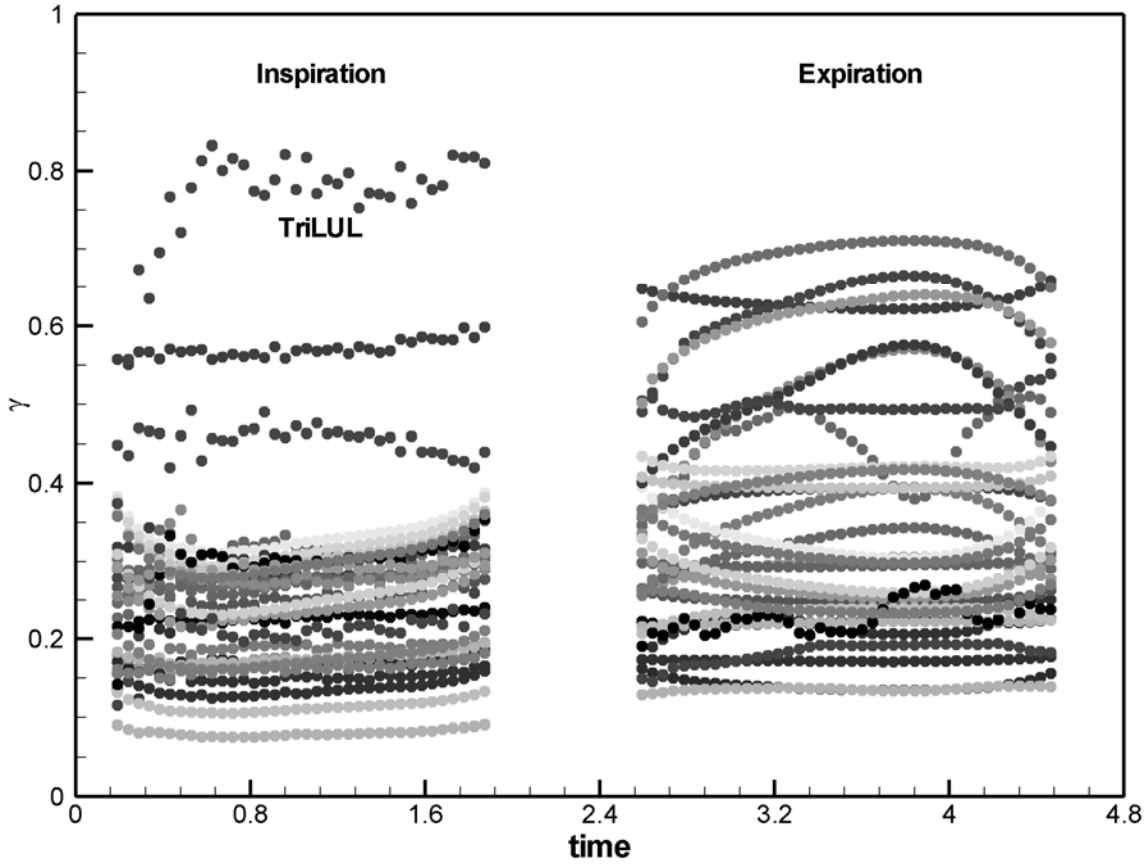

Figure 7.4 Time histories of ensemble-averaged γ model parameter for the 31 airway segments. Only data satisfying $Q_t \geq 0.00015$ m^3/s are displayed.

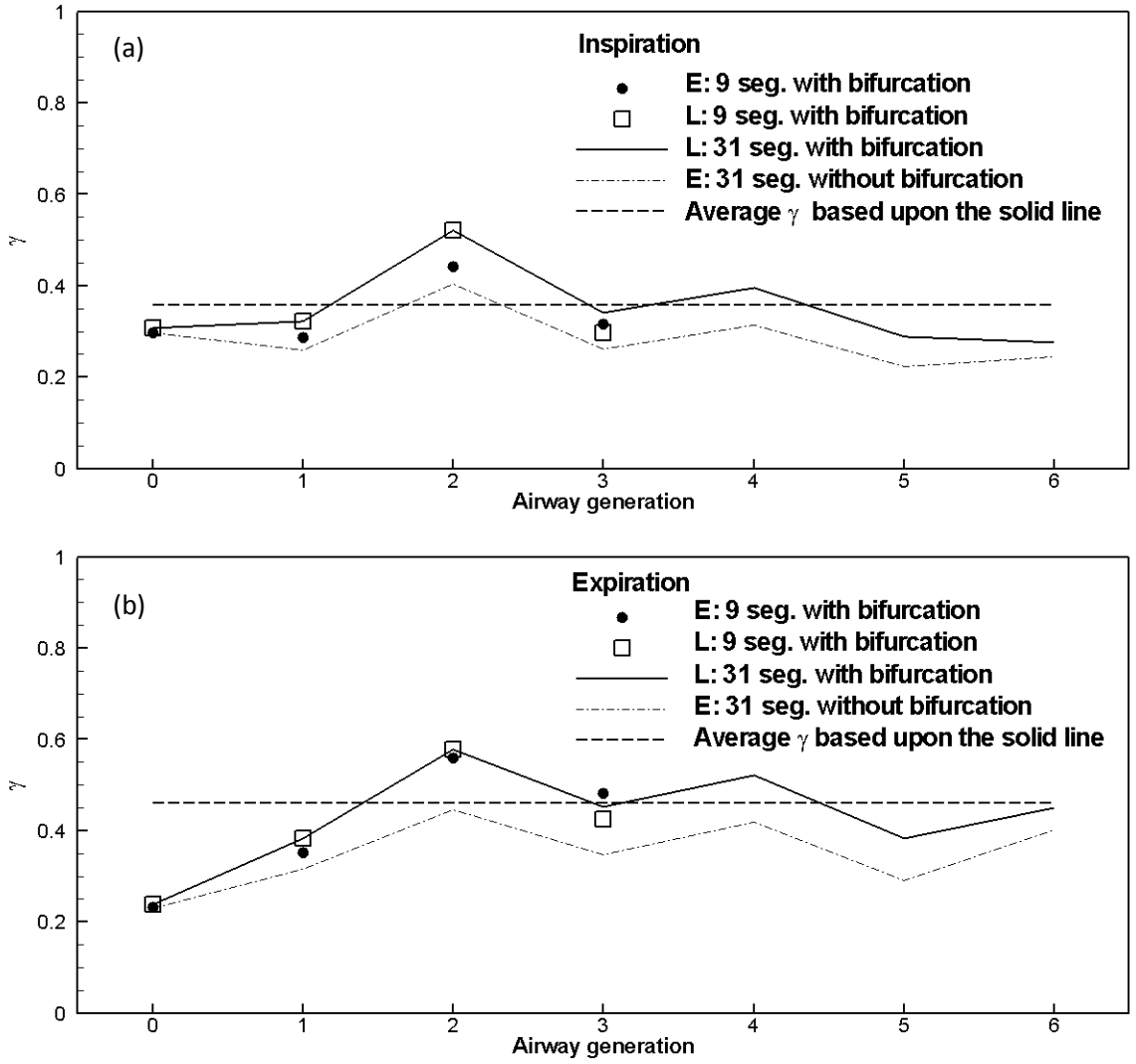

Figure 7.5 Distributions of average γ model parameter by generation at (a) inspiration, (b) expiration, computed by the energy-based ("E") and length-scaled ("L") approaches with or without bifurcation. The ensemble-averaged γ of each segment is first averaged over time for data with $Q_t \geq 0.00015$ m^3/s, and then averaged by generation.

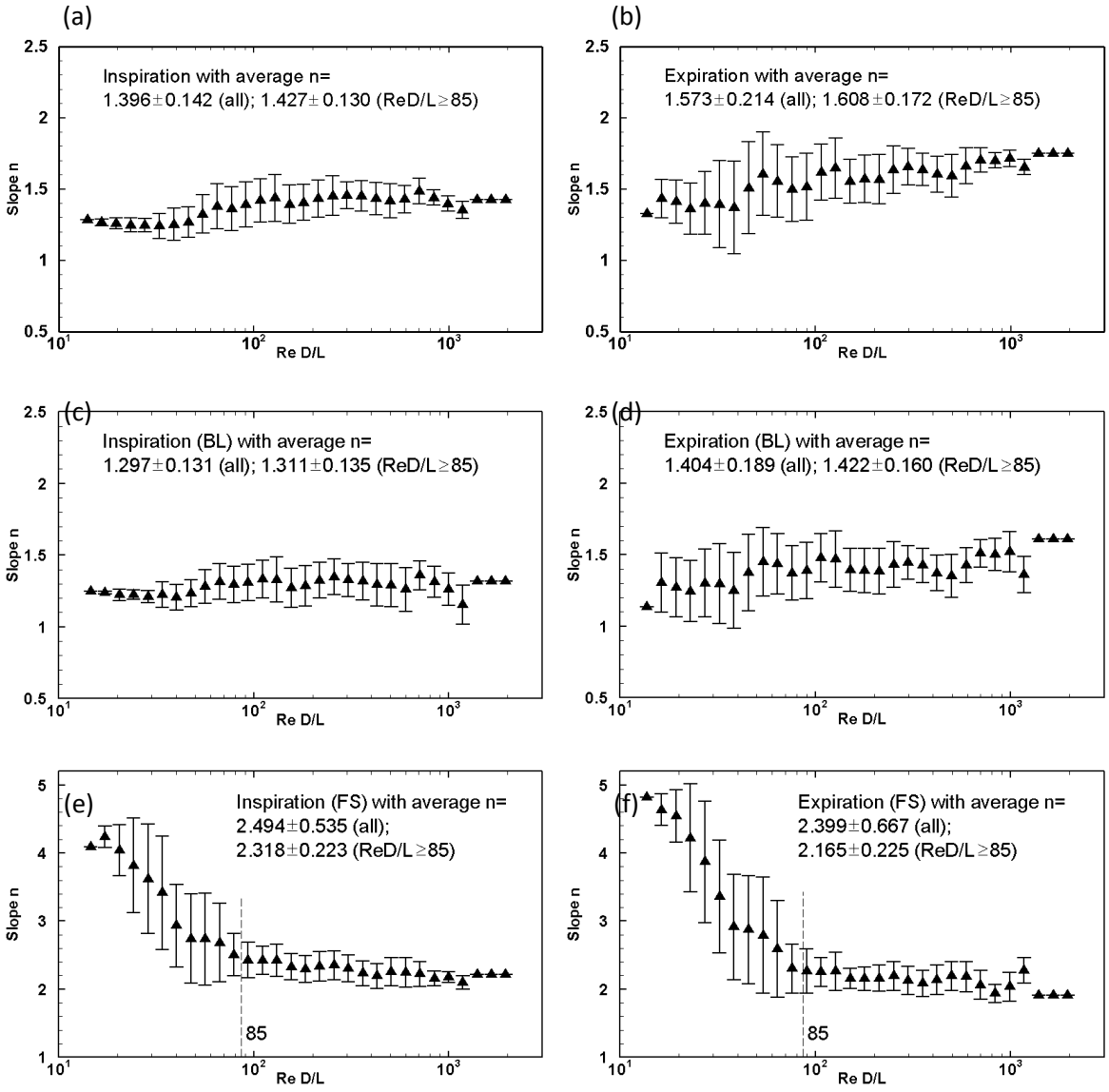

Figure 7.6 Average *n* values versus *ReD/L*. (a,c,e) inspiration, (b,d,f) expiration. (a,b) BL+FS zones, (c,d) BL zone, (e,f) FS zone.

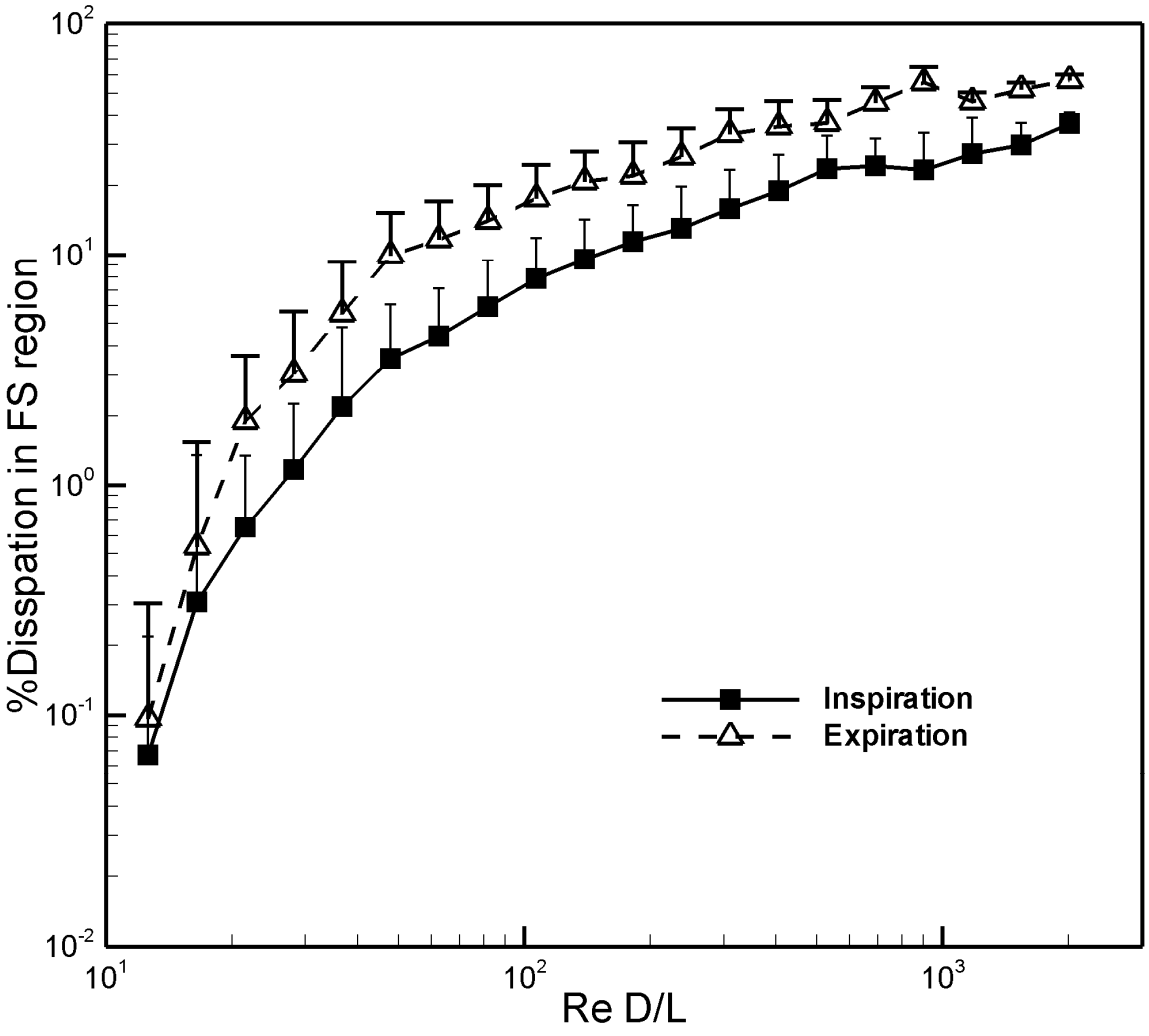

Figure 7.7 The ratio of Φ_{FS}/Φ versus *ReD/L*. Only the top error bars are displayed due to use of the logarithmic scale.

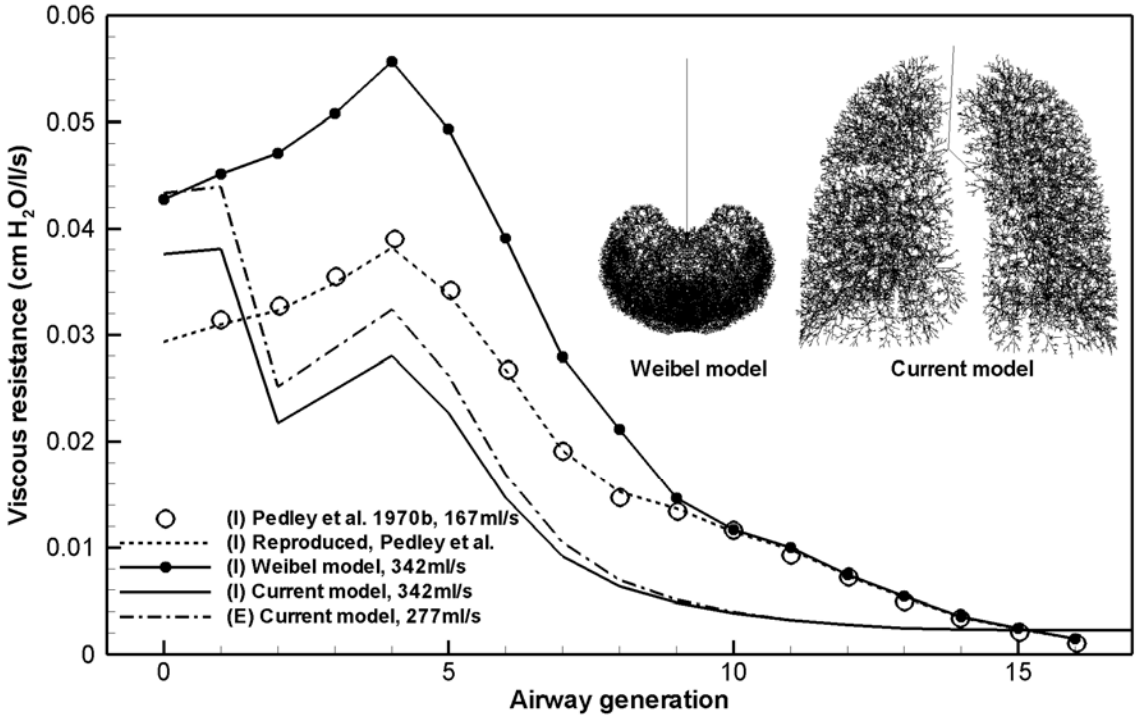

Figure 7.8 Distributions of average resistance at inspiration (denoted by (I)) by airway generation in the Weibel model and the current subject specific airway tree model at various flow rates. The open-circle data are taken from Pedley et al. (1970b) at a flow rate of 167 ml/s in the Weibel model. The dashed line is the data reproduced by our 1D flow model based upon Pedley's formula and the Weibel tree at a flow rate of 167 ml/s for verification. The solid line with solid circle uses the same flow rate as the current study. The expiratory flow (denoted by (E)) for the current model at peak expiration is also shown.

CHAPTER 8
HIGH FREQUENCY OSCILLATORY AIR FLOW AND CONVECTIVE MIXING

8.1 Introduction

Ventilatory support via invasive mechanical ventilation is often necessary for patients in an intensive care unit. Conventionally, the tidal volume of normal mechanical ventilation is approximately 75 to 150 percent of the patient's natural respiration volume (Marini 1996) based on the prediction that gas exchange volume has to exceed the anatomical dead space (the volume of conducting airways) of the lung to achieve adequate alveolar ventilation. However, this large tidal volume can cause volutrauma (over-stretch of lung tissue) and other ventilator-induced lung injuries (VILI) including oxygen toxicity (the effect of over-rich levels of oxygen on lung tissue), and hemodynamic compromises (Dos Santos and Slutsky 2006, Tremblay and Slutsky 2006). To avoid lung injuries due to volutrauma, high frequency ventilation (HFV) with smaller tidal volume has been used on patients with acute lung injury (ALI), acute respiratory distress syndrome (ARDS), and neonates. HFV is a fast and shallow ventilation mode which is postulated to minimize the lung injuries associated with cyclic opening and closing of alveolar units in conventional ventilation mode (Krishnan and Brower 2000). HFV includes high frequency positive pressure ventilation, high frequency jet ventilation and high frequency oscillatory ventilation (HFOV).

Lunkenheimer *et al.* (1972) proposed use of oscillating pumps for HFOV. This reciprocating process produces both active inspiration and expiration processes, eliminating gas entrainment and decompression of gas jets in the conducting airways. With active expiration, the lung volume can be controlled to avoid over-extension of the lung tissue, reducing the risks of lung injuries. HFOV has been used extensively both on neonates (Marchak *et al.* 1981) and adults (ARDSN 2000, Derdak *et al.* 2002, Mehta *et*

al. 2004, Moganasundram *et al.* 2002). HFV has attracted much research interest; a comprehensive review of this area of study can be found in Chang. (1984) Fluid dynamics studies include Tanaka *et al.* (1999) who used laser Doppler anemometer (LDA) to examine the secondary flow intensities and its influence on gas mixing in HFOV in a 3-generation Horsfield (1971) model. Lieber and Zhao (1998) also applied LDA to interrogate oscillatory flow in a symmetric single-bifurcation tube model, and found that the flow exhibits quasi-steady behaviors for only about 50% of the oscillatory cycle. Zhang and Kleinstreuer (2002) used a finite-volume code (CFX4.3) to study oscillatory flow in a symmetric triple-bifurcation tube model representing generations 3 to 6 of the human airways under normal breathing and high-frequency ventilation. They found that the oscillatory inspiratory flow is quite different from the equivalent steady-state case even at peak flow. Adler and Brücker (2007) studied high-frequency oscillatory flow using particle image velocimetry (PIV) in a 6 generation airway model, and observed mass exchange between child branches at end inspiration or expiration known as Pendelluft. Nagels and Cater (2009) used large-eddy simulation (CFX 11.0) to study high-frequency oscillatory flow in a 2 generation asymmetric tube model. They observed reverse flow near the walls when the driving velocity is small. Heraty *et al.* (2008) carried out PIV experiments to measure velocity fields and secondary flows in both idealized and realistic single airway bifurcations under HFOV conditions. They observed the coaxial counter-flow feature, which the flow in the core region of the airway lumen lags behind the flow in the near-wall peripheral region at flow reversal during change of the respiratory phase. They reported that the counter-flow feature persisted for a significant time period. The coaxial counter flow at flow reversal is characteristic of the Womersley (1955) solution noted in the classic high-frequency oscillatory straight pipe flow. This flow feature, however, is neither evident nor reported in Tanaka *et al.* (1999). It suggests that airway geometry (morphological structure) may also play a role in

determining flow characteristics (in association with lung function, e.g. gas transport and mixing for ventilation) under HFOV conditions.

This leads to the current work which aims to provide insight into the structure-function (geometry-flow) relationship of the human lung under different flow conditions using CFD; in particular, to understand the coaxial counter-flow feature in HFOV and quantify the efficiency of convective mixing under different flow conditions. From a kinematical point of view, fluid mixing involves stretching and folding of material lines, and is determined by the fluid velocity field. (Mackley and Neves Saraiva 1999, Ottino 1989, Roberts 1992, Roberts and Mackley 1995) Mixing of this viewpoint is referred to as convective (Darquenne and Kim 2005, Heyder *et al.* 1988) or kinematic (Henry *et al.* 2002) mixing. We consider three geometries with increasing complexity: a straight tube, a symmetric single-bifurcation tube system, and a CT-based airway model including the upper airways and the intra-thoracic airways of up to 7 generations. For the complete airway model, three flow conditions are considered to examine the effects of unsteadiness (oscillation) and convection (inertia). Mixing efficiencies are quantified by the stretch rate analysis. (Ma 2006, Ottino 1989, Roberts 1992, Roberts and Mackley 1995) The paper is laid out as follows. The mathematical formulations for the CFD analysis and the stretch rate analysis are described in the Methods section. In the Results section, oscillatory flows in a straight tube and a single bifurcation are first presented to demonstrate the features of coaxial counter flow and secondary flows. The stretch rates are used to quantify convective mixing in both cases. We then compare the characteristics of flows under three flow conditions in the complete airway model and quantify their stretch rates at the end of cycles and in the vicinity of flow reversal. In the Section 8.4, the counter-flow features and mixing efficiencies are discussed in conjunction with existing literatures. Concluding remarks are drawn in the last section.

8.2 Methods

8.2.1 Fluid solver

The airflow is simulated using large-eddy simulation (LES) which solves the filtered continuity and momentum equations for incompressible flow. Full description of the fluid solver is presented in Chapter 3. A validation case against LDV measurements will be presented later.

8.2.2 CT image based central airway model and 1D centerline model

The three-dimensional (3D) human airway model shown in Figure 8.1(a) was reconstructed from CT images for realistic representation of the human upper airway and tracheobronchial tree of subject 3 described in Section 2.1. The model is composed of upper airways and up to 7 generations of intra-thoracic airways. (Choi *et al.* 2009, Lin *et al.* 2007, and Lin *et al*. 2009) The trachea is counted as generation 0. There are a total of 70 small peripheral bronchi in this airway geometry. The distributions of the child-branch angle (the angle between two child branches) and the ratio of child-branch diameter over parent-branch diameter are displayed in Figures 8.1(b) and 8.1(c) by generation. The major (minor) diameter is that of the child branch having the larger (smaller) diameter. The average child-branch angle is 85^o and the average over generations 3-5 is 67^o, which is in good agreement with Horsfield (1971). The average diameter ratio (including both major and minor diameters) is 0.75, agreeing well with Majumdar *et al*. (2005). Beyond these CT-resolved airways, the conducting airway tree is supplemented with a physiologically-consistent 1D centerline airway model. The 1D centerline model is generated by the volume filling method (Tawhai *et al.* 2000, 2004). The resulting 1D model has 25 generations and is specific to the geometry of the subject's lung. The changes in lobar volumes are determined by two sets of CT images measured at two lung volumes. The volume changes are then used to determine lobar ventilations and the flow rates at the 1D terminal bronchioles (Section 2.4.3). The flow rates at the 3D peripheral

airways are obtained by the connectivity of the 1D tree and mass conservation (Lin *et al.* 2009, Yin *et al.* 2009b, 2010). Variants of 3D-1D and 3D-impedance coupled approaches have previously been applied to air flow in the human respiratory system (Ma and Lutchen 2006) and blood flow in the human arterial system (Formaggia *et al.* 1999, Grinberg and Karniadakis 2008, Vignon-Clementel 2006).

8.2.3 Breathing conditions for the CT-based airway model

A sinusoidal flow waveform with a parabolic velocity profile is imposed at the mouth-piece inlet of the CT-based airway model as the breathing waveform. For the HFOV case, the simulation is performed with a tidal volume (V_T) of 47 ml and a breathing frequency of 377 breaths per minute (f = 6.28 Hz), which fall in the typical range of HFOV. For comparison purpose, two other cases using the same model are computed. One case represents a normal breathing case (denoted by NORM) with V_T = 500 ml and a breathing frequency of 12.5 breaths per minute (f = 0.2 Hz). The second case is a clinically-impractical case with V_T = 16.58 ml and f = 6.28 Hz, which yields the same oscillatory frequency as HFOV and the same peak Reynolds number (*Re*) as NORM, thus being denoted as a high-frequency normal-*Re* case (HFNR). It is noted that HFNR and NORM have the same minute ventilation. The three cases allow examination of the respective effects of unsteadiness and convection. The flow parameters for these cases are summarized in Table 8.1. Time step sizes of $t = 2.0 \times 10^{-5}$, 1.0×10^{-5}, and 5.0×10^{-6} s are used for NORM, HFNR, and HFOV, respectively, to satisfy the Courant-Friedrichs-Lewy (CFL) condition.

The CFD mesh for the CT-based airway model consists of 899,465 points and 4,644,447 tetrahedral elements. We tested a series of consecutively finer meshes of **I)** 1,305,429 elements, **II)** 2,573,085 and **III)** 4,644,447 tetrahedral elements. The kinetic energies based on the radial velocity component of the secondary flow at station C in Figure 8.1(a) in the trachea are compared for these meshes at peak inspiration. The

differences of secondary flow energies between meshes **I)** and **II)** is 8.3% and it is 2.4% between meshes **II)** and **III)**, indicating the results are mesh-insensitive. The mesh **III)** is chosen for study.

8.2.4 Stretch rate analysis

The stretch rate (Ottino 1989) was adopted by Roberts (1992), Roberts and Mackley (1995), and Mackley and Neves Saraiva (1999) to quantify the extent of convective mixing, which is the non-diffusive component of the mixing mechanism. A higher stretch rate indicates higher mixing efficiency. Massless particles accompanied by three line elements, which are initially oriented in the respective x, y, and z directions $(1,0,0)^T$, $(0,1,0)^T$ and $(0,0,1)^T$, are tracked in a Lagrangian framework. For each particle, the three corresponding line elements are deformed and stretched kinematically by local velocity gradients as described below.

$$\frac{Dm_i}{Dt} = m_j \frac{\partial u_i}{\partial x_j} - m_i \left(m_j S_{jk} m_k \right) \tag{8.1}$$

$$s_I(t) = \frac{D(\ln \lambda)}{Dt} = m_j S_{jk} m_k \tag{8.2}$$

$$s_T(t) = \frac{1}{t} \int_0^t \left(\frac{D \ln \lambda}{D\tau} \right) d\tau \tag{8.3}$$

where m_i is the orientation vector of a line element and $m_i m_i = 1$, u_i is the velocity component i, $S_{ij} = \left(\partial u_i / \partial x_j + \partial u_j / \partial x_i \right) / 2$ is the symmetric stretching tensor, λ is the specific rate of stretching, and s_I is the instantaneous stretch rate, also known as the stretching function. The time-averaged stretch rate s_T is calculated from the instantaneous stretch rate as above. Both instantaneous and time-averaged stretch rates have a

dimension of s^{-1}. The stretch rates s_I and s_T computed by equations (8.2) and (8.3) are for one particle released at a specific location. The stretch rate presented later is the ensemble average based on a number of particles being released at different locations unless otherwise noted. If an oscillatory flow behaves in a kinematically reversible fashion, the time-averaged stretch rate at end cycle is zero.

8.2.5 Flow regimes

To study the characteristics of oscillatory secondary flow in a tubal branching network, it is important to know about the expected flow features in terms of key dimensionless parameters. Jan *et al.* (1989) categorized the oscillatory flow in a model bifurcation into three regimes according to two dimensionless parameters. One parameter is the dimensionless frequency α^2, where $\alpha = a\sqrt{\omega/\nu}$ is the Womersley parameter. $\omega = 2\pi/T = 2\pi f$ (T, period in s; f, frequency in Hz) is the angular frequency and a is the average radius of an airway segment (or a tube). The other parameter is the local dimensionless stroke length L/a, where $L = v_t / A$ (v_t is the local tidal volume, and $A = \pi a^2$ is the average cross-sectional area of an airway segment). The Reynolds number is given by $\mathrm{Re} = \alpha^2 (L/a)$ if the breathing waveform is a sinusoidal function.

Figure 8.2 shows the demarcation of three flow regimes: I) unsteady flow; II) viscous flow, and; III) convective flow, defined by Jan *et al*. (1989), according to the values of α^2 and L/a. The convective regime III is further subdivided into IIIa and IIIb based on the extent of unsteadiness of the flow. Because $\mathrm{Re} = \alpha^2 (L/a)$, the constant *Re* on a logarithmic scale corresponds to a line with a negative slope. For example, the bold solid line for *Re* = 30 separates the viscous and convective regimes, whereas the line for 1,500 separates the convective and turbulent regimes. The two dashed lines mark *Re* = 100 and 740. In the unsteady regime the flow is characterized by the Womersley solution, whereas in the viscous regime it behaves like Poiseuille flow. Both Womersley and Poiseuille solutions are linear solutions, in which the effects of convective inertia are

negligible, in contrast to the convective regime. The flow parameters for each of the airway segments in the 3D CT-based airway model are marked in the figure for the cases of NORM (squares), HFOV (circles), and HFNR (triangles). For NORM, the dimensionless frequency α^2 falls in the range between 0.12 and 7, and the stroke length L/a ranges from 133 to 1,353. For HFOV, α^2 is between 3.6 and 210, and L/a is between 12 and 127. Since HFNR has the same frequency as HFOV and the same peak *Re* as NORM, HFNR has the same range of α^2 as HFOV but is bounded by *Re* = 1,500 as NORM. The maximum *Re* at the trachea for NORM is 1,288, and it is 3,656 for HFOV. All of the segmental *Re* for NORM and HFNR are below 1,500, whereas six segments for HFOV exceed 1,500.

Also exhibited in Figure 8.2 are the conditions computed with the 1D centerline model using the parameters averaged by generation for the three cases (open symbols). Each open symbol represents the average flow condition for each generation of the entire airway tree beginning from the trachea to terminal bronchioles (distributing from right to left in the figure). For HFOV, the distribution curve is shifted downwards to the right and the effects of convection penetrate deeper into the lungs (note that the curve intersects *Re* = 30 at the 7th generation in both NORM and HFNR, but at the 9th generation in HFOV). Overall, the characteristics of HFOV are more turbulent in the central airways and more convective in the smaller airways. For HFNR, due to its smallest L/a and high α^2, the flow in the range of $\alpha^2 > 10$ (denoted by "IIIb-CONVECTIVE" in Figure 8.2) may behave more similarly to the Womersley solution.

To investigate the effects of unsteadiness (oscillation) versus convection (inertia), the flow parameters at point A (*Re* = 100, $\alpha = 7.0$) in Figure 8.2 in the unsteady regime I and point B (*Re* = 740, $\alpha = 7.0$) in the convective regime IIIb (more unsteadiness) are chosen for simulations of the flow in a straight tube and the flow in a symmetric bifurcating tube. The bifurcating tube model of Zhao and Lieber (1994) and Lieber and Zhao (1998) shown in Figure 8.3(a) is adopted for two purposes. One purpose is for

model validation by comparing with the data measured with LDA for oscillatory flow in the bifurcating tube model. (Lieber 1998) Their flow condition has a peak *Re* = 2,077 and $\alpha = 4.3$, corresponding to point C in Figure 8.2. The second purpose is to investigate the differences between flow structures in regimes I and IIIb, and the deviation of the flow behavior from the Womersley solution. Use of a symmetric bifurcating tube facilitates comparison with the straight tube case. The effects of airway geometry and turbulence (which can only be captured in the CT-based airway model) will be examined by comparing the flow structures at bifurcations between generations 2 and 3 (G2-3) and 3 and 4 (G3-4) at three breathing conditions of NORM, HFOV, and HFNR. The local flow parameters at the parent branches of the G2-3 and G3-4 bifurcations are marked by the color-coded boxed 2 and 3 in Figure 8.2, respectively.

8.3 Results

8.3.1 Model validation

The dimension of the symmetric bifurcating tube model is illustrated in Figure 8.3(a). The formula used to generate the model and stations 2, 4, 10, and 15 are given in Zhao and Lieber (1994). An enlarged view of the model is shown in Figure 8.3(b), where station S12.5 is located midway between stations S10 and S15. The child-branch angle of 70^o falls within the range of those at generations 3 and 4 [see Figure 8.1(b)]. The diameter ratio between child and parent branches is $1/\sqrt{2} \approx 0.7$, which also agrees with the current CT data [Figure 8.1(c)]. A sinusoidal flow waveform with the Womersley velocity profile is imposed at the boundary face of the parent branch. The mesh consists of 141,403 nodal points and 747,344 tetrahedral elements. The fluid properties and flow conditions used by Lieber and Zhao (1998) are adopted. The instantaneous velocity profiles (solid lines) at stations S2, S10, and S15 at *t/T* = 0.2 (inspiration) and 0.7 (expiration) in the bifurcation and transverse planes are plotted against the measurement data (solid squares) of Lieber and Zhao (1998). The bifurcation plane is co-planar with

the centerlines of the three branches, whereas the transverse plane for each of the three branches is perpendicular to the bifurcation plane and co-planar with the centerline of an individual branch. Overall, they are in good agreement. It is noted that the CFD solution is more symmetric with respective to $r/R = 0$ than the measurement data. For instance, in the range of $r/R < 0$ in Figure 8.3(f), the current data over-predict (under-predict) the experimental data at S2 (S15), but they agree with the CFD data of Zhang and Kleinstreuer (2002).

8.3.2 Womersley solution and flow in a straight tube

The straight tube used in the simulation is a 3D tube with radius a = 4.6 mm and length of 10a. The mesh for the tube consists of 82,144 nodal points and 453,586 tetrahedral elements. Considering a single harmonic case in a straight tube of radius a, we impose the Womersley (1955) axial velocity (u_a) profile at the inlet.

$$u_a(r,t) = \frac{A_o}{\rho}\frac{1}{i\omega}\left\{1 - \frac{J_o\left(\alpha\, r i^{3/2}\right)}{J_o\left(\alpha\, i^{3/2}\right)}\right\} e^{i\omega t} \tag{8.4}$$

where A_o is the amplitude of pulsation, ω (the angular frequency) and α (the Womersley parameter) are previously defined, r is the normalized radial position (with r = 0 at the centerline of the tube, and r=±1 at the wall), i is the imaginary unit, and J_k is the k-th order complex Bessel function of the first kind. With a given Re (or the maximum Re for a pulsatile flow), the mean velocity U is calculated using $Re = U(2a)/v$, where U is the sectional average velocity at peak inspiration. Then the maximum flow rate Q_{max} is computed by $Q_{\max} = U\pi a^2$, and A_o can be determined from

$$Q = \frac{\pi a^2}{\rho}\frac{A_o}{i\omega}\left\{1 - \frac{2}{i^{3/2}\alpha}\frac{J_1\left(\alpha i^{3/2}\right)}{J_o\left(\alpha i^{3/2}\right)}\right\} e^{i\omega t} \tag{8.5}$$

Because the axial velocity u_a in equation (8.4) and the flow rate Q in equation (8.5) are complex numbers, the real parts of equations (8.4) and (8.5) are taken in the calculation. The time in equations (8.4) and (8.5) is offset to keep Q in phase with the imposed sinusoidal flow waveform so that $Q = 0$ at $t/T = 0$, 0.5 and 1.

Figure 8.4 presents the results of the flow in a straight tube with the flow parameters of $Re = 100$ and $\alpha = 7$, at point A marked in Figure 8.2. The Womersley velocity profiles yielded from equation (8.4) at selected time points during a sinusoidal cycle are displayed in Figure 8.4(a). It is noted that the Womersley profiles do not vary along the axial direction of a straight pipe. The flow rates at $t/T = 0$, 0.5 and 1 are zero. The inspiratory and expiratory phases occur during $0 \le t/T \le 0.5$ and $0.5 \le t/T \le 1$, respectively. Coaxial counter flow (co-existence of positive and negative axial velocities due to phase lag between core and peripheral flows) is observed in the vicinity of $t/T = 0$, 0.5, and 1 when flow reversal takes place at end inspiration and end expiration. It is worth noting that the velocity profile is not symmetric in time with respect to $t/T = 0.5$ and 1. For example, the profile at $t/T = 0.375$ differs from that at $t/T = 0.625$ although they have the same time distances from $t/T = 0.5$. This is because the flow changes phase faster in the peripheral region than the core region. Nevertheless, the profiles at t/T are the mirror images of those at $t/T + 0.5$ (same shape but opposite sign), cf. those at dimensionless times of 0.125 and 0.625. As a result, a Lagrangian particle released in any location of the tube experiences zero net displacement at the end of a cycle. The profiles at peak inspiration ($t/T = 0.25$) and expiration ($t/T = 0.75$) are blunt. An increase in frequency makes the velocity profile blunter and the peripheral counter flow narrower as displayed in Figure 8.4(b), but the period-normalized time duration when counter flow exists remains essentially unchanged. The Womersley velocity profiles with the flow parameters at A are imposed as the flow boundary condition at the left-hand-side boundary face of the straight tube. A pressure boundary condition is imposed at its right-hand-side boundary face. The simulated velocity profiles at various stations along the

tube remain the same as the Womersley solution imposed at the boundary face, and are plotted against the Womersley solution at various times in Figure 8.4(c). The agreement between them is good, confirming that the flow condition at point A in a straight tube yields the Womersley solution.

With the imposition of the flow condition at point B which has the same frequency as A, but a higher *Re* than A, the CFD-simulated velocity profiles at various times during a cycle (not shown) exhibit the same shapes as those of Figure 8.4(c), but have different magnitudes. This is in agreement with the Womersley solution equation (8.4) that the shape of velocity profile depends on frequency [cf. Figures 8.4(a) and 8.4(b)], with a given frequency an increase in velocity amplitude increases *Re*. Thus, in spite of an increase in *Re* for point B which places it in the convective IIIb regime, the straight and axisymmetric features of the tube constrain the flow motion only in the axial direction. As a result, the convective terms in the Navier-Stokes equations are zero, yielding the linear Womersley solution.

8.3.3 Flow in a bifurcating tube model

The radius of the parent branch in the single-bifurcation tube model is rescaled to that of the straight tube in order to use the same flow parameters as in the straight-tube case. The Womersley profile is imposed at the parent-branch boundary face of the model [Figure 8.3(a)] to examine the effects of bifurcation on flow structures. Unlike the straight-tube case, the curvature at the bifurcation may induce secondary flow motions in the radial direction due to inertia. The flow conditions at point A (α = 7, *Re* = 100) and point B (α = 7, *Re* = 740) in Figure 8.2 are examined. For the case of *Re* = 100 (*Re* = 740), Figure 8.5 (Figure 8.6) shows the color-coded velocity vectors in the bifurcation plane at flow reversal during end expiration and early inspiration in Figures 8.5(a)-(d) [Figures 8.6(a)-(d)] and during end inspiration and early expiration in Figures 8.5(e)-(h) [Figures 8.6(e)-(h)]. The red (blue) color denotes positive (negative) axial velocity,

flowing to the right (left) side. Coaxial counter flow exists over a longer time period before flow reversal than after reversal. This is why counter flow is observed at t/T = 0.94 and 0.44, but not at t/T = 1.06 and 0.56. This is true for both *Re* cases (see Figures 8.5 and 8.6). At *Re* = 100 (Figure 8.5), in spite of the presence of the bifurcation, the counter-flow feature is evident and not distinguishably perturbed in both parent and child branches, resembling the imposed Womersley profile. However, at *Re* = 740 Figure 8.6 shows significant deviation from the Womersley profile, especially near the bifurcation. At end expiration in Figures 8.6(a) and 8.6(b), the flow coming off the child branches has relatively high inertia and appears to detach from the wall of the parent branch at the bifurcation due to bifurcation curvature. A similar effect is observed at end inspiration, but the major deviation is found in the child branch due to change of the axial flow direction. These deviations are amplified after flow reversal at t/T = 1.03 on inspiration and t/T = 0.53 on expiration. The counter-flow feature appears to be absent in some regions of the parent branch at t/T = 1.03 (red only) and the child branches at t/T = 0.53 (blue only).

To better understand the flow characteristics, Figure 8.7 shows the enlarged view of the flow near the bifurcation in the bifurcation plane and the cross-sectional velocity vectors at stations S4 and S12.5, whose location and numbering scheme are based on the formula of Zhao and Lieber (1994). Figures 8.7(a) and 8.7(b) [8.7(e) and 8.7(f)] are at end expiration t/T = 0.97 and early inspiration t/T = 1.03, respectively, for *Re* = 100 (740). And Figures 8.7(c) and 8.7(d) [8.7(g) and 8.7(h)] correspond to end inspiration t/T = 0.47 and early expiration t/T = 0.53, respectively, for *Re* = 100 (740). The velocity magnitude is much smaller at *Re* = 100 than at *Re* = 740, and the secondary flow velocity is weaker than the axial velocity. Therefore, the velocity vector length in the bifurcation plane at *Re* = 100 is magnified by 7.4 times than that of *Re* = 740, and the vector length at S4 and S12.5 is amplified by 4 times than those in the bifurcation plane for clarity. Counter-rotating vortices are observed at S4 and S12.5 although they are very weak at *Re* = 100.

These secondary flow structures are Dean vortices found in a curved pipe flow (Saric 1994). In the bifurcation plane of the *Re* = 100 case, the flow at *t/T* = 0.97 (1.03) is almost the reverse (opposite sign) of that at *t/T* = 0.47 (0.53). This is because the Womersley profiles at *t/T* are the mirror images (same magnitude, but of opposite sign) of those at *t/T* + 0.5 as shown in Figure 8.4(a). However, this is not true for the flow feature in the radial direction. For example, at S12.5 despite the change of phase in the axial flow, the counter-rotating vortices at *t/T* = 0.97 and 0.47 (1.03 and 0.53) rotate in the same directions. This is because the rotational direction of the vortices is dependent on the curvature of the tube, rather than the direction of the axial flow. With increasing *Re* to 740, the secondary flow vortices are intensified. At end expiration at *t/T* = 0.97 [Figure 8.7(e)], two pairs of counter-rotating vortices at S4 in the parent branch appear to wash away the counter flow (red) in the peripheral region toward the bifurcation plane. Likewise, a pair of counter-rotating vortices at S12.5 in the child branch at end inspiration *t/T* = 0.47 [Figure 8.7(g)] appear to wash away the counter flow (blue) in the peripheral region toward the upper side of the branch. After flow reversal at *t/T* = 1.03 [Figure 8.7(f)] and 0.53 [Figure 8.7(h)], the axial flow directions are reversed but the secondary flow characteristics remain qualitatively the same. Unlike *Re* = 100, the flow structures at *Re* = 740 in the bifurcation plane at *t/T* = 0.97 and 0.47 (1.03 and 0.53) no longer differ merely by the axial flow direction because primary secondary vortices are formed after bifurcation in the downstream flow, e.g. in the parent branch at end expiration [see S4 in Figures 8.7(e) and 8.7(f)] and in the child branch at end inspiration [see S12.5 in Figures 8.7(g) and 8.7(h)].

8.3.4 Flow in the CT-based airway model

In this section, we compare the CT-based airway cases under three different breathing conditions. They are the normal breathing case (NORM), the high-frequency normal-*Re* case (HFNR), and the high-frequency oscillatory ventilation case (HFOV).

The distributions of their corresponding dimensionless frequency α^2, dimensionless stroke length *L/a*, and *Re* are exhibited in Figure 8.2 (see also Table 8.1). HFNR is much closer to the unsteady regime than the other two cases, and its dimensionless stroke length is close to 7, which is also the average ratio of airway segment length over radius. At peak flow rate, the *Re* of HFOV in the trachea is about 3 times greater than those of NORM and HFNR. Thus, the peak speed of the turbulent laryngeal jet in HFOV is also about 3 times greater than the other two cases. At end expiration and early inspiration at *t/T* = 0.97 and 1.03 (end inspiration and early expiration at *t/T* = 0.47 and 0.53), the color-coded velocity vectors in a vertical plane for the three cases are compared in the left (right) two panels of Figure 8.8. The vertical plane is co-planar with the trachea and the left and right main bronchi. The downward (upward) vertical velocity is marked with the red (blue) color. Figure 8.8(a) shows that counter flow at flow reversal is absent in NORM. For HFNR, the flow condition at the trachea has about twice higher Womersley parameter α than A and B (see Figure 8.2), and an *L/a* value between A and B, and a higher peak *Re* of 1,288 than B with *Re* = 740. As compared with the flow structures in the single-bifurcation model displayed at *t/T* = 0.97 in Figure 8.5(b) (*Re* = 100, point A) and Figure 8.6(b) (*Re* = 740, point B), the counter-flow feature seems to be present, but is irregular due in part to the complex geometry of the realistic airway model and the higher *Re* of the flow, which can yield flow separation and recirculation. At early inspiration *t/T* = 1.03, the inspiratory flow (red) covers a greater extent with the remnant expiratory flow (blue) embedded in the core region of the trachea and the left and right main bronchi. This feature resembles those shown in Figures 8.5(c) and 8.6(c), but exhibiting a patchy appearance. At end inspiration *t/T* = 0.47, the counter-flow feature is also observed. The blue region formed at the outer wall of the bifurcation due to inertia is similar to that of the single-bifurcation case shown in Figure 8.6(f). Similarly, at early expiration *t/T* = 0.53, the remnant inspiratory flow (red) is observed as in Figure 8.6(g), but also has a patchy appearance. For HFOV, due to higher *Re* the flow is characterized by small-scale eddy

motions. For example, at end expiration t/T = 0.97 the inspiratory flow (red) near the bifurcation, which is ahead of the phase, is found in smaller regions than HFNR. This feature is also observed at end inspiration t/T = 0.47. Furthermore, the patches representing the remnant flow in HFNR at early inspiration t/T = 1.03 and early expiration t/T = 0.53 appear to break up into small pieces, obscuring the counter-flow feature if any.

Next we shall examine the flow structures at the bifurcation between generations 2 and 3. The bifurcation located in the dot-dashed box in Figure 8.1(a) is examined. The flow parameters of the parent branch of the bifurcation for the three cases are marked as boxed 2 in Figure 8.2 with their respective colors (see also Table 8.2). The flow condition for NORM is in the convective regime IIIa, being far away from the unsteady regime. The dimensionless frequencies α^2 for HFOV and HFNR are very close to those of A and B used for the bifurcating tube model. HFNR is closer to the unsteady regime I, whereas HFOV almost overlaps with B in Figure 8.2. The major differences between the CT-based-airway case and the single-bifurcation case are two-fold. First, the geometric feature of the CT-based model is more complicated, but realistic, as compared with the tubal model. Second, the upstream and downstream flow structures entering the CT-based bifurcation are computed in a whole airway setting that minimizes the effects of boundary conditions. Figure 8.9 shows the flow structures in a bifurcation plane at end expiration and early inspiration t/T = 0.97 and 1.03. Using the single-bifurcation case [Figures 8.6(b) and 8.6(c)] as a reference, Figures 8.9(a) and 8.9(b) for NORM do not reveal any counter-flow feature. For HFNR, the counter-flow feature is observed. The expiratory fluid stream (blue) at t/T = 0.97 in Figure 8.9(c) is particularly clear, resembling Figure 8.6(b). At early inspiration [Figure 8.9(d)], the remnant expiratory flow is diminishing, primarily remaining in the core region of the branches. For HFOV, the counter-flow feature is not discernible as exhibited in Figures 8.9(e) and 8.9(f), although its flow parameters are essentially the same as at B. The above features at t/T =

0.97 and 1.03 for the three cases are also observed at end inspiration and early expiration t/T = 0.47 and 0.53. Figures 8.10(a) and 8.10(b), for example, show that the flow conditions for NORM do not produce counter flow. For HFNR, the counter-flow feature is particularly evident in the child branches as shown in Figures 8.10(c) and 8.10(d) [cf. Figures 8.6(f) and 8.6(g)], despite the presence of small vortices in the parent branch. For HFOV, Figures 8.10(e) and 8.10(f) show that the flow is more disorganized, comprising several vortices so that the counter-flow feature is not discernible.

Lastly, we examine the flow structures at the bifurcation between generations 3 and 4. The bifurcation in the dashed box in Figure 8.1(a) is investigated. The flow parameters of the parent branch of the bifurcation are marked as boxed 3 in Figure 8.2 (see also Table 8.2). For NORM, it is in the convective regime IIIa. For HFOV and HFNR, their dimensionless frequencies fall on the dashed line that is extended from the demarcation line between the unsteady and viscous regimes. The dashed line further classifies the convective regime into two sub-regimes IIIa (quasi-steady) and IIIb (unsteady). Figure 8.11 shows the flow structures for the three cases at end expiration and early inspiration. The counter-flow feature is completely absent in NORM and HFOV, and is either nearly diminishing or absent in HFNR. Similarly, at end inspiration and early expiration the counter-flow feature is not observed in these cases (not shown).

8.3.5 Stretch rate analysis

For illustration of the correlation between flow structures and stretch rates, we first consider the time history of the stretching and orientation of a passive line tracer consisting of uniformly distributed passive Lagrangian particles in the straight-tube case at Re = 740 that yields the Womersley solution. The particles are initially aligned along a line in the radial direction below the interface between two opposing flows at flow reversal as denoted by red (number 1) in Figure 8.12(a). Figure 8.12(a) shows the locations and shapes of the tracer at t/T = 0, 0.25, 0.6, and 0.75, corresponding to

beginning inspiration, peak inspiration, early expiration and peak expiration, respectively. The Womersley velocity profiles at these times are also exhibited to show the corresponding local velocity gradient. At inspiration, the tracer is stretched, yielding a positive slope by the positive velocity gradient of the flow. At early expiration t/T = 0.6, the flow creates an L-shaped tracer with a negative-slope upper part and a positive-slope lower part. At peak expiration, the slope of the tracer becomes negative. At the end of one cycle, the tracer returns to its original location due to the reversible kinematics of the linear Womersley solution shown in Figure 8.4(a).

Next, we apply the stretch rate analysis to a particle released in the middle of the above tracer. The time histories of the three orientation components m_i of a line element calculated by equation (8.1) are shown in Figure 8.12(b). The initial vector (m_1, m_2, m_3) = (0, 1, 0) is in parallel to the radial direction of the tube. As time progresses, m_3 remains unchanged in the absence of shear. The line element experiences rotation with increasing m_1 and decreasing m_2 due to positive shear of the flow before reaching peak inspiration at t/T = 0.25 as in Figure 8.12(a). At expiration t/T = 0.6, the orientation of the line element is first reversed back to (0, 1, 0), and then m_1 is changed to -1 due to negative shear in response to the change of flow direction. At the end of one cycle, the line element recovers its initial orientation. In one cycle the line element experiences stretching in opposite directions and is restored to its initial orientation twice. The instantaneous (s_I) and time-averaged (s_T) stretch rates for this line element are displayed in Figure 8.12(c), and the enlarged view of s_T is plotted in Figure 8.12(b). The time history of the instantaneous stretch rate shows alternating positive and negative stretches twice, corresponding to the twice-stretched tracer illustrated above. As a result, at the end of one cycle, the time-averaged stretch rate s_T is zero, e.g. t/T = 1 and 2, signifying a reversible process. The relatively high s_T at initial time is due to small time t in the denominator of equation (8.3). The stretch rate analysis shows that there is no net convective mixing at

the end of one cycle in spite of the existence of counter flow and phase lag in the straight-tube system that sustains the Womersley solution.

For the single-bifurcation cases shown in Figures 8.5 and 8.6 for *Re* = 100 and 740, about 1,700 particles are released in the parent branch at a distance of 0.88D and 6.5D from the bifurcation for *Re* = 100 and 740, respectively. The ratio of the particle release distances for *Re* = 100 and 740 is the ratio of the stroke lengths for the two cases so that the spreads of particles with respect to the bifurcation for both cases are dynamically similar. Application of the stretch rate analysis to two cycles of data yields the maximum-instantaneous and time-averaged stretch rates of 13.2 and 1.49 (29.2 and 10.9) s^{-1}, respectively, for *Re* = 100 (740). The stretch rates are no longer zero due to the formation of secondary vortical motions. The ratio of the time-averaged stretch rates for both cases is close to the ratio of *Re*.

For the whole airway cases of HFOV and HFNR, the stretch rates based on about 1,700 particles are presented. The particle release distances of 5.27D and 1.86D relative to the carina are marked by A and B in Figure 8.1(a) for HFOV and HFNR, respectively. The ratio of the release distances is the same as the ratio of the stroke lengths for dynamic similarity of particles reaching the carina. The NORM case is not compared here because it has a much longer dimensionless stroke length (e.g. 184 in the trachea) than HFOV and HFNR (17.3 and 6.1 in the trachea) so that the majority of particles released in NORM would be advected out of the model by the end of a cycle, making the comparison difficult if not impossible. Figure 8.13 shows the instantaneous and time-averaged stretch rates for HFOV and HFNR. The instantaneous stretch rates have local minima near flow reversal at $t/T \sim 0.5$, 1, 1.5 and 2.0 for both cases, suggesting that the flow structures at flow reversal are less effective in mixing as compared with those at higher flow rates. The time-averaged stretch rates s_T at the end of two cycles are 24.5 and 81.4 s^{-1} for HFNR and HFOV, respectively. The s_T ratio between HFOV and HFNR is 3.3, which is slightly greater than the *Re* ratio of 2.8. It is noted that ~50% of particles released in HFOV are

advected out of the airway model as compared with ~5% in HFNR. The ~1,700 particles used in calculation of the above stretch rates are those remaining active inside the airway models after two breathing cycles. The number of active particles drops with time. Those being advected out of the model tend to experience higher stretch rates because of their association with high-speed fluid stream (thus reaching the exits faster). By using active particles at any time instant to compute the stretch rates in HFOV (HFNR), we obtain the thin lines in Figure 8.13(b), yielding a time-averaged stretch rate of 107 (24.6) s^{-1}. The s_T ratio becomes 4.3.

According to the Womersley solution and the single-bifurcation case, the counter-flow phenomenon is most evident between ±0.06 around t/T = 0.5 and 1. With the short time duration of 0.12t/T centered on end expiration and inspiration, we can quantify the contribution of flow structures at flow reversal, such as secondary vortices and counter flow, to mixing under different frequencies and Re along with the influence of the turbulent laryngeal jet flow for the cases of NORM, HFNR, and HFOV. About 2,000 particles are released initially in the solid box surrounding the carina in Figure 8.1(a). The particle release site is selected by taking into consideration the long stroke length of NORM. The instantaneous and time-averaged stretch rates for these cases are displayed in Figure 8.14. At end expiration and early inspiration (left panel), the instantaneous stretch rate s_I for NORM behaves quite differently from those of HFNR and HFOV, having a local minimum of nearly zero at around flow reversal t/T ~ 1. Inspection of the flow structures in Figure 8.8(a) shows weak flow activities in NORM at t/T ~ 1. As a consequence, the time-averaged stretch rate s_T for NORM at t/T ~ 1 has a small slope. The instantaneous stretch rates for HFNR and HFOV are not zero, being attributed to the irregular counter-flow structures shown in Figures 8.8(b) and 8.8(c). The oscillatory behavior exhibited in the instantaneous stretch rate s_I of HFOV may be due to the turbulent eddy motions as revealed in Figure 8.8(c). Overall, at t/T ~ 1 the maximum instantaneous stretch rates $s_{I,max}$ for NORM, HFNR, and HFOV are 29, 56 and 145 s^{-1},

respectively, and the time-averaged stretch rates s_T over the period of 0.12t/T centered at t/T=1 are 0.58, 4.9 and 9.5 s^{-1}, respectively. The $s_{I,max}$ ratio is ~1:1.9:5, and the s_T ratio is ~1:8.4:16.4.

Next we shall consider the stretch rates at end inspiration and early expiration t/T ~ 1.5. The distributions of the stretch rates for the three cases are qualitatively similar to those at t/T ~ 1. Overall, the stretch rates at t/T ~ 1.5 are smaller than those at t/T ~ 1. The maximum instantaneous stretch rates $s_{I,max}$ for NORM, HFNR, and HFOV are 26, 36 and 138 s^{-1}, respectively, and the time-averaged stretch rates s_T are 0.46, 2.4 and 6.7 s^{-1}, respectively. The $s_{I,max}$ ratio is ~1:1.4:5.3, and the s_T ratio is ~1:5.2:14.6. It is noteworthy that in the single-bifurcation model shown in Figure 7, at end inspiration t/T ~ 1.5 a pair of secondary vortices is formed in the child branches, while at end expiration t/T ~ 1 two pairs of secondary vortices are formed in the parent branch. More vortices formed at end expiration yield greater stretch rates and more effective convective mixing.

8.4 Discussion

8.4.1 Counter Flow

Heraty *et al.* (2008) investigated the spatial flow structures under HFOV in both idealized and anatomically-realistic bifurcation models using PIV. One of the important findings of their study was that the inspiratory and expiratory fluid streams co-exist (known as coaxial counter flow) in the airways for significant periods around flow reversal for both idealized and realistic models. Shear layers were formed between the opposing fluid streams, and persisted for slightly longer in the wider left child branch than in the right child branch. Vortical structures were resulted from the roll-up of shear layers in both models. More specifically, in their Figure 8.3 with Re = 740 and α = 7 (the same flow parameters as point B in Figure 8.2), counter flow and shear layers were found further away from flow reversal at early inspiration t/T = 0.057 and 0.115, at end inspiration t/T = 0.452, and at early expiration t/T = 0.623.

Contrary to their work, the current single-bifurcation case with the same flow parameters (Re = 740 and α = 7) shows that these structures are completely absent further away from flow reversal at t/T = 1.06 (or 0.06) and t/T = 0.56 [see Figures 6(d) and 6(h)]. That is, the time period for the existence of counter flow and shear layers around flow reversal reported in Heraty *et al.* (2008) is about twice longer than that of the current study. To investigate the potential effect of an imposed velocity profile on the counter-flow period, a uniform velocity profile (to mimic the blunt feature of the Womersley velocity profile) with the same sinusoidal flow waveform as before is imposed in the single-bifurcation model. The result shows that the uniform profile rapidly adjusts to the Womersley profile in the parent branch. To investigate the effect of the shape of breathing flow waveform, we impose a triangular waveform that increases the flow rate linearly from zero to the same peak inspiratory flow rate as the sinusoidal waveform, reduces it linearly to zero at end inspiration and then repeats it for the expiratory phase. The triangular waveform has the same frequency as the sinusoidal waveform, but has ~50% lower flow rate at $t/T \sim \pm 0.06$ and ± 0.56 than the sinusoidal one. The result shows that the flow characteristics are qualitatively the same as before, but having a smaller velocity magnitude. Lastly, we design a case with a sinusoidal waveform only for the inspiratory phase. After end inspiration t/T = 0.5 when the flow rate is zero, the inlet boundary velocity is set to zero, maintaining a zero flow rate for $t/T > 0.5$. The results show that the counter-flow structures similar to Figures 8.6(f) and 8.7(g) persist within the time window of t/T = 0.5 - 1.0, but with decaying velocity magnitude and shrinking thickness of the inspiratory flow region. At t/T = 0.5, the thickness of the inspiratory flow in the parent branch is approximately constant, similar to the red region in Figure 8.7(g). With increasing time, the thickness of the red zone at a distance of ~0.5D to the bifurcation point shrinks at a rate faster than other regions. At the center point of that location, the velocity magnitudes at t/T = (0.5, 0.6, 0.7, 0.8, 0.9, 1.0) are (0.47, 0.42, 0.32, 0.19, 0.11, 0.07), and the thicknesses normalized by the parent-branch diameter are (0.65, 0.42, 0.26,

0.21, 0.21, 0.23). Thus, the velocity magnitude drops by 32% (85%) from t/T = 0.5 to 0.7 (1.0). The pattern of the narrowing inspiratory flow ahead of the bifurcation resembles that shown in Figure 8.3 at t/T = 0.623 of Heraty *et al*. (2008). Thus, the "significant" periods around flow reversal reported in their observations can only be reproduced in the current study with a significantly low flow rate over a non-negligible period around flow reversal.

While the flow structures at flow reversal found in the current single-bifurcation model bear some resemblances to those observed by Heraty *et al*. (2008) they exhibit differences as well. For example, we do not observe the roll-up of shear layers due to shear instability and the subsequent vortices formed at the interface between opposing fluid streams at flow reversal under the same flow condition of Re = 740. The only vortical structures observed in the current single-bifurcation model are the secondary rotational motions, namely Dean vortices, due to centrifugal instability associated with the curvature of the bifurcation (Choi *et al.* 2009, Saric 1994) At end expiration t/T = 0.97 and early inspiration t/T = 1.03 two pairs of strong counter-rotating vortices are formed in the parent branch [see Figures 8.7(e) and 8.7(f)], whereas at end inspiration t/T = 0.47 and early expiration t/T = 0.53 a pair of counter-rotating vortices are formed in the child branch [see Figures 8.7(g) and 8.7(h)]. The primary difference between these vortices (found at flow reversal) and those found in a typical breathing condition (evident at peak flow rate rather than at flow reversal) is the spiral pattern of the current vortices that exhibit alternating positive and negative axial velocities, as indicated by the blue and red colors in the figure, along the spiral stream-traces of the vortices.

The branching angle and the diameter of the airways shall also affect the counter-flow structures. Heraty *et al.* (2008) reported the persistence of quasi-axisymmetric counter flow and shear layers to a greater extent of t/T = 0.115 at early inspiration and in the "wider" left child branch of the realistic model as shown in their Figure 8.3. In contrast, in the current study Figure 8.7(f) shows that at t/T = 1.03 (or 0.03) the counter

flow exists in the child branch, but is skewed toward the inner wall of the bifurcation. As illustrated in the straight-tube and single-bifurcation cases, deviation from axisymmetric counter flow to skewed counter flow is due to the inertia effect augmented in the flow through a curved tube. A close inspection of their idealized and realistic single-bifurcation models shows two major geometric differences between them. Both geometries features happen to yield the same effect of sustaining axisymmetric counter flow. The two features are the ratio of child-branch diameter to parent-branch diameter and the angle between the two child branches. In their idealized model the ratio is ~0.84 and the angle is ~63^{o}, whereas in their realistic model the ratio is ~0.68 (0.64) for the left (right) child branch and the angle is 44^{o}. In the current single-bifurcation model [Figure 8.3(a)], the ratio is 0.7 and the angle is 70^{o}, which fall within the ranges of the CT-based airways shown in Figure 8.1 with an average ratio of 0.75 and an average angle of 70^{o}. Their models have either a large diameter ratio (thus, yielding a smaller *Re* in the child branch) or a small angle (thus, a smaller curvature). Both reduce the effect of inertia, resulting in more apparent Womersley-like flow features. It is noted that their realistic model is based on a cadaver, while ours is based on in-vivo imaging.

8.4.2 Convective Mixing

Convective mixing is quantified by instantaneous and time-averaged stretch rates. Lagrangian particles act like micro-sensors that are advected along with the flow and measure the degree of stretching by local flow structures. Coaxial counter flow alone (and associate shear layers) does not contribute to convective mixing as demonstrated in Figure 8.12 because the Womersley solution is a linear solution such that passive tracers are reversed back to their original states at the end of one cycle or multiple cycles. With the presence of a bifurcation, at low *Re* = 100 coaxial counter flows are observed in both parent and child branches, and secondary vortices are present but weak, contributing little to mixing. Effective mixing takes place at *Re* = 740 in the single-bifurcation model when

strong secondary vortices are induced. The flow becomes irreversible in that strong vortices are formed in the “parent” branch at end expiration and early inspiration, whereas they are formed in the “child” branch at end inspiration and early expiration. Unlike the Womersley solution where the velocity profiles at t/T are mirror images of those at $t/T + 0.5$ [Figure 8.4(a)] and thus they are reversible, secondary vortices at t/T are no longer reverse processes of those at $t/T + 0.5$ due to inertia. Besides, regardless of axial flow direction, vortices on inspiration rotate in the same direction as those on expiration, which depends on the curvature of the bifurcation, contributing to irreversibility and mixing as well.

For the CT-based airway model, three breathing conditions are considered. They are the normal breathing case NORM, the high frequency normal Re case HFNR and the high frequency oscillatory ventilation case HFOV. Although HFNR is clinically impractical, it facilitates the investigation of the respective effects of unsteadiness (oscillation) and convection (inertia). Due to the long stroke length in NORM, we first compare the stretch rates for HFNR and HFOV for two cycles and then compare the stretch rates for the three cases in the vicinity of flow reversal. The results show that flow structures at flow reversal are not as effective as those at peak flow rate in mixing, but they contribute non-negligibly (~20%) to the total of time-averaged stretch rates in both HFNR and HFOV cases (based on the division that the flow structures within ± 0.06 around $t/T = 0.5$ and 1 are regarded as counter-flow related structures). A comparison of time-averaged stretch rates at the end of two cycles shows that mixing in HFOV is about 3-4 times more effective than HFNR, which is slightly greater than the ratio of Re for both cases.

Considering the flow structures at flow reversal near the first bifurcation within the time duration of $\pm 0.06t/T$, the stretch rate analysis shows that an increase in frequency by 30 fold increases the peak instantaneous stretch rate (time-averaged stretch rate) by 1.9 (8.4) fold, whereas an increase in Re by 3 fold increases the peak

instantaneous stretch rate (time-averaged stretch rate) by 2.6 (2) fold. Contrary to HFNR and HFOV, the instantaneous stretch rate at flow reversal in NORM is nearly zero and the time-averaged stretch rate is much smaller than HFNR and HFOV. This demonstrates the unsteady features of the high-frequency oscillatory flow at flow reversal that is characterized by the interplay between counter flow, secondary vortices, and turbulence. Nonetheless, according to the flow visualization at small airways (see Figure 8.11) and the flow regime (see Figure 8.2), these unsteady flow features are only evident and significant in convective mixing up to the bifurcations between the 3^{rd} and 4^{th} generations of the airways.

8.5 Summary

In this chapter, high frequency oscillatory flow was studied using CFD in three models with increasing geometrical complexity, including a straight tube, a symmetric single-bifurcation tube model, and a CT-based trachea-bronchial airway model. The focus of the study is placed on the counter-flow phenomenon at flow reversal and its contribution to mixing. While in the straight-tube case the Womersley velocity profiles are produced, in the single-bifurcation case coaxial counter flow is altered by secondary vortices especially at high *Re*, resulting in convective mixing. It is also found that counter flow can sustain over a significant time period when the flow rate is set to zero. For the CT-based airway case, three flow conditions were considered to examine the effects of unsteadiness and inertia. It is found that in the normal breathing case the flow structures at flow reversal contribute little to mixing, whereas in the high frequency oscillatory ventilation case the interplay between counter flow, secondary vortices and turbulence enhances mixing at flow reversal.

Table 8.1 Flow parameters for the three CT-based airway cases.

Case	Period T (s)	Frequency f (Hz)	Peak *Re*	Tidal volume V_T (ml)	Description
NORM	4.8	0.20	1288	500	Normal breathing
HFNR	0.16	6.28	1288	16.58	Same frequency as HFOV and same peak *Re* as NORM
HFOV	0.16	6.28	3656	47	High frequency oscillatory ventilation

Table 8.2 Flow parameters for the two bifurcations in the CT-based airway model.

	L/a	α	α^2	Peak *Re*	Local tidal volume (ml)
Generation	A bifurcation between 2nd-3rd generations enclosed by a dot-dashed box in Figure 1(a)				
NORM	163.4	1.45	2.10	343	73.1
HFNR	5.42	7.96	63.31	343	2.42
HFOV	15.36	7.96	63.31	972	6.87
Generation	A bifurcation between 3rd-4th generations enclosed by a dotted box in Figure 8.1(a)				
NORM	746	0.61	0.37	277	24.8
HFNR	24.7	3.35	11.2	277	0.82
HFOV	70.1	3.35	11.2	785	2.33

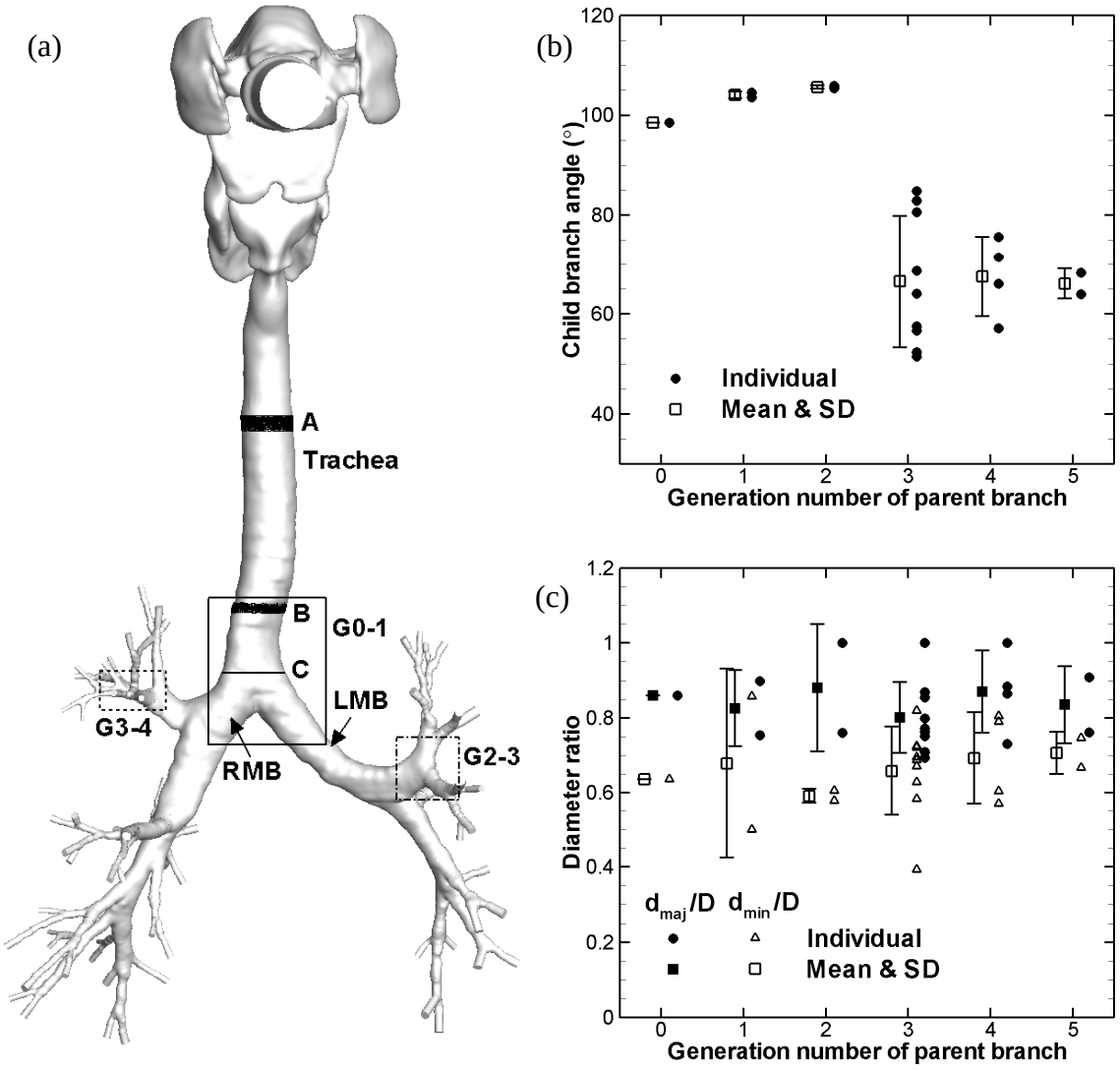

Figure 8.1 Descriptions of the airway model. (a) Front view of the CT-based airways (LMB, left main bronchus; RMB, right main bronchus). Solid, dot-dashed, and dashed boxes indicate the locations of selected bifurcations between G0-1, G2-3, and G3-4 (see Figures 8.8-8.11), respectively. A and B denote particle released locations in HFOV and HFNR, respectively, for stretch rate analysis. C denotes the cross section where the CFD solutions computed on different mesh sizes are compared. (b) The distribution of the angle between child branches (degree) by generation. (c) The distribution of the ratio of the major (minor) child-branch diameter d_{maj} (d_{min}) over the parent-branch diameter D, d_{maj}/D (d_{min}/D), by generation. "Mean" and "SD" are the mean and the standard deviation of the child branch angles or the diameter ratios from individual bifurcations by generation.

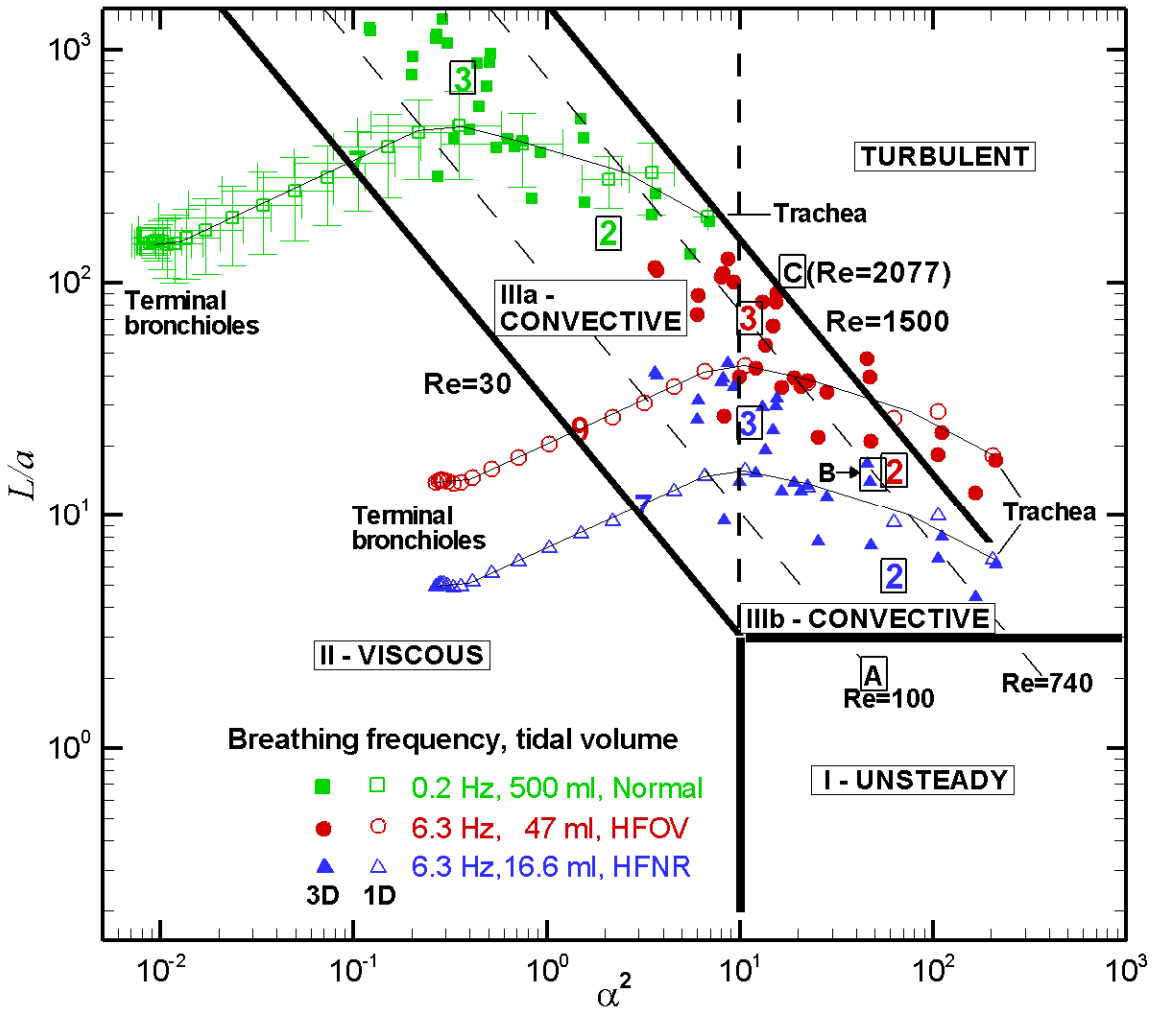

Figure 8.2 Flow regimes of the conducting airway categorized based on a dimensionless frequency α^2 (α is Womersley number) and a dimensionless stroke length L/a. The (I) unsteady, (II) viscous, (IIIa, IIIb) convective flow regimes are classified according to Jan *et al.* (1989).

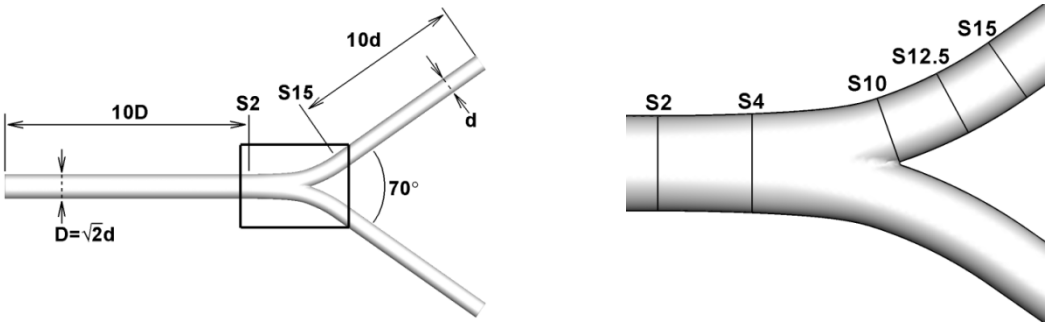

(a) Geometry of the bifurcation model (b) Closeup view of the box in (a)

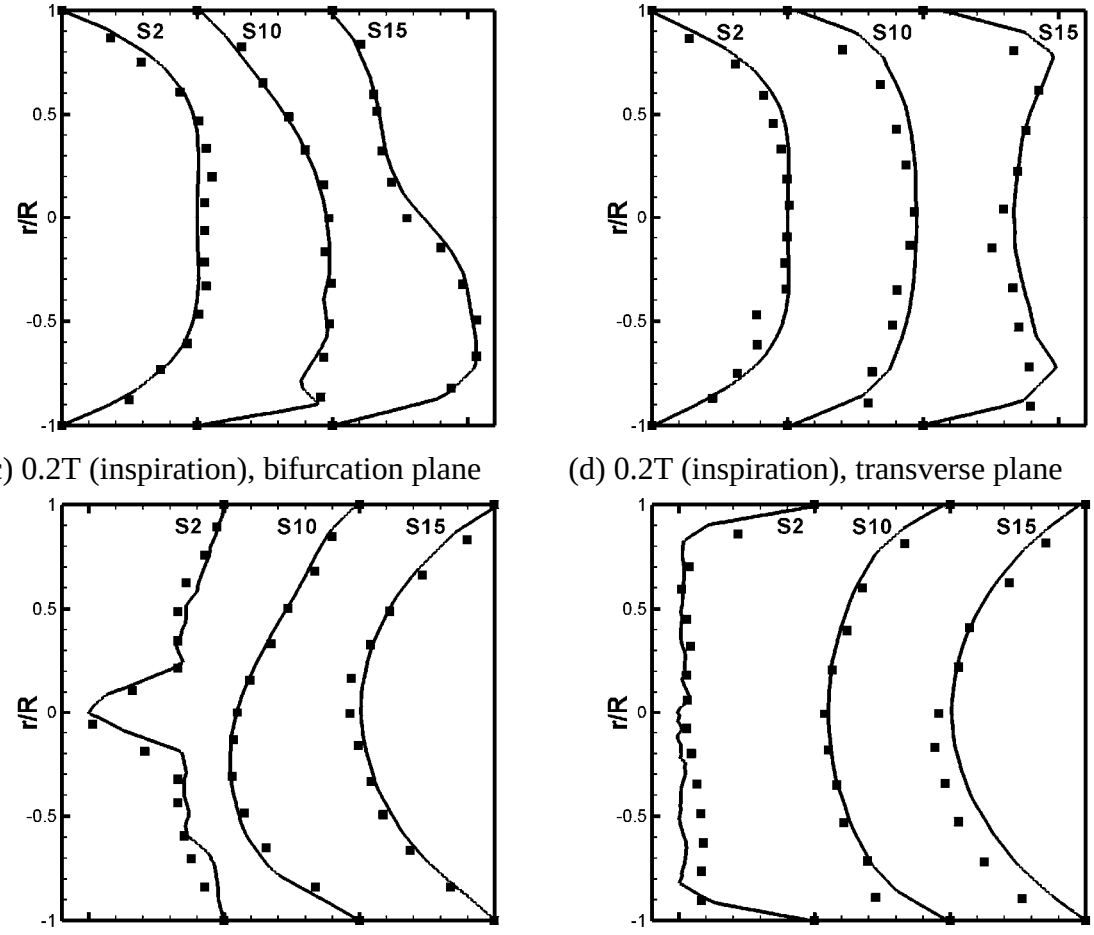

(c) 0.2T (inspiration), bifurcation plane (d) 0.2T (inspiration), transverse plane

(e) 0.7T (expiration), bifurcation plane (f) 0.7T (expiration), transverse plane

Figure 8.3 Comparison of velocity profiles in a single bifurcation with PIV measurements of Lieber and Zhao (1998). Flow parameters correspond to point C in Figure 8.2. Solid lines, current data; square symbols, PIV data. Bifurcation plane, co-planar with the centerlines of the branches; transverse plane, perpendicular to the bifurcation plane and one of the centerlines.

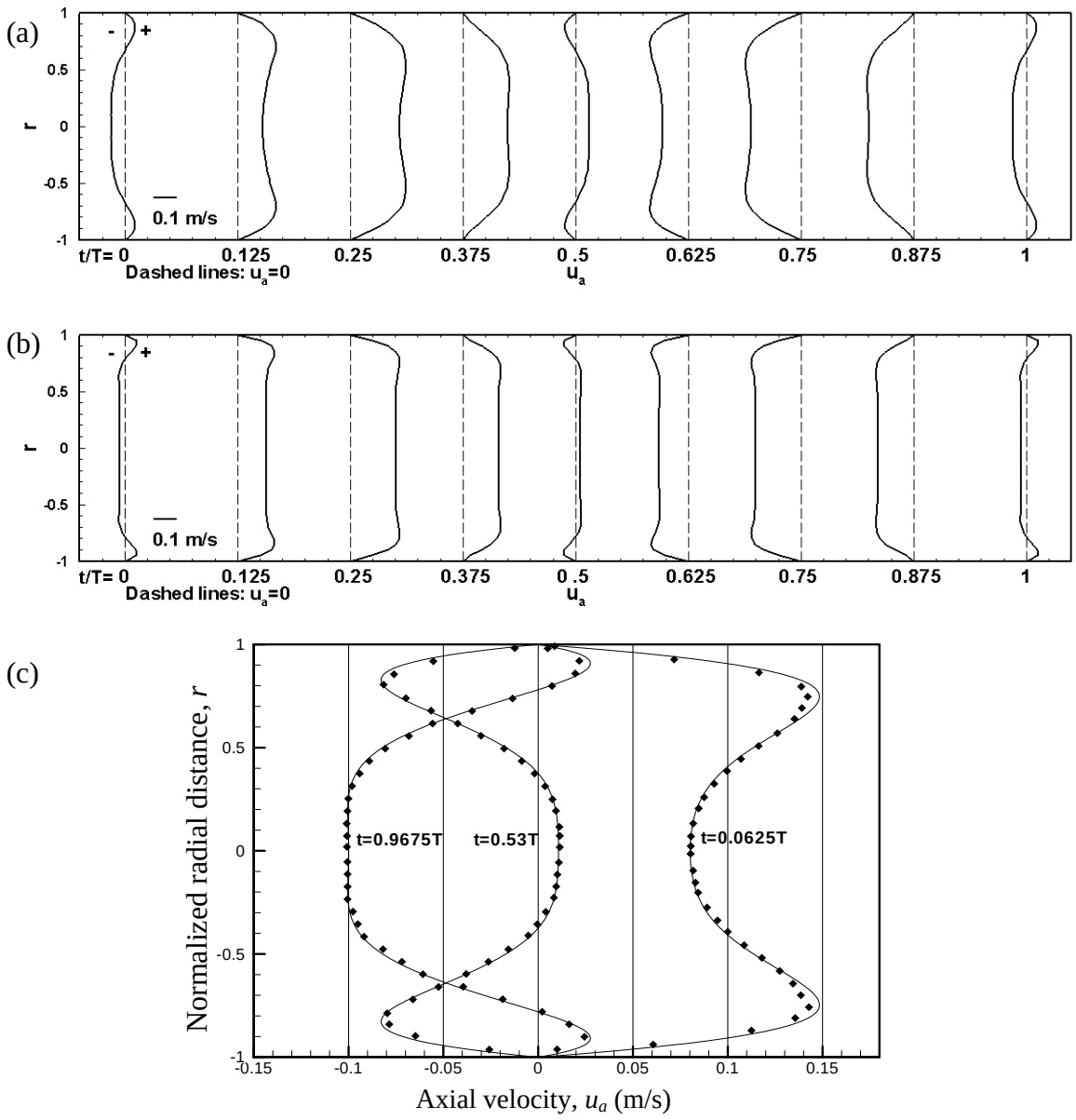

Figure 8.4 Analytical Womersley profiles at selected times during a cycle for the cases with *Re* = 100 and α=: (a) 7 and (b) 14. (c) Comparison of CFD computed profiles (line) in a straight tube with the Womersley solution (symbol) for the case of *Re* = 100 and α=7.

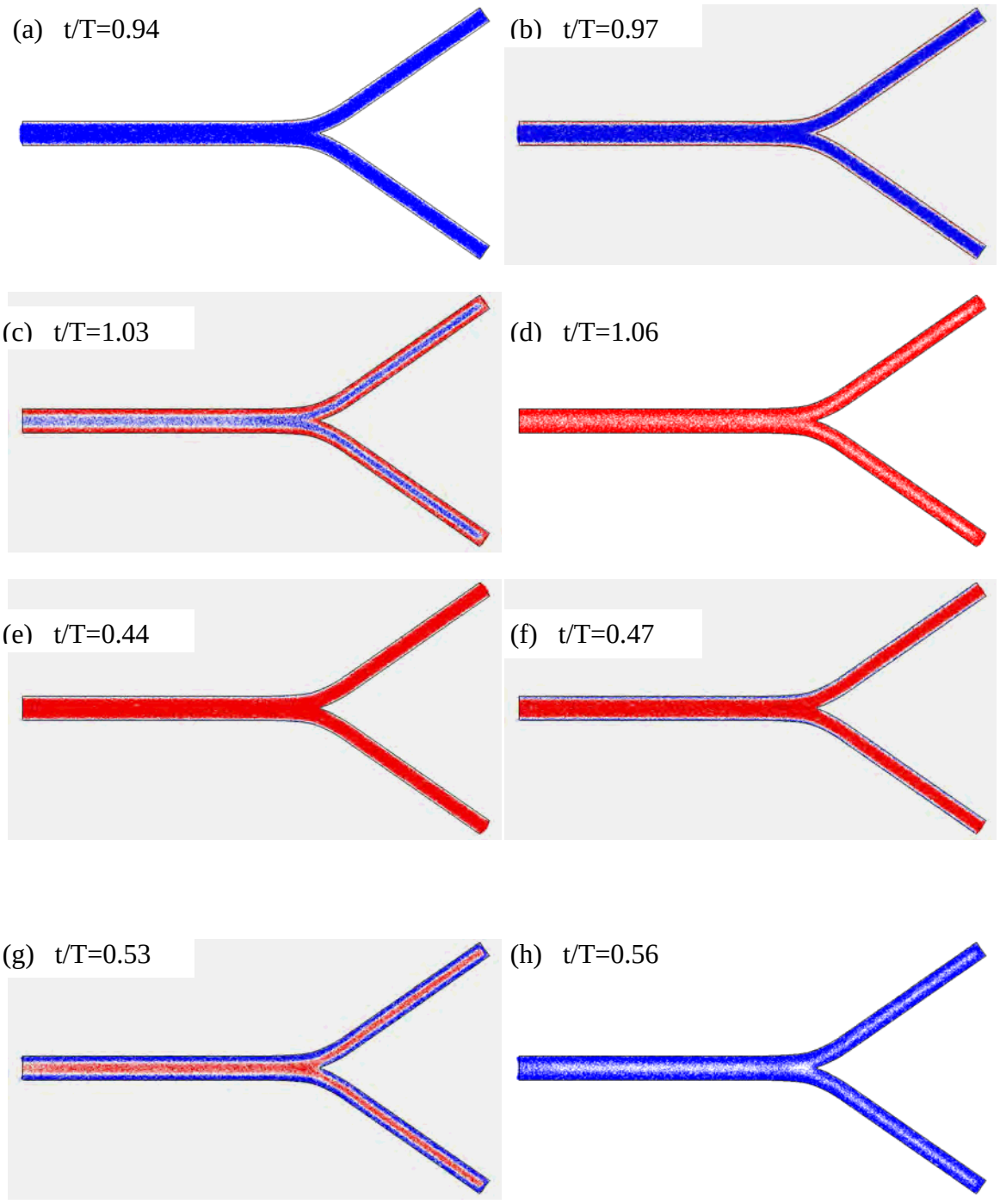

Figure 8.5 A sequence of velocity distributions in the bifurcation plane with Re = 100, L/a = 2, α = 7 (point A in Figure 8.2). Blue, negative axial velocity to the left. Red, positive axial velocity to the right.

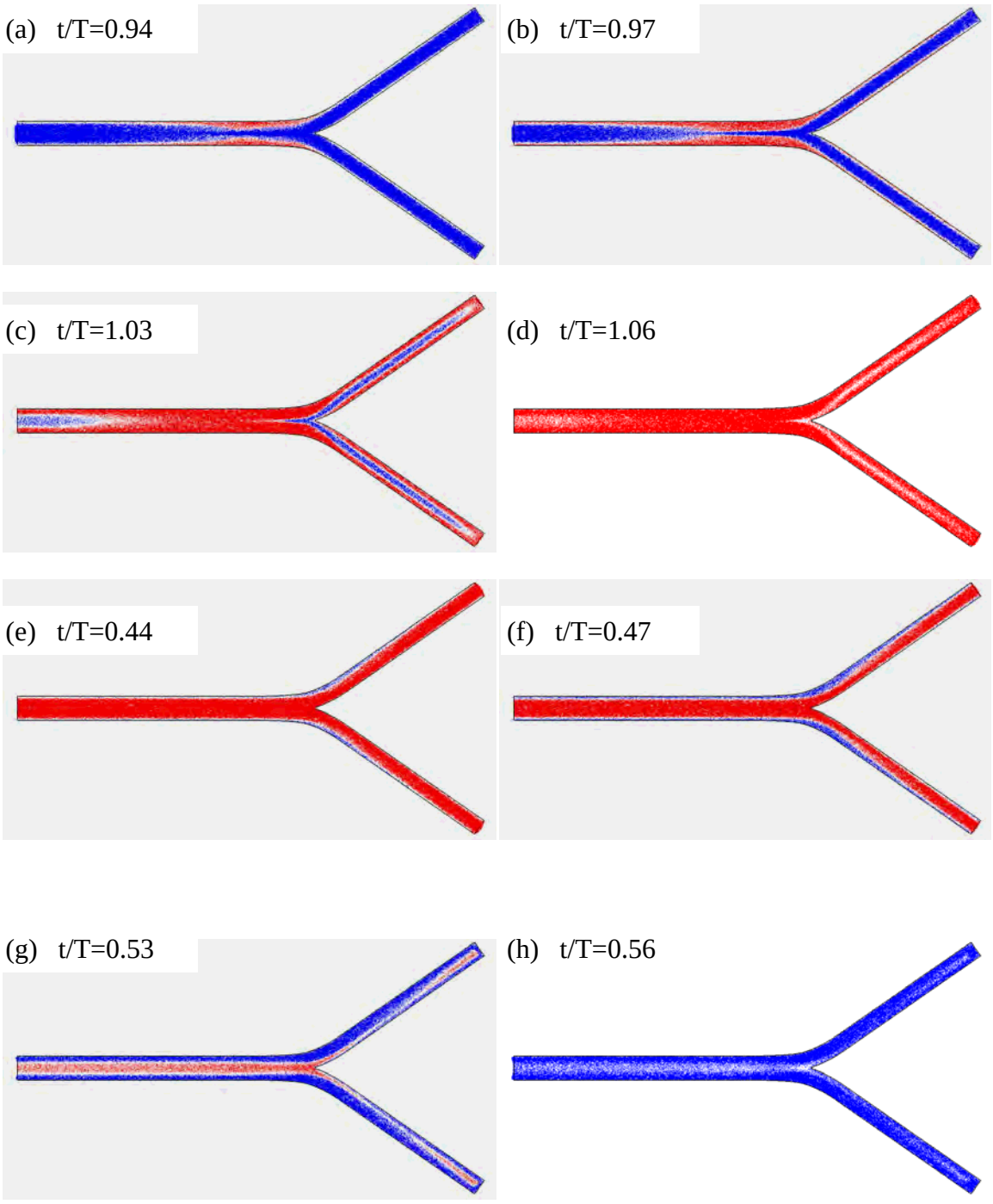

Figure 8.6 A sequence of velocity distributions in the bifurcation plane at Re = 740, L/a = 15, α = 7 (point B in Figure 8.2). Blue, negative axial velocity to the left. Red, positive axial velocity to the right.

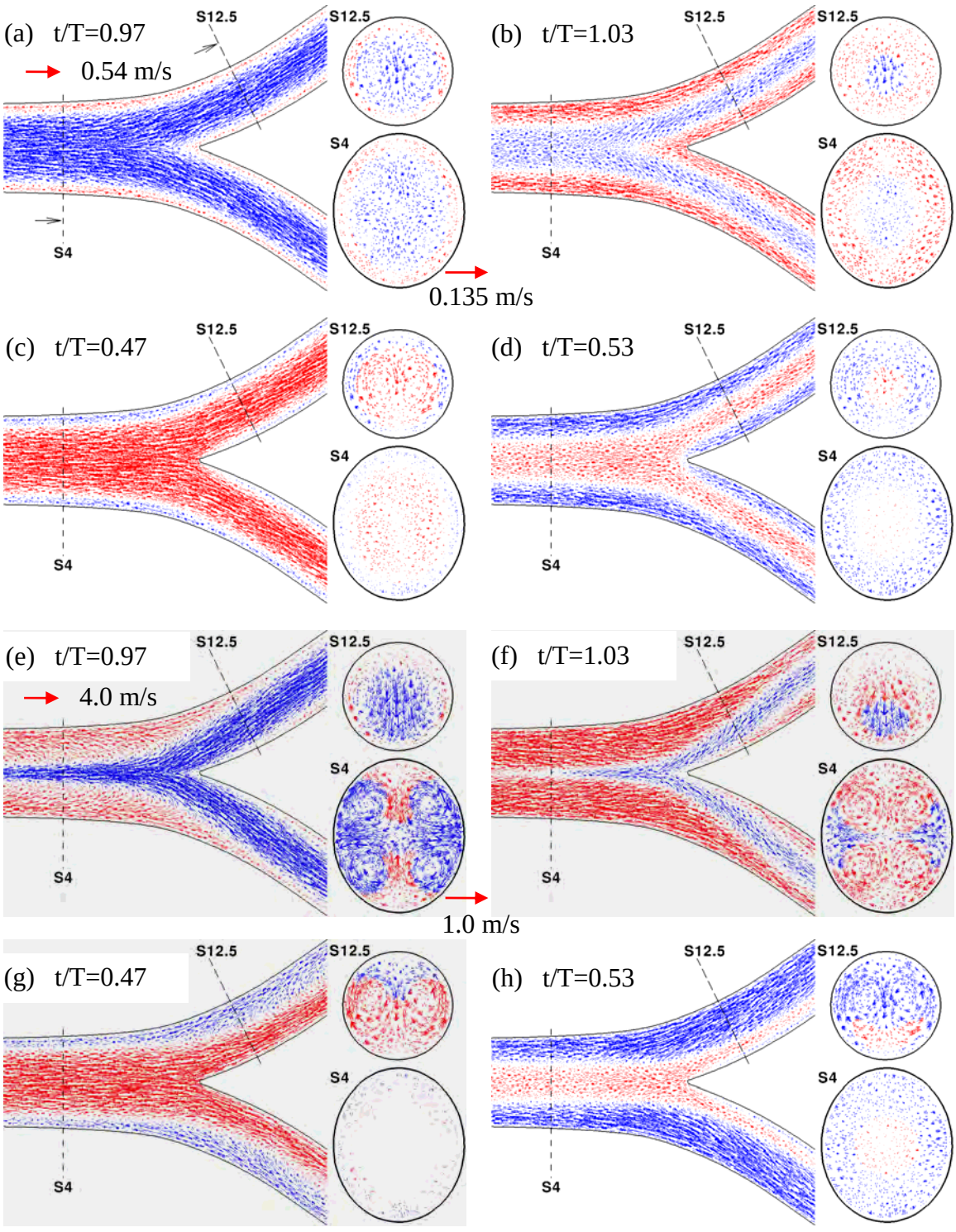

Figure 8.7 Close-up views of velocity vectors in Figures 8.5 and 8.6 and two cross sections before and after flow reversal. (a)-(d), *Re* = 100; (e)-(h), *Re* = 740. Blue, negative axial velocity to the left; red, positive axial velocity to the right.

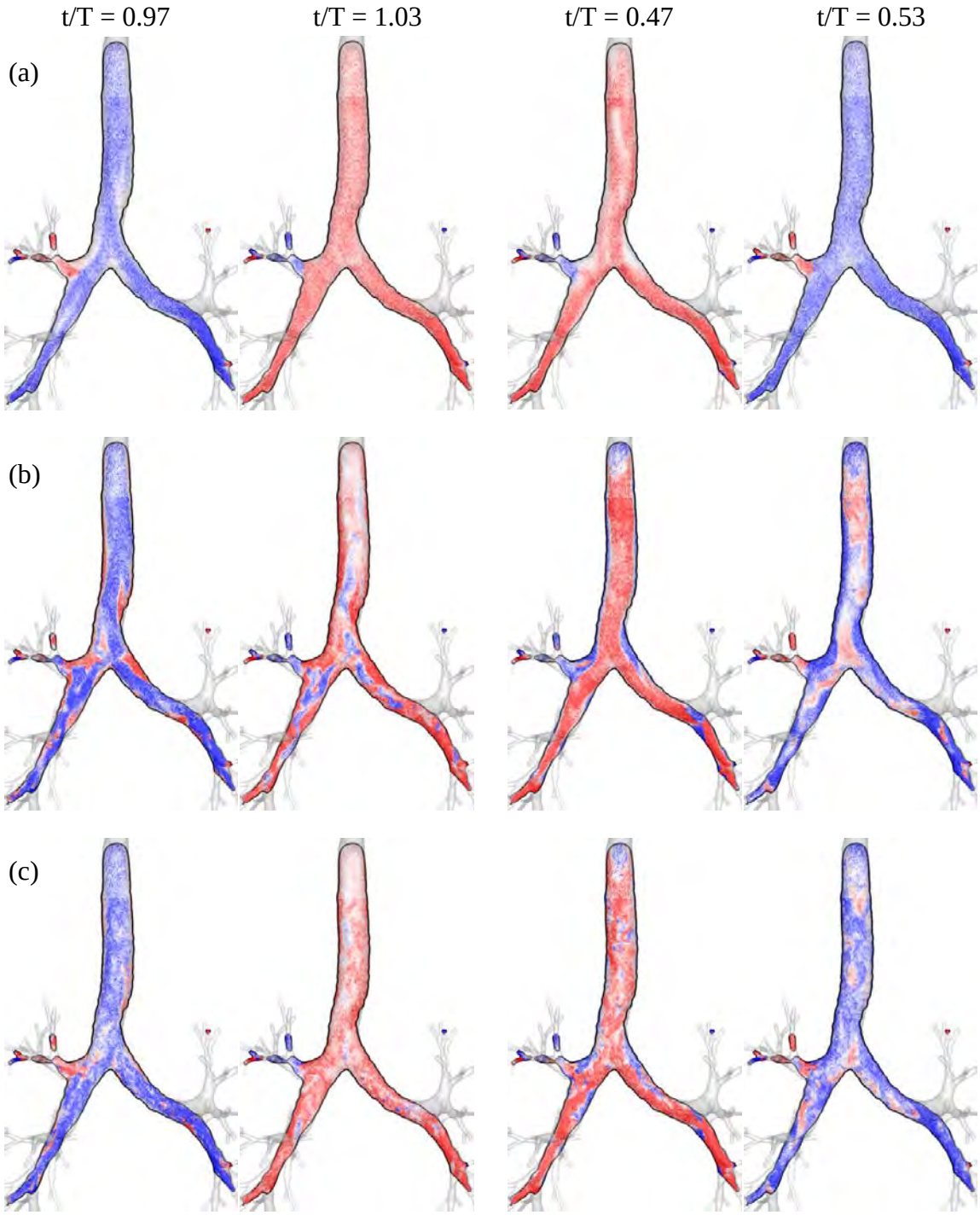

Figure 8.8 Velocity vectors in the bifurcation plane of the trachea and two main bronchi (G0-1) near flow reversal. Red, negative (downward) axial velocity; blue, positive (upward) axial velocity. (a) NORM, (b) HFNR and (c) HFOV. Instantaneous Reynolds numbers at the trachea are 241 for (a) and (b), and 684 for (c).

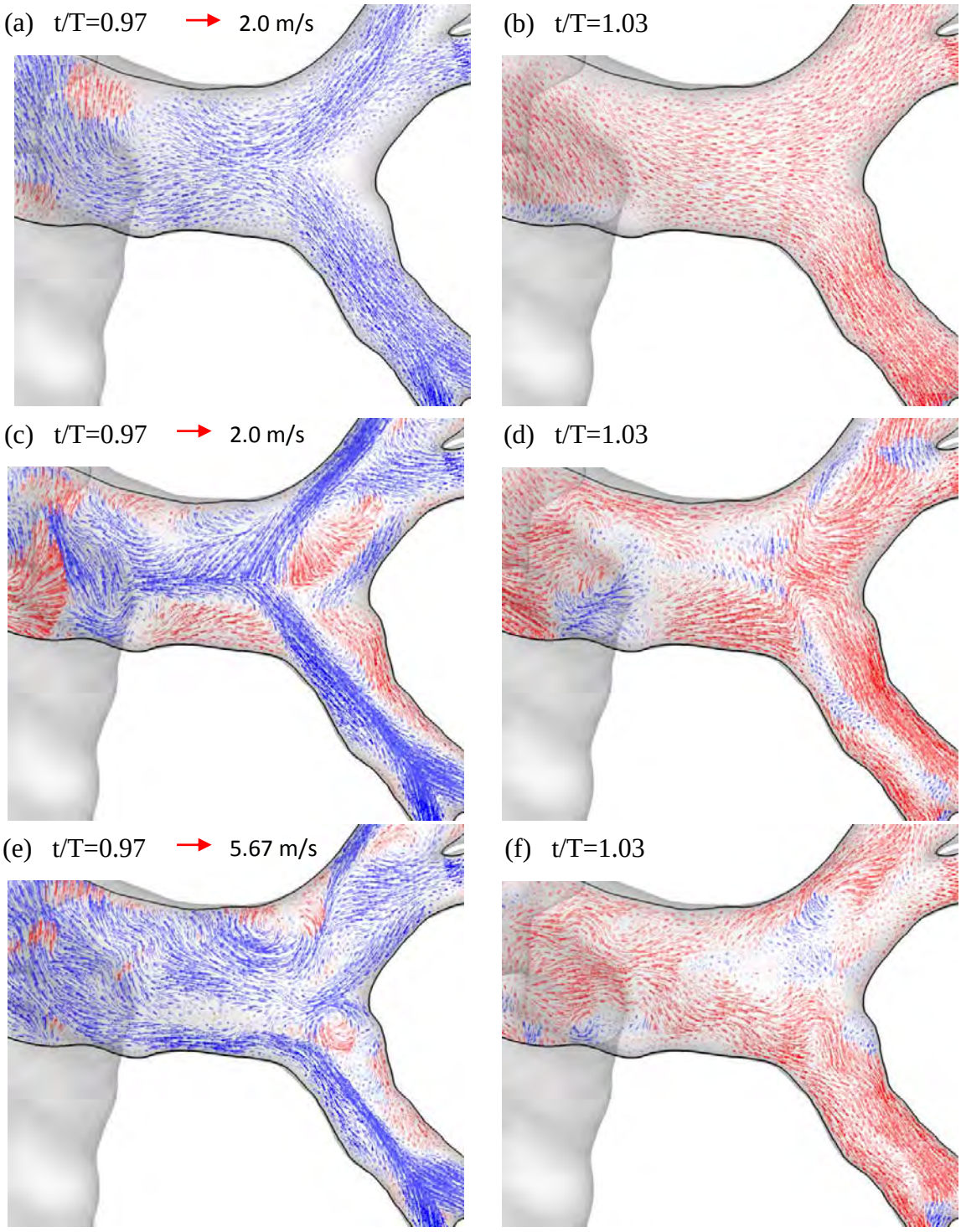

Figure 8.9 Velocity vectors at end expiration and early inspiration in the bifurcation plane at the G2-3 bifurcation. Red (blue), positive (negative) axial velocity in the parent branch to the right (left). (a,b), NORM; (c,d), HFNR; (e,f), HFOV. Instantaneous Reynolds numbers at the parent branch (G2) are 64 for (a-d) and 182 for (e,f).

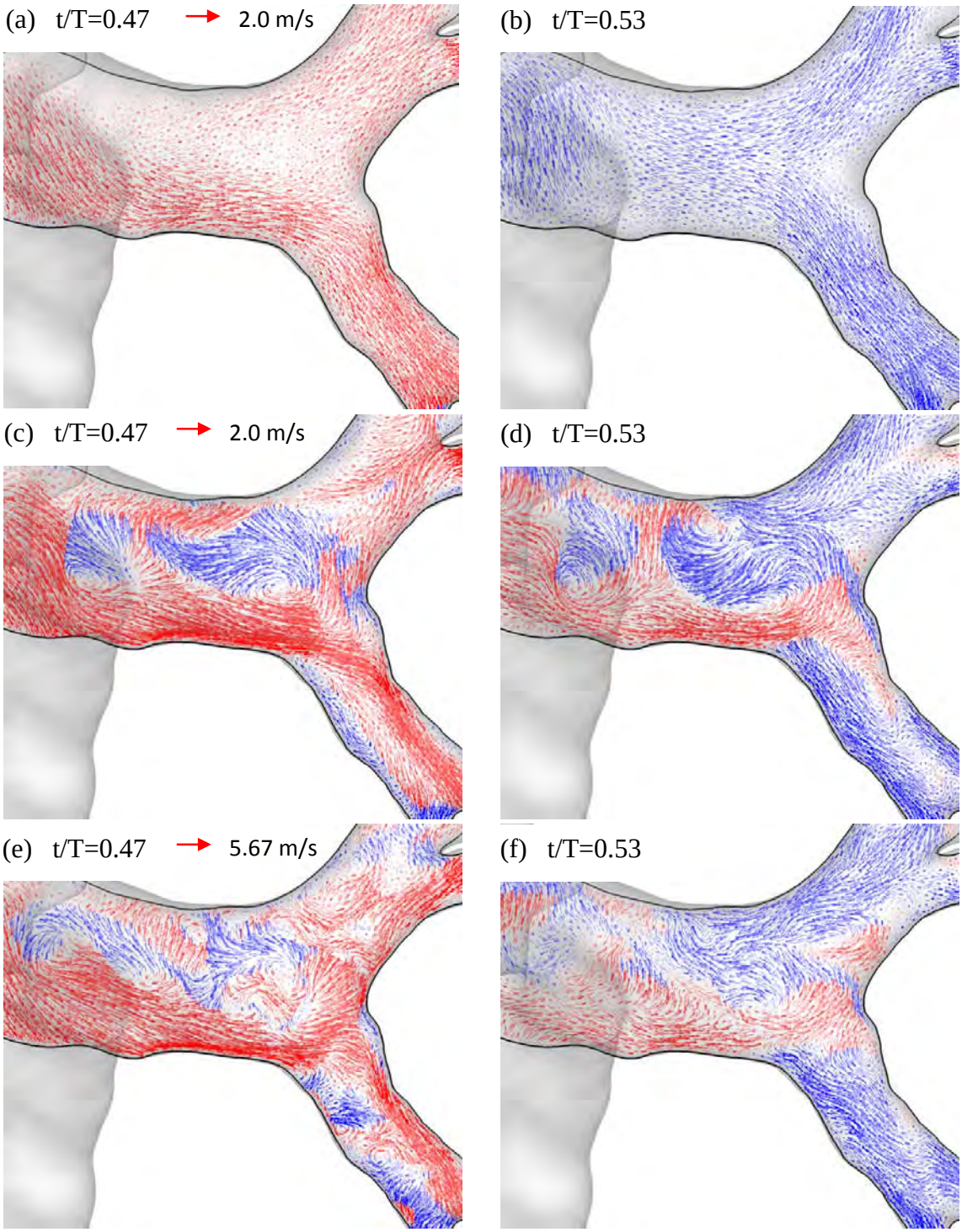

Figure 8.10 Velocity vectors at end inspiration and early expiration in the bifurcation plane at the G2-3 bifurcation. Red (blue), positive (negative) axial velocity in the parent branch to the right (left). (a,b), NORM; (c,d), HFNR; (e,f), HFOV. Instantaneous Reynolds numbers at the parent branch (G2) are 64 for (a-d) and 182 for (e,f).

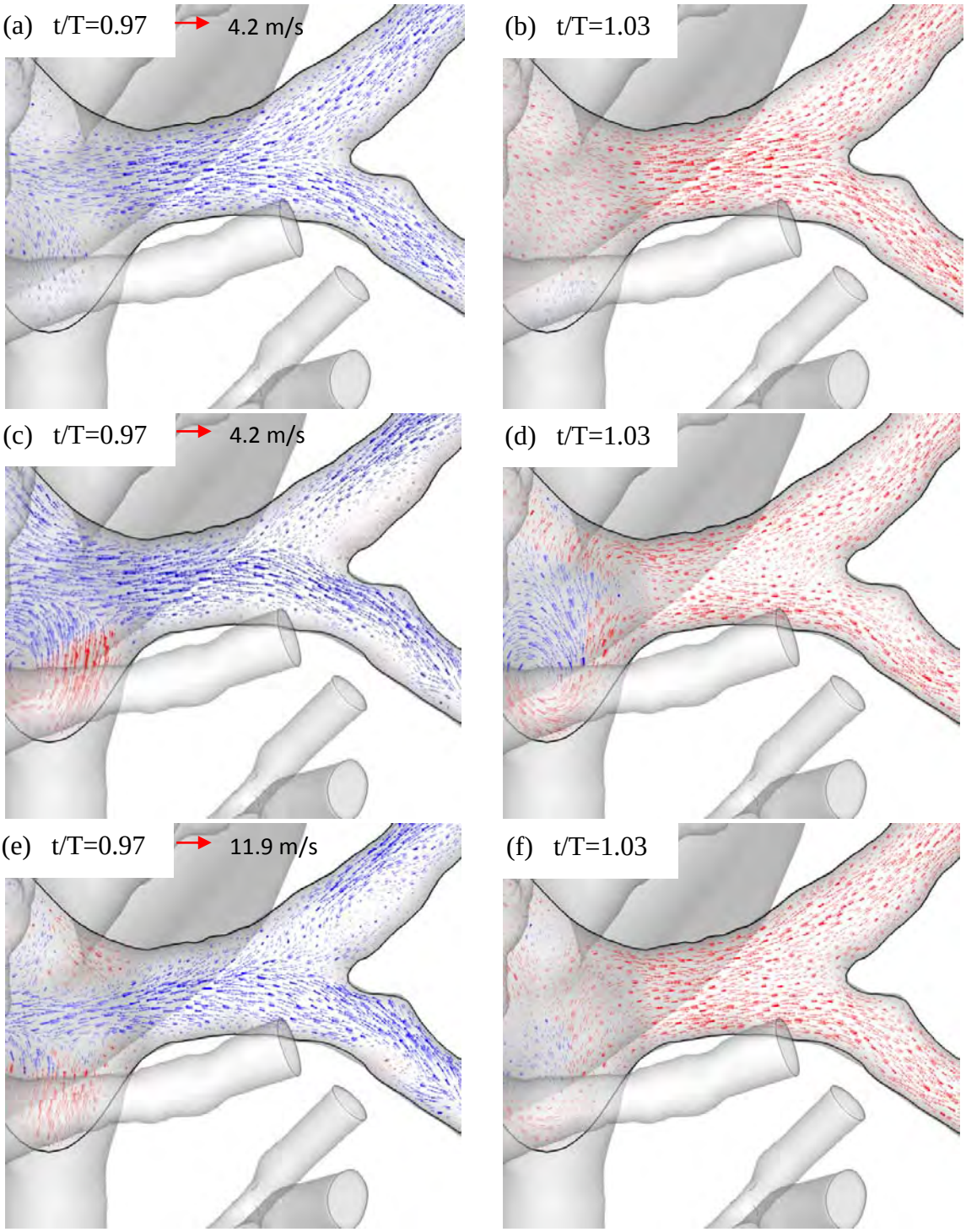

Figure 8.11 Velocity vectors at end expiration and early inspiration in the bifurcation plane at the G3-4 bifurcation. Red (blue), positive (negative) axial velocity in the parent branch to the right (left). (a,b), NORM; (c,d), HFNR; (e,f), HFOV. Instantaneous Reynolds numbers at the parent branch (G3) are 52 for (a-d) and 147 for (e,f).

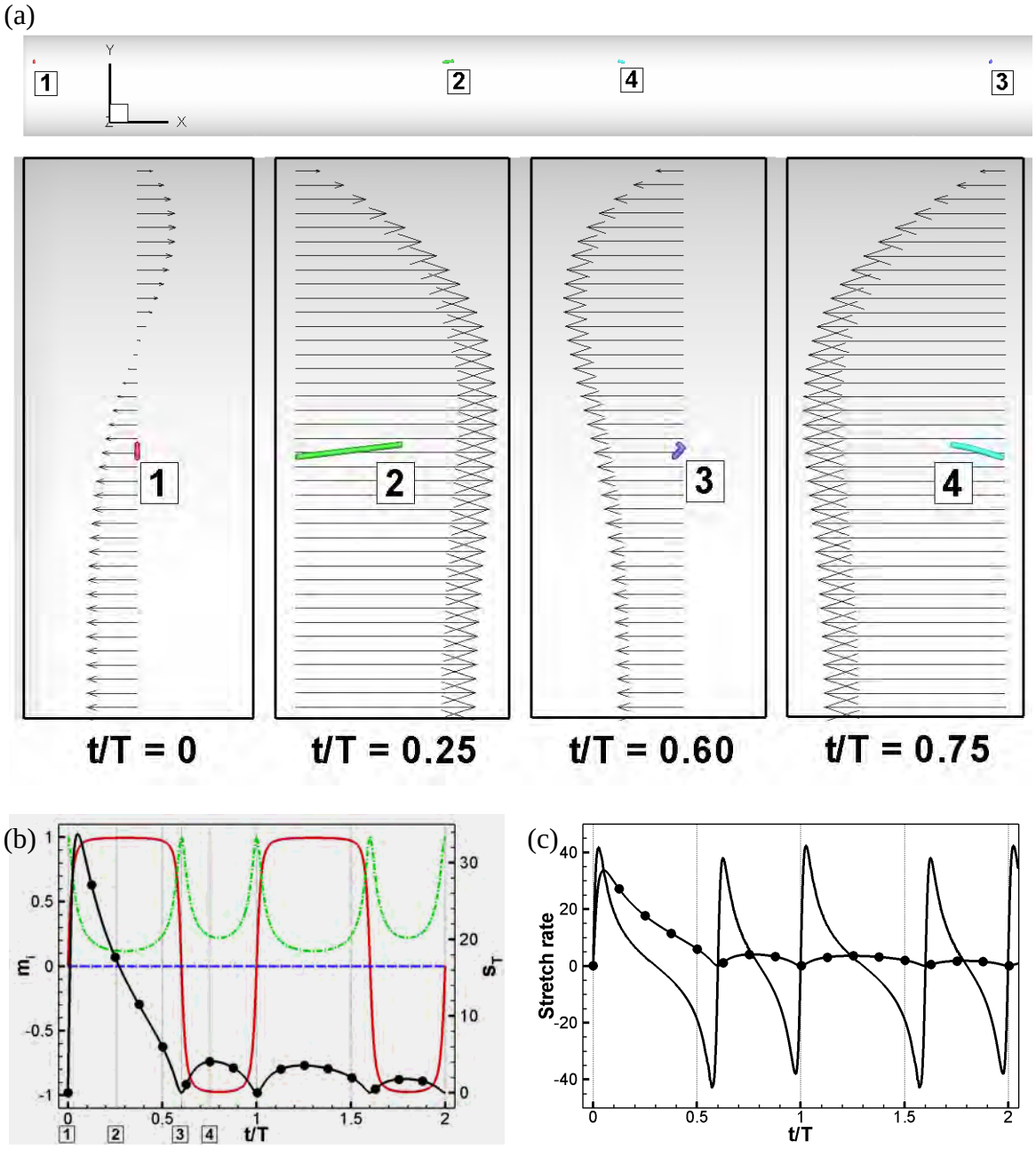

Figure 8.12 Time histories of sample tracers and stretch rates in a straight tube. (a) Deformation of tracers at 4 normalized times t/T = (0, 0.25, 0.60, 0.75) marked by (1, 2, 3, 4). (b) Time histories of orientation vector m_i released at y/a = 0.48 (the middle of the red line at t/T = 0). Subscript i (1, 2, 3) correspond to (x, y, z) in (red, green, blue). The black line with circle is the enlarged view of the s_T curve in (c). (c) Time histories of of the stretch rates of a massless particle released at y/a = 0.48. Line, s_I (instantaneous stretch rate); line with circle, s_T (time-averaged stretch rate).

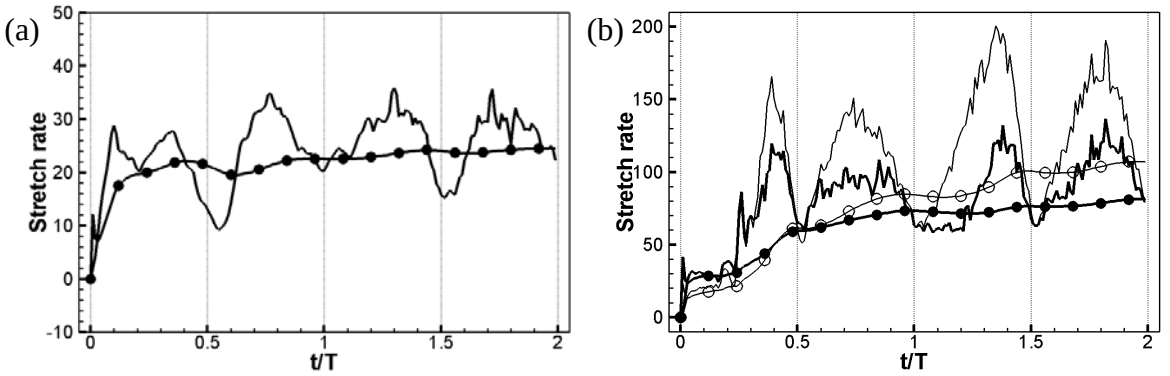

HFNR HFOV

Figure 8.13 Time histories of instantaneous and time-averaged stretch rates, s_I (line) and s_T (line with circle) for the whole airway cases: (a) HFNR and (b) HFOV. In (b), bold lines are based on the particles that remain active inside the model at the end of two cycles, whereas thin lines are based on the particles that are active at instant *t/T*. For (a) the distinction between bold and thin lines are negligible, thus only those based on active particles at the end of two cycles are shown.

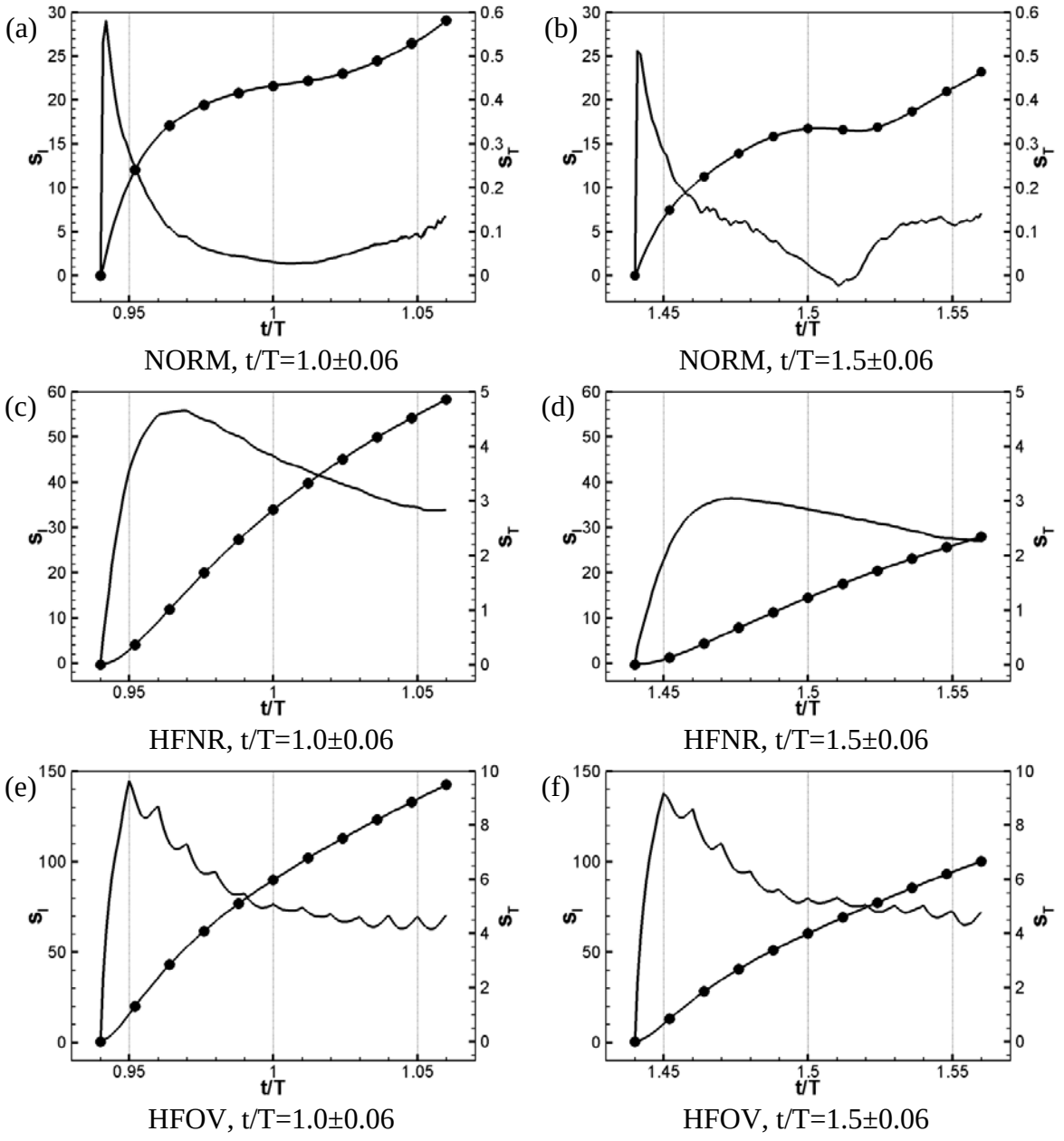

Figure 8.14 Time histories of instantaneous (s_I) and time-averaged (s_T) stretch rates near flow reveral for NORM, HFNR and HFOV at $t/T = 1 \pm 0.06$ (left panel) and $t/T = 1.5 \pm 0.06$ (right panel).

CHAPTER 9

BREATHING LUNG SIMULATION

9.1 Breathing lung

In most of the CFD studies of airflow inside lung, it is assumed that the airways are rigid. In reality, however, the airways are deformable during breathing cycles associated with mechanical properties of airway, tethering force of the airway to the surrounding lung parenchyma, and so on. Traditionally, efforts to explain the effect of airway deformation have been mostly made in a mathematical sense without resolving local flow dynamics (Espinosa and Kamm 1997) or at very local level (Bull and Grotberg 2003, Halpern and Grotberg 2003). Recently, attempts to employ the deformation of the airways on the fluid motion have been made by means of two approaches in parallel: fluid structure interaction (FSI) and image-based model. Xia *et al.* (2010) recently applied FSI technique using the ALE method to study the effects of tethering force at the airway parenchyma and motion of the airway wall in an MDCT-based airway bifurcation from the 3^{rd} to the 4^{th} generations. On the other hand, the image registration may play an important role in describing the airway deformation. The displacement field derived between two images can be employed to model the motion of 3D airway surface and 1D tree. The current chapter is devoted to demonstrate the multiscale airflow simulation in an image-based deforming airway on the 3D and 1D frameworks. A compliant airway model derived from MDCT volumetric images of subject 3 (see Section 2.1) and ALE method are implemented, in addition to the methods presented in previous chapters. An image-based approach is also proposed to determine the diameters of the local 1D airway segments during deformation. The effect of airway deformation in normal quiet breathing is discussed.

9.2 Methodology

9.2.1 Image-derived airway deformation

Displacement

Recent advances in image registration technique (Yin *et al.* 2009b, 2011) enable extraction of local displacement vector field over the airway surface. Figures 9.1(a) and 9.1(c) show sagittal slices at the same location taken at lung volumes of 85% VC (Image I_1) and 55% VC (Image I_2) of a human subject. Figure 9.1(b) is the warped image obtained by image registration, which matches voxels of two images. Registration-derived warping function is used to derive airway geometry at an arbitrary phase by using a suitable interpolation technique. Using two images, we assume that voxel trajectories are along straight lines in space. Figure 9.2(a) shows the resulting surface displacement map of the airways between Images I_1 and I_2 (center of the figure) and also shows airways corresponding to the two images (gray for I_1 and blue for I_2) at five lobes (left and right of the figure). In the same way, image-registration derived trajectories of voxels that includes with nodal points of the 1D airway tree at the reference volume (Images I_1). Front and side views in Figure 9.2(b) shows that the regional difference in 1D tree is three dimensional, attributable to the effects of motion of diaphragm, lobar segmentation, rib cage, and so on. Figure 9.3 compares 3D-1D coupled airways corresponding to the reference image at 85%VC, and the floating image at 55%VC. The coordinates at 55%VC are obtained by adding displacement vectors to the coordinates of local nodal points at 85%VC. 1D airway segments are color-coded by the central airway and the five lobes. In this study, two images are used and each resulting trajectory is on a straight line (Yin *et al.* 2010b). However, the deformation of airway surface is nonlinear since individual nodal points move in different directions and at different rate according to the global lung volume change. A cubic interpolation is used to obtain the smooth change of displacements of surface nodes as functions of time during specific breathing cycle. Given the displacement function, airflow in the deforming airway can be solved using

ALE method implemented to the 3D CFD solver (Chapter 3). If three or more CT images are used, non-straight trajectory can be obtained by the same approach.

Local volume change

Image registration is also capable of estimating the local contraction and expansion during breathing cycle. We introduce a local voxel volume $v_i(\vec{x})$ at a location $\vec{x}$ corresponding to an instantaneous total air volume in the lung (global volume) denoted by V_i. The local volume difference between two images can be determined by Jacobians for individual voxels, as the Jacobian implies a volume ratio of the deformed voxel to the original voxel and is formulated as

$$J(\vec{x}) = \frac{v_f(\vec{x})}{v_r(\vec{x})} = \frac{v_f(\vec{x})}{v_r} \tag{9.1}$$

where subscripts *r* and *f* denote reference and floating images. The voxels in the reference image have uniform volumes in the whole domain, while the voxels are deformed in the floating image and the volumes vary in space. Figure 9.4 exhibits the Jacobian distribution on the entire conducting airway tree, that reflects the regional difference in local contraction. Figure 9.4(c) exhibits the base (0%) to apex (100%) distribution of the averaged local volume (solid line) and length scale (dot-dashed line). It is shown that the deformation is greater near base than apex of the lung. The upper and the lower 5% of height are excluded in consideration of possible misunderstanding, as left to right or center to lateral distribution may need to be considered near based due to the shape of the diaphragm. A local voxel volume at a global volume (total air volume in the entire lung) of V_f can be obtained by

$$v_f(\vec{x}) = J(\vec{x})v_r \tag{9.2}$$

Using image driven local voxel volumes, intermediate local voxel volumes at a global volume of V_i can be approximated by an interpolation function. Given two images in the current study, linear interpolation is formulated as

$$v_i(\vec{x}) = \frac{V_r - V_i}{V_r - V_f}\left(v_f(\vec{x}) - v_r\right) + v_r \tag{9.3}$$

by assuming a linear relationship between global lung volume change and local voxel volume change. Higher order interpolation functions can be used if more than two images from CT scans are given. We use fractional volume with respect to TLC, to assess the volume-related analyses regardless of inter-subject variability. Local voxel volumes at TLC are also obtained by linear extrapolation using Eq. (9.3).

Local p-V curve

A pressure-volume (p-V) curve shows characteristics of a subject specific lung. In clinical situation, p-V curves are usually obtained by quasi-static process, in which the effect of airflow can be neglected. The pressure of this p-V curve refers to the transpulmonary pressure, that is of the equal absolute value and the opposite sign to the elastic recoil pressure of the lung. The volume refers to a fractional volume that the maximum of 1 corresponds to TLC. This study does not include modeling of the global p-V curve or related tissue mechanics, but only propose an approach to find a regional distribution of p-V curve at a local level in the entire lung. Exponential fittings of the global p-V curves can be found in Harris (2005), West (2005), and so on. Given a global p-V curve for the full range of fractional lung volume, a loop of p-V curve for a specific breathing cycle can be modeled, assuming that the p-V curve for a tidal breathing resides

in the global loop of p-V curve. In this section, a local p-V curve for a specific breathing cycle is modeled using the local volume fraction to the maximum volume at TLC, provides the regional distribution of the p-V relationship during a breathing cycle. The procedure to model a local p-V curve follows.

- Find local volume fractions at a specific breathing cycle by Eq. (9.3) in the previous section, at the maximum and the minimum global volumes of the cycle. The maximum and the minimum volumes correspond to the end inspiration and the end expiration.
- Determine the pressures at the end inspiration and the end expiration. In the current study, we place the end expiration point on the deflation curve in the global loop and the end inspiration on the inflation curve in the global loop.
- Scale down the global p-V curve to the individual local range, and obtain a closed loop of the local p-V curve.

Figure 9.5 shows an example of local p-V curve during a tidal breathing (red) overlaid in a model global p-V curve. Respective fractional volumes at the end expiration and the end inspiration of 0.5 and 0.7 are arbitrarily selected. Using the proposed approach, one can find local elastic recoil pressures during a specific tidal breathing, reflecting a consistent mechanical response to the global lung. This approach can be used to further study the regional distribution of pressure-volume relationship based on direct estimation of local volume ratios derived from image registration of CT scans, and there has been no attempt to derive the three dimensional representation of local p-V behaviors in accordance with local airway segments of the entire lung.

9.2.2 1D airway diameter model

Diameters of deforming airway: Registration-based airway deformation

In this section, we propose an approach to model the airway diameter in subject specific deforming lung, based on the image-registration-derived local Jacobian map,

under the condition that 1D airway tree is generated by volume-filling method, and displacement vectors at the nodal points of individual airway segments are provided from image registration results. Accurate image registration minimizes the local difference of tissue volume inside the lungs between two images, preserving tissue weight of the lungs (Yin *et al.* 2009a). Regarding that the number of voxels in an airway segment remains constant between images, we introduce a variable $k(j)$ defined as

$$k(j) = \frac{w_i(j)}{v_i(j)} = \frac{w_r(j)}{v_r} \tag{9.4}$$

where $w_i(j)$ is the estimated volume of an airway segment indexed by j. The voxel volume in an airway j is averaged at the nodal coordinates at proximal and distal ends of the segment. Then the volume of an individual airway segment in a deformed lung can be computed as

$$w_i(j) = k(j)v_i(j). \tag{9.5}$$

Once the volume of a local airway segment is obtained, the average cross-sectional area and the average diameter at a global volume of V_i can be computed, as the length of the airway $l_i(j)$ is directly calculated from displacements of nodal points. They read

$$A_i(j) = \frac{w_i(j)}{l_i(j)} \tag{9.6}$$

$$d_i(j) = \left[\frac{4A_i(j)}{\pi}\right]^{1/2} \tag{9.7}$$

To summarize, the diameter of the 1D airway segment at a global lung volume of V_i is estimated as

$$d_i(j) = \left[\frac{4}{\pi} A_i(j)\right]^{1/2} = \left[\frac{4}{\pi} \frac{k(j) v_i(j)}{l_i(j)}\right]^{1/2} = \left[\frac{4}{\pi} \frac{w_r(j) v_i(j)}{l_i(j) v_r}\right]^{1/2} \tag{9.8}$$

In this approach, the airway diameter during lung deformation is estimated solely based on the locally determined image registration data on a framework of the skeletonized 1D airway tree. For the reference image used in the current study, the voxel dimensions are (0.68 mm, 0.68 mm, 0.6 mm), and the diameter of airway segment ranges between 18.77 mm and 0.3 mm.

Comparison with approach based on p-A relationship

Lambert *et al.* (1982) introduced a relationship between transmural pressure and cross-sectional area of airway (Lambert's model hereandafter). In order to use this method, a model pressure volume curve digitized from West (2005) was adapted. Using a local p-V curve obtained by the procedure in the above section, the transmural pressures are obtained at a local level. Given a pressure, Lambert's model computes the fractional airway area to the maximal area as

$$\alpha = \alpha_0 (1 - p/p_1)^{-n_1}, \quad \text{when } p \le 0 \tag{9.9}$$

$$\alpha = 1 - (1 - \alpha_0)(1 - p/p_2)^{-n_2}, \text{ when } p \ge 0 \tag{9.10}$$

where α_0, p_1, p_2, n_1, and n_2 are parameters for the 0^{th} – 16^{th} airway generations. The model parameters from the 0^{th} to the 16^{th} generations correspond to the proximal and the distal ends of individual airway paths. As this model has been developed based on the airway

order (Horsfield 1978) starting from the terminal airway, the parameters for the 16^{th} generation in Lambert's model correspond to those for the terminal bronchiole of the 1^{st} airway order. Thus, the parameters between the 0^{th} and the 16^{th} generations are stretched to cover from the trachea to the terminal bronchioles of asymmetric subject specific airways.

Figure 9.6 shows the distribution of fractional areas of individual airway segments based on the proposed approach (dots), in comparison with the Lambert's model at selected generations 5, 10, and 12. The end expiration of this case corresponds to 55%VC and the tidal volume is set to 500 ml. Local transmural pressures are obtained from the local p-V curve, proposed in the previous section, for the local fractional volume ranges. The p-V curve digitized from West (2005, Figure 9.5) was adapted to model a global p-V curve. Overall good agreements are found.

9.2.3 Algorithm for 3D CFD simulation

ALE method

Governing equations and the numerical schemes are discussed in Chapter 3. In this section, the ALE algorithm for moving mesh treatment is introduced. The ALE method uses body-fitted meshes and does re-meshing as the boundaries of fluid mesh moves, which generally results in higher accuracy though requiring computational efforts on mesh treatment. Different ALE methods have been developed and widely used in recent studies of various area, such as airflow past the parachute (Johnson and Tezduyar 1997), flow past a flapping wing (Mittal and Tezduyar 1995), transient motion of a missile (Hassan *et al.* 1998), stokes flow in an elastic tube (Heil 1998), and among others. An efficient dynamic mesh algorithm (Zhao and Forhad 2003) is adopted to handle the motion of the fluid mesh. In this method, the shortest distance, *d(i)*, of every fluid node *i* to the moving walls is calculated and the wall node that is closest to this inner node is identified as i_{wall}.

This distance *d(i)* is non-dimensionalized by the maximum or a reference distance d_{max} of all the *d(i)*. The deformation of the fluid node $\delta\vec{r}(i)$ is calculated as the product of a distance function *f*(*i*) and the deformation of its associated wall node $\delta\vec{r}(i_{wall})$:

$$\delta\vec{r}(i) = f(i)\delta\vec{r}(i_{wall}) \tag{9.11}$$

The distant function is constructed using two exponential damping functions as:

$$f(i) = \frac{f_2^{\,2}(i)}{f_1^{\,2}(i) + f_2^{\,2}(i)} \tag{9.12}$$

where

$$f_1(i) = \frac{1 - \exp[-d(i)/d_{\max}]}{(e-1)/e}, \text{ and} \tag{9.12a}$$

$$f_2(i) = \frac{1 - \exp[1 - d(i)/d_{\max}]}{(1-e)}. \tag{9.12b}$$

The distance function approaches to 1 as *d* goes to 0 and the function approaches to 0 as *d* goes to d_{max}. This property makes the grid very rigid in areas near the wall and far away the wall while those in between areas are elastic and easy to be deformed. To make this method more robust for large mesh deformation, the calculated deformation of every node is further smoothed to eliminate highly skewed or overlapping cells. The smoothing is done by averaging the deformation of one node *k* with the deformation of its neighboring nodes as:

$$\delta\vec{r}_k = \frac{\sum_{i=1}^{nedge(k)} k_i \delta\vec{r}_i}{\sum_{i=1}^{nedge(k)} k_i} \tag{9.13}$$

where *nedge(k)* is the number of edges surrounding node *k*. k_i is the inverse of the distance from node *k* to edge *i*. The mesh velocities of the inner fluid nodes are obtained in the same way as the deformation. Fuller description of this algorithm can be found in Xia and Lin (2008).

The procedure of applying ALE method in the fluid solver is presented below.

- Update the surface nodal coordinates.
- Update the inner nodal coordinates by equations (9.11) and (9.12).
- Smooth the coordinates of the inner nodes by equation (9.13).
- Determine the mesh velocity.
- Solve the continuity and the momentum equations.

Boundary conditions

The total inhaled flow rate is given at the proximal inlet, maintaining mesh conservation as

$$Q_{\text{prox}} + Q_{\text{surf}} + Q_{\text{dist}} = 0 \tag{9.14}$$

where Q_{prox}, Q_{surf}, and Q_{dist} are the net flow rate at the proximal inlet (e.g. the mouthpiece), the integral of mesh velocities in wall normal directions around the external airway surface, and the net flow rate at the distal ends, respectively, as positive values indicate the air flux out of the domain. The procedure to update the flow boundary conditions for time integration is as follows.

- Update the flow rate at the proximal inlet.
- Update mesh velocities at the surface nodes.

- Take surface integral to compute the air flux across the entire airway boundary surface (wall flux).
- Multiply Q_{dist} obtained from equation (9.14) by the flow rate fraction (see Chapter 2) at each distal exit.

9.3 Airflow in deforming large airways: 3D simulation

We carried out three cases of LES of airflow in deforming and rigid lungs, with the tidal volume of 500 ml and the period of 4.8 s. For deforming lung case (Case I), the lung volume at the end inspiration is set to 85%VC, and results are compared with two rigid lung cases at the same flow conditions. The geometries of the two rigid lung cases correspond to the lung volumes at 85%VC (Case II) and of the volume at the peak flow rate of Case I (Case III). A sinusoidal waveform of flow rate is imposed at the mouth. The computational domain consisting of 4.6 million tetrahedral elements are divided into 128 to 256 partitions for MPI parallel computing. A time step of 1×10^{-5} s was used.

Figure 9.7 shows snapshots of pressure and air speed in 3D airway at 8 normalized times of a breathing cycle. Overall characteristics of the flow behavior, such as pressure drop, turbulent laryngeal jet, jet-like structure at the bifurcation during expiration are found to be similar in the rigid lungs. With a tidal volume of 500 ml, a little deformation is observed in 3D large airways and no dramatic change in pressure drop is found. However, this small deformation affects dynamic behavior of the flow structures in the central airways. Figures 9.8 and 9.9 compare the flow structures in the deforming and the rigid airways for inspiration and expiration, respectively. During expiratory phase, it is observed that the flow in the trachea is more stable in the deflating lung (Case I) than in the rigid lung (Case II). Assessments can be made to explain this. As $Q_{prox} < 0$ and $Q_{surf} > 0$ in the deforming lung, the absolute value of Q_{ex} in the deforming lung is less than that in the rigid lung in which $Q_{wall} = 0$. In the central airways, diameters do not change much during deformation, resulting in lower *Re* due to smaller

Q_{ex} in the upstream flow. In consequence, the flow is relatively more stable in the deforming lung compared to the rigid lung, as shown in Figure 9.8. Another possibility is the difference in geometry of distal airway. Shorter or shortening upstream geometry reduced the space for instability to develop until transition is triggered in free-shear layer. On the other hands, during inspiration phase, the lung expands. The change of geometry in the central airways mostly occurs in the longitudinal direction. The stretch of airway is accelerated during the half of inspiration phase, and accordingly the laryngeal jet is stretched. The isosurface of air speed at 2.65 m/s in the expanding lung [Figure 9.9(a)] is longer than that in the rigid lung [Figure 9.9(b)] at the peak inspiration. After that, the longitudinal stretching is decelerated, leading to the laryngeal jet shorter than in the rigid lung. There exist two factors between Cases I and II: geometry and acceleration due to deformation. The instantaneous geometry at the peak flow of Case I is more deflated than that of Case II. And the airflow in Case I is accelerated in central airway including the trachea, LMB and RMB, due to the stretching or compressing of the airway in the longitudinal direction. To clarify the main cause of difference between airflow behavior in deforming and rigid airways for inspiratory and expiratory flows, another rigid airway case (Case III) is added in comparison in Figure 9.10. At the peak expiration, velocity field and the resulting flow characteristics are found to be nearly identical between Cases I and III, of which the geometry is the same. Flow is stable in LMB and the trachea. However, Case II with the geometry at greater inflation undergoes turbulence transition for the flow entering LMB, which propagates to the trachea. This comparison confirms that the static geometry plays an important role in transition of the expiratory flow, and it is assessed that the greater curvature delays the transition (Moser and Moin 1987) of merging jet-like flows from child branches in LMB. On the other hand, at the peak inspiration, the laryngeal jet core was stretched longer only in Case I, and it is shorter in Cases II and III. It is attributable to the effect of the overall expansion of distal airways, which contributes the convective acceleration in the upstream flow in the trachea. It is

considered reasonable that the effect of detailed static shape of the downstream flow of in distal airways is not significant in the upstream laryngeal jet behavior.

9.4 1D results for entire conducting airways

The energy-based 1D flow model has been solved for flow field in deforming airway tree presented in previous sections. Coefficients found in Chapter 7 are used respectively for inspiration and expiration. Total flow rates imposed at the proximal inlets was same as the 3D simulations. Diameters of individual deforming airways are determined by the proposed method using local voxel volume fraction based on Jacobian map.

Regional distribution of airway pressure in rigid and compliant lungs

Figure 9.10 shows regional distributions of *Re* and airway pressure in the entire airway tree at peak inspiration. Exponentially divided *Re* range depicts the multiscale flow physics between proximal to distal airway segments. Airway pressures in the entire lung computed by the current 1D flow model for deforming lung exhibit the distribution that is smooth and similar to the rigid lung case (Rigid lung case not shown here).

Figure 9.11 compares pressure distributions with respect to normalized heights of the basal to apical and the dorsal to ventral levels, in a rigid lung at 85%VC (R85), a deforming lung reaching 85%VC at the end inspiration (EI85), and a deforming lung reaching 55%VC at the end expiration (EE55). A tidal volume of 500 ml and a period of 4.8 s were applied to all three cases. The difference between cases R85 and EI85 is not extinctive. Case EI85 experiences overall slightly greater pressure drop to the terminal bronchioles both in the basal to apical distribution and in the dorsal to ventral distribution. In case EE55, where the lung holds more deflated volume, the pressure drop the terminal bronchioles are further increased. In the basal to apical distribution, noticeable increase of pressure drop is observed at the central and upper (closer to apex) regions and in the

dorsal to ventral distribution, pressure drop increases at the lower (more dorsal) region. Generational distribution of airway resistance is also compared between deforming (EI85) and rigid (R85) lungs as shown in Figure 9.12. During a breathing cycle, the average diameter varies more in the higher generations, of which the range is shown in enlarged boxes in Figures 9.12(c) and 9.12(d). Average diameters decrease during deflation and increase during inflation. Accordingly, the airway resistance at each generation is greater in the deforming lung (EI85). It is noted that dominant site of airway pressure drop is large airways around generation 4 regardless the phase in a cycle, while the relative deformation occurs more at higher generations. The resistance at generation 4 in case EI85 is only 6% increased from case R85. At further deformed airway (case EE55), dramatic increase of 77% is observed (not shown).

9.5 Discussion

9.5.1 Issues on 3D model

Discussion on the current distance function to deform inner nodes of 3D mesh

Currently the coordinates of the inner nodes are updated only based on one nearest wall node. As the topology of the airway comprises a closed tube, a conflict may exist among the distance functions of adjacent nodes, to which the nearest wall nodes are located in the opposite sites of the airway wall, e.g. front and rear regions of the wall. In addition, the current approach takes only one reference diameter for mesh deformation in a global sense.

Variability for difference in flow structure

New findings in the effects of the deforming airway in Section 9.3 may address further investigation of the underlying physics of the relationship between deforming airway and the flow structure in large airways. Intra- and intersubject variability studies

for various conditions, e.g. at different inflation levels, may elucidate the structure function relationship in breathing lungs.

9.5.2 Issues on 1D model

Sensitivity to intrasubject variability and model settings

Sensitivity tests for diameter, boundary conditions, and voxel treatment in building an entire conducting airway model may need to follow. The 1D airway tree in the CT-unresolved region has been generated by assuming a fractal structure. Some of these airways may cross the region where the pulmonary blood vessels are located in the lung parenchyma. These are potential cause of inaccurate values of Jacobian map, which finally attributes the diameter calculation and the airway resistance. However, the local deformation in the parenchyma is regarded

Regional difference of local p-V behavior

In the model global static p-V curve, the pressure is transpulmonary pressure, P_L. P_L can be the same as elastic recoil pressure, P_{el}, for static condition, where airflow is zero and pressure drop due to airway resistance is consequently zero. P_{el} is a function of instantaneous volume fraction to TLC volume, and digitized values from a standard form of p-V curve were used to avoid many potential issues related to modeling of p-V curve. Authors note that more accurate modeling or finding of p-V curve is an independent study, and the current paper provides the approach to localize the p-V behavior based on local volume fraction at every instant of inflation and deflation of lung.

Boundary conditions

Image driven airflow ventilation is given at the distal ends of terminal bronchioles (Yin *et al.* 2010). Prescribed flow waveform is given at the inlet (proximal end of the whole airway tree, which can be the mouth or the trachea). Given two images, ventilation

distribution can be only a function in space, and constant in time at each site. If more than two images are given, a nonlinear interpolation can deliver four-dimensional dynamic ventilation distribution. In that case, phenomena such as Pendulluft effect can be directly derived.

Modeling of local elastic recoil pressures and pleural pressures using quasi static p-V curve

It should be noted that the pleural space exists around the lung parenchyma and is to be shown along the surface of lungs. The proposed local volume fraction model can be used to provide regional distribution of dynamic p-V behavior.

9.6 Summary

In addition to the procedures presented in previous chapters, 3D and 1D methods are introduced to incorporate the airway and lobe deformation into the multiscale CFD framework for the rigid lung. ALE is implemented in the LES process for 3D airflow motions in moving airway. Motions of both 3D and 1D airways are prescribed by the mass-preserving nonrigid image registration method (Yin *et al.* 2009b) based on CT images at two levels of inflation. The diameter estimation in the rigid airway is based on the assumption of maximum expansion of airway cross sections, which corresponds to near TLC geometry. To determine the diameters in deforming airway of 1D tree, we proposed a method that utilizes image registration derived regional Jacobian map. In this method, a reasonable assumption is made that the number of voxels per airway remains the same between reference and floating images of registration method. Application of this approach can extended to investigating physiological characteristics in a local airway level, as estimation of the regional elastic pressure distribution is demonstrated using a model pressure-volume curve. Subject specific regional ventilation BC and energy-based 1D flow model predicts the pressure and flow fields in the entire conducting airway in the

breathing lung. In more deflated lung, the greater pressure drop to the terminal bronchioles is observed, maintaining the qualitative consistency in the basal to apical and the dorsal to ventral distributions. In 3D framework, a normal breathing with a tidal volume of 500 ml and a period of 4.8 s experiences overall the similar feature of velocity, pressure, wall shear stress, and so on, in deforming and rigid lungs, when the end expiratory volume of deforming lung is set to the same as the rigid lung. However, the flow structure and turbulence transition in the central airway are affected by different factors for inspiratory and expiratory flows. Stretching of the jet core at inspiration is induced by the deformation, in specific, stretching of the airway in axial direction, and flow remains more stable in the greater curvature of the geometry at more deflated lung.

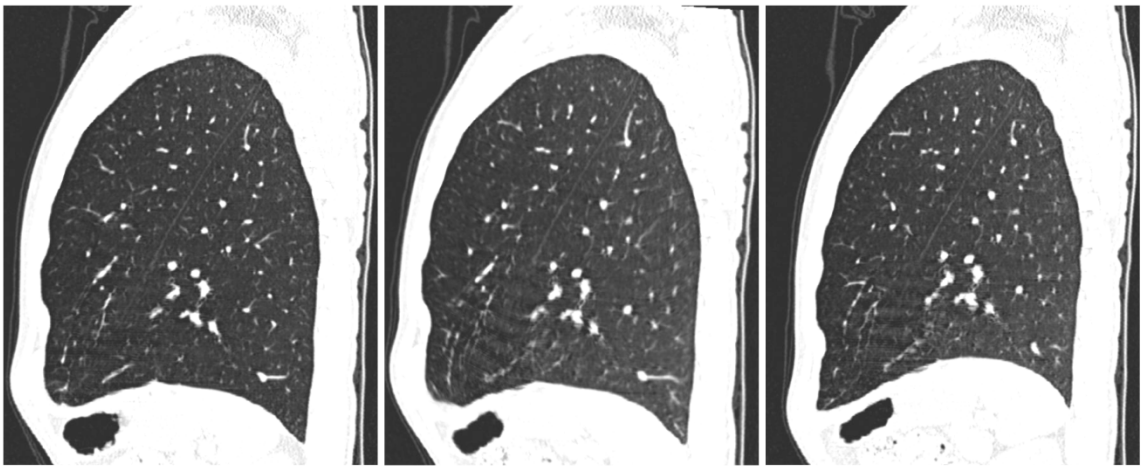

(a) Image I_1 (b) Warped Image $I_2(T(x; \phi))$ (c) Image I_2

Figure 9.1 A sagittal slice of the left lung from (a) the image I_1, (b) the warped image obtained by image registration, and (c) the image I_2 at the same axial locations.

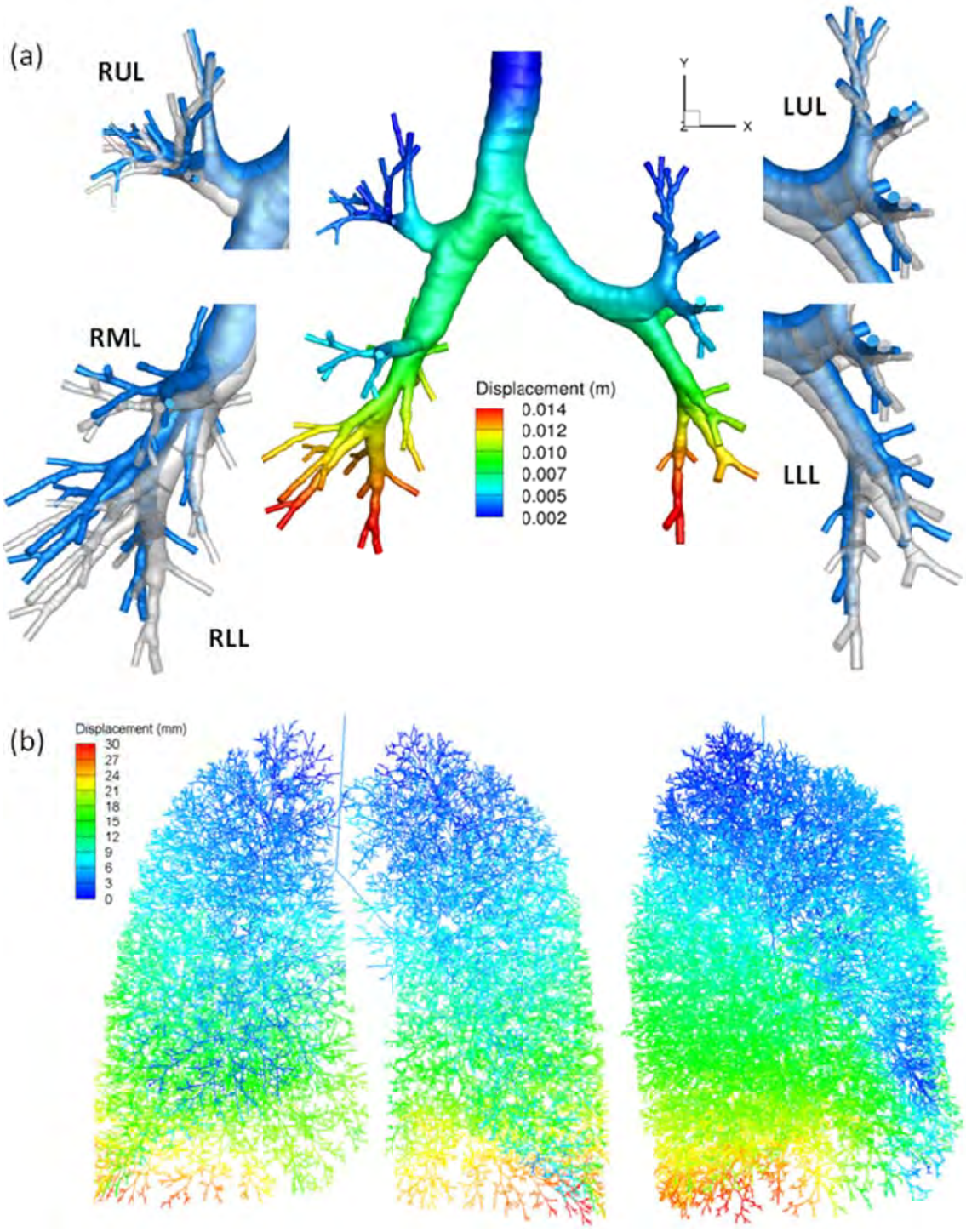

Figure 9.2 Displacement map derived from image-registration. (a) Surface displacement map of 3D airway on 85% VC geometry (center) and comparison of 3D airway models at 85% VC (gray) and 55% VC (blue) at five lobes. (b) Displacement map of the entire conducting airways of 1D tree.

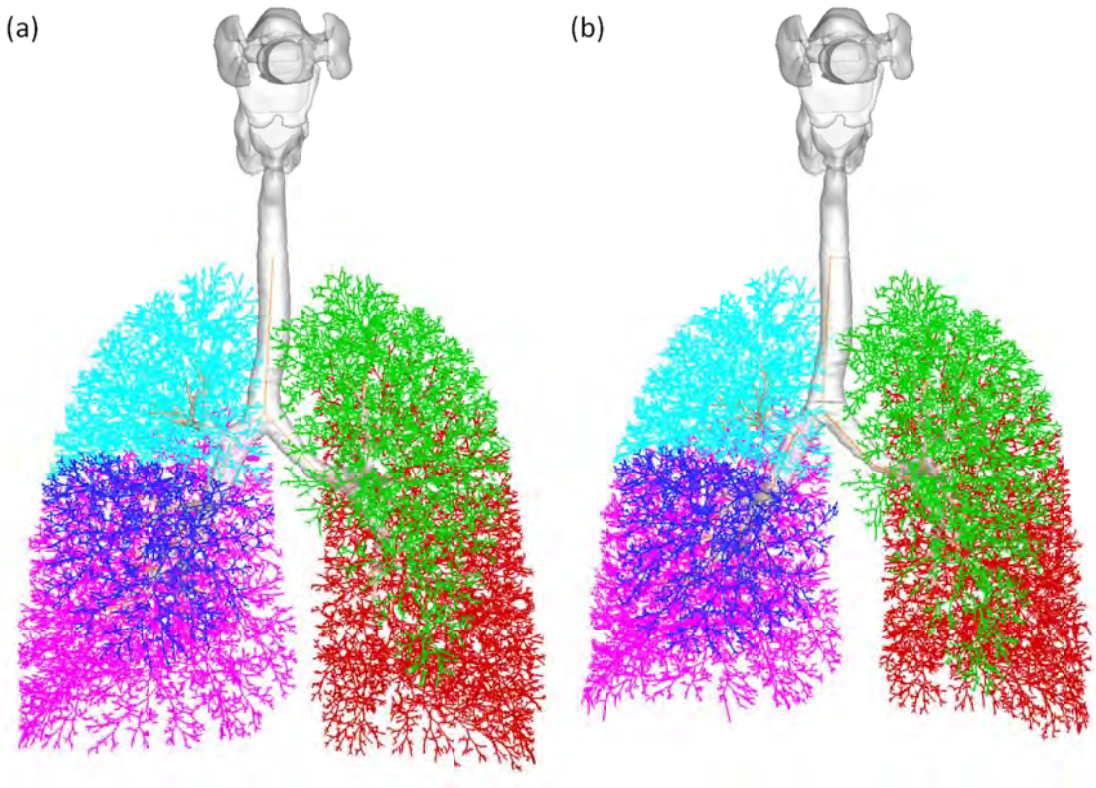

Figure 9.3 3D-1D coupled entire conducting airways at (a) 85%VC and (b) 55%VC, color-coded by lobes.

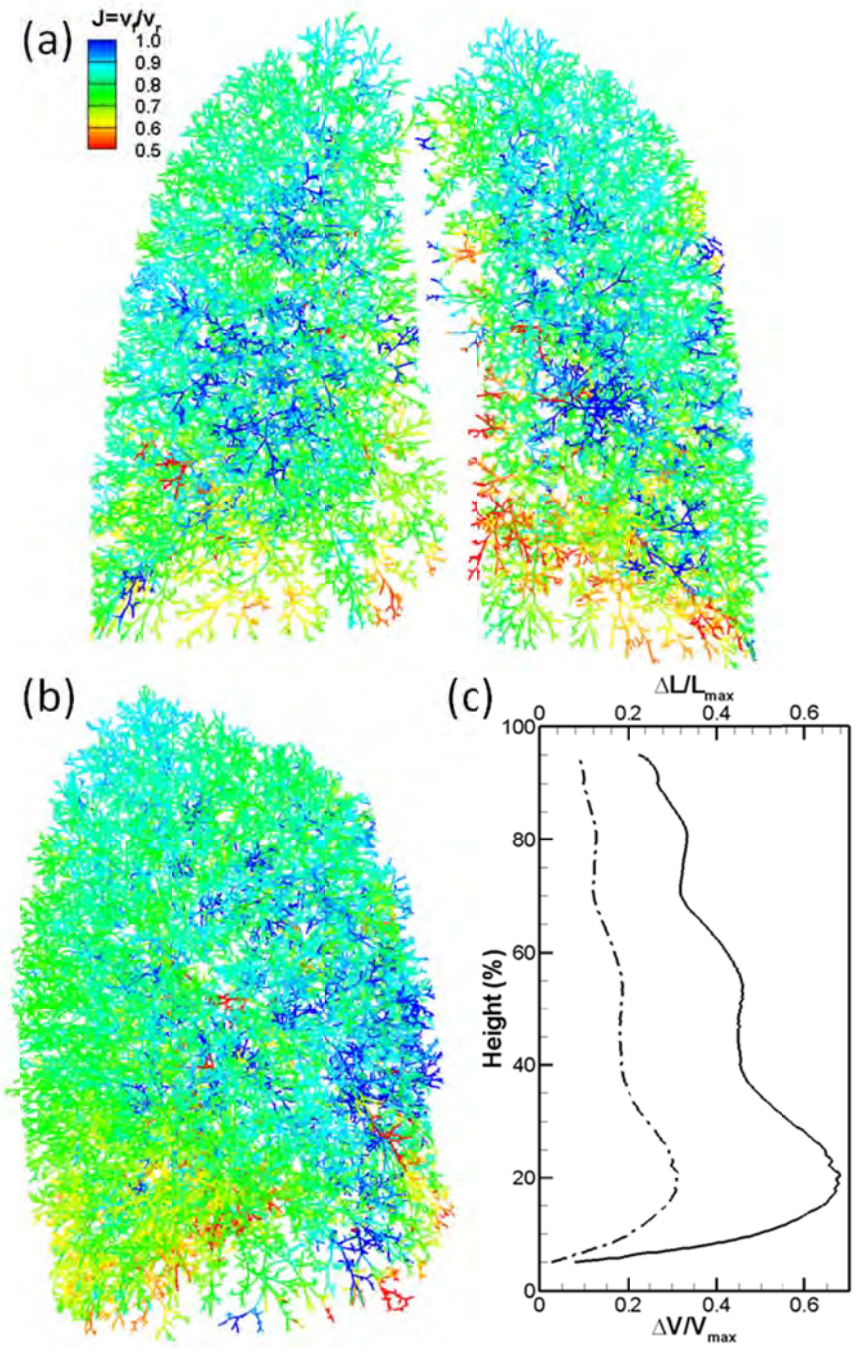

Figure 9.4 Image-derived regional deformation. (a) Front and (b) side views of the regional distribution of Jacobian in the entire lung along with the 1D airway tree, and (c) the base (0%) to apex (100%) distribution of the local volume (solid line) and length scale (dot-dashed line). Jacobians represent fractional volumes of deformed voxels of the floating image with respect to the original voxel volumes of the reference image.

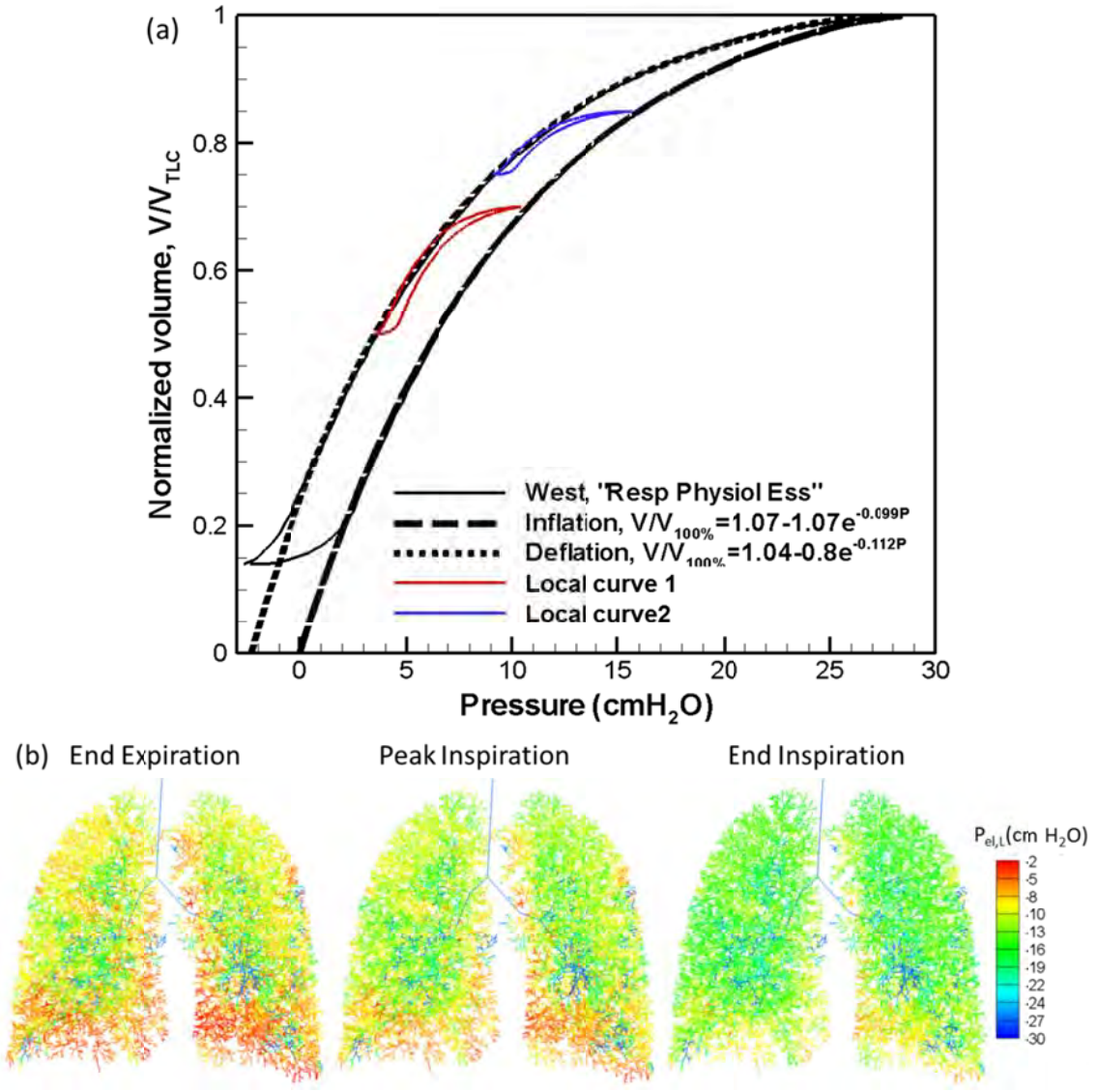

Figure 9.5 Regional p-V relationships. (a) Modeling of a local p-V curve of a tidal breathing, based on a model global p-V curve. Red loop is an exemplary local p-V curve. Long-dashed and short-dashed lines are the exponentially fitted to inflation and deflation curves, respectively. (b) A demonstration of dynamic change of distribution of local elastic recoil pressures. Local pressures vary according to the individual local loops of p-V curves that reside in the global p-V curves.

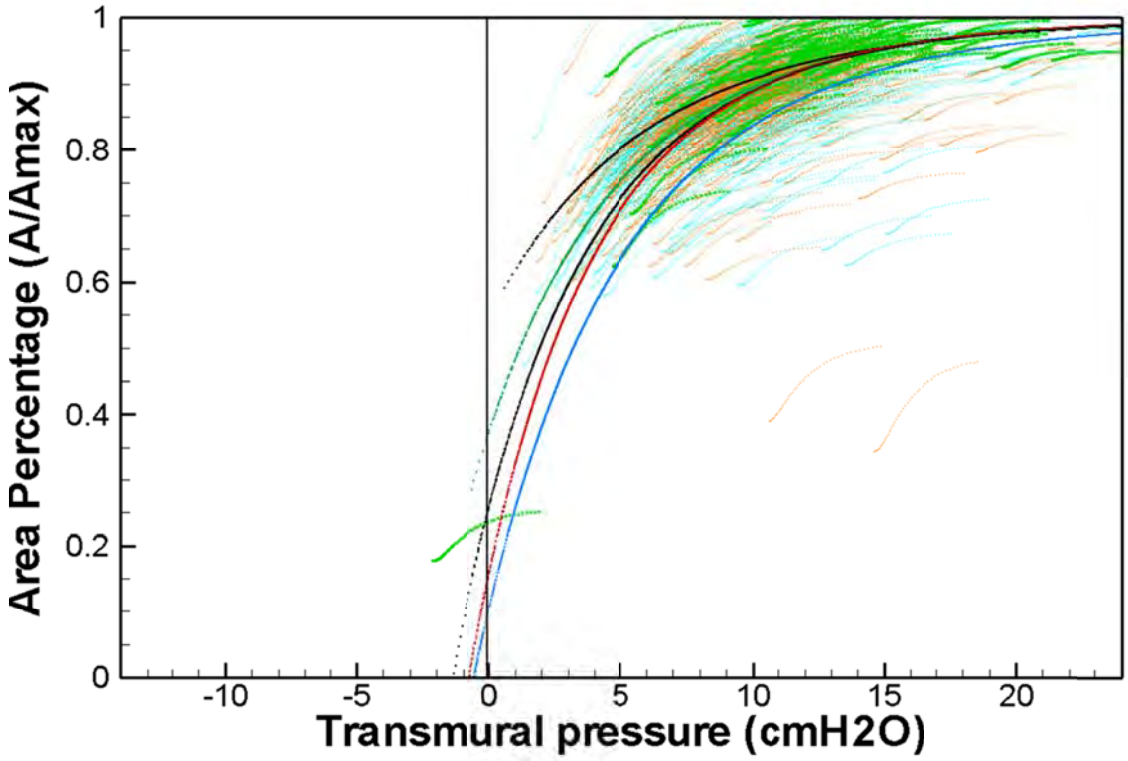

Figure 9.6. Scattered dots denote results from the direct method (model 2) to determine diameter, and the lined-up symbols are from model 1. The rescaled generations of 5, 10 and 12 are color-coded by green (dark green), orange (red), and cyan (blue) for model 2 (model 1), and the rescaled generations of 3 and 7 of model 2 are plotted in black.

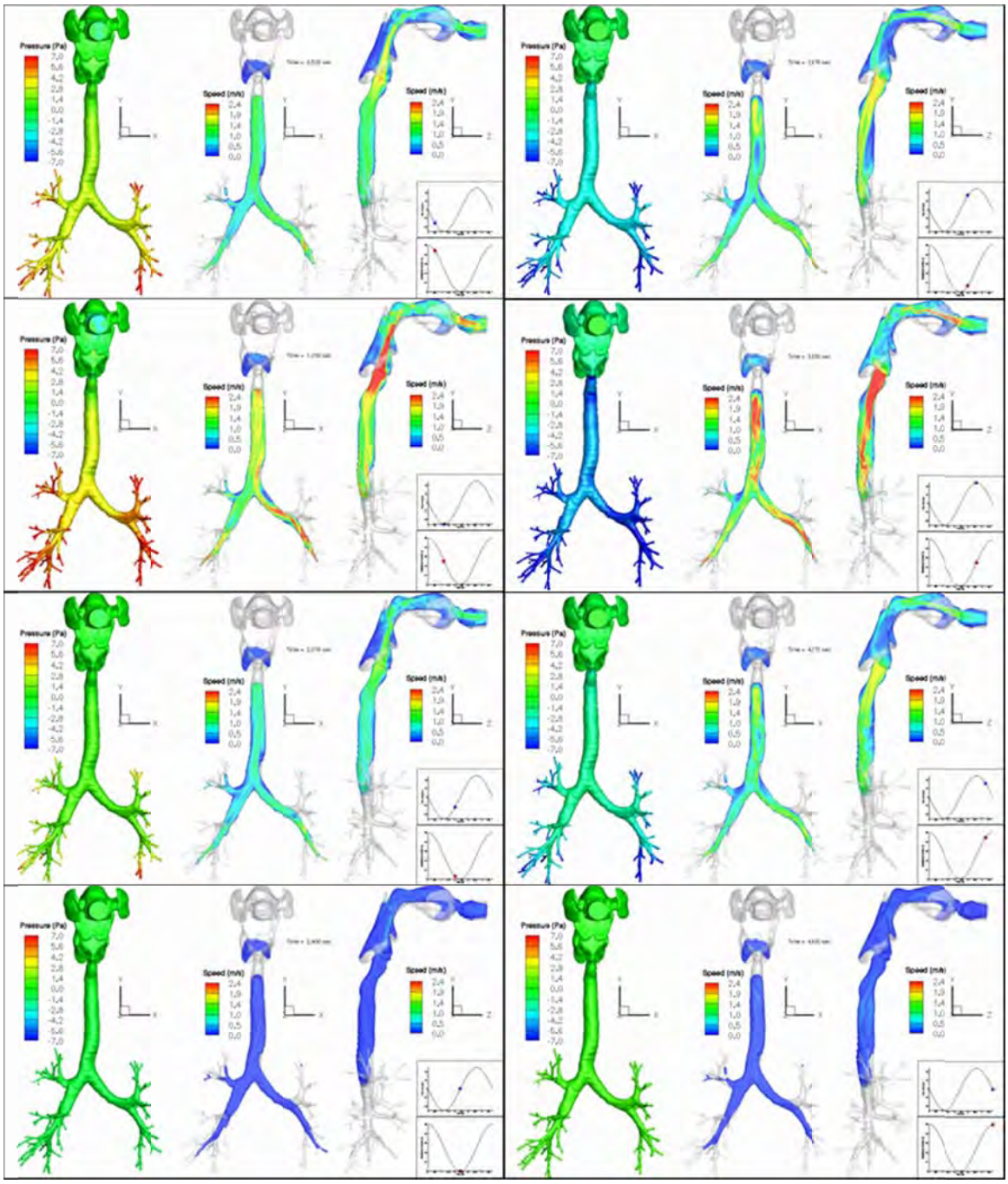

Figure 9.7 Dynamic changes of pressure (front view) and air speed (front and side views) in large airways of breathing lung at different time points in expiratory (left) and inspiratory (right) phases of a breathing cycle.

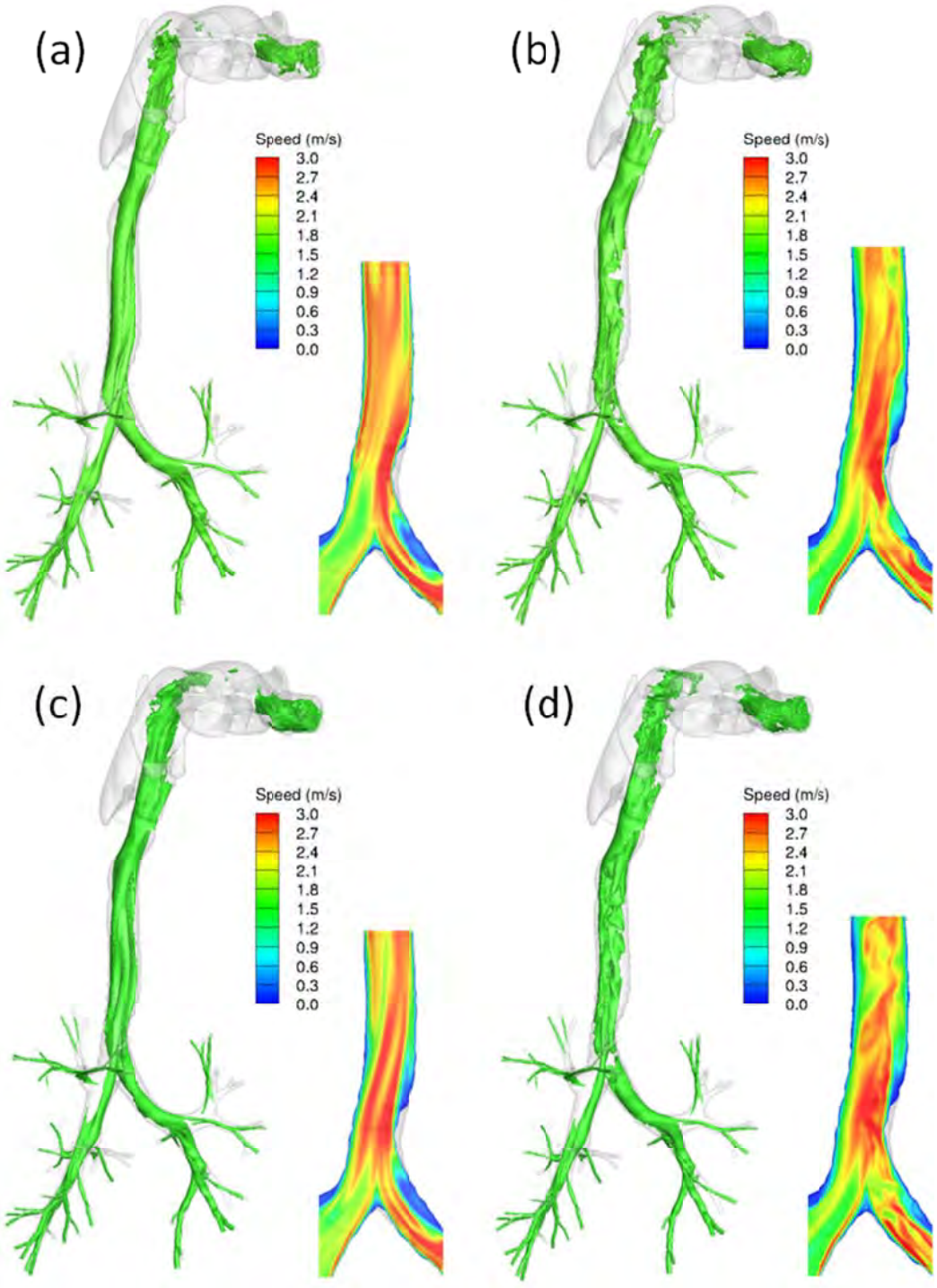

Figure 9.8 Comparison of airflow structures in central airways of (a,c) deforming and (b,d) rigid lungs, at peak expiration (t/T=0.25) (a,b), and at following deceleration (t/T=0.30) (c,d). Isosurfaces of air speed at 1.65 m/s (1.55 m/s) and velocity contours in a vertical plane exhibit the difference in detailed flow structures at t/T=0.25 (t/T=0.30).

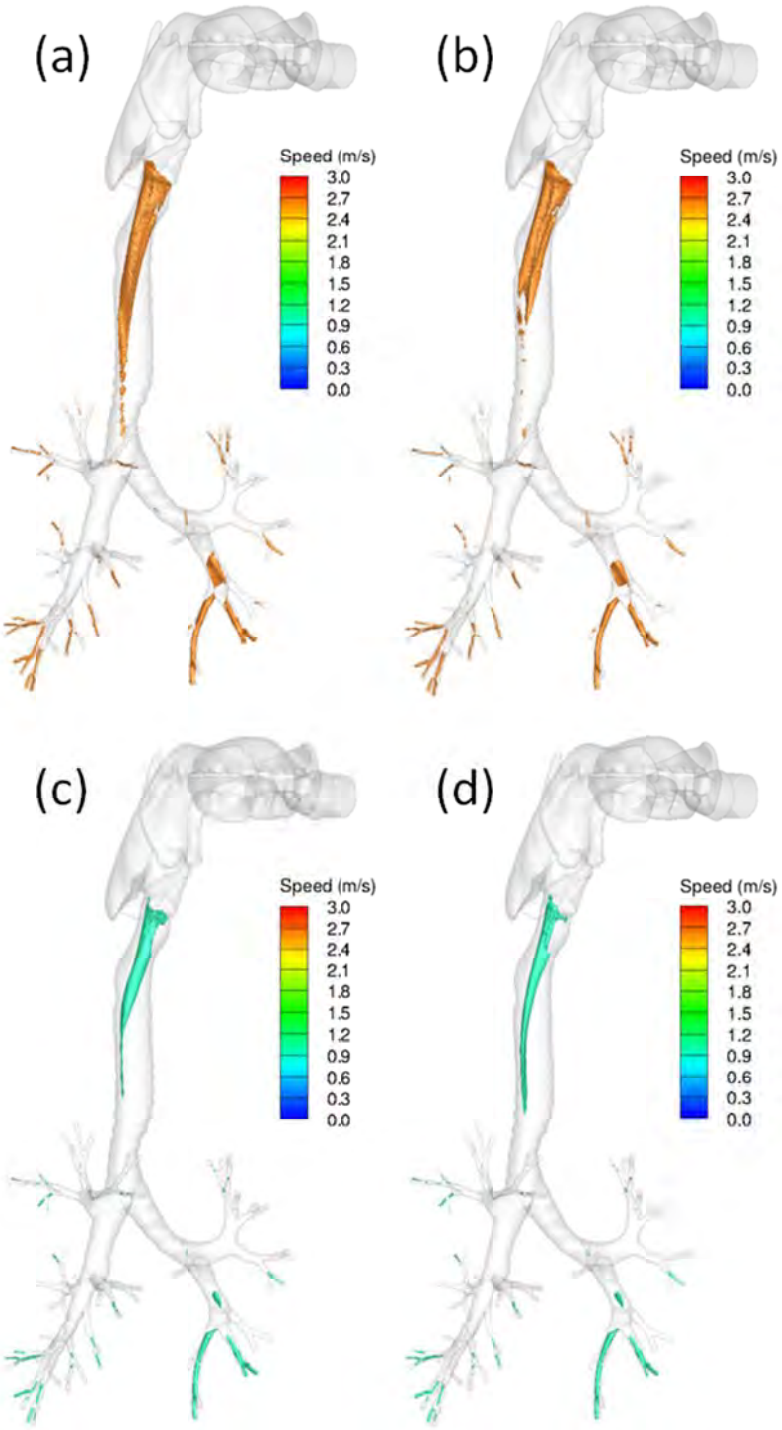

Figure 9.9 Comparison of the laryngeal jet in (a,c) deforming (Case I) and (b,d) rigid (Case II) lungs, at peak inspiration (t/T=0.75) (a,b), and at following deceleration (t/T=0.95) (c,d). Isosurfaces of air speed at 2.65 m/s (1.0 m/s) and velocity contours in a vertical plane exhibit the difference in detailed flow structures at t/T=0.75 (t/T=0.95).

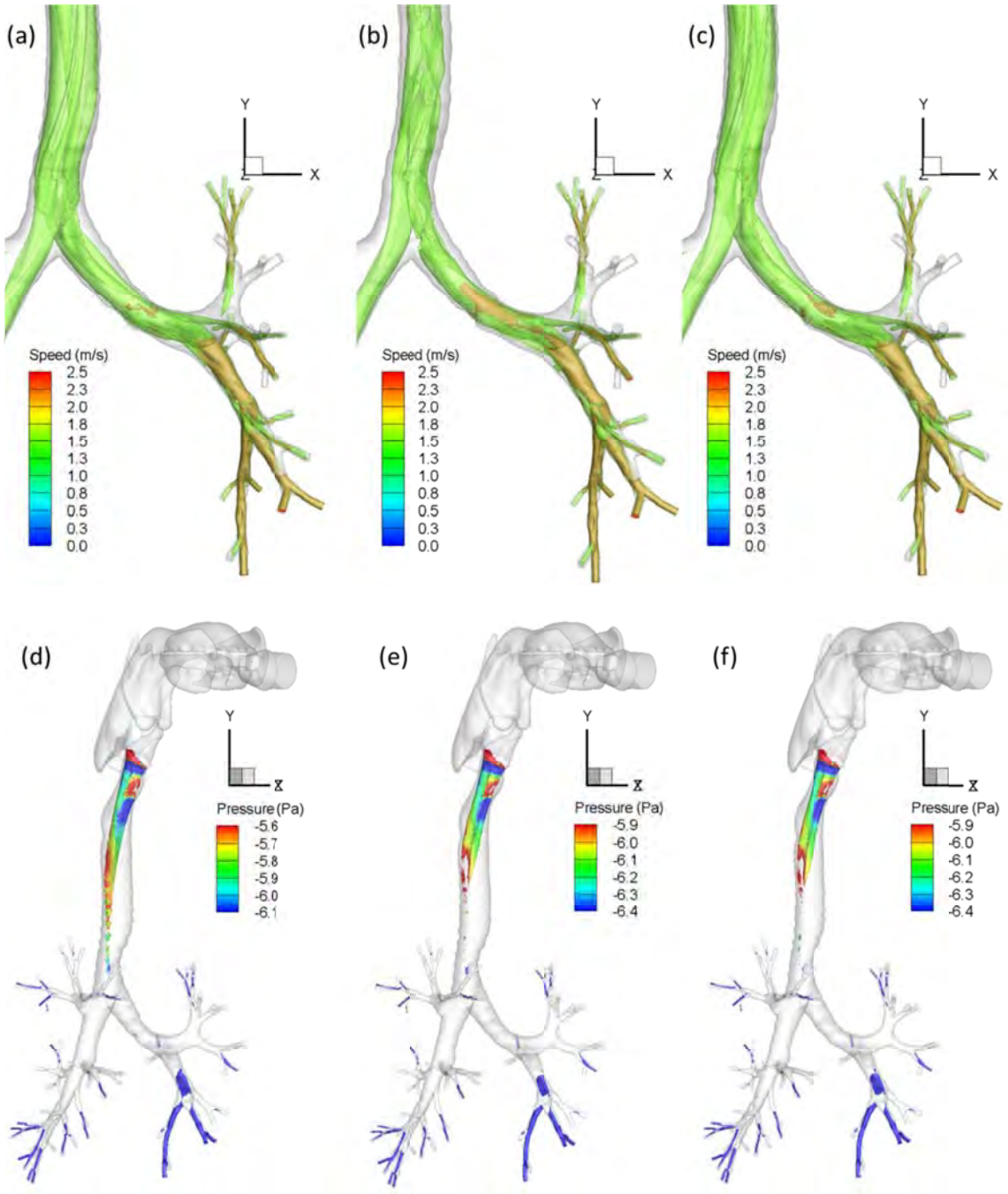

Figure 9.10 Effects of static geometry and motion on the airflow in deforming and rigid lungs at (a-c) peak expiration and (d-f) peak inspiration. (a,d) Case I, (b,e) Case II, (c,f) Case III.

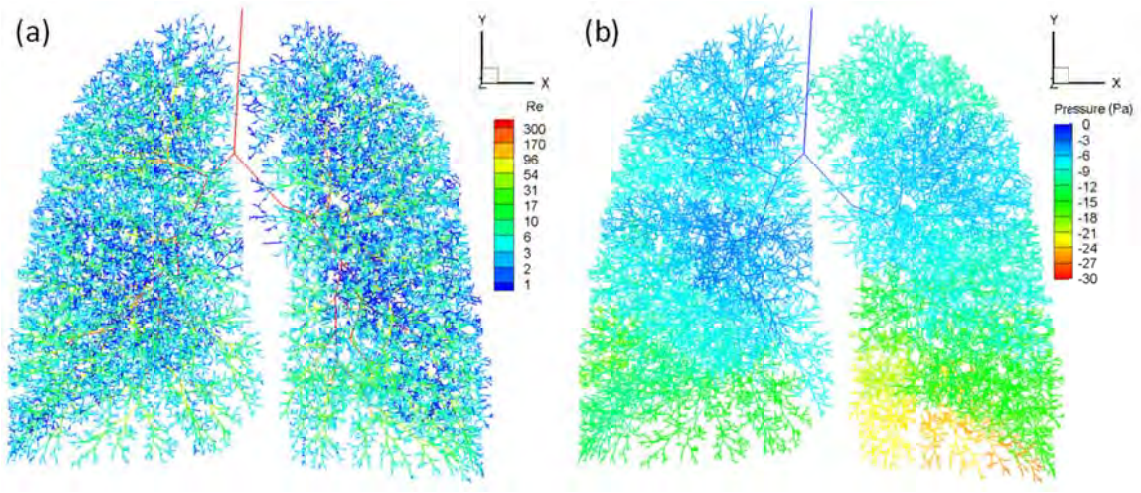

Figure 9.11 Regional distribution of (a) Re and (b) airway pressure in a breathing lung at the peak inspiration of tidal breathing near 85%VC. Exponentially divided Re levels represent the multiscale distribution of flow characteristics in the entire conducting airway.

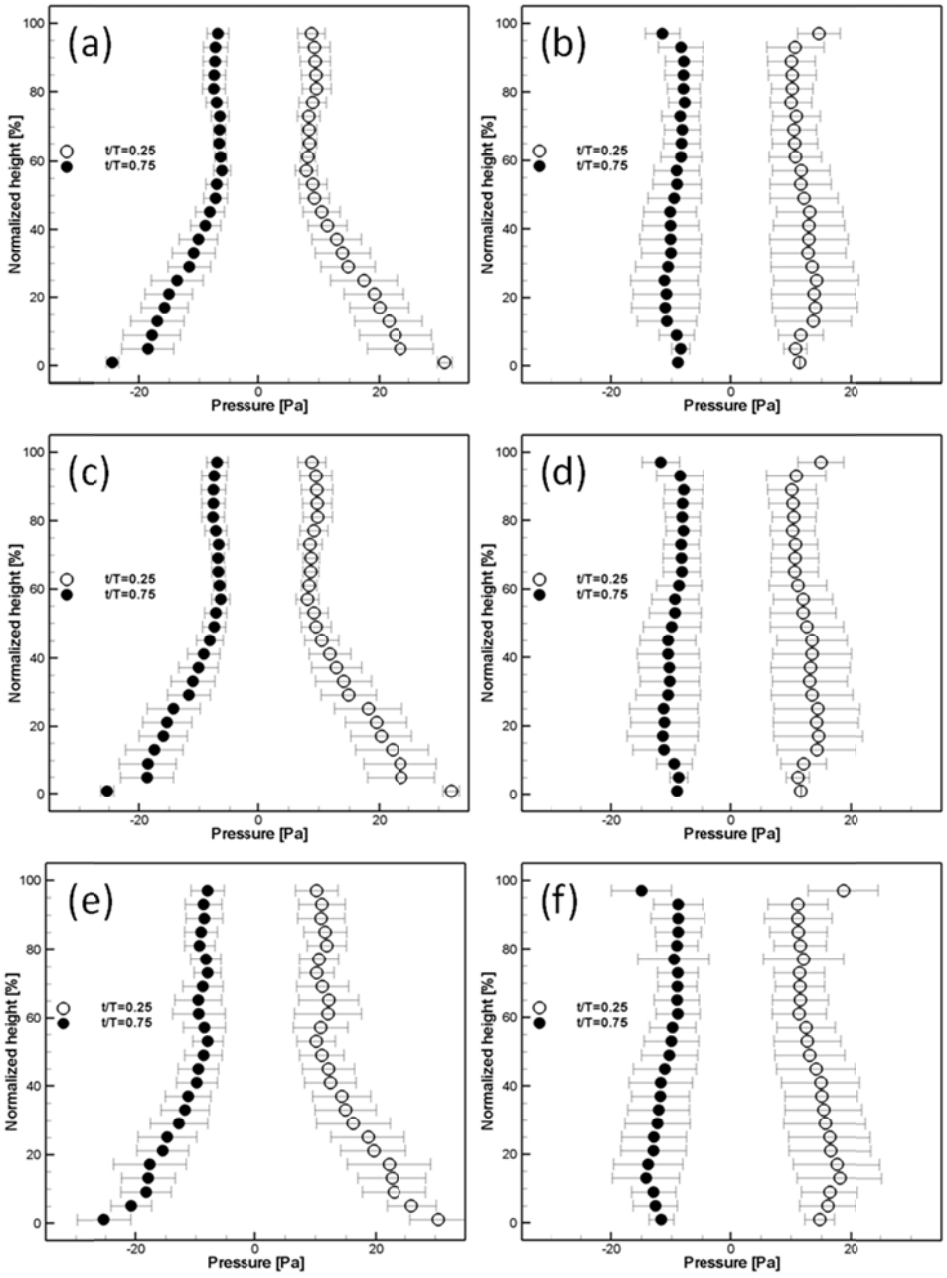

Figure 9.12 Comparisons of regional pressure distributions. (a,c,e) Base (0 %) to apex (100 %) and (b,d,f) dorsal (0 %) to ventral (100 %) distributions of the terminal airway pressure, averaged over the distal ends of terminal bronchioles at the same level of normalized height. (a,b) Rigid lung; (c,d) deforming lung with the end inspiratory volume at 85%VC; (e,f) deforming lung with the end expiratory volume at 55%VC.

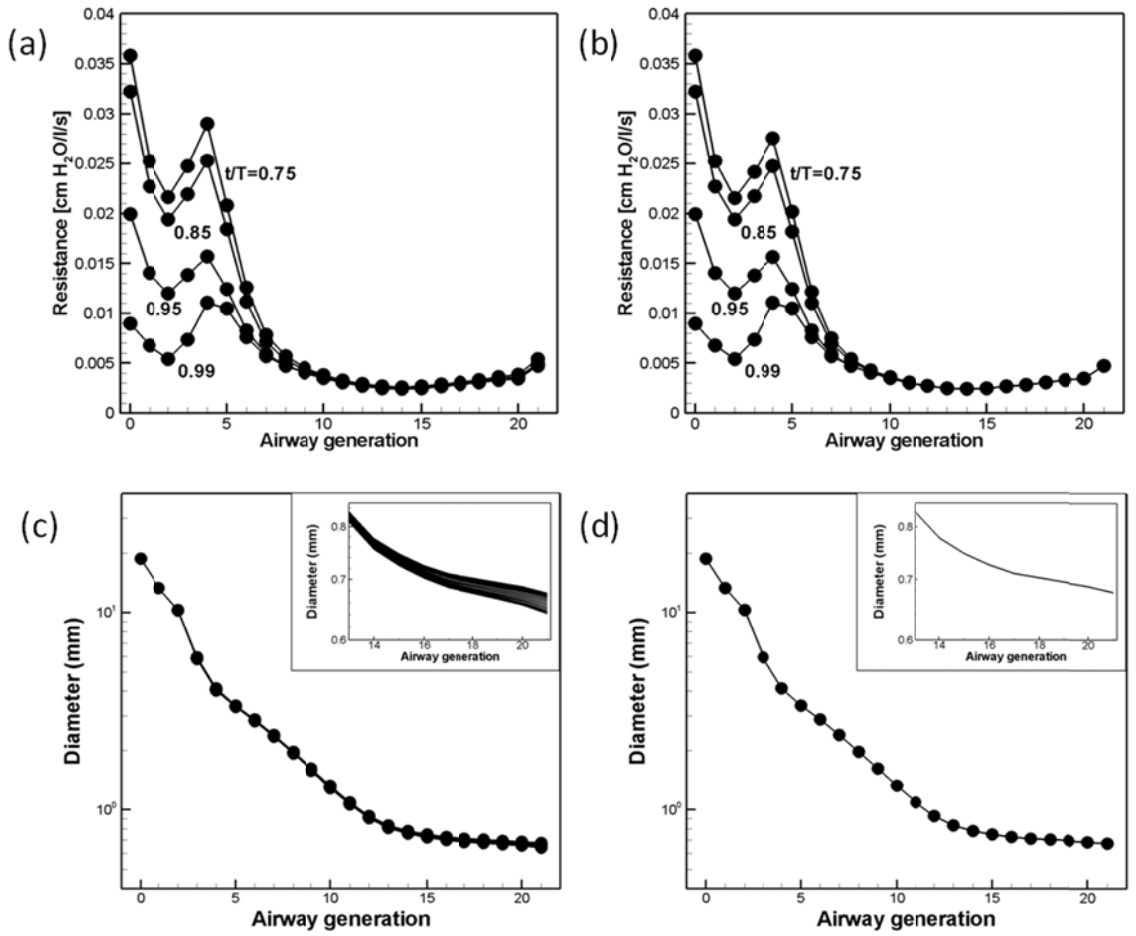

Figure 9.13 Generational distribution of airway resistance (a,b) and diameter (c,d) at the peak inspiration in a deforming lung (a,c) and rigid lung (b,d).

CHAPTER 10

CONCLUDING REMARKS

In this thesis, a comprehensive methodology is established for a CT-based multiscale numerical analysis of airflow in subject specific breathing human lungs, and applications are made to investigate the structure-function relationship in subject specific human lungs in consideration of physical and physiological issues.

From Chapter 2 to Chapter 4, the framework of a numerical analysis of 3D and 1D airway reconstruction from CT images, and proposed physiological boundary conditions, in addition to introducing CFD methods. LES captures the complex characteristics from various embedded flow types. It is shown that the current LES model is capable of high accuracy close to DNS, which is not obtained by RANS, for the airflow in subject specific large airways under normal breathing conditions. As the turbulent laryngeal jet is the most challenging feature of the airflow in the conducting airway, the in-house LES code is validated for a similar condition of stenotic pipe flow. The results successfully show reproduction of the experimental measurements in terms of the mean velocity and turbulent fluctuation, as well as the wall shear stress. The 1D energy based flow model solves the pressure-flow field in the rest of the entire conducting airway, providing physiologically consistent regional distribution. Based on these, an algorithm for the 3D-1D coupled CFD simulation and applications are discussed.

In addition, studies on the airflow in the subject specific conducting airway are presented. The effects of intra- and inter-subject variabilities of the CFD predicted airflow in the subject specific human lungs are investigated in Chapter 5. For an intra-subject study, airflows at two inspiratory flow rates are simulated on the airway geometries of the same subject with four different levels of truncation. These airway models are the original complete geometry and three geometries obtained by truncating the original one at the subglottis, the supraglottis, and the laryngopharynx, respectively.

A comparison of the airflows in the complete geometry model shows that the characteristics of the turbulent laryngeal jet in the trachea are similar regardless of Reynolds number in terms of mean velocities, turbulence statistics, coherent structures and pressure distribution. The truncated airway models, however, do not produce the similar flow structures observed in the complete geometry, with the pressure boundary condition imposed on the inlet. When the velocity boundary condition is employed, instead, to manipulate the nearly uniform distribution of velocity at the laryngopharynx, the mean flow result is significantly improved. And a spectral analysis shows that turbulent characteristics are captured downstream away from the glottis. It is worth emphasizing the role of the supraglottal space in formation of the turbulent laryngeal jet, and in correctly reproducing mean and turbulent characteristics not only in the trachea but also in the distal airway in the CT-resolved region. For an inter-subject study, although the overall flow characteristics are similar, two morphological factors are found to significantly affect the flows between subjects. These are the constriction ratio of the glottis with respect to the trachea and the curvature and the shape of the airways.

In the following Chapters 6 and 7, airflow characteristics and airway resistance in human lungs are investigated in a multiscale airway model, which consists of upper and intra-thoracic large airways of up to 7 generations, and physiologically-consistent peripheral small airways of up to 25 generations. With a pulsatile velocity waveform employed to produce a tidal volume of 500 ml, a turbulent laryngeal jet is formed in the trachea during inspiration, whereas the flow becomes laminar in the intra-thoracic airways at expiration. Viscous dissipation at both inspiration and expiration takes place in the boundary layer as well as in the core region where free shear flows prevail. The dimensionless viscous pressure drops in all the airway segments exhibit a similarity behavior proportional to $(Re)^n$ with $n \approx 1.5$ during both inspiration and expiration. This behavior is in good agreement with the classic model for airway resistance in spite of the complex subject specific asymmetric airway tree. Moreover, it is found that the viscous

dissipation is greater at expiration than at inspiration because free shear jet-like flow structures having $n \approx 2$ are more prevalent at expiration, as two flows from the child branches are merging in the parent branch. The newly calibrated model parameters for airway resistance together with a one-dimensional flow model are applied to the whole asymmetric airway tree model for a prediction of airway resistance and viscous pressure drop by generation. Strong airway viscous resistance is found at the trachea, the main bronchi, and the 4^{th} generation of the airways. In addition, the viscous resistance in the two lower lobes are higher than other lobes.

The current numerical analysis is further applied in Chapter 8 to clarify the underlying mechanism of clinical applications. High frequency oscillatory ventilation (HFOV), with a very small tidal volume and a high breathing frequency, is a clinically advantageous but not fully understood flow phenomenon. HFOV is studied using the current CFD analysis in three different geometrical models with increasing complexity: a straight tube, a single-bifurcation tube model, and a CT-based human airway model of up to seven generations. In the straight-tube model, the coaxial counter flow with opposing fluid streams is formed around flow reversal, agreeing with an analytical Womersley (1995) solution. However, the counter flow yields no net convective mixing at end cycle. In the single-bifurcation model, the counter flow at high Re is intervened with secondary vortices in the parent (child) branch at end expiration (inspiration), resulting in an irreversible mixing process, while the flow at low Re behaves similarly to the straight pipe flow. There found is an advantage of using a numerical analysis of experimental measurements. The three dimensional mixing process is hard to depict by experimental measurements. However, the current CFD model can correctly visualize the three dimensional mixing processes. In the CT-based airway model, three cases are considered, consisting of the normal breathing case, the high-frequency-normal-Re case (HFNR), and the HFOV case. The counter-flow structure is more evident in the high-frequency-normal-Re case than the HFOV case. The instantaneous and time-averaged stretch rates

at the end of two breathing cycles and in the vicinity of flow reversal are computed. It is found that counter flow contributes approximately 20% to mixing in HFOV.

Finally in Chapter 9, lung deformation is incorporated in a numerical analysis of the pulmonary airflow. Motions of both 3D and 1D airways are prescribed by the mass-preserving non-rigid image registration (Yin et al. 2009b) of the CT images at two levels of inflation. With reference diameters of the 1D airway tree from the volume-filling method, which are determined by the assumption of maximum expansion of airway cross sections (near TLC), the diameters of the deforming 1D airway are determined using the volume fraction calculated by the image-registration-derived regional Jacobian map. This method utilizes the implication of the image registration that the number of voxels per airway segment at reference and floating images can be regarded as unchanged. By dividing the volume of airway segment by the length determined by the coordinates of the branching points, the average cross-sectional area is computed and the diameter is estimated. The application of this approach can be extended to investigating physiological characteristics at a local airway level, as an estimation of the regional elastic pressure distribution is demonstrated using a model pressure-volume curve. With a subject specific regional ventilation BC, the energy-based 1D flow model predicts the pressure and flow fields in the entire conducting airway in breathing lungs. In more deflated lungs, the greater pressure drop to the terminal bronchioles is observed, retaining the qualitative consistency in the basal to apical and the dorsal to ventral distributions. When the end expiratory volume of deforming lung is set to the same as a rigid lung, a breathing cycle with the tidal volume of 500 ml and the period of 4.8 s experiences the similar features of velocity, pressure, wall shear stress, and so on, in both deforming and rigid lungs in the 3D framework. However, the laryngeal jet structure is observed to be affected. It is shown that the inflation during inspiration may cause the laryngeal jet to stretch longer in the deforming (longitudinal stretching) lungs, and the static geometry plays a key role during expiration by changing the curvature. At the smaller lung volume,

LMB has greater curvature that prohibits the triggering of instability in LMB and the trachea.

It is expected that the presented studies expand the appropriate use of a CFD analysis of pulmonary gas flows and help improving individualized medicine. Further investigations for the issues itemized below may follow up in a near future.

- Normal breathing and deep breathing with and without deformation near FRC.
- Further studies on inert gas transport and gas mixing in the conducting airway, comparing Lagrangian (with massless particles) and Eulerian (with passive scalar) approaches.
- The development of 3D-3D coupling framework combining the CT-resolved airway with the CT-unresolved airway reconstructed from the 1D centerline based geometry reconstruction.
- Population-based studies for a comparison of the subjects with normal and diseased lungs.

BIBLIOGRAPHY

Adler, K., Brücker, C., 2007. Dynamic flow in a realistic model of the upper human lung airways. Experiments in Fluids 43, 411-423.

Ahmed, S. A., and Giddens, D. P. 1983 Velocity measurements in steady flow through axisymmetric stenoses at moderate Reynolds numbers. *J. Biomech.* **16**, 505-516.

Allen, G. M., Shortall, B. P., Gemci, T., Corcoran, T. E., Chigier, N. A., 2004. Computational simulations of airflow in an in vitro model of the pediatric upper airways. Journal of Biomechanical Engineering 126, 604-613.

Aykac, D., Hoffman, E. A., McLennan, G. and Reinhardt, J. M. 2003 Segmentation and analysis of human airway tree from 3D X-ray images. *IEEE Trans. Med. Imaging* **22**(8), 940–950.

Babu, P. C., Mahesh, K., 2004. Upstream entrainment in numerical simulations of spatially evolving round jets. Physics of Fluids 16, 3699-3705.

Back, L. H. and Roschke, E. J. 1972 Shear-layer flow regimes and wave instabilities and reattachment lengths downstream of an abrupt circular expansion. *J Appl. Mech.* **39**, 677-681.

Batchelor, G. K. 2000 An introduction to fluid dynamics. *Cambridge*.

Bogey, C., Bailly, C., 2006. Large eddy simulations of transitional round jets: Influence of the Reynolds number on flow development and energy dissipation. Physics of Fluids 18, 065101.

Boyden, E. A. 1954 Segmental anatomy of the lung. *McGraw-Hill*.

Bull, J., Grotberg, J., 2003. Surfactant spreading on thin viscous films: film thickness evolution and periodic wall stretch. Experiments in Fluids 34, 1-15.

Brouns, M., Jayaraju, S. T., Lacor, C., De Mey, J., Noppen, M., Vincken, W., Verbanck, S., 2007. Tracheal stenosis: a flow dynamics study. Journal of Applied Physiology (Bethesda, Md.: 1985) 102, 1178-1184.

Caro, C. G., Doorly, D. J., Tarnawski, M., Scott, K.T., Long, Q. and Dumoulin, C. L. 1996 Non-planar curvature and branching of arteries and non-planar-type flow. *Proc. R. Soc. Lond. A* **452**, 185-197.

Cassanova, R. A. and Giddens, D. P. 1978 Disorder distal to modeled stenoses in steady and pulsatile flow. *J. Biomech.* **11**, 441-453.

Choi, J., Tawhai, M.H., Hoffman, E.A. and Lin, C.-L. 2009 On intra- and intersubject variabilities of airflow in the human lungs. *Phys. Fluids*, 21, 101901; DOI: 10.1063/1.3247170.

Choi, J., Xia, G., Tawhai, M. H., Hoffman, E. A., and Lin, C.-L. 2010. Numerical study of high frequency oscillatory air flow and convective mixing in a CT-based human airway model. *Ann. Biomed. Eng.* 38(12), 3550-3571. (in review).

Chon, D., Beck, K. C., Simon, B. A., Shikata, H., Saba, O. I., Hoffman, E. A., 2007. Effect of low-xenon and krypton supplementation on signal/noise of regional CT-based ventilation measurements. Journal of Applied Physiology 102 (4), 1535–1544.

Chon, D., Simon, B. A., Beck, K. C., Shikata, H., Saba, O. I., Won, C., Hoffman, E. A., 2005. Differences in regional wash-in and wash-out time constants for xenon-CT ventilation studies. Respiratory Physiology & Neurobiology 148(1–2), 65–83.

Christensen, G. E., Song, J. H., Lu, W., Naqa, I. E., Low, D. A., 2007. Tracking lung tissue motion and expansion/compression with inverse consistent image registration and spirometry. Medical Physics 34 (6), 2155–2163.

Collins, J. M., Shapiro, A. H., Kimmel, E., and Kamm, R. D. 1993 The steady expiratory pressure-flow relation in a model pulmonary bifurcation. *J. Biomed. Engrg*. **115**, 299-305.

Comer, J. K., Kleinstreuer, C. and Zhang, Z. 2001a Flow structures and particle deposition patterns in double-bifurcation airway models. Part 1. Air flow fields. *J. Fluid Mech.* **435**, 25–54.

Comer, J. K., Kleinstreuer, C., Zhang, Z., 2001b. Flow structures and particle deposition patterns in double-bifurcation airway models. Part 2. Aerosol transport and deposition. Journal of Fluid Mechanics 435, 55-80.

De Backer, J. W., Vos, W., Gorle, C., Germonpre, P., Partoens, B., Wuyts, F. L., Parizel, P. M., De Backer, M., 2008. Flow analyses in the lower airways: Patient-specific model and boundary conditions. Medical Engineering and Physics 30 (7), 872–879.

de Rochefort, L., Vial, L., Fodil, R., Maitre, X., Louis, B., Isabey, D., Caillibotte, G., Thiriet, M., Bittoun, J., Durand, E., Sbirlea-Apiou, G., 2007. In vitro validation of computational fluid dynamic simulation in human proximal airways with hyperpolarized 3He magnetic resonance phase-contrast velocimetry. Journal of Applied Physiology (Bethesda, Md.: 1985) 102, 2012-2023.

Dimotakis, P. E., 2000. The mixing transition in turbulent flows. Journal of Fluid Mechanics 409, 69-98.

Dimotakis, P. E., 2005. Turbulent mixing. Annual Review of Fluid Mechanics 37, 329-356.

Ding, K., Yin, Y., Cao, K., Christensen, G. E., Lin, C.-L., Hoffman, E. A., Reinhardt, J. M., 2009. Evaluation of lobar biomechanics during respiration using image registration. In: Proceedings of the 12th International Conference on Medical Image Computing and Computer-Assisted Intervention. London, UK, pp. 739–746.

Drazin, P. G., 2004. Hydrodynamic stability /. Cambridge ; New York : Cambridge University Press, Cambridge ; New York, .

Espinosa, F. F., Kamm, R. D., 1997. Thin layer flows due to surface tension gradients over a membrane undergoing nonuniform, periodic strain. Annals of Biomedical Engineering 25, 913-925.

Finlay, W. H., Nandakumar, K., 1990. Onset of two-dimensional cellular flow in finite curved channels of large aspect ratio. Physics of Fluids A: Fluid Dynamics 2, 1163-1174.

Finlay, W. H. 2001 The mechanics of inhaled pharmaceutical aerosols *Academic Press*.

Freitas, R. K., Schröder, W., 2008. Numerical investigation of the three-dimensional flow in a human lung model. *J. Biomech.* **41**(11), 2446–2457.

Fuld, M. K., Easley, R. B., Saba, O., Chon, D., Reinhardt, J. M., Hoffman, E. A., Simon, B. A., 2008. CT measured regional specific volume change reflects regional specific ventilation in supine sheep. Journal of Applied Physiology 104 (4), 1177–1184.

Gach H. M and Lowe, I. J. 2000 Measuring flow reattachment lengths downstream of a stenosis using MRI. *J. Magn. Reson. Imaging* **12**(6), 939-948

Gauderman, W. J., Avol, E., Gilliland, F., Vora, H., Thomas, D., Berhane, K., McConnell, R., Kuenzli, N., Lurmann, F., Rappaport, E., Margolis, H., Bates, D., and Peters, J. 2004 The effect of air pollution on lung development from 10 to 18 years of age. *N. Engl. J. Med.* **351**(11), 1057–1067.

George K. El Khoury, Helge I. A. , Bjørnar P., 2009. Simulating turbulent Dean flow in Cartesian coordinates. International Journal for Numerical Methods in Fluids 60, 263-274.

Green, A. S., 2004. Modelling of peak-flow wall shear stress in major airways of the lung. Journal of Biomechanics 37, 661-667.

Grgic, B., Martin, A. R., Finlay, W. H., 2006. The effect of unsteady flow rate increase on in vitro mouth–throat deposition of inhaled boluses. Journal of Aerosol Science 37, 1222-1233.

Grotberg, J. B. 1994 Pulmonary flow and transport phenomena. *Annu. Rev. Fluid Mech.* **26**, 52–71.

Grotberg, J. B. 2001 Respiratory fluid mechanics and transport processes *Annu. Rev. Fluid Mech.* 3, 421–57.

Guerrero, T., Sanders, K., Castillo, E., Zhang, Y., Bidaut, L., Pan, T., Komaki, R., 2006. Dynamic ventilation imaging from four-dimensional computed tomography. Physics in Medicine and Biology 51, 777–791.

Halpern, D., Grotberg, J. B., 2003. Nonlinear saturation of the Rayleigh instability due to oscillatory flow in a liquid-lined tube. Journal of Fluid Mechanics 492, 251-270.

Hammad, K. J., Ötügen, M. V. and Arik, E. B. 1999 A PIV study of the laminar axisymmetric sudden expansion flow. *Exp Fluids* **26**, 266-272.

Hedges, K.L., M.H. Tawhai, and P.J. Hunter., 2004. Ventilation distribution in the human lung: modeling flow in the conducting airways. *100th International Conference of ATS*, Orlando FL.

Heenan, A. F., Matida, E., Pollard, A., Finlay, W. H., 2003. Experimental measurements and computational modeling of the flow field in an idealized human oropharynx. Experiments in Fluids 35, 70-84.

Hoffman, E. A., 1985. Effect of body orientation on regional lung expansion: A computed tomographic approach. Journal of Applied Physiology 59, 468–480.

Hoffman, E. A., Gnanaprakasam, D., Gupta, K. B., Hoford, J. D., Kugelmass, S. D. and Kulawiec, R. S. 1992 VIDA: An environment for multidimensional image display and analysis. *Proceedings of SPIE: Medical Imaging* **1660**, 694–711.

Hoffman, E. A., Reinhardt, J. M., Sonka, M., Simon, B. A., Guo, J., Saba, O., Chon, D., Samrah, S., Shikata, H., Tschirren, J., Palágyi, K., Beck, K. C. and McLennan, G. 2003 Characterization of the interstitial lung diseases via density-based and texture-based analysis of computed tomography images of lung structure and function. *Acad. Radiol.* **10**, 1104–1118.

Hoffman, E. A., Clough, A. V., Christensen, G. E., Lin, C.-L., McLennan, G., Reinhardt, J. M., Simon, B. A., Sonka, M., Tawhai, M. H., van Beek, E. J. R. and Wang, G. 2004 The comprehensive imaging-based analysis of the Lung: a forum for team science. *Acad. Radiol.* **11**, 1370–1380.

Hogg, J. C., McDonough, J. E., Gosselink, J. V., Hayashi, S., 2009. What drives the peripheral lung remodeling process in chronic obstructive pulmonary disease? Proceedings of the American Thoracic Society 6 (8), 668–672.

Holmes, P., Lumley, J. L., Berkooz, G., 1996. Turbulence, coherent structures, dynamical systems, and symmetry. Cambridge University Press, Cambridge ; New York, pp. 420.

Horsfield, K., Dart, G., Olson, D. E., Filley, G. F. and Cumming, G. 1971 Models of the human bronchial tree. *J. App. Physiol.* **31**, 207.

Hu, H., Saga, T., Kobayashi, T., Taniguchi, N., 2001. A study on a lobed jet mixing flow by using stereoscopic particle image velocimetry technique. Physics of Fluids 13, 3425-3441.

Hyatt, R. E. and Wilcox, R. E. 1963 The pressure-flow relationship of the intrathoracic airways in man. *J. Clin. Invest.* **42**(1), 29-39.

Jan, D. L., Shapiro, A. H., Kamm, R. D., 1989. Some features of oscillatory flow in a model bifurcation. Journal of Applied Physiology 67, 147-159.

Jayaraju, S. T., Paiva, M., Brouns, M., Lacor, C., Verbanck, S., 2008. Contribution of upper airway geometry to convective mixing. Journal of Applied Physiology (Bethesda, Md.: 1985) 105, 1733-1740.

Jeong, J., Hussain, F., 1995. On the identification of a vortex. Journal of Fluid Mechanics 285, 69-94.

Jin, H. H., Fan, J. R., Zeng, M. J., Cen, K. F., 2007. Large eddy simulation of inhaled particle deposition within the human upper respiratory tract. Journal of Aerosol Science 38, 257-268.

Johnstone, A., Uddin, M., Pollard, A., Heenan, A., Finlay, W. H., 2004. The flow inside an idealised form of the human extra-thoracic airway. Experiments in Fluids 37, 673-689.

Kim, B. M., Corcoran, W. H., 1974. Experimental measurements of turbulence spectra distal to stenoses. Journal of Biomechanics 7, 335-342.

Kumar, H., Tawhai, M. H., Hoffman, E. A. and Lin, C.-L., 2009. The effects of geometry on airflow in the acinar region of the human lung. J. Biomech. **42**(11), 1635–1642.

Kwon, S. J., Seo, I. W., 2005. Reynolds number effects on the behavior of a non-buoyant round jet. Experiments in Fluids 38, 801-812.

Lee, T., Lin, C. L., Friehe, C. A., 2007. Large-eddy simulation of air flow around a wall-mounted circular cylinder and a tripod tower. Journal of Turbulence 8.

Lesieur, M., Metais, O., 1996. New trends in large-eddy simulations of turbulence. Annual Review of Fluid Mechanics 28, 45-82.

Liepmann, D., 1991. Streamwise vorticity and entrainment in the near field of a round jet. Physics of Fluids A 3, 1179-1185.

Lin, C.-L. and Hoffman, E.A. 2005 A numerical study of gas transport in human lung models. *SPIE Medical Imaging: Physiology, Function, and Structure from Medical Images* **5746**, 92-100.

Lin, C.-L., Lee, H., Lee, T. and Weber, L. J. 2005 A level set characteristic Galerkin finite element method for free surface flows. *Int. J. Numer. Meth.* Fluids **49**(5), 521–547.

Lin, C.-L., Tawhai, M. H., McLennan, G. and Hoffman, E. A. 2007 Characteristics of the turbulent laryngeal jet and its effect on airflow in the human intra-thoracic airways. *Respiratory Physiology and Neurobiology* **157**, 295-309.

Lin, C.-L., Tawhai, M. H., McLennan, G., and Hoffman, E. A. 2009 Multiscale simulation of gas flow in subject-specific models of the human lung. *IEEE Engineering in Medicine and Biology* **28**(3), 25-33.

Liu, J. T. C., 1989. Coherent structures in transitional and turbulent free shear flows. Annual Review of Fluid Mechanics 21, 285-315.

Liu, Y., So, R., Zhang, C., 2003. Modeling the bifurcating flow in an asymmetric human lung airway. J. Biomech. 36 (7), 951–959.

Longest, P. W., Vinchurkar, S., 2007. Effects of mesh style and grid convergence on particle deposition in bifurcating airway models with comparisons to experimental data. Medical Engineering & Physics 29, 350-366.

Lorensen, W. E., Cline, H. E., 1987. Marching cubes: A high resolution 3D surface construction algorithm. Computer Graphics 21 (4), 163–169.

Lu, P. C., Gross, D. R., Hwang, N. H. C., 1980. Intravascular pressure and velocity fluctuations in pulmonic arterial stenosis. Journal of Biomechanics 13, 291-300.

Ma, B. and Lutchen, K. 2006 An Anatomically Based Hybrid Computational model of the human lung and its application to low frequency oscillatory mechanics. *Ann Biomed Eng.*, **34** (11), 1691-1704.

Ma, B., Lutchen, K., 2009. CFD simulation of aerosol deposition in an anatomically based human large-medium airway model. Ann. Biomed. Eng. 37, 271–285.

Martonen, T. B., Yang, Y., Xue, Z. Q., 1994. Effects of Carinal Ridge Shapes on Lung Airstreams. Aerosol Science and Technology 21, 119.

Martonen, T. B., Quan, L., Zhang, Z., Musante, C. J., 2002. Flow simulation in the human upper respiratory tract. Cell Biochemistry and Biophysics 37, 27-36.

Massey, B. and Ward-Smith, J. 2006 Mechanics of Fluids. 8th-ed. *Taylor and Francis.*

Menon, A. S., Weber, M. E. and Chang, H. K. 1985 Effect of the larynx on oscillatory flow in the central airways: a model study. *J. Appl. Physiol*. **59**, 160-169.

Mittal, R., Simmons, S. P., Najjar, F., 2003. Numerical study of pulsatile flow in a constricted channel. Journal of Fluid Mechanics 485, 337.

Moin, P. and Kim, J., 1982. Numerical investigation of turbulent channel flow. *J. Fluid Mech.* **118**, 341.

Moser, R. D., Moin, P., 1987. The effects of curvature in wall-bounded turbulent flows. Journal of Fluid Mechanics Digital Archive 175, 479.

Nagata, M., Kasagi, N., 2004. Spatio-temporal evolution of coherent vortices in wall turbulence with streamwise curvature. Journal of Turbulence 5, 017.

Naib, S. A., Sanders, J., 1997. Oblique and Vertical Jet Dispersion in Channels. Journal of Hydraulic Engineering 123, 456-462.

Nowak, N., Kakade, P. P., Annapragada, A. V., 2003. Computational fluid dynamics simulation of airflow and aerosol deposition in human lungs. Annals of Biomedical Engineering 31, 374-390.

Olson, D. E., Iliff, L.D. and Sudlow, M.F. 1972 Some aspects of the physics of flow in the central airways. *Bull. Physiopath. Resp*. **8**, 391-408.

Palágyi, K., Tschirren, J., Hoffman, E. A., Beck, K. C. and Sonka, M. 2003 Assessment of segmental volume and radii of intrathoracic airway trees imaged by multi-row detector spiral CT. *Am. J. Respir. Crit. Care Med.* **167**(7), A846.

Park, N., Lee, S., Lee, J. and Choi, H., 2006. A dynamic subgrid-scale eddy viscosity model with a global model coefficient. *Phys. Fluids* **18**, 125109.

Pastur, L. R., Lusseyran, F., Fraigneau, Y., Podvin, B., 2005. Determining the spectral signature of spatial coherent structures in an open cavity flow. Physical Review E 72, 065301.

Patel, V. C., Sotiropoulos, F., 1997. Longitudinal curvature effects in turbulent boundary layers. Progress in Aerospace Sciences 33, 1-70.

Pedley, T. J. 1977 Pulmonary fluid dynamics. *Annu. Rev. Fluid Mech.* **9**, 229–274.

Pedley, T. J. and Kamm, R. D. 1997 Dynamics of gas-flow and pressure-flow relationships. In *The Lung: Scientific Foundations.* 2nd-ed. by R. G. Crystal, J. B. West, et al. *Lippincott-Raven Publishers*, 1365-1381.

Pedley, T. J., Schroter, R. C. and Sudlow, M. F. 1970a Energy losses and pressure drop in models of human airways. *Respir. Physiol.* **9**, 371–386.

Pedley, T. J., Schroter, R. C. and Sudlow, M. F. 1970b The prediction of pressure drop and variation of resistance within the human bronchial airways. *Respir. Physiol.* **9**, 387–405.

Pedley, T. J., Schroter, R. C. and Sudlow, M. F. 1971 Flow and pressure drop in systems of repeatedly branching tubes. *J. Fluid Mech.* **46**(2), 365–383.

Pedley, T. J., Schroter, R. C. and Sudlow, M. F. 1977 Gas flow and mixing in the airways. In *Bioengineering Aspects of the Lung*, ed. by J.B. West, Marcel Dekker, New York, **3**, 163–265.

Podvin, B., Fraigneau, Y., Lusseyran, F., Gougat, P., 2006. A Reconstruction Method for the Flow Past an Open Cavity. Journal of Fluids Engineering 128, 531-540.

Pope, S. B. 2003 Turbulent flows *Cambridge University Press*.

Proctor, D. F., 1977. The upper airways. II. The larynx and trachea. The American Review of Respiratory Disease 115, 315-342.

Reinhardt, J. M., Ding, K., Cao, K., Christensen, G. E., Hoffman, E. A., Bodas, S. V., 2008. Registration based estimates of local lung tissue expansion compared to xenon CT measures of specific ventilation. Medical Image Analysis 12 (6), 752–763.

Reynolds, D. B. and Lee, J. S. 1981 Steady pressure flow relationship or a model of the canine bronchial tree. *J. Appl. Physiol*. **51**, 1072-1079.

Rowley, C., Williams, D. R., 2006. Dynamics and control of high-Reynolds-number flow over open cavities. Annual Review of Fluid Mechanics 38, 251-276.

Saric, W. S., 1994. GOumlrtler Vortices. Annual Review of Fluid Mechanics 26, 379-409.

Salerno, M., de Lange, E., Altes, T., Truwit, J., Brookeman, J., Mugler, J., 2002. Emphysema: Hyperpolarized helium 3 diffusion MR imaging of the lungs compared with spirometric indexesinitial experience. Radiology 222 (1), 252–260.

Schroter, R. C. and Sudlow, M. F. 1969 Flow patterns in models of the human bronchial airways. *Respiration Physiology* **7**, 341-355.

Sera, T., Satoh, S., Horinouchi, H., Kobayashi, K., Tanishita, K., 2003. Respiratory flow in a realistic tracheostenosis model. Journal of Biomechanical Engineering 125, 461-471.

Sherwin, S. J. and Blackburn, H. M. 2005 Three-dimensional instabilities and transition of steady and pulsatile axisymmetric stenotic flows. *J. Fluid Mech*. **533**, 297-327.

Simone, A. F., and Ultman, J. S. 1982 Longitudinal mixing by the human larynx. *Respiration Physiology* **49**, 187–203.

Stănescu, D. C., Clément, J., Pattijn, J. and van de Woestijne, K.P. 1972 Glottis opening and airway resistance. *J. Appl. Physiol.* **32**(4), 460–466.

Stapleton, K., Guentsch, E., Hoskinson, M., and Finlay, W., 2000. On the suitability of k–ε turbulence modeling for aerosol deposition in the mouth and throat: A comparison with experiment. *J. Aerosol. Sci.* **31**(6), 739–749.

Taubin, G., 1995. Curve and surface smoothing without shrinkage. In: Proceedings of the 5th International Conference on Computer Vision ’95. Washington, DC, pp. 852–857.

Tawhai, M. H., Pullan, A. J., and Hunter, P. J. 2000 Generation of an anatomically based three-dimensional model of the conducting airways. *Ann. Biomed. Engineering* **28**, 793–802.

Tawhai, M. H., Hunter, P. J., Tschirren, J., Reinhardt, J., McLennan, G., and Hoffman, E. A. 2004 CT-based geometry analysis and finite element models of the human and ovine bronchial tree. *J. Appl. Physiol.,* **97**(6), 2310-2321.

Tawhai, M. H., Hunter, P. J., 2001. Multibreath washout analysis: modelling the influence of conducting airway asymmetry. Respiration Physiology 127 (2-3), 249–258.

Tawhai, M. H., Nash, M. P., Hoffman, E. A., 2006. An imaging-based computational approach to model ventilation distribution and soft-tissue deformation in the ovine lung. Academic Radiology 13 (1), 113–120.

Tawhai, M. H., Nash, M. P., Lin, C.-L., Hoffman, E. A., 2009. Supine and prone differences in regional lung density and pleural pressure gradients in the human lung with constant shape. Journal of Applied Physiology 107(3), 912–920.

Tschirren, J., Palágyi, K., Reinhardt, J. M., Hoffman, E. A. and Sonka, M. 2002 Segmentation, skeletonization, and branchpoint matching-a fully automated quantitative evaluation of human intrathoracic airway trees. *Medical Image Computing and Computer-Assisted Intervention MICCAI* Springer-Verlag Berlin Heidelberg (T. Dohi and R. Kikinis eds.) **2489**, 12–19.

Tschirren, J., Hoffman, E. A., McLennan, G. and Sonka, M., 2005a. Intrathoracic airway trees: segmentation and airway morphology analysis from low-dose CT scans. *IEEE Trans. Med. Imaging* **24**, 1529.

Tschirren, J., McLennan, G., Palagyi, K., Hoffman, E. A., and Sonka, M., 2005b. Matching and anatomical labeling of human airway tree. *IEEE Trans. Med. Imaging* **24**, 1540.

van Beek, E. J. R., Wild, J. M., Kauczor, H. U., Schreiber, W., Mugler, J. P., de Lange, E. E., 2004. Functional MRI of the lung using hyperpolarized 3-helium gas. Journal of Magnetic Resonance Imaging 20 (4), 540–554.

van Ertbruggen, C., Hirsch, C., Paiva, M., 2005. Anatomically based three-dimensional model of airways to simulate flow and particle transport using computational fluid dynamics. Journal of Applied Physiology 98 (3), 970–980.

Varghese, S. S., Frankel, S. H., 2003. Numerical modeling of pulsatile turbulent flow in stenotic vessels. Journal of Biomechanical Engineering 125, 445-460.

Varghese, S. S., Frankel, S. H. and Fischer, P. F. 2007 Direct numerical simulation of stenotic flows. Part 1. Steady flow. *J. Fluid Mech.* **582**, 253-280.

Varghese, S. S., Frankel, S. H., Fischer, P. F., 2008. Modeling transition to turbulence in eccentric stenotic flows. Journal of Biomechanical Engineering 130, 014503.

Vreman, A., 2004. An eddy-viscosity subgrid-scale model for turbulent shear flow: Algebraic theory and applications. *Phys. Fluids* **16**(10), 3670-3681.

van Ertbruggen, C., Hirsch, C. and Paiva, M. 2005 Anatomically based three-dimensional model of airways to simulate flow and particle transport using computational fluid dynamics. *J. Appl. Physiol.* **98**(3), 970–980.

Vétel, J., Garon, A., Pelletier, D. and Farnias, M.-I. 2008 Asymmetry and transition to turbulence in a smooth axisymmetric constriction. *J. Fluid Mech.* **607**, 351-386.

Wagner, E. M., Liu, M. C., Weinman, G. G., Permutt, S. and Bleecker, E. R. 1990 Peripheral lung resistance in normal and asthmatic subjects. *Am. Rev. Respir. Dis.* **141**, 584–588.

Wang, L., Wexler, A. S., Zhou, Y., 2000. Statistical mechanical description and modelling of turbulent collision of inertial particles. Journal of Fluid Mechanics 415, 117.

Weibel, E. R. 1963 Morphometry of the human lung *Springer Berlin-Academic Press*.

West, J. B. 2005 Respiratory Physiology: the essentials. 7th-ed. *Lippincott Williams and Wilkins*.

West, J. B., Hugh-Jones, P., 1959. Patterns of gas flow in the upper bronchial tree. Journal of Applied Physiology 14, 753-759.

Womersley, J. R. 1955 Method for the calculation of velocity, rate of flow and viscous drag in arteries when the pressure gradient is known. *J. Physiol.* **127**, 553-563.

Xia, G., Tawhai, M. H., Hoffman, E. A., and Lin, C.-L., 2010. Airway wall stiffening increases peak wall shear stress: a fluid-structure interaction study in rigid and compliant airways. *Ann. Biomed. Eng.* 38, 1836–1853.

Yanai, M., Sekizawa, K., Ohrui, T., Sasaki, H. and Takishima, T. 1992 Site of airway obstruction in pulmonary disease: direct measurement of intrabronchial pressure. *J. Appl. Physiol.* **72**, 1016–1023.

You, D. and Moin, P., 2007. A dynamic global-coefficient subgrid-scale eddy-viscosity model for large-eddy simulation in complex geometries. *Phys. Fluids* **19**, 065110.

Yin, Y., Hoffman, E. A., Lin, C.-L., 2009a. Local tissue-weight-based nonrigid registration of lung images with application to regional ventilation. In: SPIE Medical Imaging ’09. Vol. 7262. SPIE, p. 72620C.

Yin, Y., E. A. Hoffman, and C.-L. Lin. 2009b. Mass preserving nonrigid registration of CT lung images using cubic B-spline. *Med. Phys.* **36,** 4213-4222.

Yin, Y., Choi, J., Hoffman, E. A., Tawhai, M. H., Lin, C.-L., 2010. Simulation of pulmonary air flow with a subject-specific boundary condition. *J. Biomech.*43(11), 2159-2163. http://dx.doi.org/10.1016/j.jbiomech.2010.03.048.

Yin, Y., Hoffman, E. A., Ding, K., Reinhardt, J. M., Lin, C. L., 2011. A cubic B-spline-based hybrid registration of lung CT images for a dynamic airway geometric model with large deformation. Physics in Medicine and Biology 56, 203.

Zhang, Y., Finlay, W. H., 2005a. Experimental measurements of particle deposition in three proximal lung bifurcation models with an idealized mouth-throat. Journal of Aerosol Medicine 18, 460-473.

Zhang, Y., Finlay, W., 2005b. Measurement of the Effect of Cartilaginous Rings on Particle Deposition in a Proximal Lung Bifurcation Model. Aerosol Science and Technology 39, 394.

Zhang, Q., Johari, H., 1996. Effects of acceleration on turbulent jets. Physics of Fluids 8, 2185-2195.

Zhang, Z., Kleinstreuer, C., 2002. Transient airflow structures and particle transport in a sequentially branching lung airway model. Physics of Fluids 14, 862-880.

Zhang, Z. and Kleinstreuer, C., 2003. Low-Reynolds-Number Turbulent Flows in Locally Constricted Conduits: A Comparison Study. AIAA Journal 41, 831.

Zhang, Z., Kleinstreuer, C., 2004. Airflow structures and nano-particle deposition in a human upper airway model. Journal of Computational Physics 198, 178-210.